A POSSIBLE LOW-INTERMEDIATE TEMPERATURE PROTON CONDUCTOR BASED ON SILICON OXIDE PHOSPHATE

Stefan Saxin

A Thesis Submitted for the Degree of PhD
at the
University of St Andrews

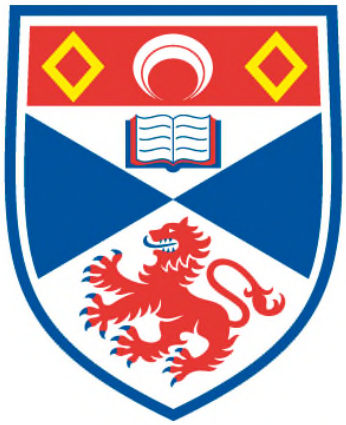

2015

A possible low–intermediate temperature proton conductor based on Silicon Oxide Phosphate

Stefan Saxin

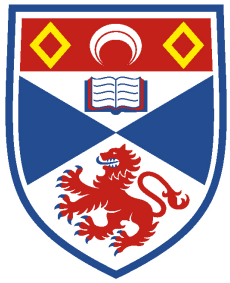

University of
St Andrews

A Thesis Submitted for the Degree of PhD
at the
University of St Andrews

29 May 2015

1. Candidate's declarations:

I, Stefan Saxin, hereby certify that this thesis, which is approximately 31,000 words in length, has been written by me, and that it is the record of work carried out by me, or principally by myself in collaboration with others as acknowledged, and that it has not been submitted in any previous application for a higher degree.

I was admitted as a research student in September 2009 and as a candidate for the degree of Doctor of Philosophy in August 2010; the higher study for which this is a record was carried out in the University of St Andrews between 2009 and 2014.

Date …… signature of candidate ……

2. Supervisor's declaration:

I hereby certify that the candidate has fulfilled the conditions of the Resolution and Regulations appropriate for the degree of Doctor of Philosophy in the University of St Andrews and that the candidate is qualified to submit this thesis in application for that degree.

Date …… signature of supervisor ……

3. Permission for publication: (*to be signed by both candidate and supervisor*)

In submitting this thesis to the University of St Andrews I understand that I am giving permission for it to be made available for use in accordance with the regulations of the University Library for the time being in force, subject to any copyright vested in the work not being affected thereby. I also understand that the title and the abstract will be published, and that a copy of the work may be made and supplied to any bona fide library or research worker, that my thesis will be electronically accessible for personal or research use unless exempt by award of an embargo as requested below, and that the library has the right to migrate my thesis into new electronic forms as required to ensure continued access to the thesis. I have obtained any third-party copyright permissions that may be required in order to allow such access and migration, or have requested the appropriate embargo below.

The following is an agreed request by candidate and supervisor regarding the publication of this thesis:

Embargo on all printed copy and electronic publication for a period of one year on the following ground: Publication would preclude future publication.

Date …….. signature of candidate …… signature of supervisor ……

Acknowledgements

During the time of doing my PhD at St Andrews there have been a lot of people whose support has been invaluable. I would like to especially acknowledge the following people who have given advice and been helpful during the course of this project.

First and foremost I would like to thank Prof. John Irvine for supervising and guiding me in this scientific endeavour, without which this project would not have been possible.

For materials synthesis of germanium oxide phosphate compositions, Mark Tham is greatly acknowledged. The same is also acknowledged together with George Carins for assisting with neutron data collection in June 2013. I am also very thankful for the assistance and help from Dr Winfried Kockelmann and the technical team at the Rutherford Appleton Laboratory that enabled successful collection of neutron data on the GEM instrument.

I would also like to thank Dr Filip Wormald and Dr Daniel Dawson for helping me collect the solid-state NMR data, Ross Blackley with SEM, Sylvia Williamson with TG and DTA, Dr Cristian Savaniu for assisting in setting up EIS measurements and Julie Nairn for helping me with equipment needed for lab work.

I am grateful to the remainder of my fellow colleagues in the JTSI group at the University of St Andrews, and to all the alumni too (I hope we will meet soon again).

I would also like to take this opportunity to thank my dear wife, Jennifer, for being very patient, loving and supportive. I am also very grateful to my parents for their strong support and encouragement.

Finally, I would like to acknowledge the funding for this project, which was provided by the Engineering and Physical Sciences Research Council (EPSRC).

"Ask, and it shall be given you; seek, and ye shall find; knock, and it shall be opened unto you"

Matthew 7:7

Abstract

The main material studied in this project is silicon oxide phosphate, often referred to in the literature as $Si_5O(PO_4)_6$. This material has highly unusual coordination of the silicon (octahedral, as well as the more common tetrahedral). The structure is hexagonal, it has been assigned to space group *R -3* and lattice parameters a ≈ 7.85 Å, c ≈ 24.14 Å.

This work's main focus is on understanding the interplay between structure and properties in order to enhance protonic conductivity for a fuel cell electrolyte.

Silicon oxide phosphate was synthesised with the solid-state method, using a gel precursor made from H_3PO_4, water and SiO_2. Various compositions were made with different P/Si starting ratios, ranging between 0.57 – 1.5.

There were small but significant differences in the a,b axes for the different compositions that corresponded to conductivity behaviour of hydrothermally treated P-Si compositions. This correlation was also found to appear in ^{31}P NMR for the chemical shift at - 44 ppm for untreated P-Si compositions as well as in the temperatures of the DTA peaks for the hydrothermally treated compositions. This all implies that this particular P-Si system with the addition of water becomes a ternary system that enables protonic conductivity.

A proposed mechanism for the protonic conductivity is given where it is suggested that protons flow along the internal channels of the structure using two waters that provide dual pathways for protons. This is possible through utilization of a proton thought to be in the structure (a P_OH bond of 1.57 Å).

Protonic conductivity could further be increased in the system by incorporating 85% H_3PO_4 in the P-Si materials, thus these materials act as matrices for the phosphoric acid.

Another composition, $Ge_5O(PO_4)_6$ with 5% extra germanium, was hydrothermally treated and found to have protonic conductivity at higher temperatures than the silicon oxide phosphate analogues.

Abbreviations

CHP	Combined Heat and Power
CPU	Central Processing Unit
DTA	Differential Thermal Analysis
EIS	Electrochemical Impedance Spectroscopy
GSAS	General Structure Analysis Software package
ICDD	International Centre for Diffraction Data
NMR	Nuclear Magnetic Resonance
PAFC	Phosphoric Acid Fuel Cell
PDF	Powder Diffraction File (card)
PEFC	Polymer Electrolyte Fuel Cell
PEM	Polymer Electolyte Membrane
P-Si	Phosphorus – Silicon
P/Si	Phosphorus : Silicon (ratio)
SEM	Scanning Electron Microscopy
SOFC	Solid Oxide Fuel Cell
TEM	Transmission Electron Microscopy
TGA	Thermogravimetrical Analysis
XRD	X-ray diffraction

Table of Contents

1. Introduction

The first fuel cell was invented by William Grove in 1839; it was in its infancy known as a "gaseous voltaic battery" [9]. Since the days of Grove much has happened. Although research interest on fuel cells sprung more from curiosity than a need, fuel cell research was revived with the space age in the 1960's [10]. NASA's interest in fuel cells was because nuclear power in space was deemed too risky, and batteries were too bulky in space vehicles.

Today fuel cells are once again interesting, this time with the call for sustainability and fuel efficiency. This is where one pillar could be the mass production of affordable and durable fuel cell systems that can replace batteries in mobile devices, substitute internal combustion engines in automotive vehicles or act as backup-systems for e.g. cell towers and hospitals [11].

What began as a scientific curiosity in the mid-1800's is today a widespread scientific field that has great potential in revolutionizing the way energy is transported and stored. It is a field of its own within materials science, and if its potential is fully tapped into through collaborative efforts between academia and industry then the resulting products will solve some of the most critical aspects of today's energy problems.

1.1 Why fuel cells?

One important factor is the current energy crisis – there is here a clear need for developing new resources in order to satisfy the world's growing energy demands. Especially in rural and / or underdeveloped areas it is important to create small independent sources of electrical energy that can benefit people and grow local economies. In sparsely populated areas it can many times be too costly to connect to the electrical grid. For those areas one could skip the step of connecting to a grid in a manner similar to how many underdeveloped regions of the world switched directly to mobile phone systems instead of first fully implementing telephone landlines.

Furthermore, fossil fuels such as oil and natural gas are not endless resources and sooner or later they will need to be replaced – oil is also a crucial chemical feedstock

and is expected to continue to be highly important for the chemical industry also in the long term future. Moreover, in the same industry there will be an increased demand for coal too along with renewable resources [12]. Therefore it would be prudent and beneficial if the available fuel and resources could be utilized in the most efficient manner. A third reason is the ongoing concern for greenhouse gases and their negative impact on climate change. Lastly, there is also the aspect of air quality, especially in regards to diesel vehicles that needs to be remedied. With widespread implementation of fuel cells emissions can be cut or in many cases cancelled out, especially when combined with clean renewable energy sources like solar, wind or wave power. Increased efficiencies in vehicles could also translate into longer range between fill-up, provided e.g. new and improved materials and technologies for hydrogen storage are developed.

1.2 What are fuel cells?

Fuel cells are electrochemical devices that convert chemical energy *directly* into electricity, thereby offering much more electrical output per unit fuel compared to classical combustion of the same fuel. They are highly efficient, silent and environmentally clean compared to any commercially available alternative today.

There are several different types of fuel cells, most of them are all solid-state units. The more common type of fuel cell system found on the market today is the Polymer Electrolyte Membrane Fuel Cell (PEMFC). PEM fuel cells are operated at low temperatures (40 – 80°C) and have the advantages of short start-up times, low emissions, low weight and small volume but disadvantages include the need for precious metals for their catalysts as well as utilizing ultra-pure hydrogen for fuel. This makes these types of fuel cells very expensive and hard to commercialize.

Another type of fuel cell is the Solid Oxide Fuel Cell (SOFC). They have much higher operational temperatures (600 – 1000°C) and enjoy the advantages of higher efficiencies and no need for precious metal catalysts. This also means they can offer higher flexibility in the choice of fuels. The disadvantages for these systems though are the longer startup times, but more seriously, the incoherent material expansions of the different components at the required operational temperatures are a problem associated with them. This issue often leads to degradation over time. Also, their

weight, volume and inherent fragility (of primarily the ceramic electrolyte materials) make them unsuitable for e.g. automotive application and mobile devices, however they are highly suitable for stationary applications. Fuel cell types are summarised in Table 1.

Fuel cell type	PEFC	PAFC	SOFC
Operating temperatures	40 - 80°C	150 - 220°C	600 - 1000°C
Electrolyte	Hydrated polymer (e.g. Nafion)	Phosphoric acid in SiC matrix	Primarily YSZ
Catalyst	Pt	Pt	Electrode material
Advantages	Short startup time	Intermediate temperature	High efficiency
Disadvantages	Lower efficiency, only ultrapure H_2, Difficult thermal and water management	Pressure induced corrosion	Incoherent material expansion, long startup times

Table 1 *Overview of a few main fuel cell systems. Based on [13].*

1.3 Areas of application

Although some type of energy is needed to produce or extract hydrogen for low–intermediate temperature fuel cell systems there is one great advantage that this enables, which is *the storage of energy*. Unlike a battery, energy cannot be stored in the fuel cell. It is however stored elsewhere, because it is chemically bound in the hydrogen itself. Effective storage of the hydrogen is the key to realizing the inherent advantages of fuel cells over other energy converting devices.

In the most efficient fuel cell systems, converting chemical energy to electrical power yields efficiencies of up to 60% (it can be over 80% if the heat is taken care of by adding a combined heat and power module, CHP). This can be contrasted to the petrol engine which efficiency is limited by the Carnot cycle, and in the ideal case can obtain 25% efficiency. If fuel cells were to substitute internal combustion engines in transportation, this would mean that the remaining reservoirs of fossil fuel could be used in a more optimal way.

1.3.1 The electrical grid

Moreover, in today's society the supply and demand patterns for e.g. domestic use of electricity varies depending on geographical location and time of day.

A chief principle by which all electrical grids function, is that there must always be a balance maintained between electricity input and output. If no auxiliary system exists to address over- and under production, then there will be losses due to overproduction at times when demand temporarily decreases or serious instabilities leading to grid failure if demand of electricity exceeds the production. The former issue of overproduction within the UK power grid are currently being temporarily remedied by e.g. paying out money for large wind farms not to operate during times of overproduction [14]. This is obviously non-sustainable, and yet it comes down to a seemingly simple question of managing temporary energy storage.

There are systems already in use to take care of these cases, some more renewable than others. One can for instance have a backup of oil-powered electrical power stations which have a quick startup time, but on the other hand burn fossil fuels. Another alternative is to use hydroelectric power through a dam, however this requires that the operating conditions permit taking out the required amount of power at that point in time – there could be a drought and too little water available, or conversely, too much water in the dam and a restriction on the amount of water allowed through in order to avoid flooding below the dam. Naturally, renewables like wind, solar and wave power all have their respective weather dependencies; therefore outputs can subsequently vary to a large degree during very short time-spans making the electrical power-grid vulnerable. This would make widespread expansion of renewables highly difficult, especially when considering a large future part of any national power grid. One possible way of solving this problem would be to use renewables as independent power sources, separately and independently from any power grid. A farm could for instance have its own wind farm and solar panels to run everything from, yet there would still be electricity at a surplus at times and at other times a deficit would be the case (making it necessary to be connected to either a grid or a generator of some sort). The solution to both these cases (widespread implementation of renewables and making singular units self-sufficient on renewable energy) would be to couple renewable energy systems with fuel cell and electrolyzer

systems. This way a farm could use e.g. solar panels during sunny days to not only power all electrical units but also electrolyze water and make hydrogen gas. The gas could then be stored and used in a fuel cell when the renewable source is unable to produce the amount of electricity needed.

It is far from being technically impossible; however, because these units produce a varying amount of electricity depending on current weather conditions, whereas oil-, coal- or nuclear power plants can produce a stable amount of electricity, the latter become far more appealing than the former. It also comes down to economics and cost – investing in e.g. off-shore wind and hydrogen infrastructure is more expensive than simply using oil or other already available energy infrastructure [15]. Nevertheless, it still stands to reason that if fuel cell technology can be applied, there would be a way of taking care of all the power generated by renewables, thereby maximizing the use of the renewable power stations and harnessing a great deal more renewable energy.

Another more localized solution would be to have a fuel cell driven vehicle that runs all the time (including charging a battery in the vehicle), also when parked at home or at a workplace. If the hydrogen is supplied and derived from stored hydrogen gas obtained from electrolysis of water via solar panels on the roof, this would provide renewable electrical energy to a home or office building as well as power the vehicle itself when on the road. The benefit of running a fuel cell system continuously like this would be that the stress is minimized and the durability of the materials in the fuel cell are extended, in addition, it would cut down consumption of electricity taken from the grid. Electricity generated from a renewable source in the home would, apart from the installation and component costs, be completely free.

Today fuel cells have established themselves on a few markets, e.g. for fork lifts, cell towers and military portable power units.

1.3.2 Replacing batteries

Perhaps one new area before the full implementation into automotive vehicles will be laptop devices and smartphones. The reason for this is that these devices are becoming increasingly power consuming, as demands for greater processing power for computing and graphical rendering increase from year to year. Developments in

battery technology have up until now been able to keep up to a certain degree, as better and better batteries have been engineered to handle the increased loads. For example, in the past few years it has been quite common to have a battery life of around 7 hours in a standard laptop. Later years' MacBook Airs from Apple (13.3" models with either Intel's Haswell or Broadwell processor and an all-solid-state architecture) have up to 12 hours of battery life depending on how they are used [16]. This is a very similar battery life compared to the very first Apple Macintosh Portable (from 1989) which had a lead-acid battery (similar to the battery technology found in cars); this was a portable computer that could run for 6 – 12 hours unplugged [17]. In the case of Apple portable computers the progression has gone from lead-acid, to Ni-Cd, to Ni-Mh, to Li-ion and Li-polymer. For the last type of battery one has gone to great lengths to reduce redundant space (e.g. the safety enclosure) in order to use more of the available space for energy storage, effectively making the battery non-removable, as well as optimizing the rest of the computer infrastructure (screen, hard-drive and CPU) to make it less power consuming. The alternatives a laptop manufacturer like Apple faces is to either make the battery bigger, or keep it the same size or smaller and get a device that needs to be charged more frequently; or lastly, find a better technology that will power the device for much longer times than the current Li-polymer battery technology. Such an approach could well include a fuel cell setup that attaches to the computer or is built-in, provided adequate materials are found and the incentive for launching such a product is there. Indeed, Apple did file a patent for a fuel cell system for a portable computing device in August 2010 [18], and then a follow-up patent in April 2011 [19], and it is therefore conceivable that this type of application will find its way into some of the product line for its mobile devices in the near future. If this will be the case, then there is a great likelihood that other computer and mobile phone companies will follow suit by introducing their own fuel cell powered devices – companies like Samsung, Acer and Dell. This would be a true revolution that would familiarize people to fuel cell technology as well as trigger third-party solutions for small scale fuel storage and reforming. A related area where a smaller type of fuel cell would fill a critical need would be in smartphones, as these currently struggle to keep a day's charge when operated normally.

Deep cycle (heavy duty) batteries for mobile homes could also be replaced or complemented with a fuel cell for harnessing electricity produced by a renewable

source. One could e.g. run a SOFC in electrolysis mode to produce synthetic fuel and then switch to fuel cell mode to utilize the electricity when needed. Or one could have a low–intermediate temperature option that could run on methanol. This would enable campervans, caravans and small cottages to be completely off-grid and store energy well beyond today's options.

1.4 Filling the temperature gap

Despite the number of benefits that PEM fuel cells have compared to other kinds of fuel cells there are a number of drawbacks. One major aspect is that the low operating temperature will yield slower kinetics. More specifically, CO from the fuel gasses will bind to the platinum sites of the catalysts, thereby poisoning the catalyst (i.e. there will be inhibition of the desired electrochemical reactions). This can be overcome by using ultra pure hydrogen as fuel, however this would not be feasible when fuel cells become more commercially available as it would be too expensive. If a variety of fuels are to be used, the operating temperature of the fuel cell would have to be increased to over 150°C for the chemisorption of CO not to be a problem.

Moreover, the relative humidity should not be too high as this requires humidifiers which adds to the weight and volume of the fuel cell system.

1.5 The hydrogen economy

The hydrogen economy is a term ascribed to a future global system in which hydrogen and electricity are the main energy vectors. It is widely held that oil is a limited resource and that it is only a matter of time until the modern world economy will have to adjust to a world that is less dependent on fossil fuels, and more dependant on renewables. Adjustments on a global scale have occurred before – the world economy has gone from wood to coal, to oil and is now moving toward natural gas – increasing the ratio of hydrogen to carbon for each fuel added. It is therefore not

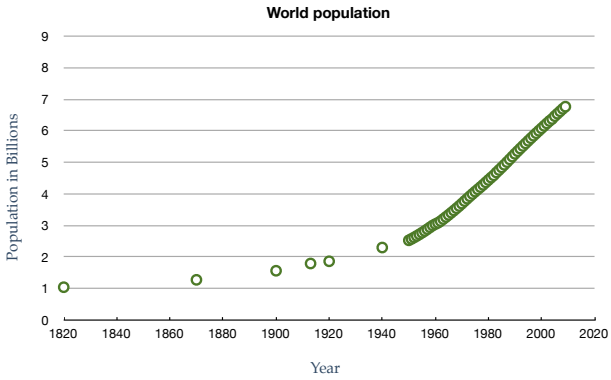

Figure 1 *The world population since 1820, after an estimate by Prof Angus Maddison [3].*

inconceivable that hydrogen one day will become the main fuel.

To gain historical perspective it is worth looking at the world population (Figure 1) as well as taking a look at the actual world energy consumption of the past century, see Figure 2. This latter figure contains an estimate on world energy production data compiled from the Shift project [6]. According to this data one can draw the conclusion that when a new type of fuel becomes established it does not go away – it merely adds to the total amount of fuels available and yields a more diversified portfolio of available fuels. In the same graph, Figure 2, it can be noted that oil is the predominant fuel, although the energy production from coal which has been around for a long time has almost doubled in the recent decade – this is likely due to developing countries like China and India which are increasing their production as they seek to take their economies to a more developed state.

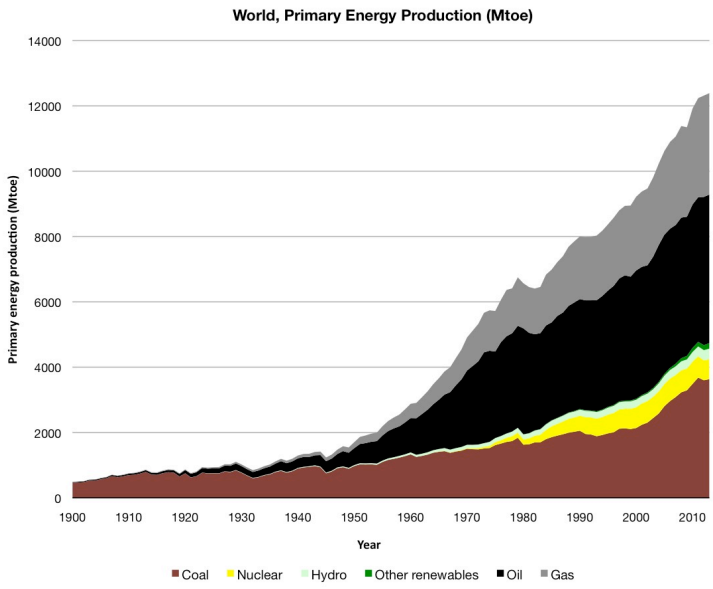

Figure 2 *An estimate of the world energy production since the year 1900. Data summarised from the Shift Project [6], originally sourced from Bouda Etemad and Jean Luciani, "World Energy Production 1800 – 1985" for the period 1900-1980 and from "US EIA Historical Statistics for 1981-2013" for the period 1981-2013.*

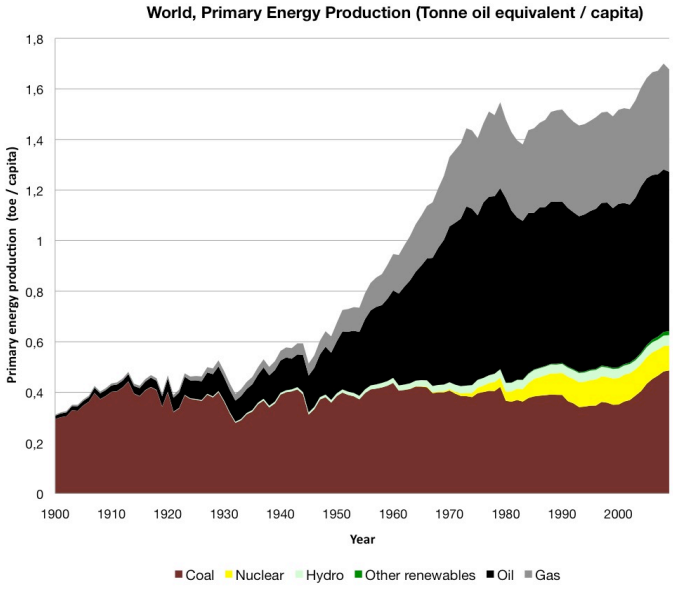

Figure 3 *An estimate of world energy production per capita since the year 1900. Summarized data from the Shift Project [6] divided by an interpolated approximation of world population, originally approximated by Prof Angus Maddison [3] then interpolated linearly by the author for the missing years in the early 1900's.*

Although the total world energy production does look quite

dramatic (as seen from Figure 2), one has to bear in mind that the world population has grown a lot during the same time. Looking at the same energy production data and dividing it by a yearly estimate of the world population, so that a per capita figure over time is obtained, one can conclude that the total world energy production per capita has more than doubled since the mid-1950s, see Figure 3.

Moreover, a decrease in growth rate for the past few decades seems to be the case compared to the massive growth period between 1945 – 1970, when looking at the energy production estimates on a per capita basis.

The timing for when the hydrogen economy needs to be implemented depends on a number of factors. If indeed the current usage of fossil fuels is unsustainable then that certainly is a reason for a quicker implementation. This does hold true in the long run but there is also great uncertainty as to when the fossil fuel resources will be too expensive to extract, and when oil production in particular will peak [20]. The other aspect is whether the hydrogen economy can deliver on its promises. If for instance hydrogen is produced from fossil fuels one may as well use fossil fuels directly.

1.5.1 Hurdles on the road toward a Hydrogen economy

The main problem to implementing the hydrogen economy is that the technology is too expensive at the moment. A major reason for the high cost is because it is not mass manufactured, and because of the usage of exotic materials such as rare-earth catalysts in low temperature fuel cell systems. Currently hydrogen technology is only produced in small volumes due to a low demand (which in turn is largely due to that prices are too high). Although calculations have been made suggesting that we are close to a point where the unit cost for producing hydrogen from a renewable source (wind) and running a fuel cell vehicle would correspond to a petrol cost of $1.7 / litre [21] which is below the current UK sale price of petrol.

If prices came down to the point where it makes financial sense to the users, then it follows that it would be more attractive for companies and people to invest in hydrogen technology in order to harness the great benefits of renewable energy.

It is however a simplification to solely attribute the reason for the lack of hydrogen infrastructure to a modern chicken and egg problem. From the materials side of the

issue many practical problems still remain to be solved, before we see the hydrogen economy gaining any foothold. The chief things to solve are the sustainable production of hydrogen, cheap and efficient hydrogen-storage and making sure fuel cell systems are robust, long-lived and affordable. These are major challenges that are currently being addressed but will take some time to solve and implement on a large scale. Once viable solutions for these obstacles are on the market, hydrogen has the potential to become an energy vector on equal footing with electricity.

1.5.2 The need for new infrastructure and new materials

Hydrogen is a very small and light molecule which will readily escape, moreover, it can embrittle certain metals such as steel and other metals [22]. Therefore, to for instance use current infrastructure, such as e.g. pipelines, gas tankers and trucks to transport hydrogen gas may not be a realistic option.

Moreover, storage and handling of hydrogen gas raises questions of safety primarily because it is a very much unknown area in the consumer environment [23] and because of hydrogen's odourless nature. In current PEM automotive technology high pressures are required which means a number of safety measures have to be taken such as hydrogen sensors and intricate design of the fuel tank [24]. Being able to refuel hydrogen gas into high pressure fuel tanks requires even higher pressures in the tanks at the filling stations, and to compress the gas in the first place requires extra energy, which of course impacts the overall efficiency. One candidate for solving some these problems could be a type of solid-state storage for hydrogen, perhaps in the form of metal hydrides, metal organic frameworks (MOFs) or carbon nanotubes.

Currently a system with metal hydride would be considerably heavier than high pressure tanks, but the advantage would be that it is safe solid-state storage removing the need for high pressures; this would enable refuelling stations for hydrogen to have a simpler layout – because they would not require the high pressure capabilities but something more akin to what goes into a car tyre.

There are also efforts to try and make an affordable and efficient liquid storage for hydrogen, using e.g. hydrous hydrazine or formic acid [25].

Whichever technology comes out as the standard for delivering and storing hydrogen

there will be more refuelling stations offering hydrogen in the coming decades, this in turn will make it more appealing for the average consumer to consider buying a vehicle that runs on hydrogen. Therefore, finding a lightweight, safe and cheap material that can store the necessary amounts of hydrogen gas needed (c:a 5 - 10 kg) is an ongoing challenge for materials scientists.

A last but not unimportant bit to the puzzle would be the car manufacturers' and electric power producers' willingness to do research and development programs so that products can be on the market. With an extensive research program there are financial risks involved and as long as the demand for e.g. automotive vehicles with combustions engines is sufficiently high, there is little that will convince automotive manufacturers to implement a new long term strategy. Would the infrastructure be in place, then things would be very much different and there would be a direct incentive for the manufacturers to develop standardized technologies.

The positive news is though that there are a number of car manufacturers that have ongoing research into fuel cell technology, among them are Ford, Volkswagen and Toyota. As examples of this can be mentioned a joint project between Ford, Daimler and Renault-Nissan who joined forces in 2013 in order to develop a hydrogen powered fuel cell for a vehicle. Their hope when doing this was to speed up the research process and introduce a vehicle in 2017 [26]. In 2013 Volkswagen AG announced that they signed a contract with Ballard Power Systems to develop and manufacture fuel cells for their demonstration fleet [27]. In early 2015 Toyota released all their fully owned fuel cell patents so that anyone can use them on a royalty-free basis. This should be interesting especially for hydrogen production and supply as those patents are released for unlimited time, whereas their fuel cell vehicle patents will only be available royalty-free until end of 2020. [28]

Concept cars are also available by Toyota (their FCV), Honda has had their Clarity FCX available through leasing in California and Mercedes-Benz offers their B-Class F-cell for leasing in USA, Europe, Japan and Singapore. Both the Clarity FCX and the B-class F-cell have a range of 240 miles and are powered with electrical engines of 134 horsepower, their pressurized hydrogen storage tanks have capacities of 4.1 kg and 3.7 kg, respectively [29]. Recently Toyota introduced a new fuel cell vehicle based on their FCV concept, the Toyota Mirai, which started selling in December

2014 in Japan. It features two hydrogen tanks as well as a Nickel metal hydride battery which together gives the vehicle a range of 400 – 435 miles. The retail price is $57,600 before taxes and production volumes are planned to 400 in Japan and 300 in the rest of the world for 2015. [30]

The world's first mass produced fuel cell vehicle is the Hyundai ix35 Fuel Cell which in Korea is set to be lowered in price from the equivalent of about $138,000 to about $77,000 [31] – this vehicle is a SUV with an official range of 369 miles according to Hyundai [32] however has been shown in real-life conditions to manage 435 miles on a full tank [33].

In summary, fuel cell research is a promising field as products are being launched to the market, however there is a great need for infrastructure in order for it to develop its full potential. Because fuel cells offer higher efficiencies in converting fossil fuels for powering e.g. vehicles and portable appliances, this will in the long run fill an important role in society. Coupled with efficient electrolyzers and viable hydrogen storage they would enable widespread implementation of renewables, both for small independent units and for connecting to the electrical grid. The current challenges that fuel cells face are primarily a lack of hydrogen infrastructure (for hydrogen production, storage and re-fuelling [21]), high production costs and material issues.

If the two primary problems of production and storage of hydrogen are not solved, then it is likely that one would have to use other fuels – e.g. methanol to power a future generation of fuel cells for automotive vehicles. It may be necessary to introduce fuel cells that are not primarily linked to hydrogen, which would be an intermediary step to hydrogen-based fuel cells.

Another alternative could be to use SOFCs, even though this has its own set of problems due to the higher temperatures at which they operate.

One important aspect here is the higher physical requirements on the materials – such as stability over time and the need for small thermal expansion coefficients. It is not unlikely that a reversed trend will occur for SOFCs compared to that of PEFCs – that a decrease in operating temperatures is at the horizon if other materials than YSZ come into question and other designs. As an example of this can be mentioned one such proposed system, "the Cube", by Redox, which if realized promises to change

the market for SOFC at costs that are substantially lower (≈ $800 – 1500 per kilowatt depending on scale of production) than what the standard is today – compared to e.g. Bloom's energy server at an estimated $10,000 per kilowatt. [34]

1.6 The fuel cell electrolyte

In PEM and PAFC-types of fuel cells, protons are transported through the electrolyte from the anode to the cathode. The electrolyte must have a number of properties, such as being mechanically and thermally stable over time, show no electrical conductivity, have high proton conductivity and show no permeability to fuel (i.e. be gas tight).

Solid state proton conductors that are thermally and mechanically stable would be an integral part of the hydrogen economy, especially when it comes to making fuel cells that need to be mobile, contain little or none precious metals, have short start-up times and offer some fuel flexibility. From a materials perspective, the hydrogen economy hinges on adequate storage and means of transportation for the hydrogen but also that the criteria set for the hydrogen fuel cell systems are met. Thus, there is a great need for finding inexpensive and well-performing materials for all the components of a hydrogen fuel cell, the electrolyte being no exception.

1.7 The case for intermediate temperatures

High temperature fuel cells are more efficient because waste heat to a large extent can be reused. In addition, no special catalysts are required and as a consequence more fuels are available.

Low temperature systems on the other hand, may have less corrosion and are therefore more stable over time – they also start up quickly. Low temperature fuel cells could be used in mobile devices, such as laptop computers and smartphones because of their limited size.

Fuel cells for the application of automotive vehicles have the potential to be air cooled instead of water cooled. Cooling with water uses more energy and takes up more space, and most importantly, lowers the overall efficiency of the fuel cell system. If the operating temperature is around 200°C, the heat will be of sufficiently high grade to be used elsewhere, moreover heat management will be both less

complicated and less energy consuming compared to any low temperature options.

Using a higher temperature (as in SOFC) will lead to problems concerning mismatch of thermal expansion coefficients for the different components of the fuel cell, especially when powered on and off many times, which can lead to a failure of the system. An SOFC is also sensitive and fragile because of its ceramic construction; this severely limits its use in any non-stationary application.

Thus, a fuel cell system for automotive vehicles should ideally operate in the temperature range of 180 – 400°C. If developed for a mobile device the operating temperature could be lower as small amounts of rare-earth catalysts may then be utilized. Such a fuel cell could run at temperatures around 100°C e.g. using excess heat from the CPU and would be a superior alternative to any battery.

Developing a good proton-conducting electrolyte in the low-intermediate temperature range that shows stability over time is an objective of this project.

1.7.1 Scientific query and scope of this thesis

The scientific queries that this work will answer are:

I) Is there a solid solution[1] for the P-Si system which belongs to the *R -3* space group, i.e. can there occur substitution between silicon and phosphorus in the ionic lattice?

II) What are the possibilities to improve protonic conductivity for the silicon oxide phosphate system?

III) Can a relationship be established for predicting protonic conductivity based on e.g. given cell parameters, that applies to the family of phosphosilicate materials that are structurally related to $Si_5O(PO_4)_6$?

1.7.2 Future scientific query

A future question, that will only lightly be discussed in this thesis, is:

Can this relationship be extended and developed into a theory also pertaining to other

[1] One definition for a solid solution is a "mixture of two crystalline solids that coexist as a new crystalline solid, or crystal lattice." (35. Perkowitz, S., *Solid solution*, in *Encyclopædia Britannica*.)

systems with the same structure, such as to $Ge_5O(PO_4)_6$?

This latter question is the starting point for continued future work, to which this thesis hopes to have laid the ground work in developing an approach and a methodology that takes into account the issues that have been encountered during the project, so that the development of a solid state proton conductor can be realized.

1.8 Overview of this thesis

In chapter 2 the parent composition, $Si_5O(PO_4)_6$, is reviewed from the literature as well as SiP_2O_7. Also, a brief overview of different types of fuel cells is presented in this same chapter.

Chapter 3 presents an overview of the experimental and characterization techniques used in this project.

Chapters 4 and 5 discuss the results from the project; the first part is for the pure silicon oxide phosphate system and the second part is for substituted phosphate systems. Lastly, chapter 6 discusses the findings and conclusions of the project and offers a theory for how the protonic conductivity is related to water and structure of $Si_5O(PO_4)_6$.

Appendix A1 presents bond lengths and bond angles from Rietveld refinements based on neutron data where some occupancies were varied.

Appendix A2 displays the coordinates and UISO values for both the fixed occupancies and varied occupancies Rietveld refinements.

In Appendix B a couple of examples of Rietveld refinement methodologies are given, there is also a section at the end for the sequential refinements and how they were done.

Appendix C contains combined TG and DTA data for the P-Si gels.

Appendix D gives the sintering temperatures and times for all the important samples in this thesis, along with stoichiometries for the substituted silicon oxide phosphate samples in chapter 5.

Appendix E1 displays the bond lengths for the untreated and hydrothermally treated compositions as a function of temperature, derived from neutron diffraction data where all occupancies were fixed to 1. Appendix E2 shows the same data (as well as bond angles) in table form.

Appendix F gives some supplementary ^{2}H NMR data which has been properly scaled to compensate for longer collection time on one of the hydrothermally treated compositions.

Appendix G shows the model generated by GSAS and the collected neutron data for each bank of the GEM instrument at room temperature, untreated and hydrothermally treated parent composition in a side-by-side comparison.

2. Literature review

2.1 The intermediate temperature gap

There are a number of different fuel cell systems available today – from low temperature to high temperature systems. High temperature fuel cells (SOFCs mainly) take advantage of the oxygen conductive nature of certain ceramics; whereas low temperature (PEFC and PAFC) are built around proton conducting electrolyte membranes. As pointed out in the previous chapter, these all have their respective pros and cons and are thus suited for different application areas, however, the main thing is that they all convert electrochemically stored energy to electricity without any combustion step.

There is a temperature gap between these fuel cell technologies where a good ionic conductor is needed in order to make a more optimal fuel cell. This gap is known as the intermediate temperature gap (illustrated in Figure 4) and has become an area of much interest for fuel cell and materials scientists. An ideal candidate for bridging this gap would be a true proton conductor, i.e. a material that conducts protons without the aid of humidity or liquid water.

2.2 Fuel cell overview

2.2.1 The polymer electrolyte fuel cell (PEFC)

Amongst the different types of fuel cells perhaps the most relevant for this project is the polymer electrolyte fuel cell (PEFC). These fuel cells operate at a low temperature (normally between 80 – 90°C) and are composed of a proton conducting electrolyte that fully or

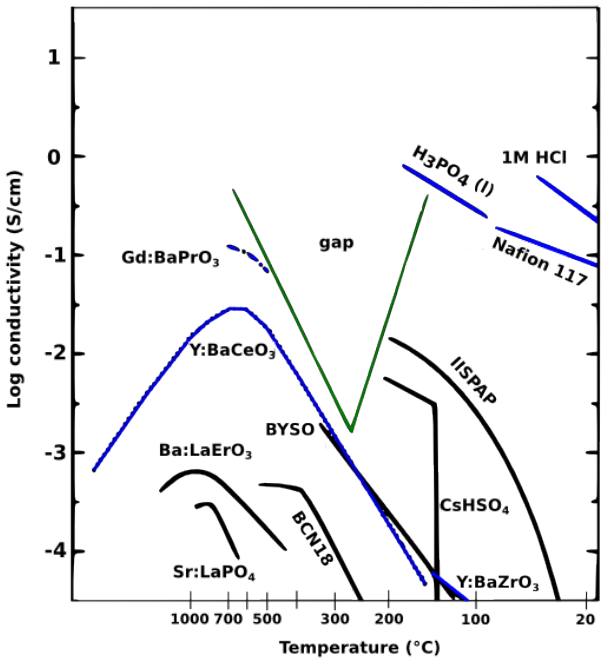

Figure 4 *The intermediate temperature gap for protonic conductors. Adapted from Norby [4].*

partly consists of a polymer. A common electrolyte is Nafion®, which has good chemical and thermal stability thanks to a perfluorinated backbone [36] (similar to Teflon®). To conduct protons well it has to be soaked in water or an acid first, it then forms regions that are hydrophobic, as well as hydrophilic clusters. The protons are conducted through ionic channels that arise as a result of the interaction between hydrophilic SO_3^- groups and the hydrophobic perflourinated backbone and sidechain – the result is a clustering of hydrophilic domains which is where proton conduction occurs. Although Nafion® could can be operational up to 190°C, this is not possible when it has been made in membrane form (due to losses of both mechanical strength and water), and it is therefore operated at no higher temperature than 100°C.

Durability has been identified as the most critical issue to be solved before full commercialization of PEM fuel cells can occur [37]. The main problem with diagnosing degradation mechanisms is that a fuel cell is a solid electrochemical system with several interacting parts, where different components will affect one another in complex ways. Development of better methods for diagnosing the different problems of fuel cell degradation is presently something much needed. Clear is also that more real-life condition field studies will be needed accompanied with improved diagnostic and analytical methods for monitoring and studying durability and degradation.

There are three types of classifications for membrane degradation: mechanical, thermal and chemical / electrochemical (ibid.)

Generally for these systems it holds true that if humidity is held low with temperatures exceeding 100°C the electrolyte will lose its proton conducting properties due to that it cannot retain enough water. At the same time higher temperatures are desired in order to suppress CO-poisoning of the platinum catalysts. If this can be done without decreasing the proton conductivity then higher efficiencies will follow and eliminate the need for complex water management of the fuel cell system (since the only water phase would be steam). The heat coming from the fuel cell could then be re-used, which is not possible with low temperature fuel cells because of its low grade character.

A large part of the costs for a low temperature fuel cell system is in the fuel

processing system, which is about 40 – 50% of the total cost [38]. The CO-purification part of that fuel processing system is a major part therein, and if it could be eliminated it would make the fuel cell cheaper, lighter and smaller.

Using polymers derived from organic materials will limit the operational limit to below 150°C [39]. Inorganic materials however are thermally more stable and therefore more promising candidates for the electrolytes when designing new PEFCs.

Moreover, raising the operational temperature in the PEFCs would open up options for a wider selection of fuels. For best performance only ultra pure hydrogen can be used at low temperatures. This is because of the presence of CO in reformed hydrogen which will strongly block the Pt-catalyst sites below 150°C [40]. Using ultra pure hydrogen is a limiting factor because of cost of this fuel and the difficulty of hydrogen storage. However, at an intermediate temperature one could e.g. steam reform methanol or ethanol using the thermal energy from the waste heat and thereby produce hydrogen as needed, this can be done at temperatures of approximately 250°C for methanol and over 300°C for ethanol [41]. If all performed in closely connected units, heat losses would be minimized and efficiencies high and the fuel storage would be a non-issue since the hydrogen would be derived from a liquid hydrocarbon fuel.

2.2.2 Fuel cell chemistry

The reaction at the anode is $H_2 \rightarrow 2H^+ + 2e^-$, whereby hydrogen molecules are split into protons with the help of a catalyst. A catalyst may consist of small Pt-particles scattered onto the surface of graphite particles (see Figure 5) – this gives a lower cost compared to pure Pt-electrodes; it also enables higher conductivity of electrons through the graphite and overall better fuel cell performance. Another advantage with this setup is that

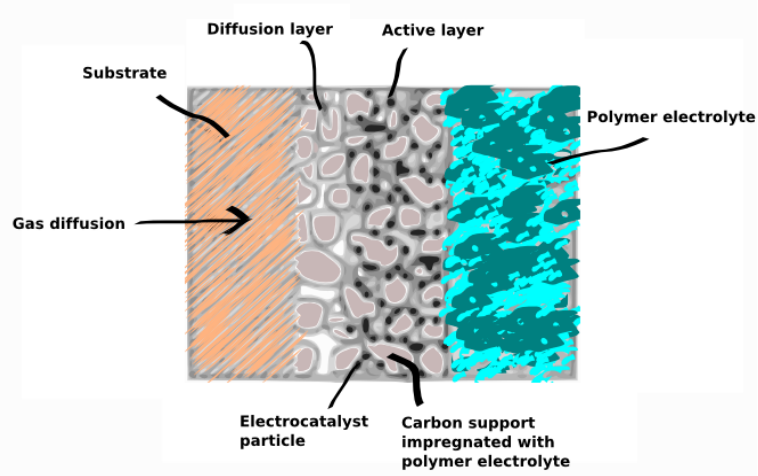

Figure 5 *The carbon supported catalyst in a PEFC, covered with small Pt-particles (centre of schematic). To the right of this is the polymer electrolyte and to the left of it is where the fuel (hydrogen) enters. Once split up, the protons will conduct through the electrolyte. Adapted from [5].*

hydrogen gas can easily pass between the particles. The electrolyte must however be sealed so no gas can diffuse through; and since it has taken up water this must not go into the electrodes (else no gas will pass through the electrodes).

In order to address the CO-poisoning problems of Pt-catalysts, a PtRu catalyst can be used. The reactions as described by reference [5] will then be:

$$Pt + CO \rightarrow Pt\text{-}CO_{ads}$$

$$Ru + H_2O \rightarrow Ru\text{-}OH_{ads} + H^+ + e^-$$

$$Pt\text{-}CO_{ads} + Ru\text{-}OH_{ads} \rightarrow Pt + Ru + CO_2 + H^+ + e^-$$

Even though this type of catalyst is superior in comparison to many others, it does show significant performance loss if operated at low temperature (80°C) when more than 100 ppm of CO is present [38]; therefore either CO-purification of the fuel is necessary or operating at higher temperatures.

Although less platinum is used, the amount of these and similar catalysts required will still be expensive to produce and therefore non-precious metal catalysts should be developed if PEFC's are to be commercially feasible.

From the catalytic sites at the anode the protons are then transported through the electrolyte, being drawn by an electrochemical potential in order to recombine at the cathode where the following reaction takes place:

$$½O_2 + 2H^+ + 2e^- \rightarrow H_2O$$

Again, a catalyst is needed, but this time to reduce oxygen in the oxygen reduction reaction (ORR) which is a slower reaction than that at the anode. This means the cathode requires more Pt-catalyst compared to the anode, and it is therefore of greater importance to first find a cheap solution for cathodes. Efforts are being made to substitute the Pt-containing catalysts with non-precious cathode catalysts for PEFCs. One interesting development is a cobalt-polypyrrole composite that shows good performance and stability over time in PEFCs run with either H_2-O_2 or H_2-air, see [42].

For the electrolyte, apart from having good proton conducting properties and being

stable over time, it is important that it is an electrical insulator, since it is paramount that the electrons take a different route than the protons (i.e. through whatever device one wants to power electrically). This, in combination with the electrolyte being gas and water tight[2], places quite a few requirements on a single material.

2.2.3 The phosphoric acid fuel cell (PAFC)

The phosphoric acid fuel cell (PAFC) works with reformed hydrogen as fuel, but uses a SiC matrix soaked in phosphoric acid as the electrolyte. Anode and cathode reactions are the same as for the PEFC, although the operating temperature is higher (≈200°C) compared to the PEFC, and therefore the CO-tolerance is also much higher.

2.2.4 The solid oxide fuel cell (SOFC)

Unlike PEFCs the solid oxide fuel cell (SOFC) operates at much higher temperatures and has normally an oxide ion (O^{2-}) conducting electrolyte. This electrolyte is usually yttria stabilized zirconia (YSZ), which has unique oxygen ion conduction properties at higher temperatures.

At the cathode, oxygen gas is split apart (through the help of a catalyst) resulting in oxygen ions according to the formula:

$$\tfrac{1}{2}O_2 + 2e^- \rightarrow O^{2-}$$

Conversely, at the anode these oxygen ions combine with hydrogen gas (or any other suitable fuel) and form water. This electrochemical oxidization of the fuel results in the production of electrons, which in turn are lead through an external circuit. The reaction at the anode is:

$$H_2 + O^{2-} \rightarrow H_2O + 2e^-$$

It is important that the electrolyte is thin so that internal resistance can be kept low. However, as with the other fuel cell systems, the electrolyte must also be gas tight in order to avoid chemical combustion of fuel.

[2] If the electrolyte is not gas tight then chemical combustion of the fuel will occur, and if it is not water tight then the electrodes will be flooded.

One of the main advantages of the SOFCs is that different types of fuels can be utilized. Moreover, kinetics are very fast which yields higher efficiencies, and thanks to the high operating temperatures there is no poisoning of the catalysts.

The drawbacks with SOFCs are that they need longer start-up time compared to fuel cells operating at lower temperatures. Especially planar geometries for the fuel cell require even and well-regulated heating, leading to start-up times until operational of about an hour. Newer non-planar designs, so called tubular designs, could be the answer to considerably shorting the start up time, although currently their areal power density is an order of magnitude lower than planar designs and their manufacturing costs are higher. [43]

In summary, SOFCs are good to use as stationary modules, however they are less suitable for mobile applications. This is due to that they are ceramic in nature (making most of them fragile). The high operating temperatures require longer start-up times and produce incoherent thermal expansions in the different materials of the fuel cell. A possible solution is to lower the operating temperature and this involves developing better materials.

2.3 Structure of investigated material

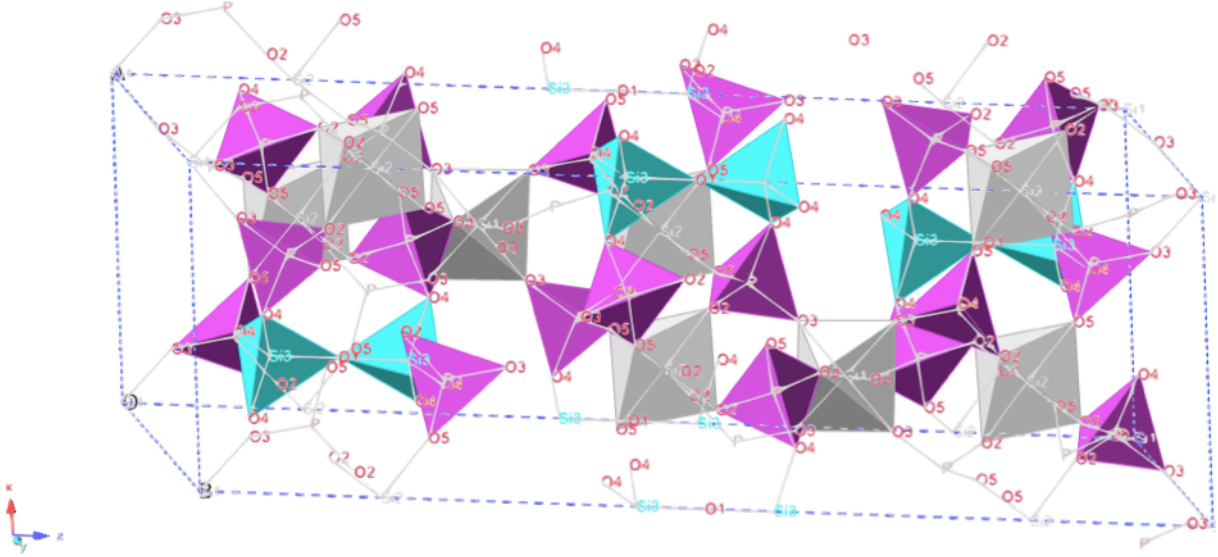

Figure 6 *Unit cell of $Si_5O(PO_4)_6$ viewed slightly off the b-axis. Phosphorus tetrahedra depicted in magenta, silicon tetrahedra in turquoise and silicon octahedra in light grey.*

Silicon oxide phosphate, $Si_5O(PO_4)_6$, is an interesting material from a number of viewpoints. One is that it has two types of silicon coordinations present at the same time (Si^{+IV}, in tetrahedral and octahedral coordination). This is very unusual among the phosphosilicates. In the case of glasses the octahedral coordination is rare, and it only occurs in a few crystalline materials such as SiP_2O_7 [44] and $Si_5O(PO_4)_6$. Another unusual characteristic is that there is a theoretical possibility of element substitution as also the P^{+V} is tetrahedrally coordinated which, if observed, would be rare [45].

Silicon oxide phosphate's three-dimensional structure shows a network with cavities when viewed down the a- or b-axis, which may enable transport of oxide ions through these channels or make it suitable as a molecular sieve (see Figure 6).

There is a report of the structure for the $Si_5O(PO_4)_6$ material which suggests a hexagonal unit cell, space group *R -3* with a ≈ 7.8 Å and c ≈ 24.0 Å [8]. Although the structure will eventually change upon increased amounts of phosphorus (into silicon pyrophosphate, SiP_2O_7), there should also be more subtle structural changes, if it indeed can be proven that P^{+V} goes onto the sites of Si^{+IV}.

Figure 7 shows a proposed binary phase diagram between SiO_2 and P_2O_5. Although the materials synthesized in this project do show some amorphous phase for the silicon-rich samples compared to the parent $Si_5O(PO_4)_6$ this is not to say that the composition cannot deviate from what is known. The phase diagram gives a mixture of $Si_3P_4O_{16}$ and SiP_2O_7 when going from P/Si =1.33 – 2.0. On P/Si ratios lower than 1.33 it gives a mixture of $Si_3P_4O_{16}$ and SiO_2 (quartz).

A question that this project attempts to answer is whether there is a solid solution for the SiO_2 – P_2O_5 system or not. Poojary *et al* [8] make the claim that there is no solid solution, only the $Si_5O(PO_4)_6$. This is in opposition to the conclusion of Liebau *et al* [46] who proposed a solid solution for $Si_{(1+5x)}P_{4(7-x)}O_{72}$, with x ≈ 2.5 – 3.5 (i.e. a system where the P/Si ratio can be varied between 1.33 – 0.76).

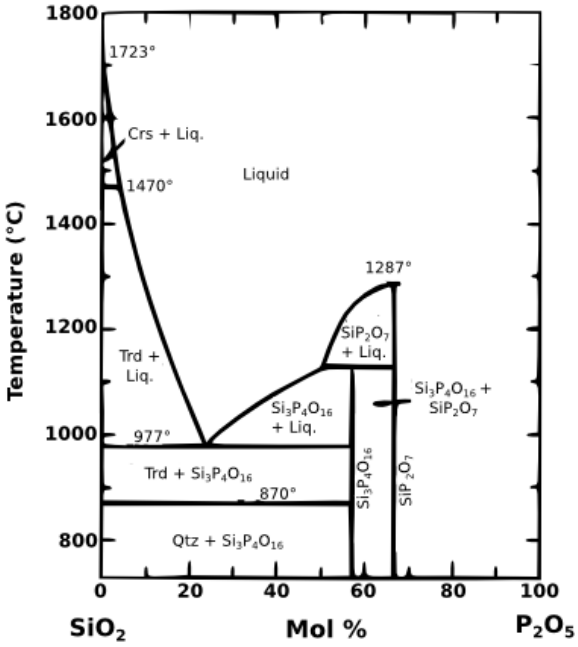

Figure 7 *Phase diagram between SiO_2 and P_2O_5. Adapted from [2].*

2.4 Water and / or phosphoric acid among phosphosilicates

Surprisingly little is to be found in the literature about $Si_5O(PO_4)_6$ when it combines with water. Krawietz *et al* came across the monohydrate $Si(HPO_4)_2 \cdot H_2O$ when investigating their solid acid catalyst which consisted mostly of silicon oxide phosphate [47]. The same monohydrate species was observed by Coelho *et al* [48].

Poojary *et al* assign the weight losses in the 25 – 100°C region to desorption of physisorbed water and in the 100 – 200°C region to desorption of chemically bound water. From 200°C and up to 750°C they believe there could be dehydroxylation of –OH groups. Finally, at 900°C and above the mass loss is assigned as volatilization of chemically bound phosphorus species. Two of their samples were synthesised at lower temperatures – 200°C 5h (P/Si = 1.33) and 300°C 5h (P/Si = 2.9) – and both

these samples showed weight losses (from 50°C to 1000°C almost 6% for the former, and from 400°C up to 1000°C at almost 2% for the latter).

The third sample (300°C 5h, P/Si = 2.9) had had an extra firing at 1000°C for 2 hours, and this displayed a stable TG profile throughout the temperature range. Samples had been washed in acetone after synthesis and dried in an air oven at 80°C.

The most important conclusions that Poojary *et al* reach is that the formula for silicon orthophosphate is $Si_5O(PO_4)_6$, that there is no solid solution, and that the true P/Si ratio is 1.2 instead of 1.33. The weight loss for the low temperature compositions they assigned to H_3PO_4 gassing off as well as P-OH group condensation [8].

2.4.1 Related systems

In this project some substitutions were made in which aluminium and titanium were put into the phosphosilicate system.

Also, hydrothermal treatments were done in order to obtain protonic conductivity. This may be analogous to the case of alumina which forms a ternary system with phosphate and water [49].

A question raised later in the project was, what would happen if silicon oxide phosphate compositions interacted with H_3PO_4 – how would this affect conductivity? This has raised the issue that it is likely a quarternary system for silica, phosphate, water and phosphoric acid. This has earlier been shown to be the case for aluminium, phosphate, water and phosphoric acid [50] and the conductivity data suggests there is more to explore and understand.

2.4.2 Protonic conductivity for phosphosilicates

There are no reports of the protonic conductivity for crystals of $Si_5O(PO_4)_6$ made by the solid state sintering method. There are however reports on protonic conductivity for *gels* of various P/Si ratios. For example, Matsuda *et al* [51], tested hydrated P-Si gels of compositions 0.5, 1.0, and 1.5 and found that the best conductivity was that of the 1.0 ratio. They showed that protonic conductivity (10 mS / cm) can be achieved for a P/Si ratio of 1 at 150°C, keeping it sustained after 400 mins with 0.4% relative humidity.

The underlying reason for protonic conductivity is the material's ability to retain water at these temperatures, due to the formation of Si-O-P-OH groups. In this case it is theorized that the crystals of $Si_5O(PO_4)_6$ are not helpful for protonic conductivity unless they are hydrolyzed. When this occurs it forms phosphoric acid and Si-O-P-OH-units, which is good for the conductivity.

This is also verified in a paper by Tadanaga *et al* [52], where the conductivity decreases as $Si_5O(PO_4)_6$ crystals form. When their fuel cell was supplied with dry N_2 at 180°C the amorphous gel started to form crystalline $Si_5O(PO_4)_6$. The conductivity of their cell was found to be 2.5 mS cm^{-1} at 180°C under 0.4% relative humidity.

From the literature that concerns these gels it seems that if water vapour is introduced the crystallization of $Si_5O(PO_4)_6$ is suppressed and protonic conductivity enhanced.

Nakamoto *et al*, 2004 [53], constructed a polymer electrolyte fuel cell using small (<5 μm in diameter) gel particles of P/Si ratio 1.0 with 25% polyimide. It was tested continuously for 10h at 150°C at 4% RH without observing any degradation, the measured current density was 50 mA cm^{-2}.

Nogami *et al* [54] concluded that protonic conductivity in water containing phosphosilicate *glasses* is due to that water molecules are adsorbed onto P_OH groups and are strongly hydrogen bonded, leading to better retention of water. In their case they claim that the protons are hopping via water (creating H_2O^+ radicals), the proton originating from dissociation of P_OH and / or Si_OH bonds.

2.4.3 $Si_5O(PO_4)_6$

Poojary *et al's* paper [8] contained three samples that showed different TGA behaviour. Their high temperature sample (P/Si starting ratio = 2.9) displayed no mass loss, whereas their two low temperature samples (P/Si starting ratios = 1.33 and 2.9) showed some mass losses.

From the XRD in the same paper, the low temperature samples (P/Si = 1.33) showed some evidence of amorphous phase which appeared to be absent in the other compositions, at 20 – 27° 2θ. This is fairly consistent with the findings in this thesis – that a high enough P/Si ratio leads to absence of amorphous phase. However, because the synthesis method differs so much compared with the materials of this thesis, it is

not conclusive that Poojary's composition can be directly compared with those of this thesis.

Their cell parameters for the high temperature composition ('RB255C', P/Si = 2.9) a, b = 7.8481(2) Å and c = 24.1780(6) Å, agree relatively well with samples produced for this thesis (P/Si ≈ 1.2). However, their P/Si starting ratio is beyond that of silicon pyrophosphate which has an altogether different structure [55].

For their low temperature ('RB210') with P/Si = 1.33, a = 7.8985(5) Å and c = 24.022(2) Å, this does not resemble anything in this thesis even though the P/Si ratio is supposedly closer.

Their 1.33 sample was washed with acetone after synthesis but this was prior to characterization. Furthermore, the material was made at a very low temperature (200°C) and showed signs of having a small amorphous component in the final XRD. For the other high temperature composition the high temperature firing (1000°C, 2h) would have made sure the structure was free from water and anything extra, which explains the stable TG result.

The fact that the cell parameters are different for the two samples, yet both are pure crystalline phases, is an indication that the samples have different compositions – this in turn constitutes supporting evidence for a solid solution despite the authors' claim to the contrary.

Furthermore, there is a discrepancy in the Si_O bond distances in the silicon tetrahedra that supports partial occupancy of phosphorus at least for the high temperature sample, see right part of Figure 8. Also noteworthy in the same figure is that almost every bond angle is different when compared side by side. This indicates subtle structural differences that could be due to phosphorus replacing some of the silicon at the tetrahedral silicon sites, which indicates a solid solution.

Note further that the P_O bond distances have an average of 1.522 Å and 1.530 Å. The longest P_O bond is 1.526 Å and 1.535 Å for each sample, respectively. In this work one of the bonds, P_O4, was found to be 1.57 Å, the other P_O bonds were comparable to Poojary's results (cf. Appendix A1).

RB210					RB255C			
Si octahedra	**Bond length (Å)**		**Angle (°)**		**Si octahedra**	**Bond length (Å)**		**Angle (°)**
Si1_O3	1.789(5)	O3_Si1_O3	180.00		Si1_O3	1.783(5)	O3_Si1_O3	180.00
		O3_Si1_O3	95.2(5)				O3_Si1_O3	92.7(3)
		O3_Si1_O3	84.8(5)				O3_Si1_O3	87.3(3)
Si octahedra					**Si octahedra**			
Si2_O2	1.818(6)	O2_Si2_O2	85.6(9)		Si2_O2	1.813(7)	O2_Si2_O2	88.0(4)
Si2_O5	1.697(10)	O5_Si2_O2	95.6(9)		Si2_O5	1.696(7)	O5_Si2_O2	91.9(4)
		O5_Si2_O2	95.6(5)				O5_Si2_O2	88.6(3)
		O5_Si2_O2	178.1(11)				O5_Si2_O2	176.6(5)
		O5_Si2_O5	82.8(8)				O5_Si2_O5	91.5(5)
Si tetrahedra					**Si tetrahedra**			
Si3_O1	1.706(14)	O4_Si3_O1	110.1(6)		Si3_O1	1.659(8)	O4_Si3_O1	108.1(4)
Si3_O4	1.654(6)	O4_Si3_O4	108.8(6)		Si3_O4	1.5299(6)	O4_Si3_O4	110.8(4)
Phosphate group					**Phosphate group**			
P_O2	1.526(14)	O3_P_O2	109.0(6)		P_O2	1.533(7)	O3_P_O2	113.5(4)
P_O3	1.518(6)	O4_P_O2	110.0(7)		P_O3	1.525(7)	O4_P_O2	107.3(5)
P_O4	1.518(6)	O5_P_O2	113.0(7)		P_O4	1.535(6)	O5_P_O2	111.5(5)
P_O5	1.525(6)	O4_P_O3	111.3(7)		P_O5	1.529(7)	O4_P_O3	109.8(5)
		O5_P_O3	105.9(7)				O5_P_O3	103.8(6)
		O5_P_O4	107.6(7)				O5_P_O4	110.9(5)

Figure 8 *Sample RB210 (left) and RB255C (right) compared side-by-side, results after Poojary et al's paper [8]. Note the short Si3_O4 bond lengths for the latter sample which are very similar to P_O bond lengths. In addition, the P_O4 bond length is shorter than 1.57 Å as obtained in this project.*

2.4.4 SiP_2O_7

Although SiP_2O_7 on its own is not the best protonic conductor of the pyrophosphates (only a few mS cm^{-1} at the most [56]) it has been shown to be involved in enhancing the protonic conductivity at intermediate temperatures through the reaction with CsH_2PO_4 to form $CsH_5(PO_4)_2$ ([57], [39]). Without any apparent chemical reaction[3], it indirectly enabled the conductivity of the composite to that higher than CsH_2PO_4. It is further claimed that $CsH_5(PO_4)_2$ is in the molten state yet since it is stabilized at the interface with SiP_2O_7, the composite is in the solid state at intermediate temperature. The maximum observed conductivity was 44 mS / cm at 266°C in 30% H_2O / Ar atmosphere.

2.5 Oxygen conductivity

If significant oxygen ion conductivity were to be found, it is expected to be due to the free oxygen in the parent composition $Si_5O(PO_4)_6$, similar to the case of apatite, cf. Slater *et al* (2004) [58]. Thus it would not be due to any oxygen deficiency, as is the case in e.g. perovskite systems.

[3] Although, judging from X-ray diffraction from before and after heat treatment, it does appear that the structure of SiP_2O_7 is no longer intact. See figure 1, 39. Matsui, T., et al., *Development of Novel Proton Conductors Consisting of Solid Acid/pyrophosphate Composite for Intermediate-temperature Fuel Cells.* Journal of the Japan Petroleum Institute, 2010. **53**: p. 1-11..

The structure must however, be properly established and compared with measured data before the reasons for any oxygen conduction can be properly established. As with protonic conductivity impedance measurements can be used to extract the data on oxygen ion conductivity.

A recent literature search in SciFinder has found no articles on the subject of oxygen conductivity for the silicon oxide phosphate system, or indeed for the composition $Si_5O(PO_4)_6$. AC Impedance measurements have been carried out though and high temperature conductivity data is presented in chapter 4.

3. Experimental and characterization techniques

3.1 Experimental methodology

The applied methodology for the work of this thesis has been in accordance with established scientific empirical methods within solid-state chemistry.

Samples have been synthesised and analyzed with various characterization techniques and structural modelling has been undertaken to establish the chemical structure. Electrochemical impedance measurements have been used to evaluate the conductivities of the materials and this data has then been linked to the cell parameters. The result has been a model that considers the cell parameters to explain the physical characteristics that various P-Si compositions exhibit.

As much as has been possible, various characterizations have been done on individual samples taken from the same batch. If this is not the case (for example, if an extra firing was done between different types of measurements) then this is mentioned either in the text or in diagrams or both.

3.1.1 Methodology for diffraction

In order to characterise crystals, which by definition are repetitive arrays of atoms, a very commonly used method is diffraction. What is taken advantage of here is the electromagnetic waves' interaction with the atomic planes of the crystal.

Most commonly used in chemistry labs is X-ray diffraction, although electron diffraction uses the same principles, however interacts much weaker and can be used to study surfaces in conjunction with microscopy. X-rays go deeper and since they interact with the electron shells of the atoms, atomic positions etc will be a result of this interaction. Neutrons can also be used for diffraction, and in this case the interaction is with the atomic nuclei – yielding more accurate positions than with X-ray diffraction (XRD). Neutrons are also useful for mapping magnetic moments, for distinguishing between neighbouring elements and for mapping light elements like hydrogen.

The most important equation for this is the Bragg equation, or Bragg's law:

Equation 1: $n\lambda = 2d_{hkl}\sin\theta$

where

θ = incident angle = refracted angle
d_{hkl} = lattice spacing
λ = X-ray wavelength
n = integer (usually 1)

If the incident rays (provided they are parallel and monochromatic) fall in with angle θ and Bragg's law is fulfilled then constructive interference will occur resulting in diffraction. Bragg's law is fulfilled if the angle of incidence equals the angle of reflection when atoms from different planes of the lattice scatter in phase. There will be different intensities as a function of the angle (due to constructive and destructive interference) and this is what produces the diffraction pattern.

In XRD the sample is placed in a sample holder, usually made from stainless steel. Powder is placed in the centre of the sample holder and caution is taken to make sure the surface of the powder is absolutely flat and in line with the rest of the holder. When the sample is mounted in the diffractometer and the doors to the machine are closed, the shutter will open and the monochromatic X-ray beam will interact with the atoms and molecules of the sample and diffract. During this whole time the sample holder will rotate in its own plane (in order to statistically spread any error).

Not all of the beams that diffract from the sample will reach the detector, however a sufficient amount will. Each intensity that the detector registers will be recorded in the computer as a function of the angle of incidence. This is what produces the diffractogram and for solids (crystals) it becomes a structural fingerprint.

If the structure changes, but the elements remain the same, there will be a change in the type of pattern, i.e. a visibly different diffractogram. If however, one element is substituted by another and it is the same structure, then it will be harder to see a difference in the diffractogram[4].

3.1.2 Rietveld refinement methodology for neutron data

Manual refinements for the neutron data were done in two series shown in the logs in

4 However, examining the peak positions usually will reveal differences – if e.g. all the peaks shift a little to lower two-theta then one can conclude that the unit cell has expanded.

Appendix B. The refinement data presented in Chapter 4 is for the latter series (some fractional occupancies were varied, however the same XYZ positions retained in both). Tables with summaries of the results can be found in Appendix A1 and Appendix A2, the latter also containing data from the refinements where the occupancies were all fixed.

More fixed occupancy data is also given in Appendix E1 and Appendix E2, where bond lengths and bond angles are given as a function of temperature for the parent compositions, both untreated and hydrothermally treated with D_2O.

Figure 9 shows an example of two plots from the refinements of the untreated parent composition, $Si_5O(PO_4)_6$, at room temperature (from bank 2, top, and from bank 4, bottom). Note that the calculated model (following space group *R -3*) matches the observed neutron data, further that peaks occur at the predicted position. This shows that the suggested model for this system displays high agreement with the measured data.

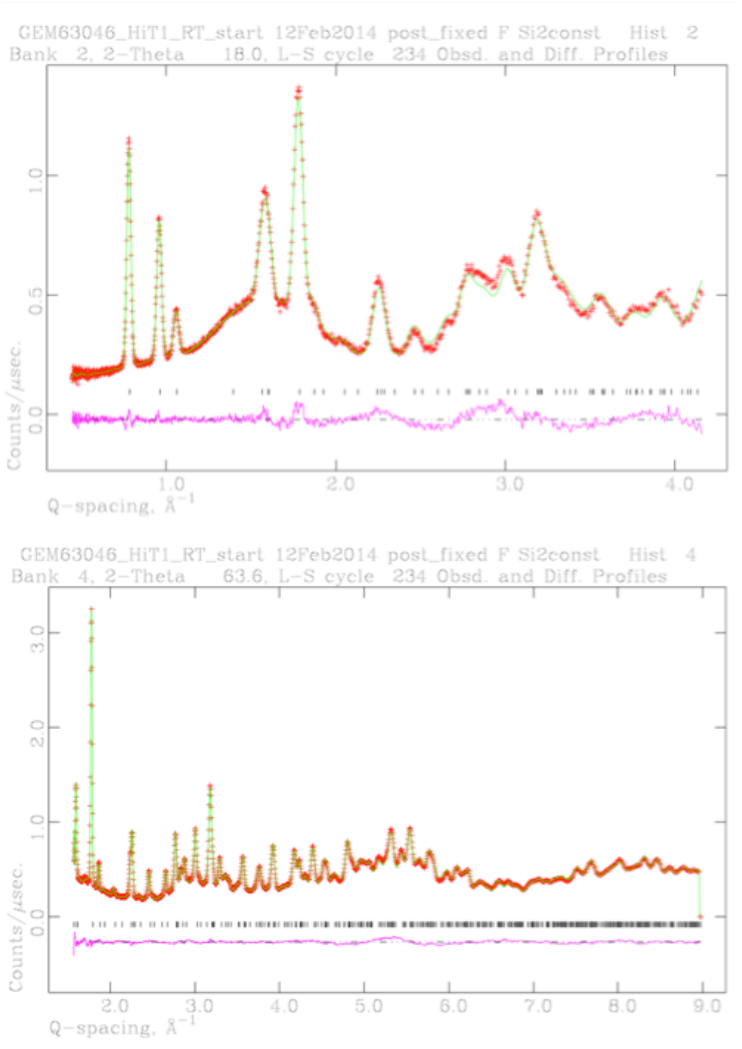

Figure 9 *Refinement result from the untreated parent composition from bank 2 (top) and bank 4 (bottom). Note the correlation between the calculated pattern and the observed data. Additional plots are found in Appendix G for this sample and the hydrothermally treated sample.*

3.2 Synthesis

The method of synthesis throughout this project was the solid-state sintering method [59], which is a common high-temperature method.

The two oxide ingredients, SiO_2 and $NH_4H_2PO_4$, were ground together with a little acetone in an agate mortar resulting in a white powder mixture. For each composition these mixtures were then calcined at 200°C (or just above) for three hours or more. After the calcination step the powders obtained a greyish colour, and they started to absorb water when crushed or stirred, or if left out for many hours (the samples rich in phosphorus content appeared to absorb most water).
Finally the preheated powder mixtures (without further treatment, such as grinding or pressing pellets etc) were fired in alumina crucibles at elevated temperature. During the firing at the higher temperature the powders obtained a white colour. Upon grinding they all remained white and were no longer hygroscopic. A pellet of each composition was then pressed and re-fired at the same or higher temperature.

After this stage pellets were pressed and re-fired from the different samples at either 900°C or 1000°C provided the previous step was the same temperature or lower. The best results seemed to be two firings at 1000°C for the P/Si ratios of 1.2 and 1.5, and one single firing at 800°C for 24h in the case of ratio 2.0.

By using this method it proved problematic however to obtain a pure phase. Not only was there a crystalline impurity phase present (SiP_2O_7) but also amorphous content. When the method of synthesis was modified so that the source of phosphorus was H_3PO_4 the end result was a composition that was single-phased with only minor amounts of amorphous content when fired optimally.

For later synthesis, the precursor was made by stirring stoichiometric amounts of SiO_2 and 85% H_3PO_4 together along with distilled water in a teflon vessel. This mixture (a fairly wet slurry) was put inside a sealed hydrothermal vessel and then heat-treated at 120°C for two hours, followed by being dried on a glass plate in a drying oven at 80°C until it had become solidified gel.

The resulting dehydrated gel was placed in an alumina crucible in the furnace and pre-fired at 300°C for 3h before being sintered at 950 – 1000°C for 12 – 50 hours.

The key here was to make sure the solid gel was homogenous before calcination. This was no problem when only SiO_2 and H_3PO_4 in water were present, since the SiO_2 came in the form of a finely dispersed pulp which would dissolve uniformly in the H_3PO_4-water mixture if stirred properly with a glass stirrer. However, when adding a third ingredient (e.g. GeO_2) care had to be taken that the mixture was stirred regularly upon dehydration, or else the third ingredient would sink to the bottom of the gel as it was drying – a phase-impure composition would be the end result upon firing.

3.3 Analytical techniques and equipment

3.3.1 Solid-state NMR

In order to establish the proper structural relationships for the phosphorus and silicon in respective compositions a good technique is solid-state NMR. Since one can here differentiate between the two main elements, see e.g. Lejeune *et al* 2005 [60] or Coelho *et al* 2006 [61] for examples of how the technique can be applied more specifically. One great advantage with solid-state NMR is that amorphous phases also can be studied; these are not identifiable with XRD (since they are non-crystalline and therefore no diffraction peaks occur).

In this project most solid-state NMR spectra were obtained using a Bruker Avance III spectrometer equipped with a 9.4T superconducting magnet. The rotors that were used were 4mm ZrO_2.

3.3.2 X-ray powder diffraction (XRD)

In this project the X-ray diffractometer used for sample characterization was initially a Stoe Darmstadt operating in transmission mode. This was eventually replaced by a PanAnalytical Empyrean running in reflection mode. Lastly, some high temperature scans were undertaken on the same type of machine fitted with an Anton Paar HTK 1200N high-temperature chamber using Mo-radiation instead of Cu.

On the Stoe instrument quick scans were done (30/90 mins) for phase characterization, as well as high resolution scans for Rietveld refinement (12 h); the typical range of the scans were 10–30° and 10–75° (2θ), respectively. The PanAnalytical instrument ran scans typically one hour each (10–50° 2θ), whereas the

high resolution scans were 1–3 hours over 10–90° 2θ.

3.3.3 Neutron powder diffraction

The principle for neutron diffraction is very much the same as for X-ray diffraction – the differences being mainly that neutrons are much harder to produce and therefore require more expensive facilities. There are two ways that neutrons are generated – either from a nuclear fission reactor (continuous flow) or from a spallation source producing a pulsed neutron beam. All in all there are about 10 major neutron facilities worldwide, the two major ones in Europe being ISIS[5] and Institut Laue–Langevin (ILL). Each neutron facility houses many instruments that have different areas of application.

Neutron diffraction is many times a superior technique, especially when it comes to mapping lighter elements like hydrogen and also in many cases when differentiating between elements that are close in the periodic table. Figure 10 shows the neutron cross section for elements of the periodic table as a function of their respective atomic number. The neutron cross section is a measurement of how likely an incoming neutron is to interact with a target nucleus.

Since neutrons interact with the atomic nuclei magnetic studies can also be undertaken (one can e.g. map the magnetic moments in a crystal lattice). For the same reason neutrons are superior when it comes to obtaining greater accuracy in determining atomic positions.

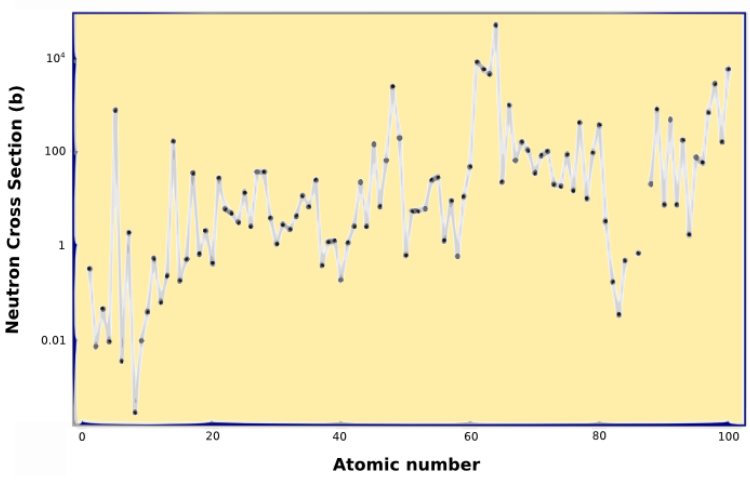

Figure 10 *Neutron cross section (logarithmic axis) for elements in the periodic table. Adapted after [1].*

In the case of X-rays, one will often obtain good structural information, however

[5] Name refers to the ancient Egyptian goddess and local name for the river Thames. The facility was formerly known as Spallation Neutron Source (SNS).

since X-rays only interact with electron densities there is also more uncertainty of the true positions of the nuclei. For most cases X-rays are sufficient for general characterization of a crystalline material, but in some cases neutrons may be the only viable choice.

Lastly, X-rays do not penetrate much more than the surface of a material, whereas neutrons go much further into the bulk, enabling e.g. *in situ* studies of more complex systems such as studying stress in an airplane's wing or the operation of a battery or fuel cell.

Figure 11 *Overview of the GEM instrument at the Rutherford Appleton Laboratory in Harwell, United Kingdom. The sample (pictured middle-right) is lowered down into the high temperature sample tank (lower left picture). For lowering the sample tank down into position a crane is used (top middle). Also pictured is a schematic overview describing the positions of the sensor banks on the GEM instrument (lower right), adapted after [7]. The GEM instrument and its banks is not visible other than from the sides when going beneath floor level, because the neutron beam runs under floor level.*

An overview of the instrument used for the neutron data collection is shown in Figure 11. The sample is placed in a sample holder (middle-right), then placed into e.g. a specially designed furnace (bottom-left). The furnace is lifted in by using a crane (top-middle). A schematic of the GEM instrument itself is pictured in the bottom-right corner of the figure, the very advanced instrument is situated below the floor (bottom-middle and top-right). There is also the possibility to run many samples in a sample changer (top-left).

3.3.4 Thermogravimetrical analysis (TGA)

This technique is used to constantly record a specimen's mass upon heating and cooling in a gas flow of choice. After the experiment is done it is possible to calculate what the different phases were if one has positively identified the formula at start or at the end of the run. Phase transitions can be detected by combining the TGA with a DSC or DTA in the same setup (see next subsection). The instrument used for all the runs was a Stanton Redcroft STA-780. For a normal run about 20–25 mg of sample was used.

Most measurements were done in air (25–28 mL / min) from room temperature to 1000°C at 5°C / min with a 30 minute isotherm at both start and when programmed temperature had been reached, others were done with the same parameters however with lower maximum temperatures (500, 350°C etc).

3.3.5 Differential Thermal Analysis (DTA)

The DTA is a technique that is very useful for studying phase transitions. The basic principle is that the instrument has one chamber (the furnace) with two thermocouples close to two identical ceramic crucibles, one empty reference and one which contains the sample. As the furnace is heated, equal amounts of heat go into the two sub-chambers and the difference in absorbed heat between the two crucibles is calculated and plotted.

3.3.6 Scanning Electron Microscope (SEM)

The SEM works by the principle of bombarding a surface with an electron beam from an electron gun (usually a tungsten filament that is heated up with current). The beam is focused with the help of electromagnets (magnetic lenses) onto the sample in the specimen chamber, where secondary electrons from the material are emitted as a result of the focused electron beam's impact. When some of these secondary electrons are passed through a collector they will hit a scintillator detector producing photons which are amplified in the photomultiplier. The signal again becomes electronic and as the electron beam scans the surface of the sample the signal changes strength, which is rendered as an image with contrast in the computer.

The specimen chamber needs to be evacuated due to that air otherwise will interfere with the electron beam.

3.3.7 Electrochemical Impedance Spectroscopy (EIS)

AC impedance data was collected with an HP 4192A Impdeance analyzer (in air only) and a Solartron SI 1260 Impedance/Gain-Phase Analyser (in air and humidified 5% H_2 in Argon).

Pellets had Pt-paste painted for electrodes and were then heated to 850°C for 30 minutes. Prior to measurements the pellets were put in a partially water filled autoclave and heated for 2h at 120°C. The hydrothermal pressure at this temperature corresponds to 1.9 atm, and enables water vapour to enter the structure, which enables protonic conductivity. The hydrothermal method was chosen as a means of delivering water into the system and both pellets and powders underwent this treatment. In both cases the material was put in a glass vial and this floated on the water inside of the bigger Teflon container. The Teflon container had a lid in the same material that ensured a closed vessel. The outer vessel was a stainless steel bomb, and this screwed on putting a bit of initial pressure on the Teflon lid in order to keep it in place. Once the stainless steel bomb was placed in a preheated furnace, the temperature inside the vessel would start rising and because of the presence of liquid, the vapour pressure would rise correspondingly.

Alternatively, for H_3PO_4-doped samples, these pellets were refluxed in 85% H_3PO_4 for about one hour, and then Ag-paste was applied as electrodes which dried a few minutes at ≈ 80°C.

The instrument then measures the impedance of the material over a range of frequencies by applying an electric field.

Once complex impedance plots were obtained the conductivity could be calculated by using the following simple relationship:

$$\sigma = \text{pellet thickness} / (R \times \text{pellet area})$$

where R can be the entire resistance of the primary arch (if capacitance value ≈ 10^{-11} F); alternatively, it can be where the arch intercepts the real axis (if capacitance value ≈ 10^{-5} – 10^{-7} F). The unit for σ is Siemens / centimetre, provided the pellet thickness and area in the formula are given in cm and cm^2, respectively.

For then plotting the conductivity against temperature, the logarithm of the conductivity value is applied because the σ-value will vary quite extensively over the chosen temperature range. If the logarithm of the conductivity is plotted against the inverse temperature (1/T) then an Arrhenius plot is the result. From Arrhenius plots one can calculate the activation energy.

From each electrochemical measurement one would in the ideal case obtain a double arc and followed by an electrode response (beginning of a third arc) as pictured in Figure 12. The first arc would originate at origo and is the bulk response. Directly following this arc, as frequency decreases, is the grain boundary arc followed by the electrode response, respectively.

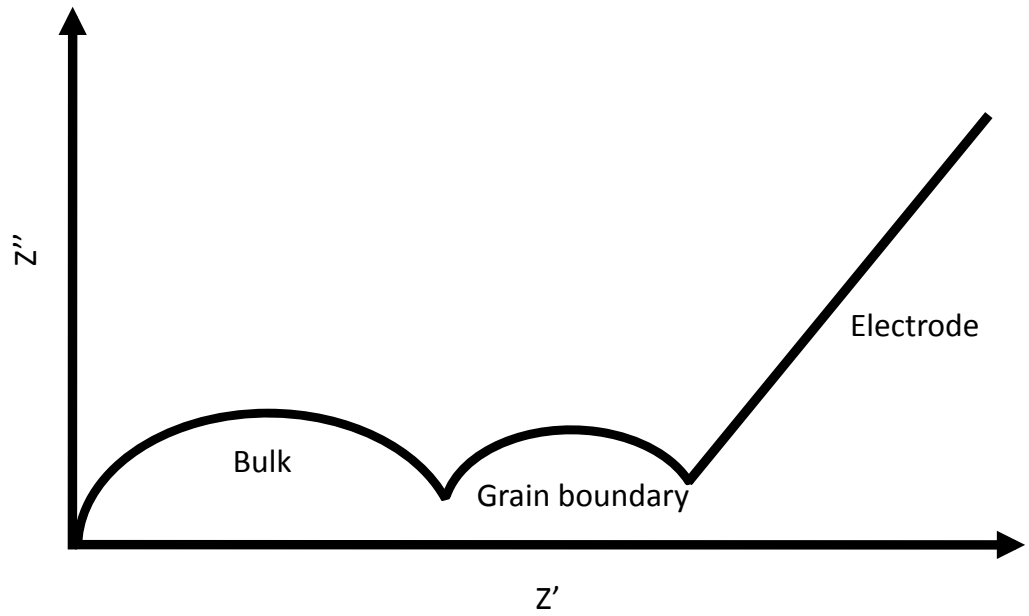

Figure 12 *A Nyquist plot of an ideal impedance response. On the y-axis is the imaginary component of the resistivity and on the x-axis is the real component of the same.*

The total conductivity for the measured sample would be based on a real resistance value where the grain boundary arc ends on the Z' axis. In this project focus has been on the bulk conductivity, and it is these values that have been presented. If the impedance analyzer could not record a bulk response however, and only a small grain boundary response, then values for the total conductivity are presented – these values are essentially the same as the true bulk conductivity.

Each obtained arc has a characteristic frequency, i.e. that frequency that is at the highest Z'' value. In some cases this value can help in identifying the type of arc

(bulk, grain boundary or electrode) if the characteristic frequency at that temperature is previously known for the measured system. A more reliable way however is to make a quick estimate of the capacitance of the arc. If the estimated capacitance is in the order of 10^{-11}F one can conclude that the fitted arc is not an electrode process, but must be a physical property of the material. i.e. the conductivity of the bulk. For a more comprehensive overview of impedance spectroscopy, see [62].

3.3.8 EIS on gel using a Teflon setup

In order to measure the impedance response from the P-Si gels a special teflon setup was designed as shown in Figure 13. It was made from three teflon rings that sandwiched the gel in the middle ring between two sheets of copper foil, all held together with a spring made from a paper clip. Some teflon tape was also wrapped around the three rings to prevent short-circuiting of the copper sheets when measuring the impedance response.

Figure 13 *The teflon setup built for measuring conductivity in P–Si gels. A very basic construction was used, utilising teflon rings, as pictured. Copper foil was used as electrodes on both sides in direct contact with the gel. A bit of Teflon tape was wrapped around the mid-section, as to avoid any accidental electrical contact between the two copper foil bits (not shown here).*

The top and bottom were held together by a thick paper clip that had been reformed to act as a spring (lower-left).

At higher temperatures the P-Si gel loses water, and afterward a solid pellet is the result (lower-right).

4. Results and discussion, pure P-Si system

Introduction

The project's initial aim was to study the pure P-Si system, focussing on structure and properties in order to see whether these materials could be suitable candidates for future fuel cell electrolytes, in particular, as solid state protonic conductors that can operate at higher temperatures than e.g. Nafion.

Moreover, the structure, and in particular the cell parameters, would have to be investigated in order to see if there are any differences between different P/Si starting ratios, and if these properties can be linked to the observed protonic conductivities. A theory for the system can then be constructed which will help in understanding how to boost conductivity in the future.

In Table 2 it is given the peak positions for silicon oxide phosphate (PDF card 00-040-0457 from ICDD [63]). This was for a composition where the a,b axes = 7.875 Å and c = 24.09Å and the chemical formula is $Si_5P_6O_{25}$, i.e. that same composition as the parent $Si_5O(PO_4)_6$.

Note further from Figure 14 the XRD diffractogram for one of the samples synthesized for this project (1.2 KM). Comparing this figure with Table 2 shows full agreement, i.e. the aimed material was successfully synthesized.

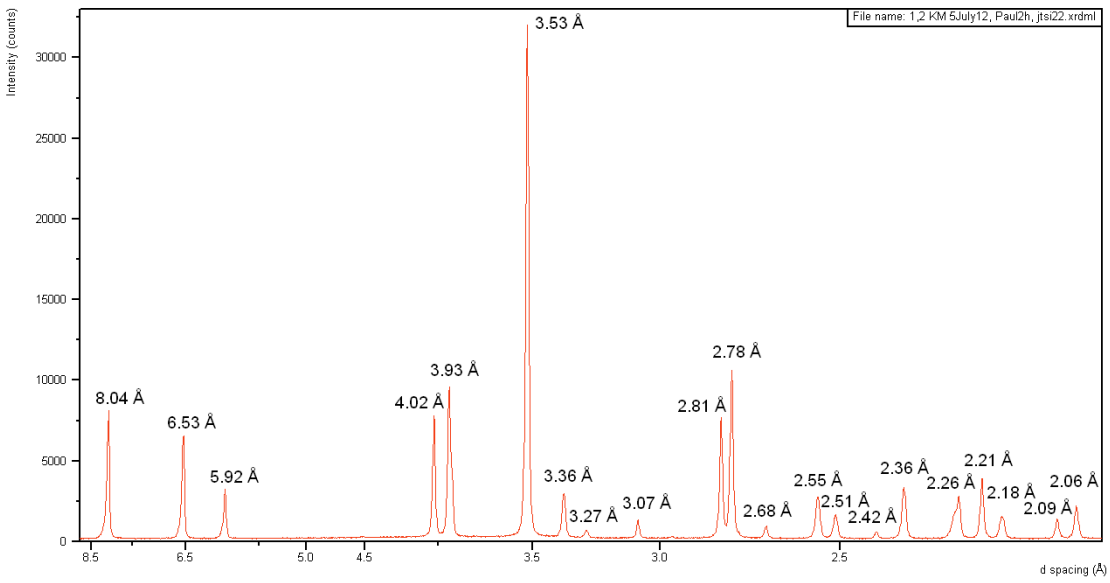

Figure 14 *XRD of P/Si composition with starting ratio 1.2. Values on X-axis are d-spacing and each peak is annotated with its respective d-spacing value. Compare values to table 2.*

2 theta °	d (Å)	Intensity (%)	h	k	l
10.9544	8.070000	35	0	0	3
13.4865	6.560000	30	1	0	1
14.8766	5.950000	13	1	0	2
22.0937	4.020000	37	0	0	6
22.5482	3.940000	40	1	1	0
25.2078	3.530000	100	1	1	3
26.2671	3.390000	12	2	0	1
27.2492	3.270000	5	2	0	2
29.0622	3.070000	3	1	0	7
31.8193	2.810000	25	1	1	6
32.1719	2.780000	40	2	0	5
33.4069	2.680000	4	0	0	9
35.0222	2.560000	10	2	1	1
35.7431	2.510000	8	2	1	2
37.1200	2.420000	3	2	0	7
37.9327	2.370000	12	2	1	4
39.8551	2.260000	8	2	0	8
40.7964	2.210000	20	1	1	9
41.1858	2.190000	6	0	0	11
43.4716	2.080000	4	1	0	11
43.9154	2.060000	12	2	1	7

Table 2 *Peak position values for $Si_5P_6O_{25}$ from ICDD database [63].*

4.1 Early synthesis and characterization

The first series of experiments utilized $NH_4H_2PO_4$ and SiO_2 mixtures that had been pre-treated at 200°C for 3h at four different temperatures: 600°C, 800°C, 900°C and 1000°C for 24 hours. The firing was done in a muffle furnace under ambient atmosphere. After initial calcination, the powders were too hygroscopic to be pressed into pellets, thus they could only be fired as powders to begin with.

The XRD data for the 1.2, 1.5 and 2.0 compositions are shown in Figure 15. The top-left stack plot, after 600°C, there is a lot of amorphous material (seen from the high background intensity at low 2θ), also, any main phases have not formed yet. After 800°C, see bottom-left stack plot a pure phase of SiP_2O_7 has formed for the 2.0 ratio, and a small emerging phase of the parent composition for the 1.5 P:Si ratio is beginning to form. As expected the structure was different for P/Si = 2.0, i.e. SiP_2O_7, compared to the parent composition, $Si_5O(PO_4)_6$. At 900°C the main phase is

dominating for the 1.2 and 1.5 ratios (see top-right stack plot) and there is now also some amount of this phase in the 2.0 composition. At 1000°C, bottom right stack plot, it is close to phase purity for the 1.2 and 1.5 starting compositions. The 2.0 starting composition has a smaller amount of SiP_2O_7. Moreover, all three compositions have a "hump" in the baseline amorphous due to formed amorphous content.

It was further observed that the structures for the remaining compositions, i.e. those with a P/Si starting ratio of 1.5 or lower, were isostructural with the parent composition. The XRD plots in Figure 15 and Figure 16 can be compared to the simulated pattern found in Figure 9 – this latter figure shows agreement between the calculated and observed neutron pattern, hence the main phase for silicon oxide phosphate can be compared and found to be in agreement (cf. Figure 5 in Poojary et al's paper, [8] compared to Figure 16 in this thesis).

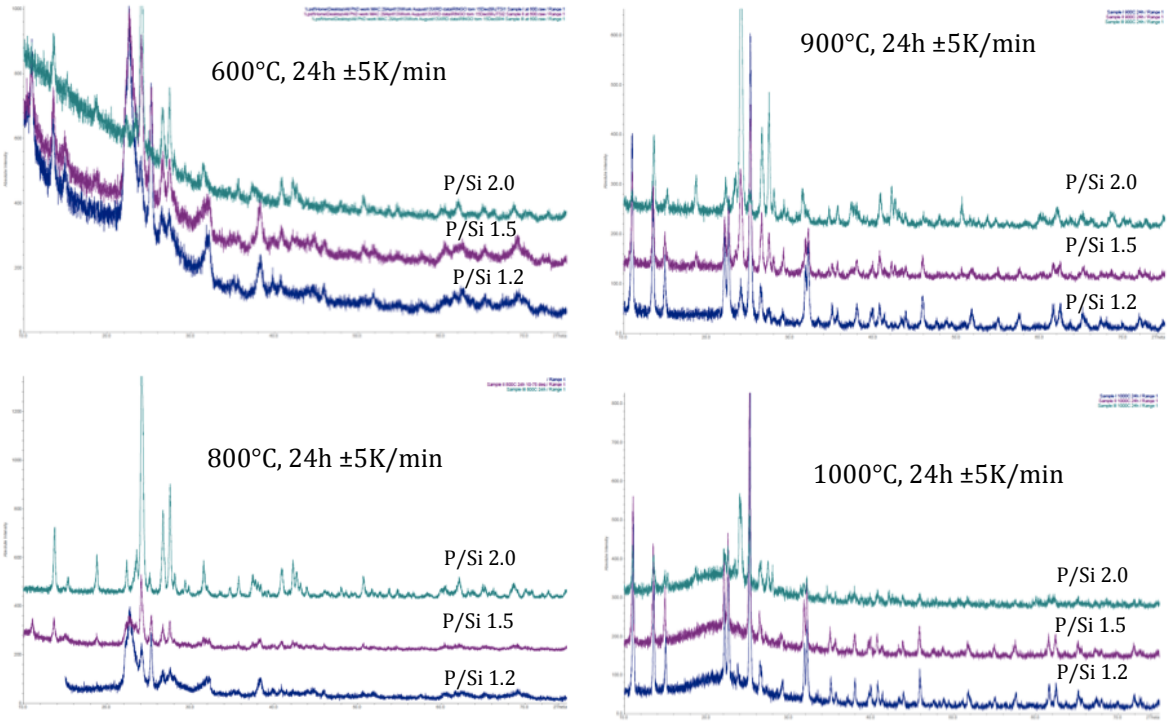

Figure 15 *Firings of different P-Si ratios for 24 hours at different temperatures.*

When calcined powders of P/Si ratios 1.0 – 1.5 were sintered at 950°C for 24 hours and then for another 24 hours at 975°C, see Figure 16, it was evident that higher phosphorus content lead to less amorphous contribution, as seen from the intensity of

the background between 15-35° 2θ in the same figure. This suggests that the silicon content is important when understanding the amorphous phase. When sintered this way, the purest phase was the P/Si starting ratio of 1.5 which did not have any signs of the secondary crystalline phase, i.e. SiP_2O_7. This was initially thought to be due to evaporation of phosphorus during the sintering process, however, it is more likely that the sintering conditions needed further adjustment for the lower P/Si starting ratios. The two other P/Si starting ratios (1.0 and 1.2) had in addition to more amorphous content also a small amount of secondary phase, the main peak of SiP_2O_7 is seen just below 24° 2θ in Figure 16.

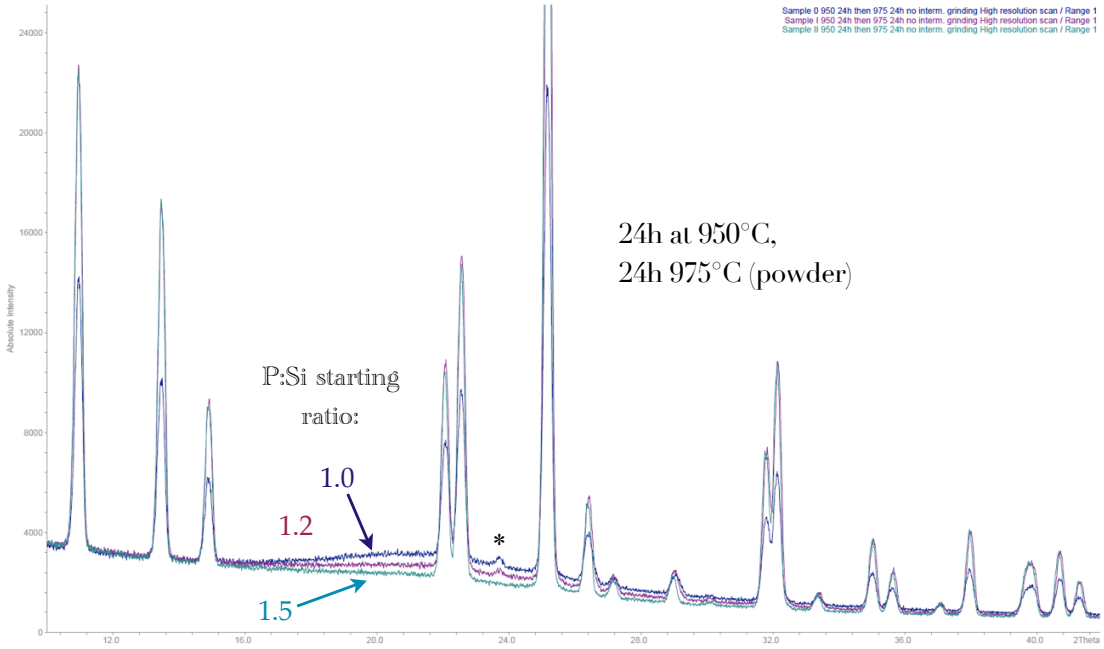

Figure 16 *Samples sintered at 950°C for 24h and then again at 975°C for another 24h, P/Si ratios 1.0 – 1.5. Note the increasing amount of amorphous content with decreasing P/Si ratio (i.e. increasing amount silicon).*

** denotes impurity peak, SiP_2O_7.*

When the first sintered samples had been sintered into pellets they produced very poor conductivities. It was in conjunction with these initial impedance measurements, that it was further discovered that water needed to be a crucial component of the system. A simple hydrothermal high-pressure treatment was chosen for delivering water into the system, thereby also boosting protonic conductivity.

4.1.1 Synthesis with H_3PO_4

Once the phase purity became better, a problem that remained was that of reducing

the amorphous content. The amount of amorphous content could later be reduced through modification of the synthesis method, by using H_3PO_4 as the phosphorus source. This amounted to using a gel-precursor, which coincidentally sintered at similar temperatures as previously mentioned samples. By using this latter method the phase purity became better and more consistent too. An overview of the sintering times and temperatures for each sample is given in Appendix D.

One observation that was made was that increasing the batch size required additional time of firing. This could be because having large batches requires more work to obtain the same degree of mixing; if mixing was insufficient then longer firing times would help.

When making samples with the gel-method it was again clearly observed that decreasing the P/Si ratio increases the amount of amorphous phase, and conversely increasing the P/Si ratio decreases the amount of amorphous phase. A possible explanation to this was that the relative amounts of phosphorus and silicon are the same in the crystalline phase, and any surplus of either of these elements would go into the amorphous phase. However, small differences in cell parameters indicated that the amounts of phosphorus and silicon in the crystalline phase could be varied. To know for sure that this is the case collecting and analyzing neutron diffraction data was necessary. The results from that are presented in section 4.5 Main neutron diffraction study, and the following sections.

4.1.2 Hydrothermal treatment

It was discovered that using the same setup for hydrothermal treatment the material could be made amorphous. The temperature of the furnace was set to 180°C and a pellet was treated over night at a pressure corresponding to 7.5 atm. Prior to undertaking X-ray diffraction, a small amount of blu-tac was used to mount the pellet in the sample holder. Upon diffraction a new pattern resulted, which turned out to be the diffraction pattern of blu-tac, see top (green) XRD pattern in Figure 17. There was however an amorphous region between 16-28° 2θ that did not appear in the pure blu-tac pattern (cf. right part of Figure 17), and this XRD pattern matches that of the hydrothermally treated pellet. Thus the material in the pellet had undergone a structural transition from crystalline to amorphous caused by the high hydrothermal

pressure of 7.5 atm.

Regular hydrothermal treatments, typically at 120°C but also at 150°C, would not structurally transform the material to the extent of destroying crystallinity, but regular hydrothermal treatment would have other structural implications.

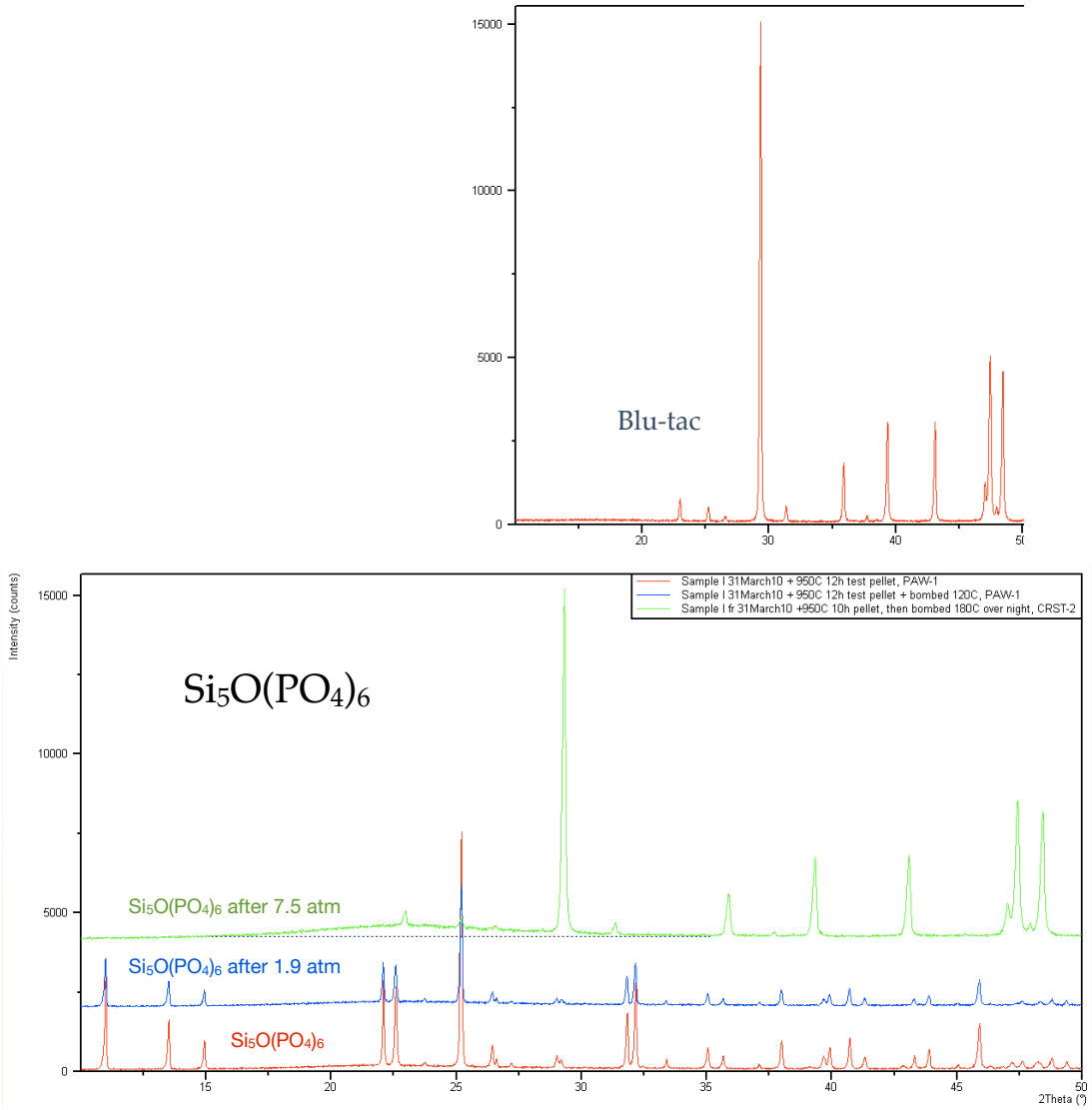

Figure 17 *XRD stack-plot (bottom). The red diffractogram (bottom curve) is the untreated parent composition, the blue (middle curve) is the same after hydrothermal treatment at 120°C. The top green diffractogram is the parent composition after hydrothermal treatment at 180°C. All XRDs were done on pellet surface. The very top part of the figure shows the XRD pattern for blu-tac. A small amount of blu-tac was used to keep the pellet in place on the XRD holder. Evidently, hydrothermal treatment at 180°C makes the crystalline material amorphous, thus only the blu-tac pattern remains.*

To simply measure the impedance in the low temperature range in air for untreated P-Si compositions proved to be impossible (when attempted the samples were too resistant to give an impedance plot). It was therefore decided to hydrothermally treat the pellets, and when this was done impedance data was obtained.

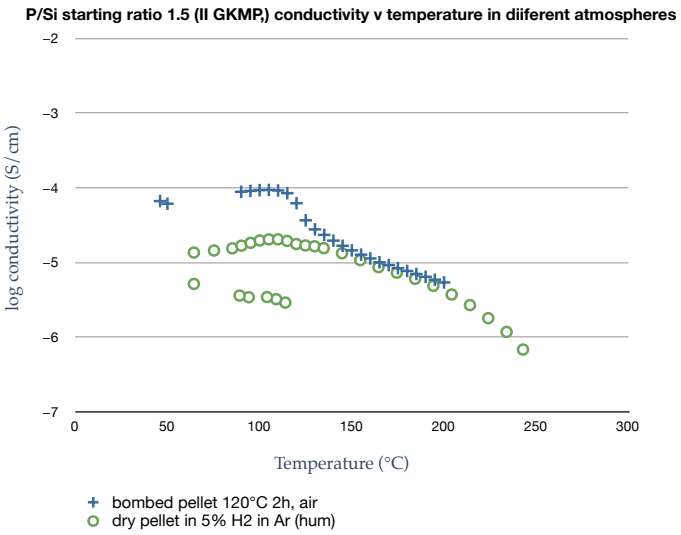

Figure 18 *Conductivity for a hydrothermally treated composition (P/Si=1.5) measured in air (blue data) compared to the same dry composition measured in humidified 5% H_2 in Argon (green data points).*

It was possible to get some measurements in humidified 5% H_2 for a dry sample of P/Si ratio 1.5 (i.e. not necessarily untreated, but a close approximation), see Figure 18, where the sample is compared to a hydrothermally treated P/Si 1.5 composition in air. Between the two compositions there is quite a noticeable difference in conductivity in the low temperature region, and from about 140°C the conductivity becomes the same. For the dry sample the conductivity was likely influenced by the humidity of the surrounding atmosphere affecting the sample, most likely corresponding to a light hydrothermal treatment which enabled a conductivity value.

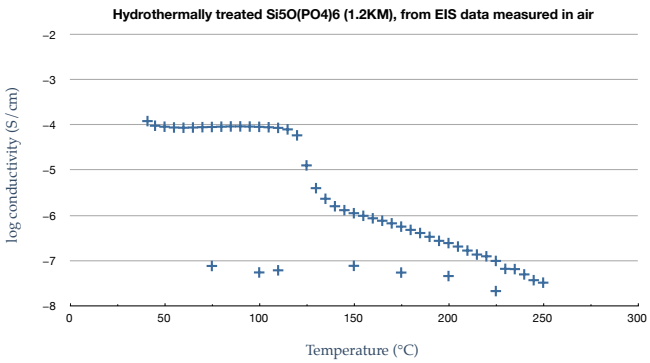

Figure 19 *Conductivity in air for the hydrothermally treated parent composition plotted against temperature. Note the large difference in conductivity upon cooling.*

To get an idea of what untreated pellets measured in air would yield in conductivity, conductivity data in air for the hydrothermally treated parent composition was measured when both increasing and decreasing temperature, see Figure 19. This data shows that after being tested up until 250°C and then subsequently cooled, that the difference in conductivity from 125°C and below was

about three orders of magnitude to that of when the sample started off hydrothermally treated. This strongly implies that there are significant benefits to hydrothermally treating the compositions.

Conductivities in air for the hydrothermally treated P/Si compositions are found in Figure 20. From this data it is evident that at 125°C the conductivity depends on the P/Si starting ratio. The lowest conductivity value is the 0.57 starting ratio, followed by 0.7, 0.8, 1.0, 1.2 and 1.5. Data for the lower P/Si ratios was not recorded however it is reasonable to assume that it would continue to decline as is the case with all the other compositions. The 1.5 composition was measured to about 150°C, it appears to closely follow the same conductivity pattern as the 1.2 composition. The composition that was overall best was the 1.0 composition, both at low temperature and from 135°C this is the case.

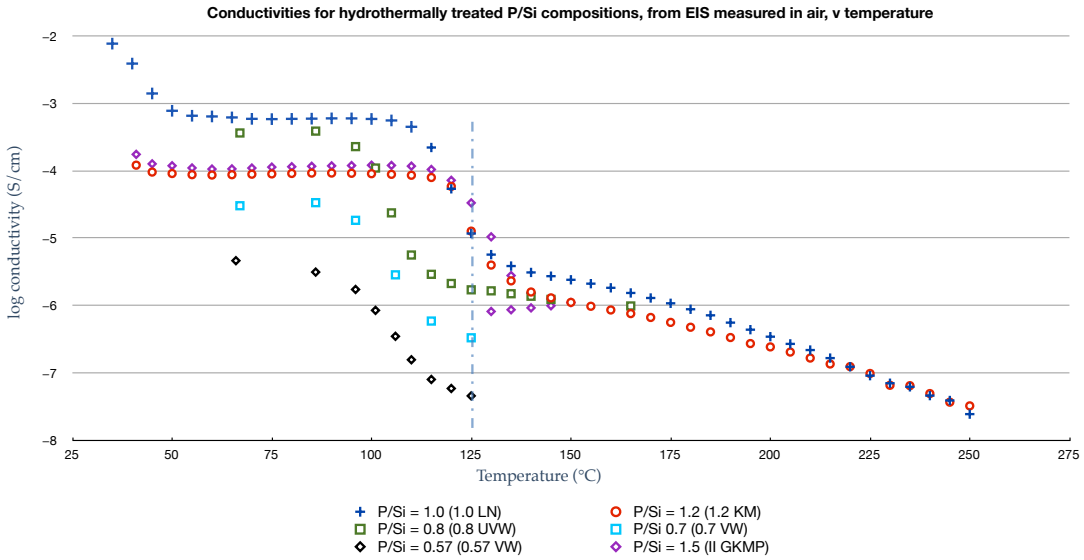

Figure 20 *Conductivities for hydrothermally treated compositions derived from EIS data measured in air. The different compositions have the following P/Si starting ratios: 0.57, 0.7, 0.8, 1.0, 1.2 and 1.5. Note that at 125°C the conductivity depends on the P/Si starting ratio.*

Since the hydrothermal treatment with water affected the conductivity, it was of interest to see the possible change in cell parameters. After refinement what was found was a small expansion in the c-axis for the parent composition compared to the untreated parent composition, and a measurable contraction in the a,b, axes for the hydrothermally treated composition. Another sample from the same batch was fired at 500°C (to ensure it was dry), and scanned at room temperature shortly thereafter. For this dried sample the c-axis appeared to shrink a bit in comparison to the untreated

sample, whereas the a,b axes expanded. Overall for the c-axis the changes were very minor and could as seen by Figure 21; the changes in a,b axes are more relevant. The conclusion is that there seems to be a trend, however the cell parameter change is quite small considering the values of the axes.

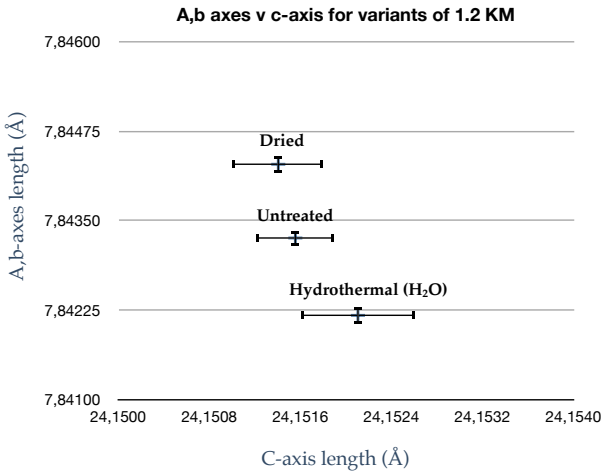

Figure 21 *Cell parameters for the dried (500°C), untreated and hydrothermally treated parent composition plotted against one another. Error bars are given by GSAS, (refined from XRD data) in reality it may be an even greater error.*

4.1.3 SEM analysis

A hydrothermally treated sample (120°C for 7h) of $Si_5O(PO_4)_6$, shown in Figure 22, was investigated with SEM. The microstructure of this sample was compared to an untreated sample of the same P/Si starting ratio, the resulting micrographs are depicted in Figure 23.

In regard to the microstructure there were some distinct differences between these two samples, the untreated composition (Figure 23) seemed to have a lot smoother surfaces and be more crystalline whereas the hydrothermally treated sample (Figure 22) had vast domains of rough-looking surfaces. Most likely it is the amorphous phase that becomes more visible on the surface of the crystalline domains, cf. the increased background from XRD after hydrothermal treatment. This does not necessarily mean the amorphous phase is only on the surface of the crystals, in fact it can be in the crystals too (e.g. in the form of water occupying the channels). It may well be that this amorphous phase which is coating the surface is what gives the high initial step in proton conductivity (compare e.g. P/Si = 1.0 at start in Figure 20). One would expect it to leave the material first at low temperatures, after which proton conductivity carries on inside of the crystals.

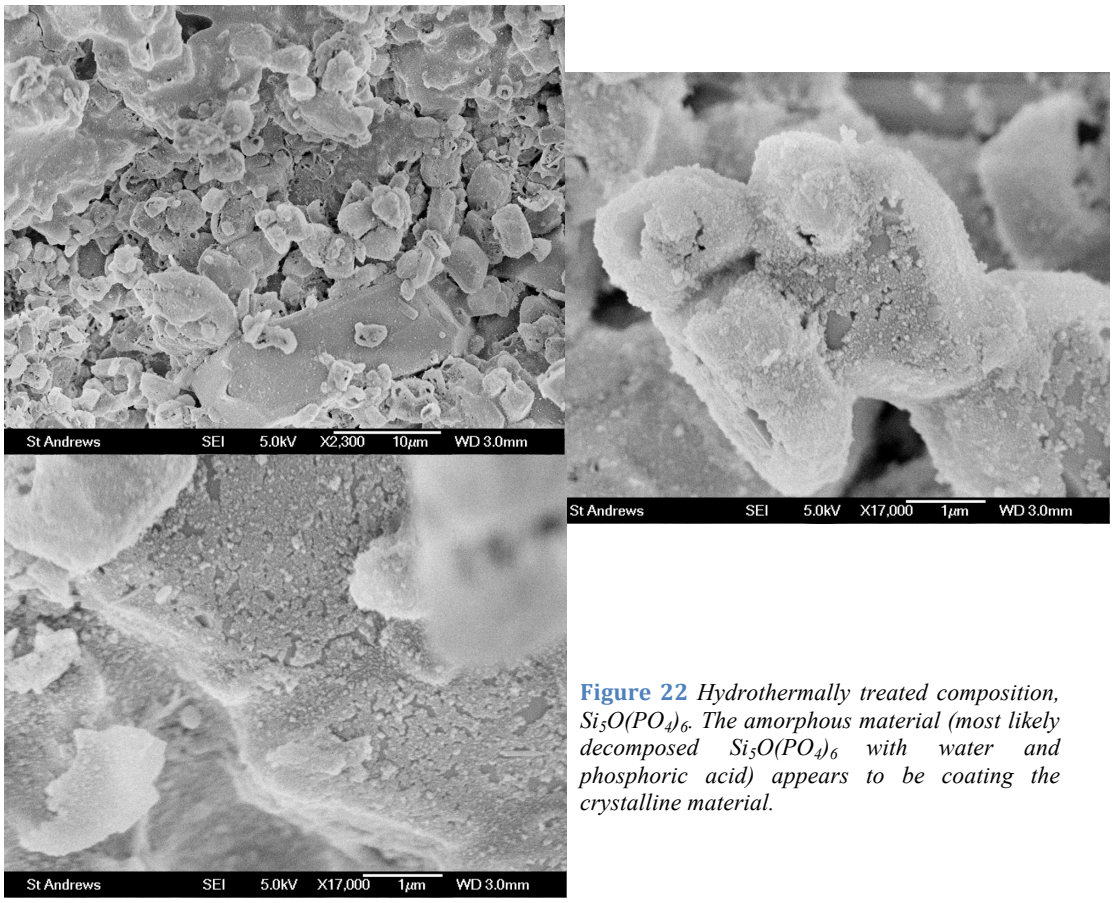

Figure 22 *Hydrothermally treated composition, $Si_5O(PO_4)_6$. The amorphous material (most likely decomposed $Si_5O(PO_4)_6$ with water and phosphoric acid) appears to be coating the crystalline material.*

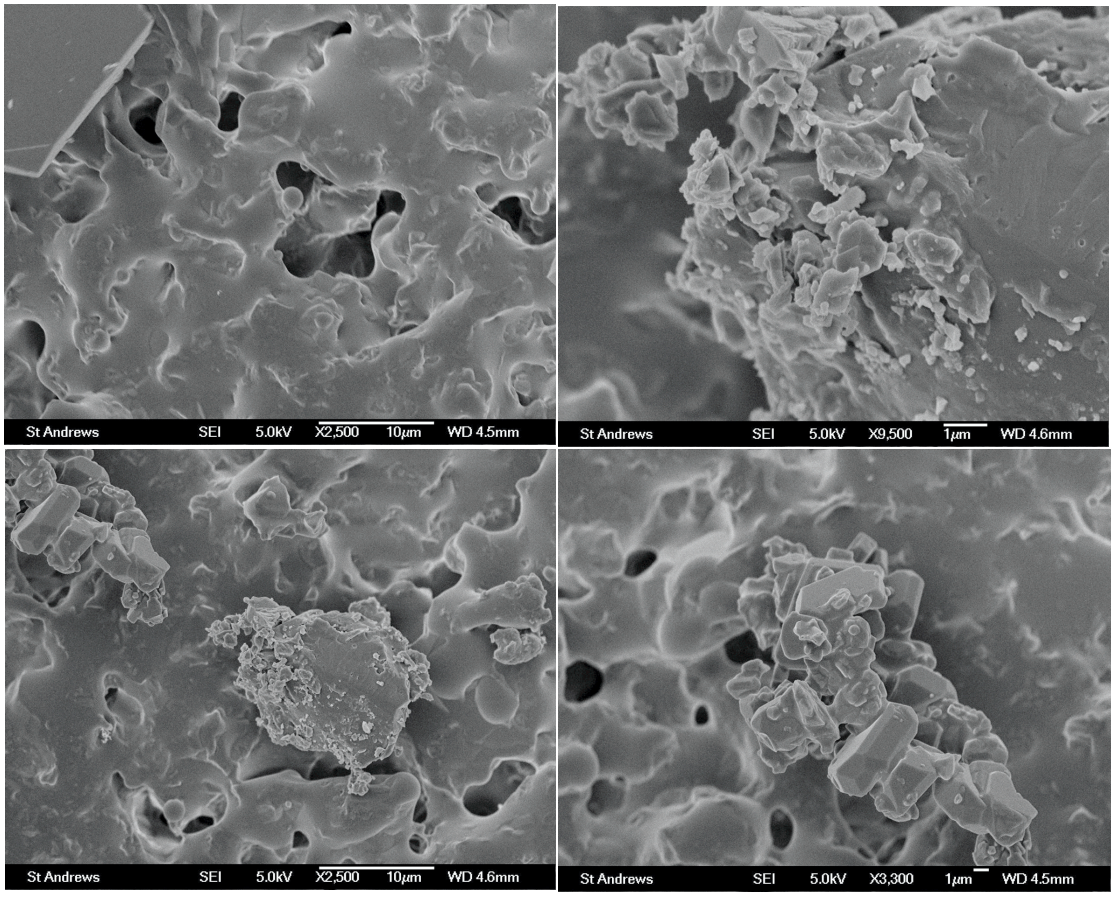

Figure 23 *SEM micrographs of the untreated parent composition, $Si_5O(PO_4)_6$. Note the general smoothness and formation of the crystalline particles.*

4.2 Solid state NMR data

The solid-state NMR data was acquired from samples packed in 4 mm rotors with a volume of around 80 µL. These rotors, although not weighed, were just about full during each measurement, therefore it is reasonable to assume that the volume was close to constant during all NMR measurements. The green area at the top of each figure is that part of the NMR range which is pictured in each main figure.

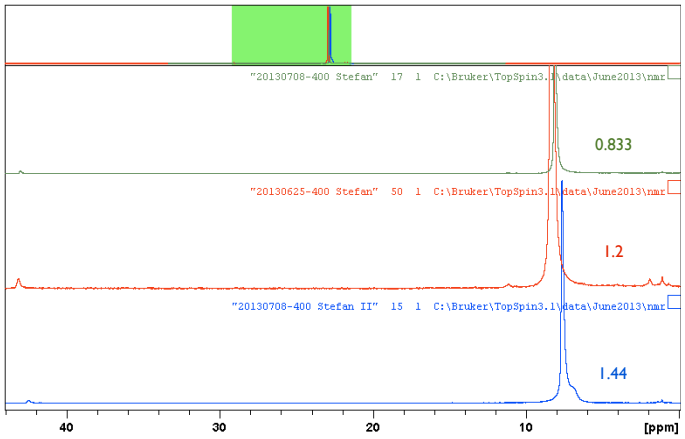

Figure 24 *^{1}H NMR spectra of the three untreated P-Si compositions. Note the difference in peak position for the chemical shifts at about 8 ppm. The chemical shift at 42.5 ppm is a spinning sideband. The green area is that part of the NMR range which is pictured in main figure.*

The ^{1}H NMR scans for the untreated compositions in Figure 24 show a visible difference in chemical shift for the 8 ppm peak.

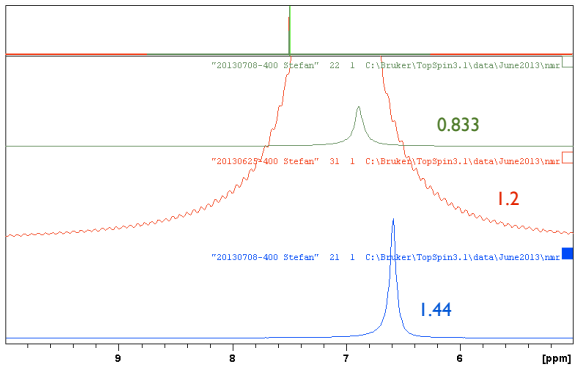

Figure 25 *^{2}H NMR spectra of the three hydrothermally treated (D_2O) P-Si compositions. The relative shift is similar to that in the previous figure. See Appendix F for scaled figure (parent composition did have a longer collection time for the ^{2}H scan, hence higher magnitude in peak).*

Figure 25 shows the ^{2}H NMR spectra for the three hydrothermally treated compositions. Noted from this figure is that the intensity is very high for the 1.2 composition, and that the relative positioning is the same as encountered in the ^{1}H NMR scans for the untreated compositions (previous figure). The difference in magnitude was due to a longer collection time, Appendix F shows the scaled spectra.

Returning to the ^{1}H NMR data, it can be noted that there is also a change in chemical

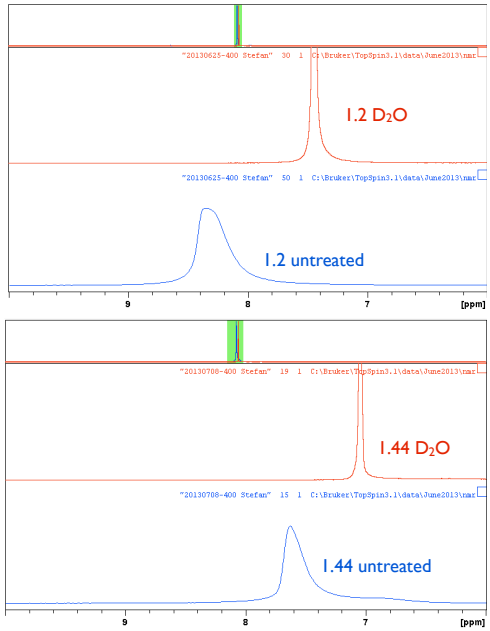

Figure 26 *Comparison of ^{1}H spectra for the parent composition (top) and the 1.44 (lower), hydrothermally treated with D_2O (red colour) v untreated (blue colour). Note the difference in peak shape as well as chemical shift.*

shift as a result of hydrothermally treating with D_2O (see Figure 26 where the ^1H spectra are compared for the 1.2 composition and 1.44 composition, before and after hydrothermal treatment). The change in chemical shift is likely due to D_2O entering the channels of the material and interacting with the material, as the shape of the chemical shift has become much more well-defined. The chemical shift due to hydrothermal treatment with D_2O changes character and becomes an average of that of D_2O at 4.79 ppm [64] and that of the untreated sample, which indicates that there is high mobility of protons in the structure post hydrothermal treatment. The chemical shift for the untreated samples is likely due to a proton linked to the phosphate group, as this is not an unusual chemical shift for phosphates at circa 8 ppm [65].

In addition, there were some significant differences between the untreated compositions and those treated with D_2O in the ^{31}P NMR. What was most apparent was the much stronger occurrence of the phosphoric acid peak for the hydrothermally treated compositions, shown in Figure 27. This implies that phosphoric acid becomes more a part of the system upon hydrothermal treatment. Prior to hydrothermal treatment there was still some phosphoric acid peak, although this was small in comparison to the – 44 ppm chemical shift, see Figure 28. After hydrothermal treatment the 0 ppm chemical shift is larger compared to the - 44 ppm chemical shift.

Furthermore, there was a profound difference in the signal strength for the chemical shift at - 44 ppm when comparing the untreated compositions (Figure 28) to those that were hydrothermally treated (Figure 27).

In the samples that were hydrothermally treated with D_2O the intensity of this peak (at - 44 ppm) is much stronger than with the same peak for the untreated samples. Indeed, if plotted against the cell parameters – which are derived from the neutron diffraction results, shown in Figure 30 – it is clear that there is a substantial difference in peak area and unit cell parameters especially for the parent composition, cf. Figure 29. The areas in Figure 29 were calculated through integration of the absolute intensities from the ^{31}P NMR chemical shift at - 44 ppm, by using the integration function in TopSpin. These values have been visualized by plotting them against the cell parameters and then labelled and connected (between respective untreated and hydrothermally treated composition) so that they can be identified. The purpose of doing this is in order to visualize two parameters at the same time and see whether there is correlation or not.

In the case of the - 44 ppm chemical shift there does not seem to be anything that indicates a full correlation to cell parameters.

Figure 30 shows moreover three graphs of lattice parameters derived from the neutron diffraction data obtained at room temperature: unit cell volume versus P/Si starting ratio (left graph), a,b axes length versus P/Si starting ratio (middle graph) and c-axis versus P/Si starting ratio (right graph) for untreated samples (blue data points) compared to the same samples after they have been hydrothermally treated with D_2O (red data points). For the P/Si starting ratio of 1.2 it can be noted that hydrothermal treatment with D_2O yields expansion in all axes. The silicon-rich composition

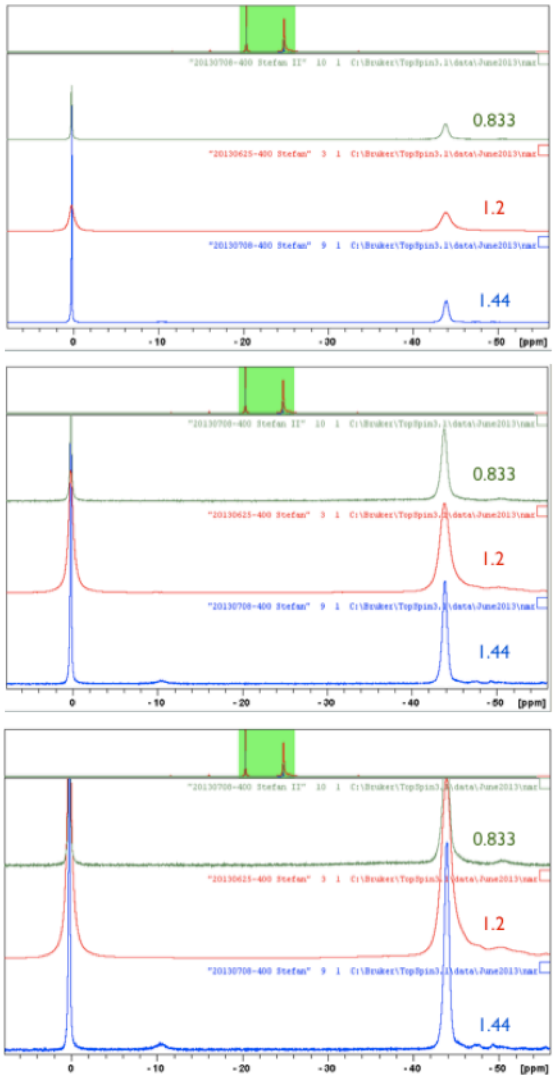

Figure 27 *^{31}P NMR of the P-Si compositions that were hydrothermally treated with D_2O. The same spectrum is pictured with different magnification, largest in bottom figure. Note the strong phosphoric acid peak at 0 ppm. The peak at - 44 ppm is that of the $Si_5O(PO_4)_6$ unit [48].*

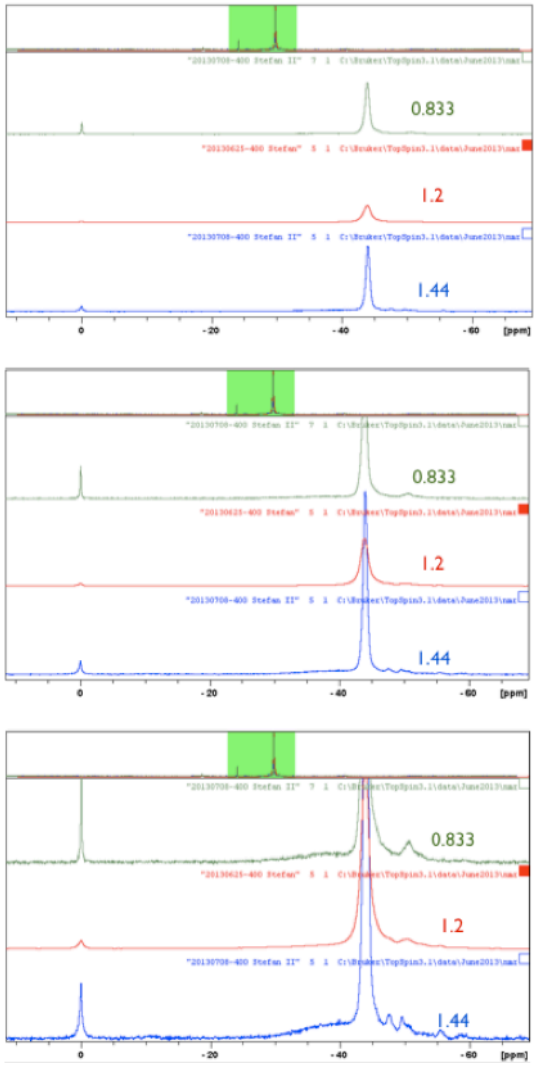

Figure 28 *^{31}P NMR of untreated samples with varied P/Si starting ratios. The same spectrum is pictured with different magnification, largest in bottom figure. Note for this figure the smaller intensity of the phosphoric acid peak, which may be there as a result of water absorption from the air.*

contracts somewhat in all axes when hydrothermally treated, whereas the phosphorus-rich composition also contracts in the a,b axes but stays virtually the same in the c-axis.

This shows that there are definite differences between the samples, and that there are different responses to the hydrothermal treatment. The conclusion must then be that these structural responses are due to differences in not only stoichiometry but also other factors may come into play – e.g. the amount of D_2O in each of the hydrothermally treated compositions. From the DTA it was clear that the 1.44 sample had far more D_2O to get rid off, it also has the longest a,b, axes of the three untreated compositions.

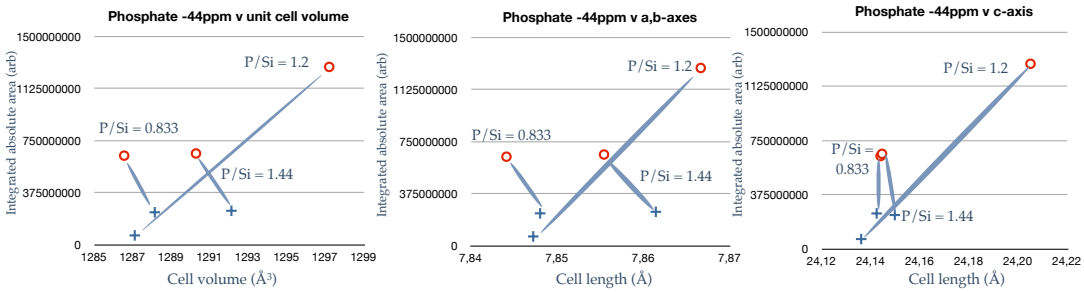

Figure 29 *Integrated signal of the -44ppm chemical shift from ^{31}P NMR plotted against unit cell volume (left), a,b axes length (middle) and c-axis (right) for the untreated samples (blue data, +) and hydrothermally treated with D_2O (red data,* o*). Cell parameter data from neutron diffraction results.*

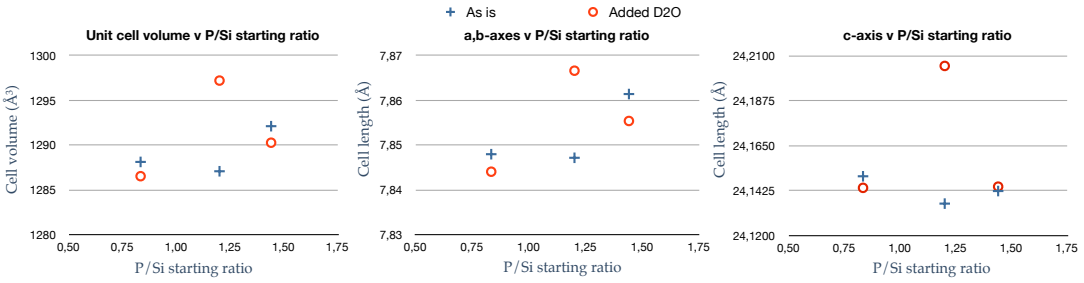

Figure 30 *Graphs of lattice parameters derived from neutron diffraction data at room temperature: unit cell volume v P/Si starting ratio (left), a,b axes length v P/Si starting ratio (middle) and c-axis v P/Si starting ratio (right) for untreated samples (blue data, +) and hydrothermally treated with D_2O (red data,* o*). For the P/Si starting ratio of 1.2 it can be noted that hydrothermal treatment with D_2O yields expansion in all axes.*

In the same way were the plots below constructed in Figure 31, integrating instead the chemical shift at 0 ppm. The data presented like this produces a visual of what the

hydrothermal process accomplishes: there are stronger signal strengths in the chemical shifts from the $Si_5O(PO_4)_6$ unit and phosphoric acid, and the hydrothermal treatment has an impact on the cell parameters. The a,b-axes and the unit cell volume appear to be a function of the phosphoric acid content for the hydrothermally treated compositions in Figure 31, whereas it is harder to establish any real correlation between the intensity of the $Si_5O(PO_4)_6$ chemical shift compared with the same cell parameters in Figure 29.

The most important result is from Figure 31 as it gives a vital clue to what is going on. It appears that the final cell length for the a,b axes of the hydrothermally treated compositions depend on the amount of phosphoric acid in the system. Since only D_2O has been added it must be that the close proximity of D_2O molecules and phosphate units create a chemical shift that is identified with phosphoric acid. Apart from the surface of the crystals it is only in the channels of the structure where water can reside. Moreover, a three-dimensional network of channels going through the structure filled with water or D_2O is likely to cause a much stronger signal than merely covering the surface.

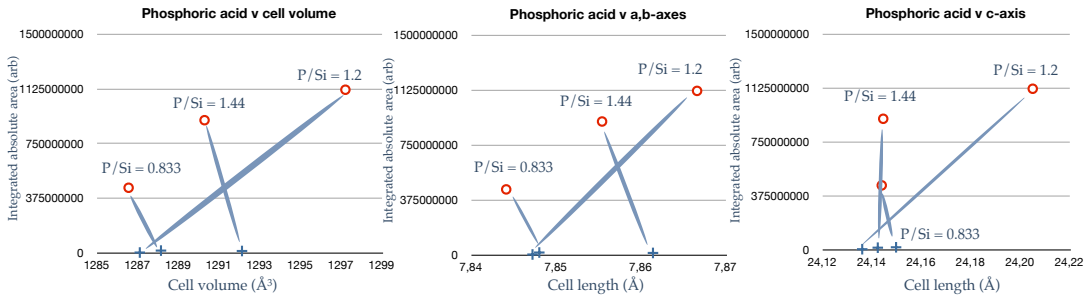

Figure 31 *Phosphoric acid content as derived from integration of the 0 ppm chemical shift from ^{31}P NMR spectra plotted against unit cell volume (left), a,b axes length (middle) and c-axis (right) for untreated samples (blue data points, +) and hydrothermally treated in D_2O (red circles). Cell parameter data from neutron diffraction results.*

Apart from the high intensity change, there is also a small change in chemical shift for the phosphoric acid peak – all samples increase by 0.2 ppm after hydrothermal treatment with D_2O (see Table 3). This can be compared with a different sample of the parent composition (1.2 D) which was hydrothermally treated with H_2O instead – this chemical shift is found at 0.028 ppm, which can be compared to an untreated 1.2 sample where the shift is at 0.00 ppm, and a D_2O treated parent composition at 0.207

ppm. Again, this could be showing that any surface adsorbed water is being substituted by D_2O, not merely stopping at the surface but also entering the channels of the P-Si materials.

A summary of the chemical shifts for the solid-state NMR data from primarily the neutron diffraction samples can be found in Table 3.

Name	P/Si starting ratio	Chemical shift – 44ppm in ^{31}P NMR (ppm)	Chemical shift 0 ppm in ^{31}P NMR (ppm)	Chemical shift 7-9 ppm in ^{1}H NMR (ppm)	Chemical shift 7ppm in ^{2}H NMR (ppm)
II GKMPR untreated	1.5	- 43.95	0.00	7.5951	
1.44G untreated	1.44	- 43.975	0.012	7.6318	
1.44G D_2O	1.44	- 43.92	0.1835	7.0474	6.5887
1.2F untreated	1.2	- 43.889	0.00	8.3407	
1.2F D_2O	1.2	- 43.895	0.207	7.4462	7.0824
1.2F with H_3PO_4	1.2	- 43.90	- 0.1697	9.14	
1.2D H_2O	1.2	- 43.873	0.028	7.4319	
1.0LN untreated	1.0	- 43.996	- 0.015	8.249	
0.833A untreated	0.833	- 43.884	- 0.039	8.0951	
0.833A D_2O	0.833	- 43.858	0.20	Data missing	6.8927
0.8UV untreated	0.8	- 43.873	-	7.957	
0.7V untreated	0.7	- 43.82	-	7.673	
0.57V untreated	0.57	- 43.793	-	7.62	

Table 3 *The chemical shifts from ^{31}P, ^{1}H and ^{2}H solid state NMR. The -44ppm ^{31}P-NMR chemical shift is assigned to the entire $Si_5O(PO_4)_6$ unit [48], the 0ppm chemical shift in ^{31}P-NMR is phosphoric acid (ibid). The ^{1}H chemical shift at 7 or 8 ppm is believed to be a proton linked to the phosphate group, as this is not an unusual chemical shift for phosphates at circa 8 ppm [65].*

4.2.1 Enriched sample

A sample of the parent composition $Si_5O(PO_4)_6$ was prepared with stoichiometric amounts of H_3PO_4 and SiO_2, except that 20% of the SiO_2 was substituted for $^{29}SiO_2$. After multiple firings a phase pure sample was obtained. This sample was laid aside for five weeks before NMR was undertaken (red spectrum in Figure 32). The second NMR was done more recently after another firing on the same sample (see blue spectra in the same figure).

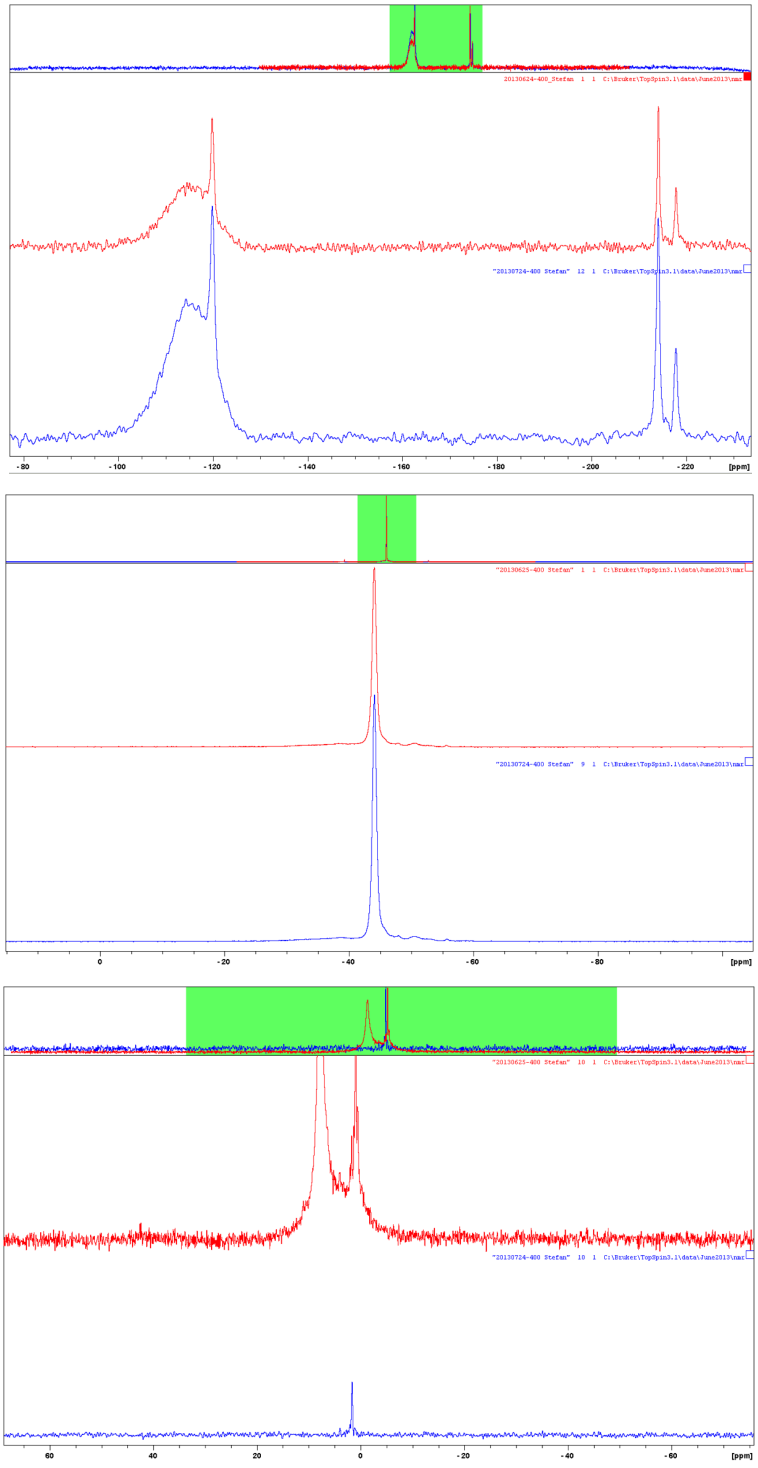

Figure 32 *^{29}Si NMR (top), ^{31}P NMR (middle) and ^{1}H NMR (bottom) of the sample that had 20% SiO_2 substituted for $^{29}SiO_2$. The sample represented by the blue lines is the same sample as the one represented by the red lines, except for an extra firing on the former.*

From the ^{29}Si NMR an increase in amorphous SiO_2 appears to be the case (at -112 ppm). The chemical shifts between -210 to -220 ppm belong to the octahedrally coordinating silicons, and the chemical shift at -120 ppm is the tetrahedral silicon [47].

There is a marked difference in the ^{1}H NMR, with the peak at 7.8 ppm entirely disappearing – this could be a water related peak that occurred as a result of absorbing humidity from

the air over time.

4.3 High temperature behaviour

A stoichiometric and phase pure sample of $Si_5O(PO_4)_6$ was prepared and analyzed in a high temperature XRD setup, from room temperature up to 1000°C. From the same batch a hydrothermally treated sample was produced and analyzed in much the same way except that more temperature steps were recorded including cooling data. It is clear that there are distinct differences between the two samples[6].

Regarding the untreated sample, it is evident that very little change occurs throughout the temperature range which is also what is seen from TG and DTA, see top part of Figure 34. The only visible and valid change that occurs is close to 1000°C on heating and about 950°C on cooling in the DTA (the other peaks on heating are likely instrumental errors). The important thing is that the DTA curve makes no changes in the low–intermediate temperature region. The hydrothermally treated (using H_2O) composition on the other hand shows significant change as the temperature increases, in the two mass losses and double DTA peaks, see lower part of same figure.

From the XRD (top part of Figure 33) there is little change in the untreated composition, however significant change (especially in the amorphous region) of the hydrothermally treated composition (bottom part of Figure 33). This happens especially in the low temperature region, although there is also a decrease all the way up to 1000°C.

The amorphous phase decreases substantially between 125° – 150°C, see Figure 35. On cooling the background returns however there appears to be less of it, cf. red and dark green diffractograms in Figure 36. Note from this figure also the lower peak intensities in the peaks at lower 2θ, for the diffractogram at 1000°C (pink colour), with exception for the peak at just over 16° 2θ which is stronger.

What likely happens is that water is leaving the structure on heating – hence the diminishing amount of background. On cooling background does appear to return a

[6] Due to that the instrument was very new at the time it had not been not properly calibrated, and in addition the instrument parameter files were not available and thus the obtained data could not be refined.

bit, however this cannot be water due to the fact that there is no mass increase on cooling, cf. lower part of Figure 34.

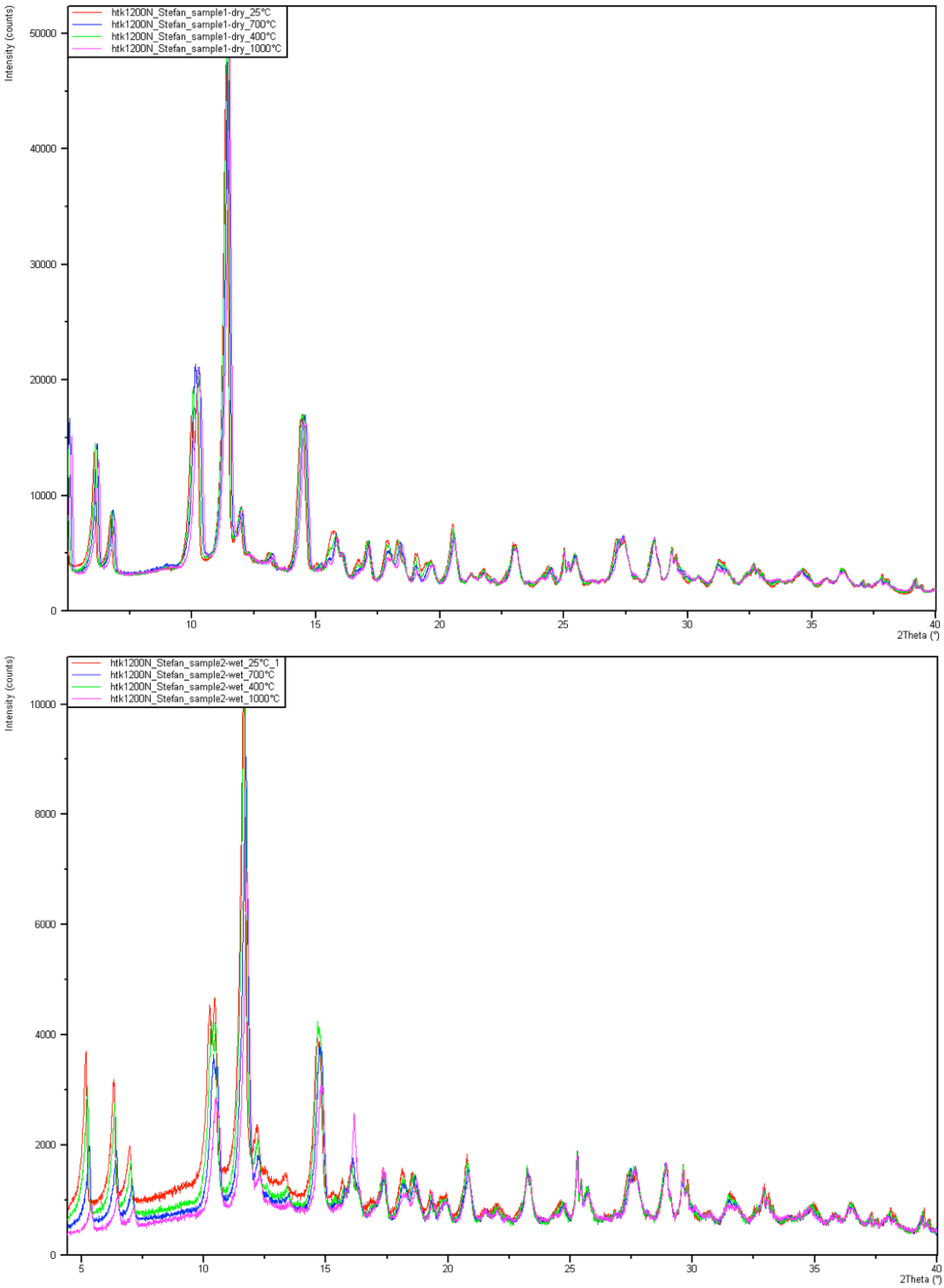

Figure 33 *High temperature XRD plots of untreated parent composition (top) compared to XRD plots of the hydrothermally treated (H_2O) parent composition (bottom). The colour code for the diffractograms is: red = 25°C, green = 400°C, blue = 700°C and purple = 1000°C.*

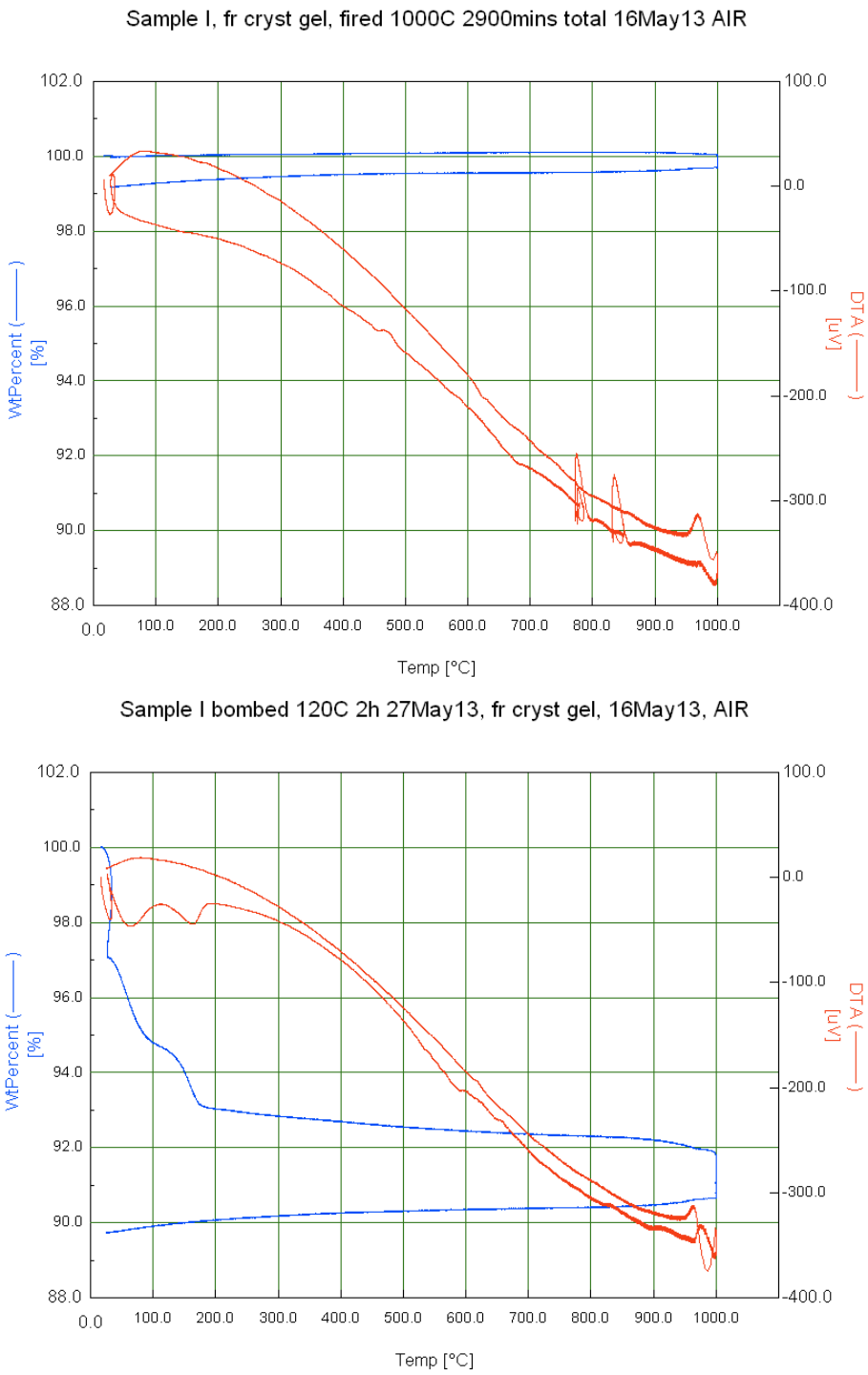

Figure 34 *TG and DTA data for the untreated parent composition (top) contrasted with the corresponding data for the hydrothermally (H_2O) treated parent composition from the same batch (bottom).*

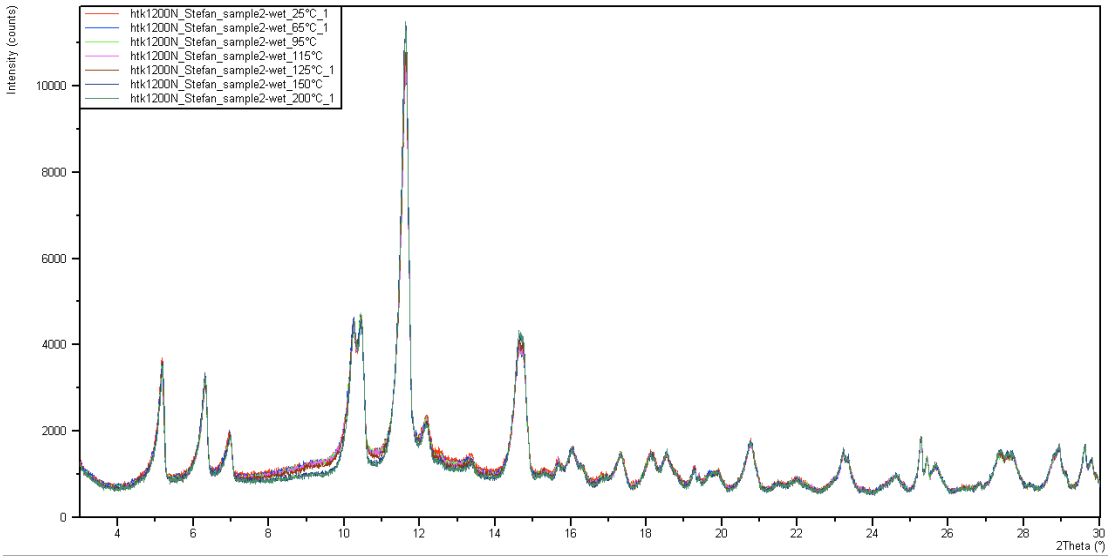

Figure 35 *XRD stack-plot of the hydrothermally treated parent $Si_5O(PO_4)_6$ in the low temperature region. Note the larger drop in amorphous content between 125°C and 150°C.*

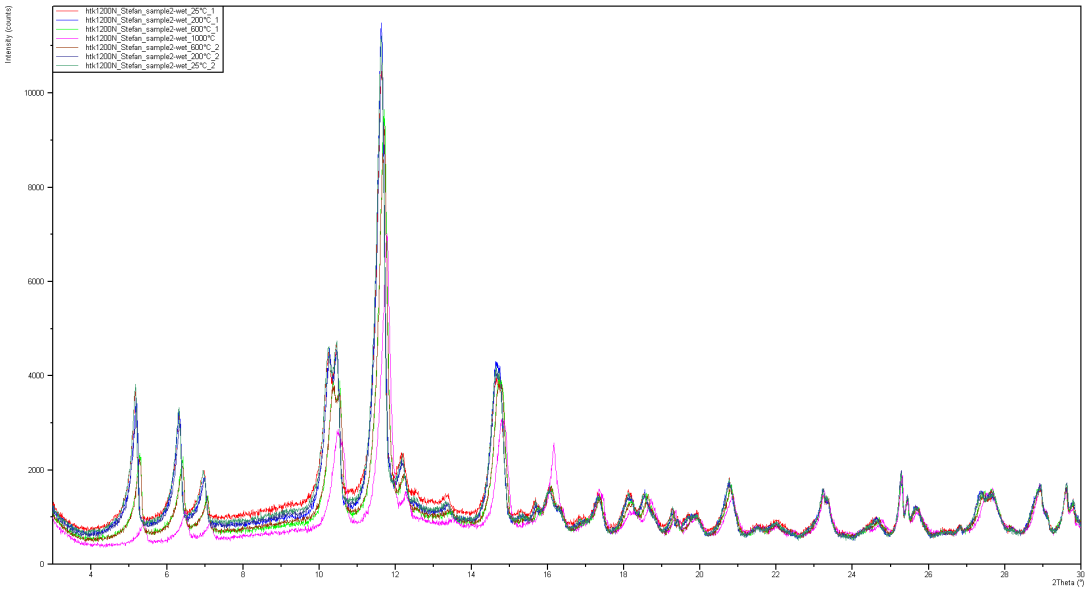

Figure 36 *XRD stack-plot of the hydrothermally treated parent $Si_5O(PO_4)_6$ over the measured temperature range and then down to room temperature again. The amorphous phase decreases throughout the temperature range and is not fully retained upon cooling to room temperature. The temperatures are: room temperature start (red), 200°C heating (light blue), 600°C heating (light green), 1000°C (pink), 600°C cooling (light brown), 200°C cooling (dark blue) room temperature final (dark green).*

4.4 A first look with neutrons

A P/Si = 1.2 sample was initially tested in the GEM instrument as well as a sample which had been hydrothermally treated with D_2O. This was a first test and performed in between changing other samples and therefore happened to be done in a cryostat at a temperature of - 63°C.

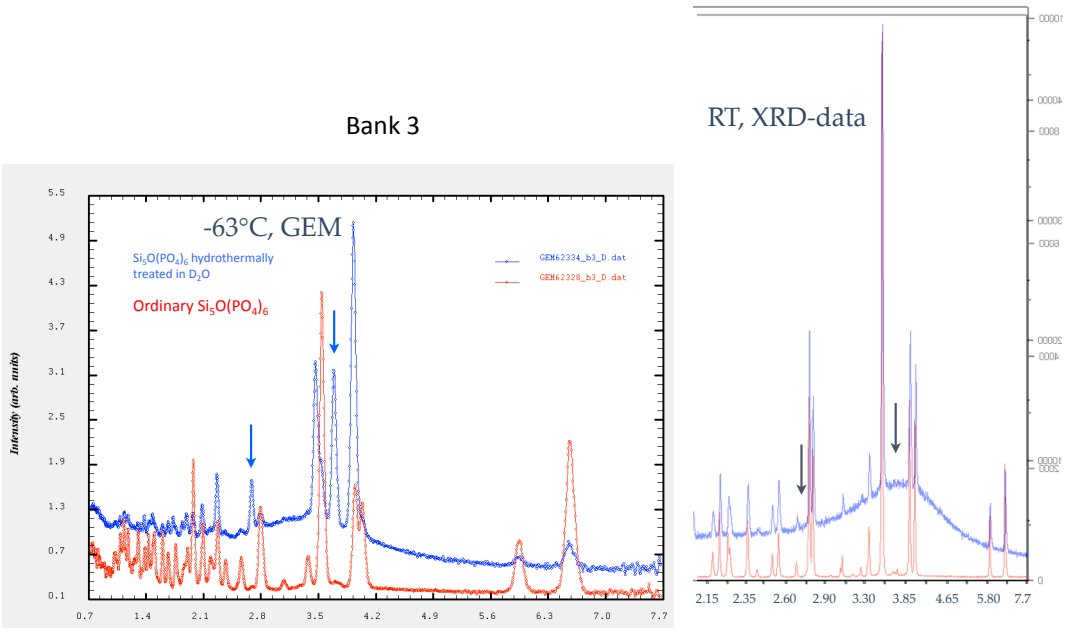

Figure 37 *A neutron diffraction pattern (left) of the P/Si = 1.2 composition at – 63°C. The bottom red diffractogram is the untreated composition and the top blue diffractogram is the hydrothermally treated composition. The corresponding XRD patterns at room temperature are shown to the right.*

In this preliminary test there appeared to be a couple of extra peaks in the hydrothermally treated composition, which did not occur in the XRD of the same sample at room temperature, see Figure 37. Eventually it was found that the extra peaks matched a pattern for ice, which was not too surprising considering the experimental environment.

A deeper study was undertaken in June 2013 at the same centre, at the Rutherford Appleton Laboratory in Harwell, UK. All measurements were done in the GEM instrument. A brief schematic of the GEM instrument can be found in Figure 11 in chapter 3, along with photographs showing parts of the experimental setup.

4.5 Main neutron diffraction study

The compositions that were made for the main neutron study had the P/Si starting ratios of 0.833, 1.2 and 1.44. All compositions were measured as prepared and also as hydrothermally treated counterparts with D_2O. All these runs were done at room temperature.

Two comparative high temperature studies of the 1.2 composition were also undertaken – one dry and one hydrothermally treated with D_2O. Both of these samples came from the same batch and were in the same experimental setup and running the same program.

For the high temperature runs a quartz tube was used and in the case of all other measurements at room temperature, 6 and 8 mm Vanadium cans sealed with Indium wire were employed.

A series of Rietveld refinements were carried out on the accumulated SUM-files (about 45 minutes of collection time) as well as sequential GSAS runs for the five minute runs. The refinements were all done in pretty much the same way in order to be able to more accurately compare results, see example in section 3.1.2 Rietveld refinement methodology for neutron data. Initially all the occupancies were held constant at 100% according to the structural model $Si_5O(PO_4)_6$, and from there the coordinates were fixed. The occupancies were then varied (apart from the Si2 site and the O5 site that remained fixed at 100%), and again the atomic displacement parameters, UISO values, were varied (however not at the same time as the occupancies). Any occupancy value that exceeded 100% was manually changed to 100%. The χ^2 values for the parent compositions were a bit high at the end of the refinements, this could be due to that these two measurements were done in a quartz vessel.

The results showed that the unit cell expanded for the parent composition as a result of the hydrothermal treatment with D_2O, and it remained expanded throughout the temperature range. For the other two compositions there was slight contraction in the unit cell volume. The results of the refined cell parameters can be found in Table 4.

Room temperature cell parameters	P/Si starting ratio	Cell volume (Å^3)	a, b axis (Å)	c-axis (Å)	c/a	Reduced χ^2
1GEM63213_818_0.833A_dry_8mm_FixedF	0.833	1288.14(21)	7.8480(7)	24.1497(23)	3.077	1.935
GEM63215_A_6mm_0.833A_D2O	0.833	1286.55(24)	7.8441(9)	24.1439(27)	3.078	2.024
GEM63046_HiT1_RT_start	1.2	1287.1(4)	7.8472(13)	24.136(4)	3.076	5.144
HiT2 D2O	1.2	1297.2(6)	7.8666(19)	24.205(6)	3.077	7.113
1GEM63214_831_1.44G_dry	1.44	1292.12(21)	7.8614(7)	24.1423(23)	3.071	2.960
GEM63416_1.44G (D2O)	1.44	1290.28(20)	7.8554(7)	24.1445(22)	3.074	1.791

Table 4 *Lattice parameters obtained from neutron data at room temperature for untreated as well as hydrothermally treated compositions. The statistical* χ^2*-value is given for each refinement in the far right column. The occupancy was held constant for the Si2-site at 1.000 as well as for the O5 site. Occupancies for these refinements are given in table Table 5.*

What can be clearly seen from the obtained cell parameters at room temperature is that both the unit cell volume for the phosphorus-rich composition (P/Si = 1.44) as well as for the silicon-rich composition (P/Si = 0.833) contract when subjected to hydrothermal treatment with D_2O. The opposite trend occurs for the parent composition, $Si_5O(PO_4)_6$: a 0.78% expansion in the total unit cell volume which is quite large in comparison to the contractions of the 0.833 (-0.12%) and 1.44 (-0.14%) compositions. The parent composition's expansion upon hydrothermal treatment is due to that all the axes in the unit cell are expanding; a, b axes (+ 0.25%) and in the c-axis (+ 0.29%).

Comparing the c/a ratios it is clear that they increase marginally in all cases when each composition is hydrothermally treated with D_2O – most for the 1.44 composition where it increases from 3.071 to 3.074, this is mainly due to contraction in the a,b axes accompanied with a small expansion in the c-axis. For the two other compositions there is contraction (0.833) and expansion (1.2) in all axes, respectively.

The biggest unit cell volume for the as prepared samples, was the 1.44 composition which had a total unit cell volume of 1292.12 Å^3. Unlike the other compositions, this had an extra firing at 1100°C for 20h. Before this happened there was a presence of silicon pyrophosphate, this decomposed and went into the crystalline phase; as it was incorporated into the primary phase, this most likely made the primary phase more

phosphorus-rich. The hydrothermal treatment of the 1.44 composition leads to a decrease in its cell volume (to 1290.28 $Å^3$). From the occupancies in Figure 38 a decrease in phosphorus occupancy can be noted, accompanied by a much smaller decrease in Si3, see Table 5. Interesting to note is that there is a decrease in the occupancy for all elements when hydrothermal treatment is applied, and this could explain the unit cell contraction.

Inversely, for the parent composition there is an overall increase in the occupancy for all elements and this could explain the cell expansion for that composition seen earlier in Figure 30.

From the left diagram in Figure 38 it can be noted that the 0.833 composition decreases its occupancy of the tetrahedral Si3 site upon hydrothermal treatment – this is likely what causes this composition to contract its cell parameters despite extra phosphorus being added to the phosphorus site and despite a small addition of octahedral silicon to the Si1 site.

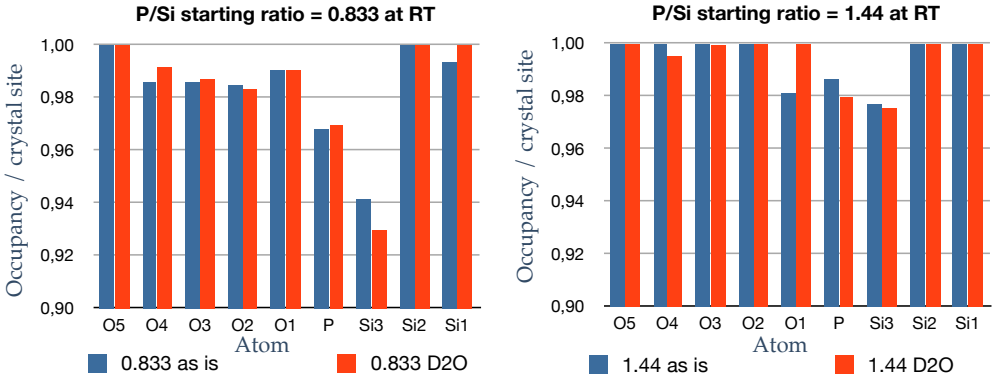

Figure 38 *Fractional occupancies for the 0.833 compositions (left) and the 1.44 compositions (right) before and after hydrothermal treatment with D_2O. Blue bars are the occupancies of the untreated compositions, red bars (to the right of the blue) are the occupancies for the hydrothermally treated compositions with D_2O. The multiplicity factor has not been considered here but is considered in Table 4.*

Atom	Multiplicity	0.833 as is	0.833 D2O	0.833 difference	1.2 as is	1.2 D2O	1.2 difference	1.44 as is	1.44 D2O	1.44 difference
O5	18	1.0000	1.0000	**0.0000**	1.0000	1.0000	**0.0000**	1.0000	1.0000	**0.0000**
O4	18	0.9858	0.9915	**0.1026**	0.9888	0.9832	**- 0.1008**	1.0000	0.9950	**- 0.0900**
O3	18	0.9857	0.9870	**0.0234**	0.9825	0.9972	**0.2646**	1.0000	0.9992	**- 0.0144**
O2	18	0.9845	0.9829	**- 0.0288**	0.9908	0.9883	**- 0.0450**	1.0000	1.0000	**0.0000**
O1	3	0.9903	0.9904	**0.0003**	1.0000	1.0000	**0.0000**	0.9811	1.0000	**0.0567**
P	18	0.9679	0.9695	**0.0288**	0.9613	0.9714	**0.1818**	0.9864	0.9795	**- 0.1242**
Si3	6	0.9413	0.9293	**- 0.0720**	0.9232	0.9378	**0.0876**	0.9769	0.9753	**- 0.0096**
Si2	6	1.0000	1.0000	**0.0000**	1.0000	1.0000	**0.0000**	1.0000	1.0000	**0.0000**
Si1	3	0.9933	1.0000	**0.0201**	1.0000	1.0000	**0.0000**	1.0000	1.0000	**0.0000**
Sums	Atoms / unit cell in $Si_5O(PO_4)_6$	Atoms / unit cell	Atoms / unit cell	Change in occupancy / unit cell	Atoms / unit cell	Atoms / unit cell	Change in occupancy / unit cell	Atoms / unit cell	Atoms / unit cell	Change in occupancy / unit cell
Total O	75	74.1789	74.2764	0.0975	74.3178	74.4366	0.1188	74.9433	74.8956	-0.0477
Total P	18	17.4222	17.4510	0.0288	17.3034	17.4852	0.1818	17.7552	17.6310	-0.1242
Total Si	15	14.6277	14.5758	-0.0519	14.5392	14.6268	0.0876	14.8614	14.8518	-0.0096

Table 5 *The fractional occupancies for each atomic site derived from neutron data. The difference columns in bold show the increase or decrease with multiplicity taken into consideration when hydrothermally treating with D_2O and given in the unit of atoms per unit cell. The lower part of the table has the sums of each element.*

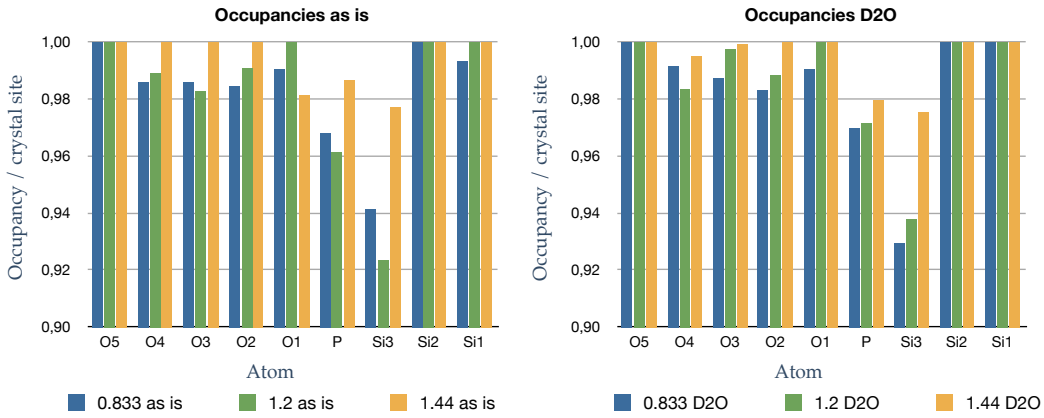

Figure 39 *Fractional occupancies for each atomic site derived from neutron data for untreated compositions (left) and hydrothermally treated with D_2O (right). For the parent composition there is an increase in the Si3 and P occupancies with hydrothermal treatment.*

Comparing what happens to all three compositions, the silicon-rich composition, 0.833A D_2O, has an even smaller unit cell volume (1286.55 $Å^3$) and compared to both the hydrothermally treated 1.2 and 1.44 compositions it has a lower occupancy of both tetrahedral phosphorus and tetrahedral silicon (Si3), see right part of Figure 39. The hydrothermally treated 1.44 composition on the other hand has more phosphorus, which is not surprising since it had a higher amount of phosphorus to begin with (as

well as over 98% occupancy for the regular as prepared sample).

Solely taking the total occupancies into account, the overall trends can be observed in Figure 40 where the total number of atoms per unit cell for each element is plotted against the P/Si starting ratio. What emerges is that for all the hydrothermally treated samples (red circles) there is a trend of increasing occupancy for each element as the P/Si starting ratio goes toward more phosphorus. For the untreated compositions (blue crosses) there is also a similar trend as far as the total oxygen content, however not for silicon and phosphorus. This latter discrepancy is likely due to a problem with the modelling (as they all were modelled the same, with the same starting stoichiometry, i.e. that of the parent composition). A different strategy will be adopted for future

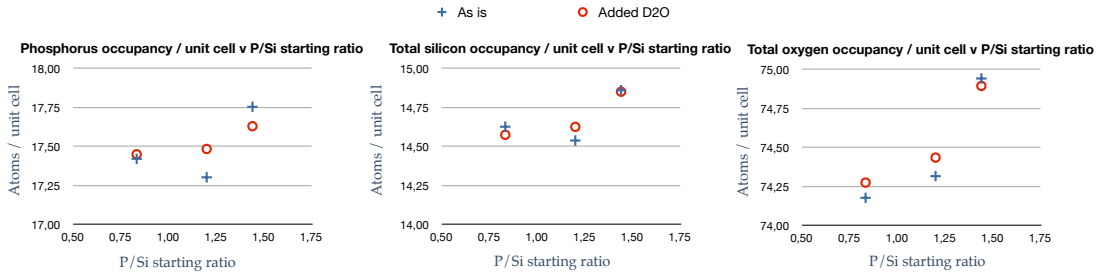

Figure 40 *Total occupancies for the unit cells derived from neutron data, plotted against the P/Si starting ratio. Note the increasing trend in oxygen occupancy as the P/Si starting ratio increases for both untreated (blue data, +) and hydrothermally treated compositions (red data, o).*

work, in which the starting ratios are varied (i.e. the same as respective starting ratio) and the occupancies of silicon and phosphorus set to full occupancy values.

The graph of interest is that of the oxygen content. If this truly is the case then it means that there is some flexibility in oxygen content, and that a corresponding amount of phosphorus will accompany the higher oxygen content to balance the charge. Future work should investigate this aspect too as well as that mentioned in the previous paragraph.

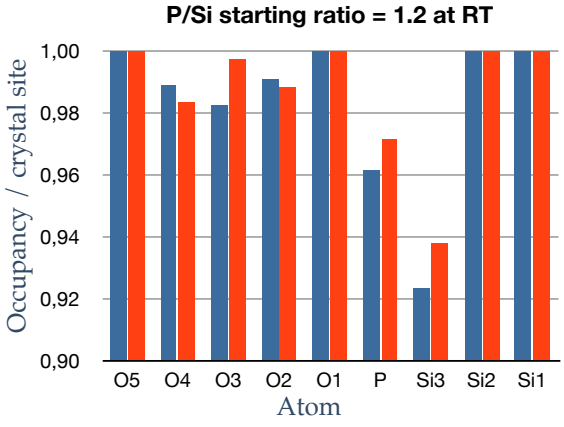

Figure 41 *Fractional occupancies for the 1.2 composition before and after hydrothermal treatment with D_2O. Blue bars (to the left) are the occupancies for the untreated composition, red bars (to the right) are the corresponding occupancies for the hydrothermally treated sample. The multiplicity factor has not been considered here but is considered in Table 5.*

The positive c-axis shift for the parent composition upon being hydrothermally treated can possibly be explained by the increased occupancy of the tetrahedral Si3 site, pictured in Figure 41. Indeed, the parent composition is the only sample that increases in occupancy on the Si3 site and expands in the c-axis – whereas 0.833 decreases in Si3 along with its c-axis.

The hydrothermally treated 1.44 composition appears to have quite a bit more tetrahedral silicon, as seen in Figure 39. It could well be in the case of the 1.44 compositions that some of the atoms on the tetrahedral silicon site are in fact phosphorus; this would explain why there is so little change in the c-axis when considering the larger occupancy of the Si3 site compared to the 0.833 and 1.2 compositions.

4.5.1 Bond length analysis

Neutron data for the three main compositions (P/Si starting ratio: 0.833, 1.2 and 1.44) and for their hydrothermally treated (with D_2O) counterparts was analyzed with the disaglviewer function in GSAS. This program calculates the bond distances between atoms in the structure as well as gives the angles in between as a result of the refined coordinates.

The refinements were based on the structural model found in Poojary's paper, i.e. $Si_5O(PO_4)_6$ [8]. To a large extent the bond distances agree with Poojary's paper, however, there are some anomalies that are worthy of consideration. Figure 42 shows Poojary's results which can be compared to these here, graphically represented in Figure 43 for the P_O bonds and Figure 44 for the Si_O bonds, respectively. The observed bond lengths are also given in numerical form in the tables in Appendix A1.

Comparative bond lengths were calculated from Shannon [66], and can be found in Table 6. These bond lengths were calculated by adding the quoted ionic radii for pairs of various conceivable elemental species. The observed bond lengths can be matched to a calculated one in almost all cases.

For the 0.833 compositions there is no difference in the phosphorus – oxygen bond lengths upon hydrothermal treatment, and for the other two compositions the following can be noted: P_O3 and P_O5 expand a bit for the parent composition upon

hydrothermal treatment with D_2O, whereas for the 1.44 composition there is small expansion in P_O2 instead and almost negligible contraction in the P_O3 bond.

The Si3_O4 bond is the same for the both 1.44 compositions, whereas it contracts a bit for the parent composition and still a bit more for the 0.833 compositions when those are hydrothermally treated.

The overall trend for the parent composition is an expansion in bond lengths when it undergoes hydrothermal treatment, and this is most likely due the influence that D_2O has.

RB210					RB255C			
Si octahedra	**Bond length (Å)**		**Angle (°)**		**Si octahedra**	**Bond length (Å)**		**Angle (°)**
Si1_O3	1.789(5)	O3_Si1_O3	180.00		Si1_O3	1.783(5)	O3_Si1_O3	180.00
		O3_Si1_O3	95.2(5)				O3_Si1_O3	92.7(3)
		O3_Si1_O3	84.8(5)				O3_Si1_O3	87.3(3)
Si octahedra					**Si octahedra**			
Si2_O2	1.818(6)	O2_Si2_O2	85.6(9)		Si2_O2	1.813(7)	O2_Si2_O2	88.0(4)
Si2_O5	1.697(10)	O5_Si2_O2	95.6(9)		Si2_O5	1.696(7)	O5_Si2_O2	91.9(4)
		O5_Si2_O2	95.6(5)				O5_Si2_O2	88.6(3)
		O5_Si2_O2	178.1(11)				O5_Si2_O2	176.6(5)
		O5_Si2_O5	82.8(8)				O5_Si2_O5	91.5(5)
Si tetrahedra					**Si tetrahedra**			
Si3_O1	1.706(14)	O4_Si3_O1	110.1(6)		Si3_O1	1.659(8)	O4_Si3_O1	108.1(4)
Si3_O4	1.654(6)	O4_Si3_O4	108.8(6)		Si3_O4	1.5299(6)	O4_Si3_O4	110.8(4)
Phosphate group					**Phosphate group**			
P_O2	1.526(14)	O3_P_O2	109.0(6)		P_O2	1.533(7)	O3_P_O2	113.5(4)
P_O3	1.518(6)	O4_P_O2	110.0(7)		P_O3	1.525(7)	O4_P_O2	107.3(5)
P_O4	1.518(6)	O5_P_O2	113.0(7)		P_O4	1.535(6)	O5_P_O2	111.5(5)
P_O5	1.525(6)	O4_P_O3	111.3(7)		P_O5	1.529(7)	O4_P_O3	109.8(5)
		O5_P_O3	105.9(7)				O5_P_O3	103.8(6)
		O5_P_O4	107.6(7)				O5_P_O4	110.9(5)

Figure 42 *Sample RB210 (left) and RB255C (right) compared side-by-side, results after Poojary et al's paper [8]. Note the short Si3_O4 bond lengths for the latter sample which are very similar to P_O bond lengths. In addition, the P_O4 bond length is shorter than 1.57 Å as obtained in this project.*

Central atom	Bonds	Sum of ionic radii	Note
Octahedral Si	Si(VI)_O(IV)	1.78	2 hydrogens at end
	Si(VI)_O(II)	1.75	
	Si(VI)_O(II)_H(II)	1.57	
	Si(VI)_OH(II)	1.72	
	Si(VI)_OH(II)_H(II)	1.54	
	Si(VI)_OH(III)	1.74	
	Si(VI)_OH(III)_H(II)	1.56	
Tetrahedral Si	Si(IV)_O(IV)	1.64	2 hydrogens at end
	Si(IV)_O(II)	1.61	
	Si(IV)_O(II)_H(II)		
	Si(IV)_OH(II)	1.58	* subst P_O4?
	Si(IV)_OH(II)_H(II)		
Tetrahedral P	P(IV)_O(IV)	1.55	2 hydrogens at end
	P(IV)_O(II)	1.52	
	P(IV)_O(II)_H(II)		
	P(IV)_OH(II)	1.49	
	P(IV)_OH(II)_H(II)	1.31	
Octahedral P(5+)	P(VI)_O(IV)	1.76	2 hydrogens at end
	P(VI)_O(II)	1.75	
	P(VI)_O(II)_H(II)	1.57	
	P(VI)_OH(II)	1.72	
	P(VI)_OH(II)_H(II)	1.54	
Octahedral P(3+)	P(VI)_O(IV)	1.82	2 hydrogens at end
	P(VI)_O(II)	1.79	
	P(VI)_O(II)_H(II)	1.61	
	P(VI)_OH(II)	1.76	
	P(VI)_OH(II)_H(II)	1.58	

Table 6 *Bond lengths computed from Shannon [66]. Coordination numbers given within parenthesis.*

The bond lengths for P_O4 are highly interesting because they are considerably larger than the rest of the phosphorus – oxygen bonds, see Figure 43 where phosphorus – oxygen bond lengths are drawn. Poojary's paper has the bond lengths for phosphorus–oxygen at about 1.52 Å, and the P_O4 bond in particular at 1.518(6) and 1.535(6) Å for the two samples given [8]. In comparison the samples here – both untreated and hydrothermally treated have that same bond around 1.57 Å (see Figure 43), which suggests there is something making that bond longer. In the literature a 1.57 Å bond length matches that of a P_OH bond for a phosphorus atom in tetrahedral geometry [67].

Also noteworthy is that the Si3_O4 bond is smaller than the Si3_O1 bond as seen from Figure 44, where silicon – oxygen bond lengths are pictured. This means that the bridging oxygen (O4) between the tetrahedral silicon and phosphorus sites, is shifted more toward the tetrahedral silicon atom than normal. It may well be that a hydrogen

is linked to the O4, which is pushing the O4 further away from the phosphorus and closer to the Si3 atom.

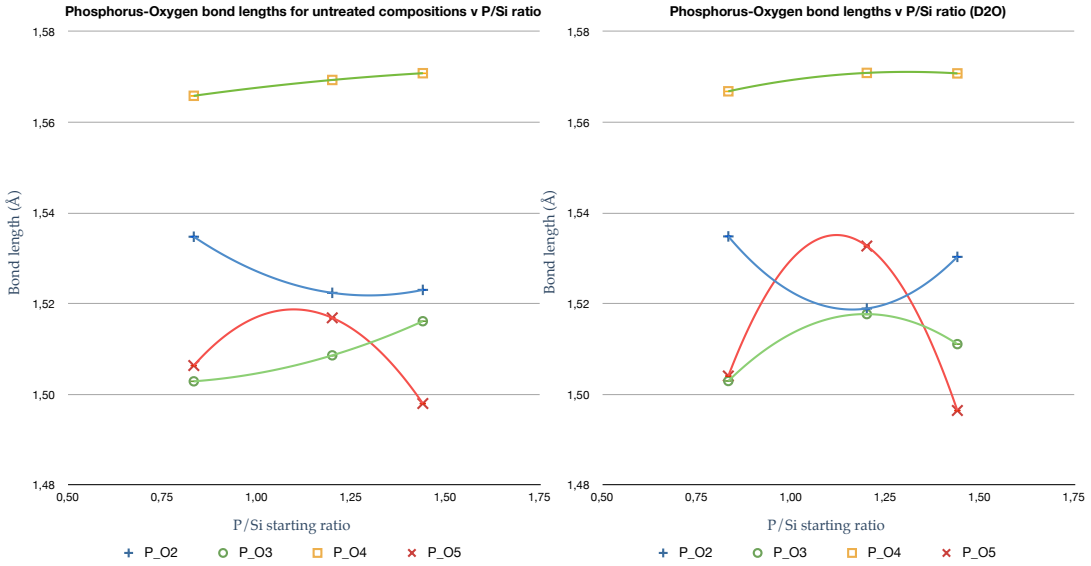

Figure 43 *The bond lengths for the P_O bonds for the untreated (left) and hydrothermally treated compositions (right). Note the longer bond length for the P_O4 bonds compared to the remaining P_O bonds.*

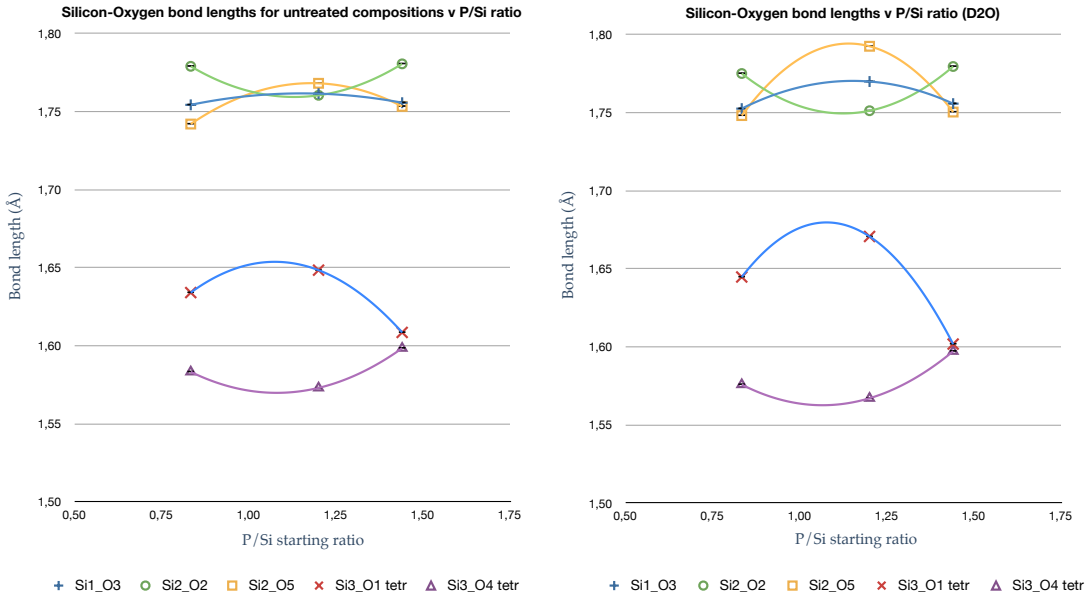

Figure 44 *The bond lengths for the silicon-oxygen bonds for the untreated (left) and hydrothermally treated compositions (right). Note that for the tetrahedral Si3 the Si3_O4 bonds are shorter than the Si3_O1 bonds.*

Bond lengths for the untreated parent composition, as well as for the hydrothermally treated parent composition, are also given as a function of temperature in Appendix E1 and Appendix E2. As can be seen from those bond lengths they do not vary in the same manner between the untreated and hydrothermally treated parent composition throughout temperature, meaning that systematic error in the P/Si 1.2 case is not a significant factor to explain the variation in bond lengths over the P/Si ratio shown in the previously mentioned figures.

4.5.2 Atomic coordinates at room temperature for varied P/Si ratios

Figure 45 depicts the atomic coordinates for the six different samples at room temperature as a function of P/Si starting ratio. The changes in atomic positions resulting from the hydrothermal treatment with D_2O, affects the positions for the parent $Si_5O(PO_4)_6$ the most.

For the phosphorus atom there is almost no change whatsoever in all XYZ coordinates for the 0.833 and 1.44 compositions (top part of Figure 45). For the parent composition there is most change in the phosphorus X coordinate, which becomes smaller upon hydrothermal treatment.

The only visible change in atomic coordinates for the 0.833 and 1.44 compositions is for the Si3 tetrahedra, where the Z coordinate is lower after hydrothermal treatment for the 0.833 composition, also for the parent $Si_5O(PO_4)_6$ and a bit higher for the 1.44 composition. Just comparing this coordinate it is clear there are some differences between the six samples.

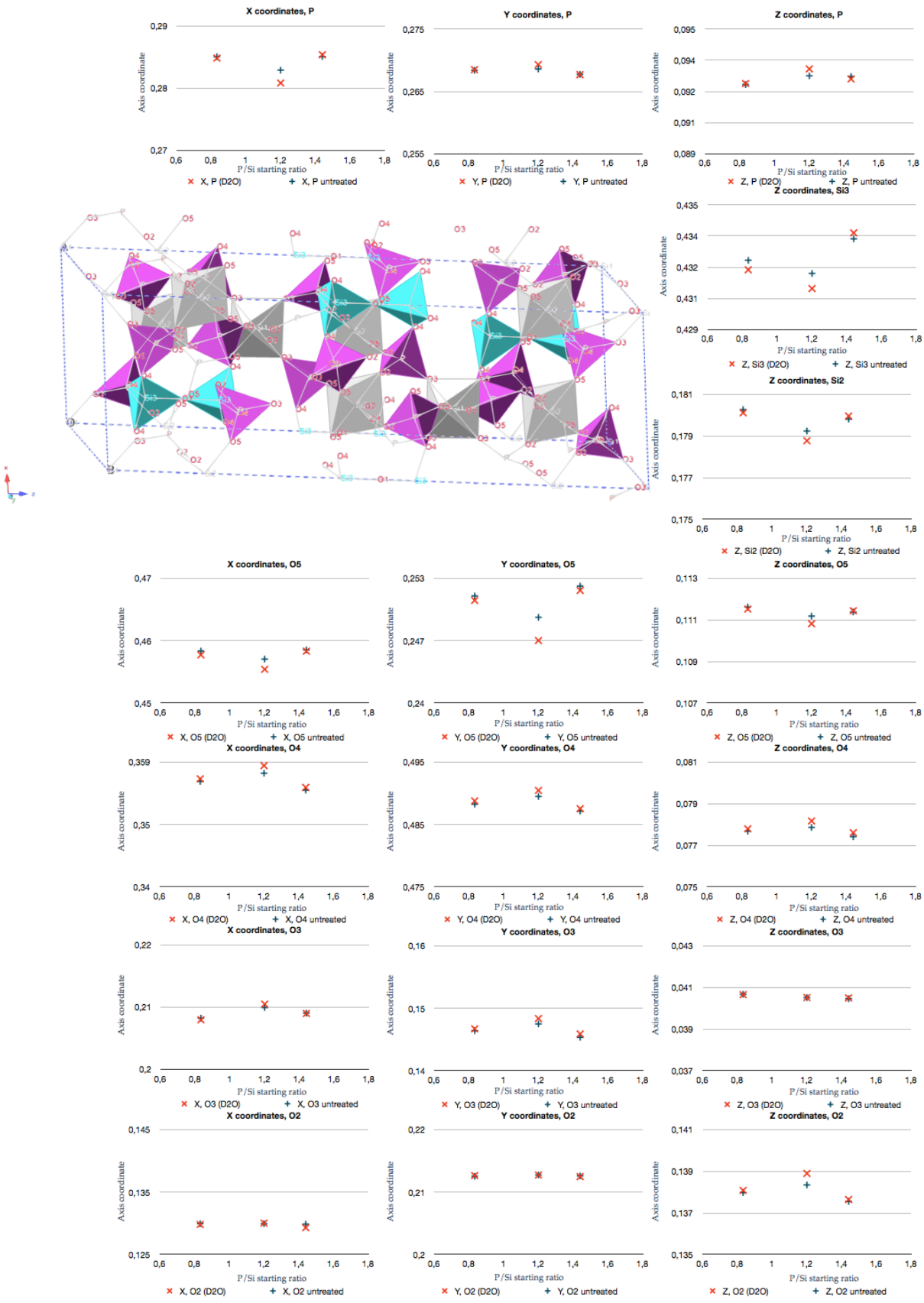

Figure 45 *Diagrams of coordinates for the atomic positions of the atoms plotted against the P/Si starting ratio for each composition, untreated samples (blue data, +) and hydrothermally treated samples (red data, x). There is a difference between different P/Si starting ratios, as well as an effect caused by the hydrothermal treatment with D_2O. X,Y coordinates for Si3, Si2 and X,Y,Z for Si1 and O1 have been omitted due to that they are special positions, i.e. they do not change during the refinement.*

4.5.3 TG and DTA for hydrothermally treated (D_2O) neutron diffraction samples

The three hydrothermally treated compositions that went in to the neutron beam, P/Si = 0.833, 1.2 and 1.44, can be compared alongside one another. The data obtained from the TG setup is displayed in Figure 46 and the same data as a function of time in Figure 47.

From Figure 46 it can be noted that these hydrothermally treated compositions show a similar mass loss up to about 70°C, upon which they begin to diverge: the 0.833 has the lowest mass loss, followed by the parent composition, followed by a larger mass loss for the phosphorus-rich (1.44) composition. An interesting distinction can be made for the 1.44 composition compared to the other two. Not only is its mass loss quite significant in the 70-100°C region, but there is also a noticeable increase in rate of mass loss at 550°C which is not seen for the other compositions. This is of interest as it reveals that there was still some water above 500°C. In conjunction with this is also a DTA peak at 560°C as can be seen when tracing the red line in Figure 48.

In the case of the hydrothermally treated solids, it thus appears that a high mass loss is a good indication of good protonic conductivity. The TG data strongly suggests that the displayed mass losses are revealing of the total water content available. Thus, if a significant mass loss occurs it is due to that water was present to a significant degree, and if it is lost to a smaller degree it is because water was only present to a small degree. Therefore, the samples with small water content will have lower protonic conductivity. All three samples show the same rate of mass loss when 1000°C has been reached and during subsequent cooling, see Figure 47.

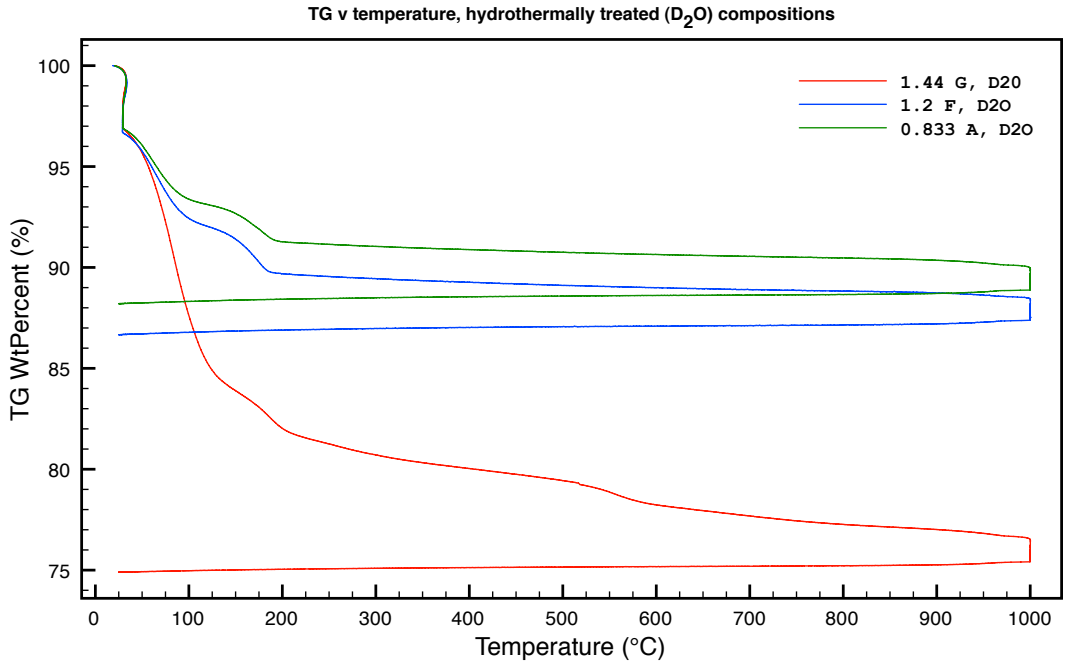

Figure 46 *TGA of the hydrothermally treated compositions plotted as a function of temperature. Note the increased rate in mass loss seen for the hydrothermally treated 1.44 sample at 550°C.*

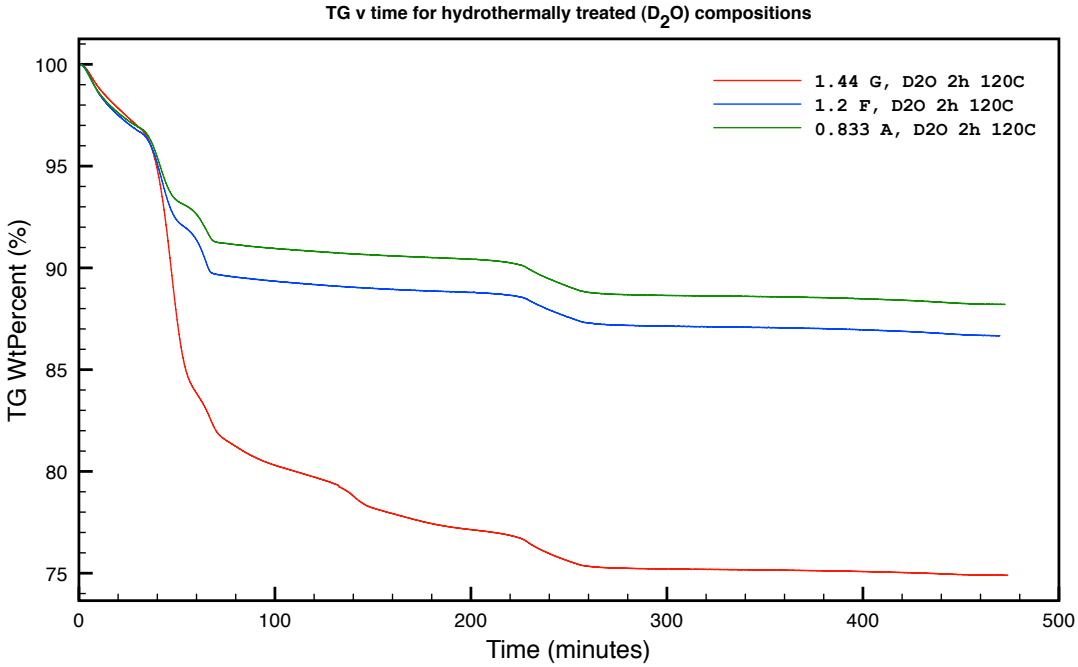

Figure 47 *TGA of the hydrothermally treated compositions plotted as a function of time.*

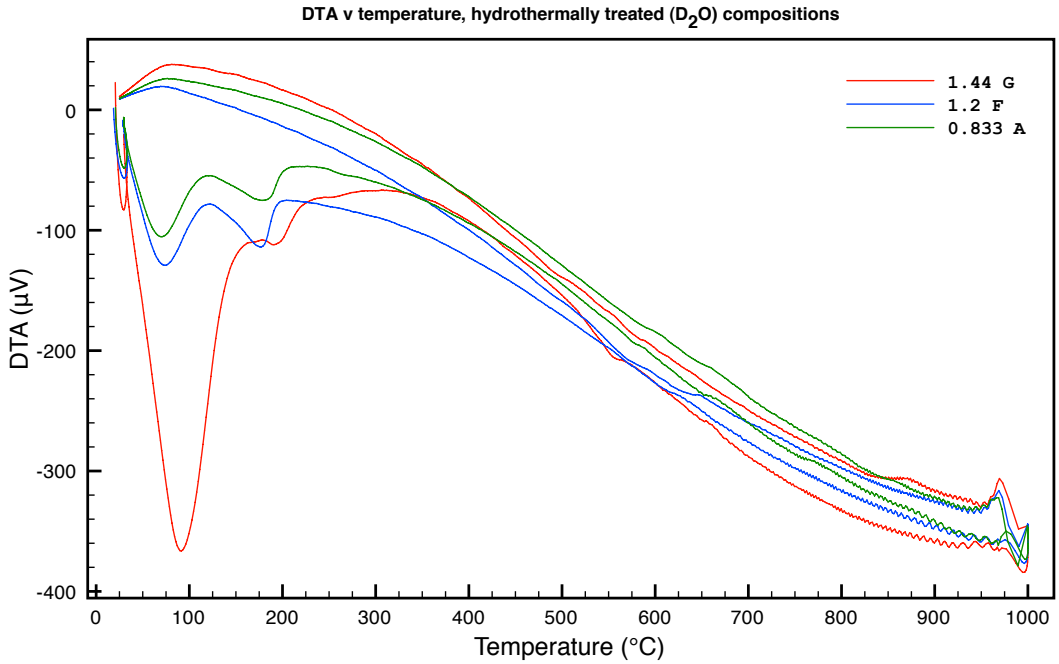

Figure 48 *DTA of the hydrothermally treated compositions as a function of temperature. In addition to the low temperature peaks, there is a small response for the hydrothermally treated 1.44 sample at 550°C.*

4.6 Neutron diffraction: high-temperature study

Two near identical[7] high temperature programs were run of the stoichiometric parent composition, $Si_5O(PO_4)_6$ – one for the untreated and one for the hydrothermally treated sample. The heating programs are pictured in Figure 49 below.

The hydrothermally treated sample was treated with D_2O and came from the same batch as the untreated sample. Therefore, any change in occupancies or cell parameters etc would be entirely due to the hydrothermal treatment.

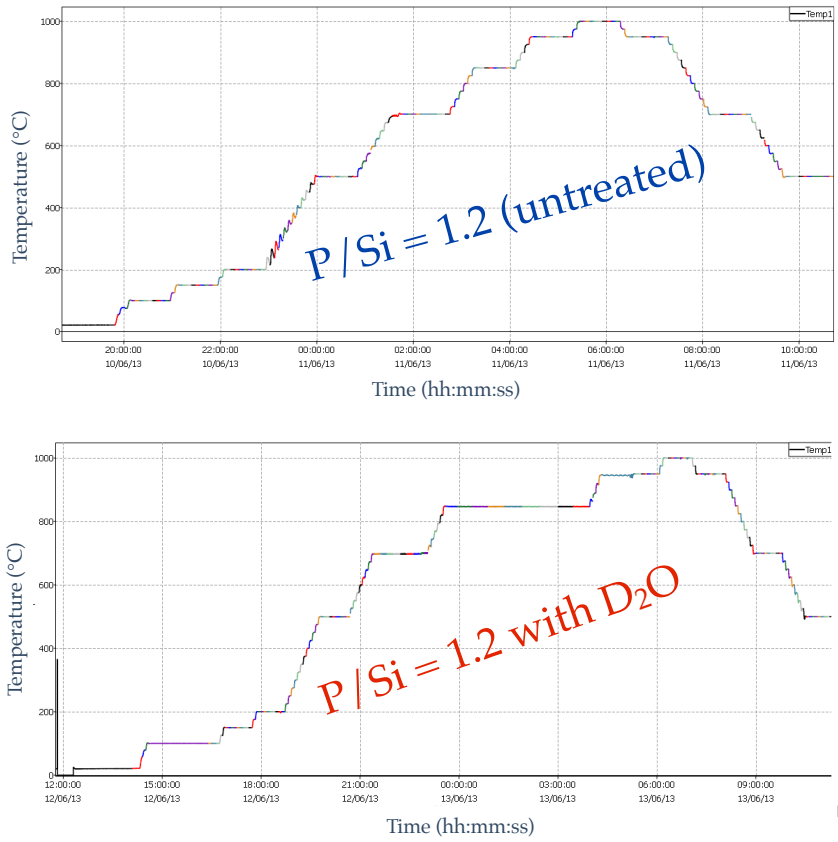

Figure 49 *Temperature profiles for the two high temperature neutron diffraction experiments. The first run was the untreated parent composition (1.2F), and the second run was the hydrothermally treated parent composition (1.2F D_2O).*

Previously, the initial room temperature runs of these two compositions were described in the earlier part of this chapter.

The refinements for the high temperature experiments were done in the same manner as those for the room temperature experiments, these are all referred to as manual refinements. These were all based on SUM-files, which are packets of data files at the same temperature that have been lumped together. This gives higher reliability due to

[7] The two runs were almost identical. Due to an adjustment to the ramp made in the second run (to make it smoother) and an error that occurred at above 900°C for the second run (which was quickly corrected), the two runs would deviate a bit from one another. These deviations are however small and therefore the two runs can be treated as virtually identical.

the longer collection time.

The collected neutron diffraction data for the entire temperature program is pictured for the two samples in Figure 50 – to the left of this figure is the hydrothermally treated (with D_2O) parent composition and to the right is the untreated parent composition. What can be noted in the left part of the figure are the turqoise regions at the early parts of the experiment; these regions are missing for the untreated parent composition. They translate into higher background, indicating amorphous phase presence. The interpretation that can be made is that this amorphous phase presence is due to liquid D_2O, tentatively occupying the channels in the structure that run along the a and b axes.

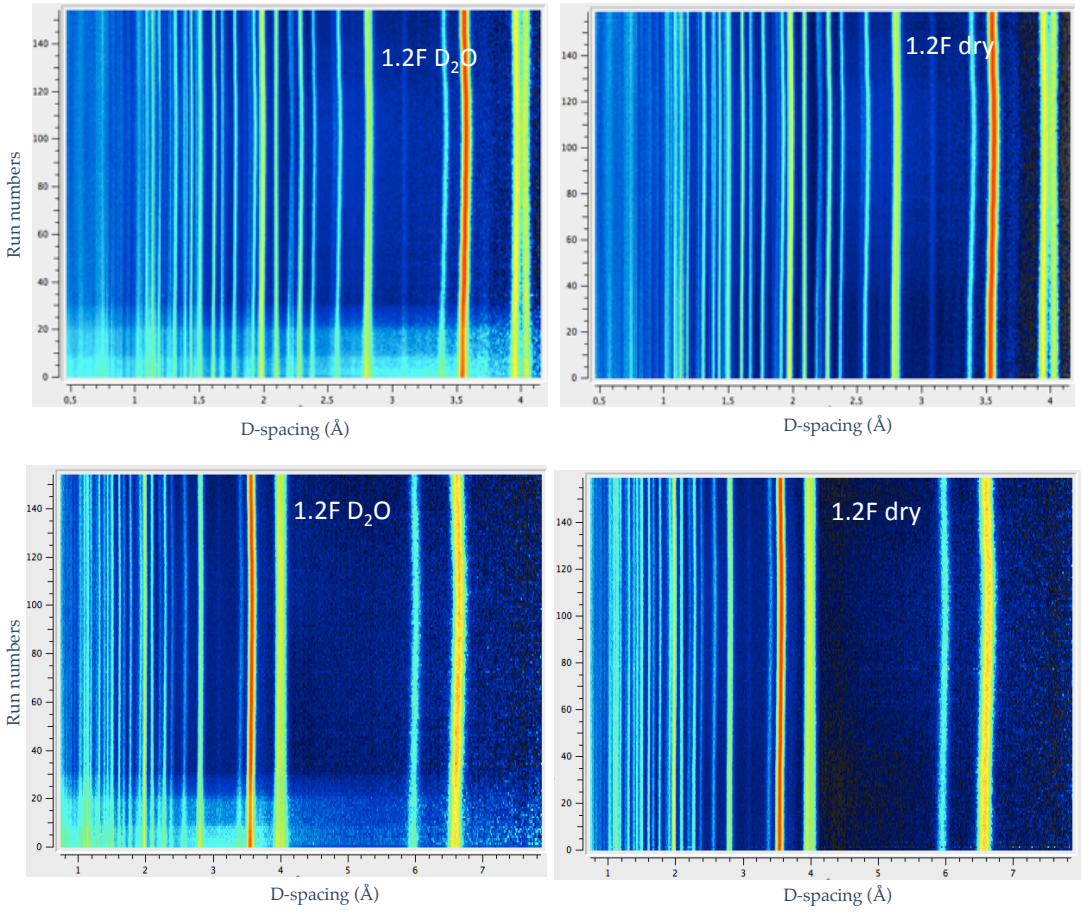

Figure 50 *Thermoplots of the two high temperature runs. Observe the extra amount of amorphous contribution (a partially higher background in the left part of the figure at lower run numbers) for the sample that had been hydrothermally treated with D_2O. The backgrounds look similar after a few hundred degrees. Run number 10 = 150°C, 20 = 183°C and 30 = 223°C for the high temperature run of the hydrothermally treated composition.*

4.6.1 Sequential GSAS refinements

The basic methodology for performing the sequential GSAS refinements was to keep the number of variables as low value as possible. On the other hand, care had to be taken to not fix too much either, since only a small amount of information can then be extracted.

It was decided to take the UISO values from each respective run at 500°C (on heating), and use these as the fixed UISO values for all temperatures from room temperature to 1000°C. This would be a crude approximation and its validity must be verified against the results of the manual refinements; this should be borne in mind when evaluating the results that if two conflicting results then it is more likely the result of the manual refinement is correct. Not only is the data from a SUM file more accurate and less noisy, the manual refinements do all start from the same starting values whereas a sequential refinement starts with values from the previous refinement in the sequence.

The benefit of doing the sequential refinements was that an approximation of how the cell parameters changed could be made throughout the measured temperature range. Also the occupancies were all allowed to vary, save for Si2, O1 and O5 which were set to 1. Only about three peak parameters were allowed to vary – these had been chosen due to that they all were varied in the manual refinements, and those parameters were excluded that for any reason could not be varied in any of the manual refinements.

The positions of the atoms were all allowed to vary also (unless of course they were on a special position, e.g. 0.0.0). The refine cell option was ticked for both sequential runs as well as zero, DIFA and background (with 20 terms).

The principle for a sequential GSAS run is that a refinement must be done for the first file (room temperature, in this case). In this first refinement, which is done manually, the print option must be enabled “Output parameter name, value, and esd to file (1024)”. This will write the parameters to the .EXP file. The sequential program in GSAS, SEQGSAS, will take the information generated from the previous refinement and put it as input for the next refinement. This process is repeated until there are no more GSAS data files (.gss files). The precise instructions for how to set up sequential

refinements are available online [68].

The results revealed fairly similar cell parameters when comparing manual refinements to the sequential refinements. The differences were in the occupancies at certain temperature, and here one would have to rely on the manual refinements, because the sequential refinements had fixed UISO values – and this will impact the occupancies as the two are linked. UISO values will change with the temperature, and therefore to obtain the occupancies with the highest accuracy, one would have to fix UISO values for each temperature step and run the sequential runs between these steps.

The general trends in cell parameter results are quite reliable from the sequential refinements, even if the individual errors are larger than for the manual refinements. Also, the two sequential runs can be directly compared as they were done very much similarly.

Two sets of sequential refinements were done for each run – one where all the occupancies of the oxygens and Si2 were set to 1 and not allowed to vary, (V4A). Another set of refinements was done where the occupancies for the O2, O3 and O4 were allowed to vary, whereas the occupancies for all silicons and the phosphorus were fixed to 1, (V4B). This was done in order to minimize any effects that varying all the occupancies at once would have.

In both above cases the UISO values were fixed, and all the profile options were un-ticked. The cell parameter results were taken from the runs where all the oxygens were held at full occupancy. As can be seen from Figure 51 where the c-axis is compared for the hydrothermally treated composition for the same run but using two different sequential refinement runs the results look very similar.

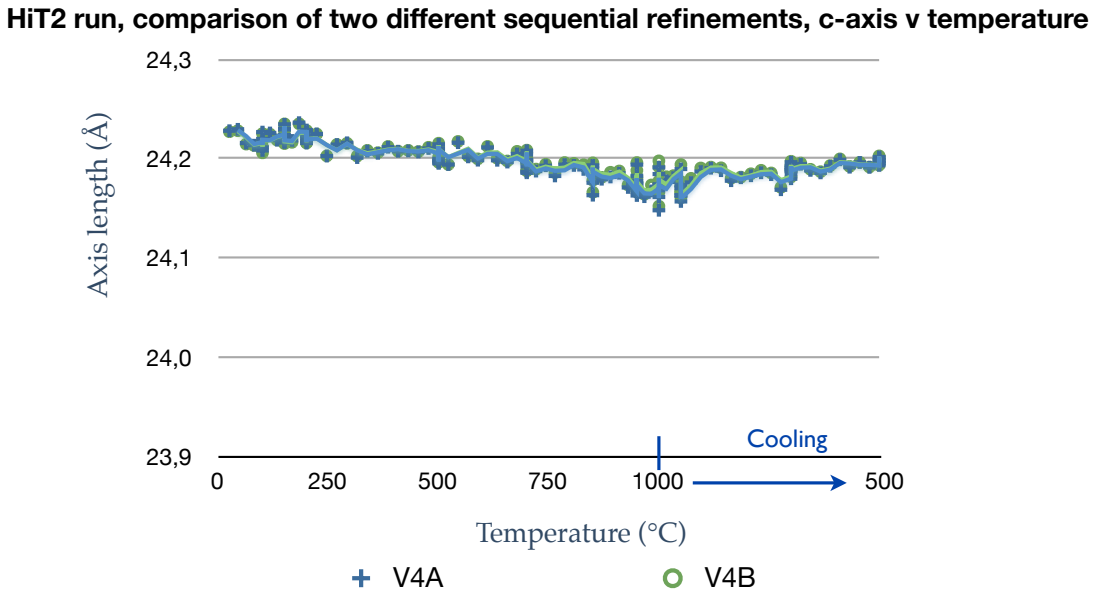

Figure 51 *The c-axis for the hydrothermally treated composition, results from two different sequential refinements as described in the text.*

In order to see what the effect might be on the phosphorus and silicon occupancies results from the firstly described sequential refinement (V4A) presented in the following sub-chapter.

4.6.2 Similarities between manual and sequential refinements

For the manual refinements it can be pointed out that there was a bit more occupancy on the phosphorus site for the hydrothermally treated parent composition, compared to the same composition not being treated at room temperature, as can be seen from the difference plot in Figure 52. This was the case at room temperature, then the occupancy for the P-site becomes similar at around 100°C, 500°C and 1000°C. The biggest differences were at 850°C and 950°C going up and down in temperature, as well as at 500°C on cooling.

Further from Figure 52 the tetrahedral silicon occupancy also shows some difference from the start between the hydrothermally treated and untreated composition. Between 100-150°C the occupancies for this site are the same, also at 500°C, around 750°C and close to 1000°C is this the case. The biggest differences are at room temperature, and 850-950°C heating and 850°C cooling. These variations between the samples are smaller than for the phosphorus site, as can be seen from Figure 52.

When comparing the cell parameters done with the sequential refinement (see Figure 53) to the result of the manual refinements in Figure 54 it is clear that they are very similar, and when comparing the ratio of the c/a axes these values correspond very precisely due to it being a ratio of two values with what is likely similar amounts of relative errors.

The largest discrepancy is at 950°C on cooling for the untreated composition – here the cell parameters are significantly smaller for the manual refinements compared to the sequential refinement, as seen when comparing Figure 54 to Figure 53 at 950°C cooling.

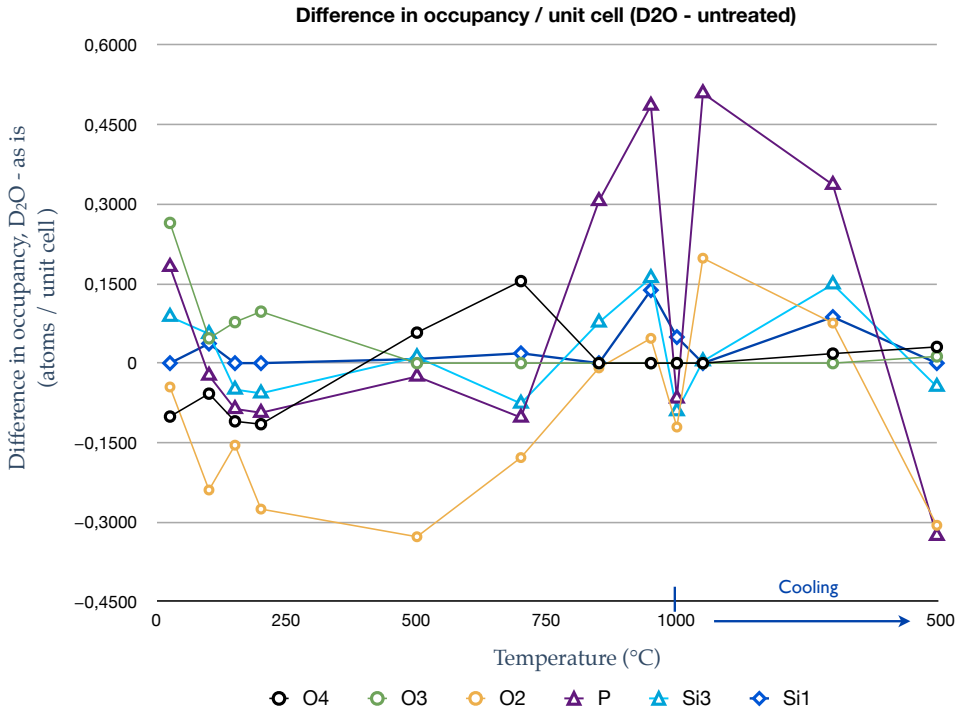

Figure 52 *The difference in occupancies for the two runs for each atomic site from the manual refinements: Occupancies for the untreated parent composition subtracted from the same hydrothermally treated composition. Notable is the difference in phosphorus occupancy from 850-950°C. There is not much difference in O2 occupancy at room temperature, however as temperature increases it becomes more pronounced and is significant at 500°C.*

O1, O5 and Si2 have been excluded from the graph since their occupancy was set to 1 in the refinements.

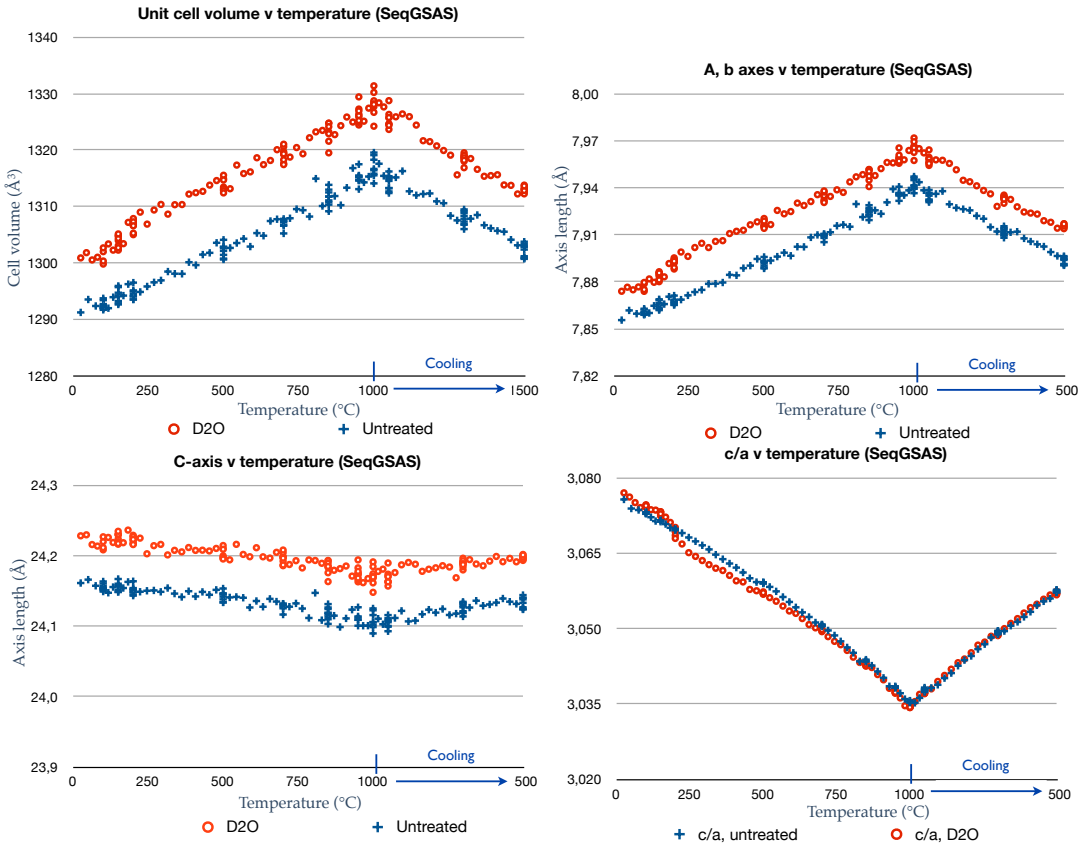

Figure 53 *Unit cell volume versus temperature (top left) for the untreated parent composition, and its hydrothermally treated (D_2O) counterpart. This unit cell volume corresponds well with the a, b axes lengths depicted in the top-right corner. Also depicted bottom left is the c-axis as a function of temperature, and to the right of this is the c/a values throughout the temperature range. Note how well these latter correspond to the manual refinements in the next figure. For these sequential refinements the occupancies for Si2 and all oxygens were held at 1, and UISO values set to those that each composition had at 500°C on heating (V4A).*

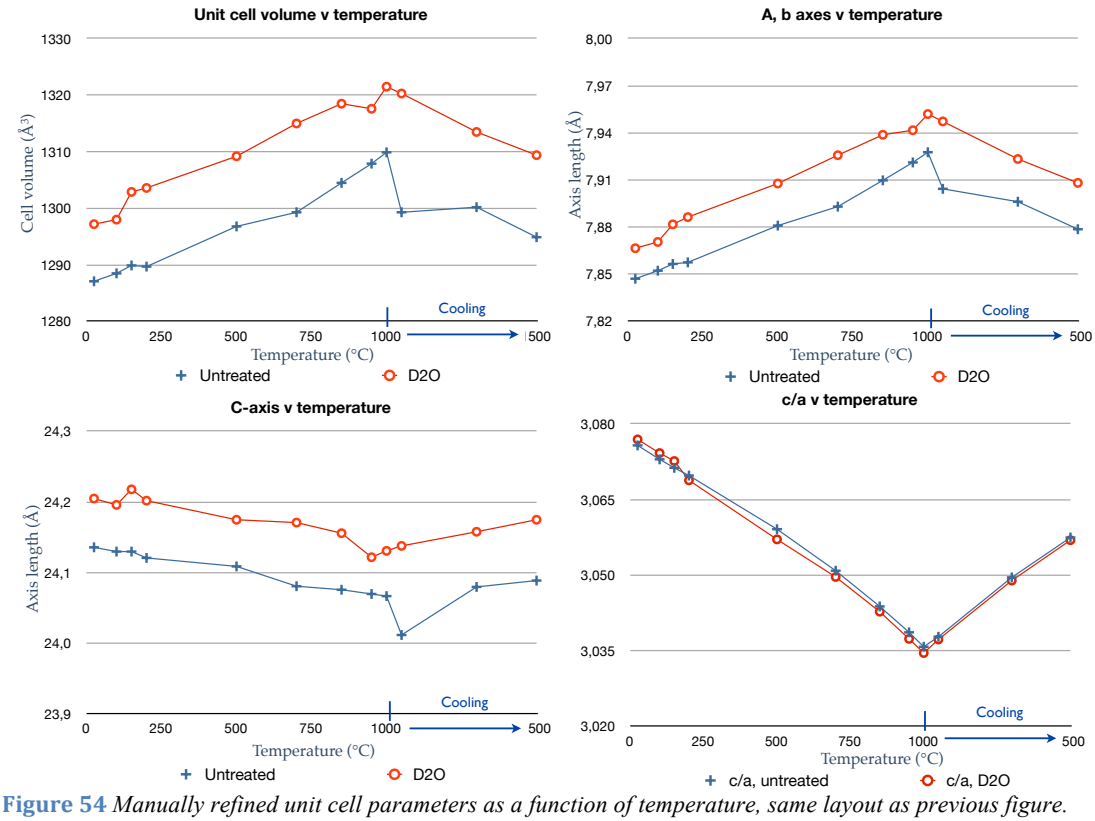

Figure 54 *Manually refined unit cell parameters as a function of temperature, same layout as previous figure. Note the discrepancy for the untreated composition at 950°C upon cooling.*

Figure 56 and Figure 57 describe the results from the occupancies obtained from the manual and sequential refinements, respectively. The trends in occupancy for the Si3 site in the low temperature region is described well by the sequential GSAS data, albeit a bit overestimated compared to the manual refinements – the result is nonetheless that the hydrothermally treated parent composition has higher occupancy on this site than that of the untreated counterpart. Judging from the manual refinement data, the Si3 occupancy for both runs appear to intersect at about 125°C and then diverge upon further heating.

Likewise it is for the occupancy of the phosphorus site in regards to the effect of hydrothermal treatment, i.e. the two refinements follow the same trend compared to the manual refinement data. The phosphorus occupancy is however a bit lower for the sequential runs compared to the manual refinements.

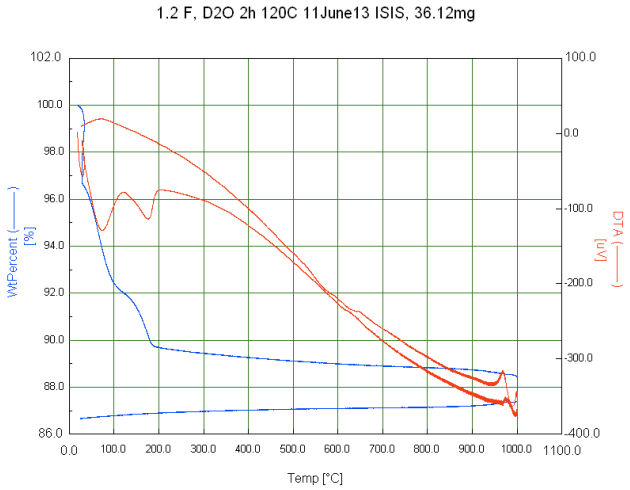

Figure 55 *DTA and TG plot of the hydrothermally treated (D_2O) parent composition that was subjected to neutron diffraction at high temperature.*

The low-temperature occupancy data in Figure 56 suggests that the first peak in the DTA is connected to a process of D_2O desorption at the phosphorus site, and that the second peak in the DTA involves D_2O desorption at the tetrahedral Si3 site. TG and DTA data for the hydrothermally treated parent composition is given in Figure 55. It is the same data there as was given earlier for this sample in Figure 46 and Figure 48, only this time it is combined. Noteworthy is that the same characteristics of the DTA and TG are there as for the hydrothermally treated parent composition where H_2O was used.

From the manual refinement data in Figure 56 one can conclude that at 100°C the occupancy for the phosphorus sites appears the same for the two samples, see lower-left part of Figure 56. Below this point there is good protonic conductivity for the hydrothermally treated (with H_2O) parent composition as seen from Figure 63, most likely as a result of phosphoric acid in the structure. Above 100°C the protonic

conductivity becomes gradually lower, likely as a result of water leaving the material.

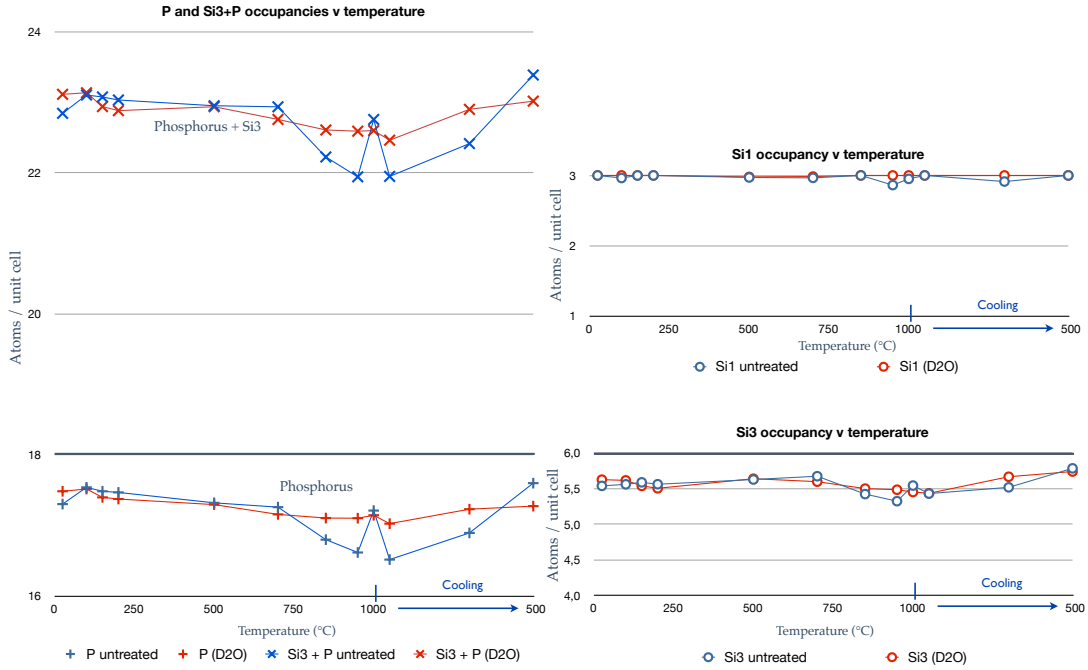

Figure 56 *Occupancy results for the manual Rietveld refinements plotted against temperature. The occupancy factor has been multiplied with the multiplicity to yield the above graphs. Note the differences in the low as well as high temperature regions. Si2 was held constant at 1 as well as O5 and O1.*

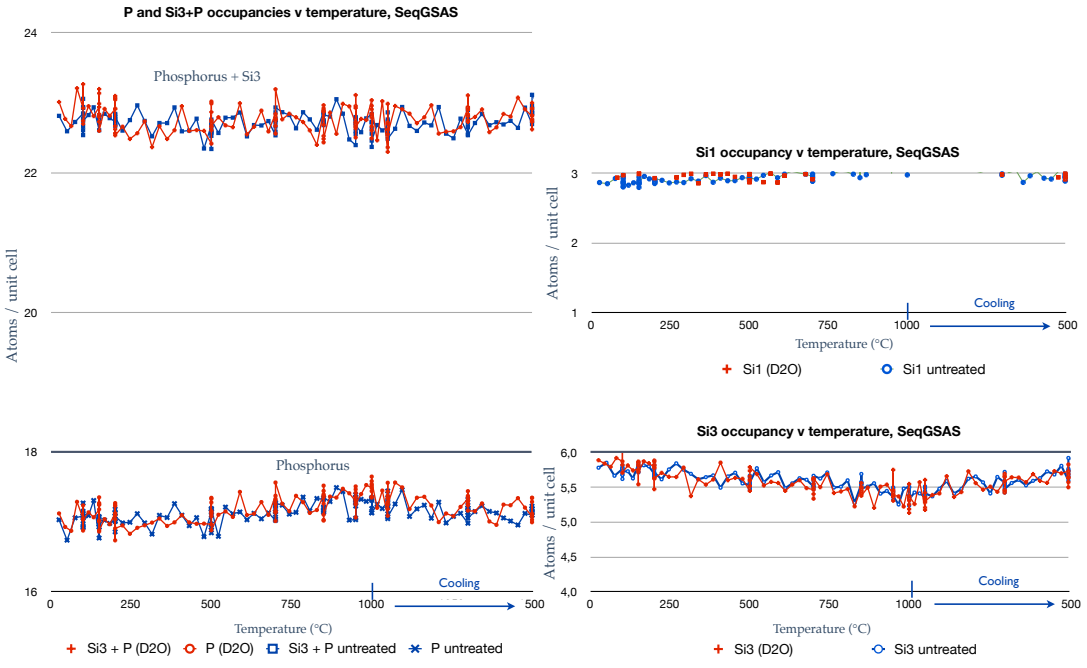

Figure 57 *Occupancy results from the sequential GSAS runs for the same two high temperature runs as were in the previous figure. The occupancy factor has been multiplied with the multiplicity to yield the above graphs. Note the similar trends for the Si3 and Si1 compared to the manual refinements. The phosphorus occupancies show a different trend compared to what was found in the manual refinements, see previous figure.*

This sequentially refined data was generated by fixing the occupancies for Si2 and all oxygens to 1. Missing data points for Si1 occupancies exceed the maximum allowed value for that site, and should be equal to 100% (i.e. 3).

From the top-left diagram in Figure 59 the following occurs with the X coordinate of the phosphorus atom in the low–intermediate temperature region: for the untreated composition a steady decrease is seen from 100°C, whereas for the hydrothermally treated composition only a temporary decrease occurs at about 150°C. There are very small differences between the two samples from 500°C all the way up to 1000°C.

The sequential GSAS refinement for this coordinate (see diagram below previous in Figure 59) records the same trends in the low–intermediate temperature region, however shows a bit more difference at the higher temperatures that remains throughout. The overall trends are the same for the two diagrams.

In the top-middle diagram of Figure 59, the phosphorus Y coordinate is somewhat larger at 100°C for the hydrothermally treated composition, however both compositions appear to otherwise be the same throughout the rest of the temperature range. In the diagram below, the sequential refinements have yielded much the same result and overall trend as the manual refinements.

The phosphorus Z coordinate is slightly smaller in the low-intermediate temperature region for the untreated composition, and then becomes the same for the two samples, see top right diagram in Figure 59. The diagram below this shows a very similar trend for the sequential refinements.

From Figure 59 the Z coordinate for the Si3 atom is also shown (lower left part). Although otherwise similar trends for the untreated and hydrothermally treated compositions, a distinction can be made in the low temperature region where the Si3 for the hydrothermally treated composition is closer to the Si1.

The position for the octahedrally coordinating Si2 compares differently for each temperature, see lower right part of Figure 59. The general trend is an increase in the Si2 Z coordinate as temperature increases. This is contrary to the overall contraction in c-axis as a function of increased temperature, shown earlier in Figure 54. This means that there is significant and continuous movement of the Si2 octahedra toward the Si1 octahedra as temperature increases and the c-axis contracts.

Figure 58 depicts the structure of three stacked unit cells for the parent composition viewed down the b-axis, noteworthy here is the channel structure.

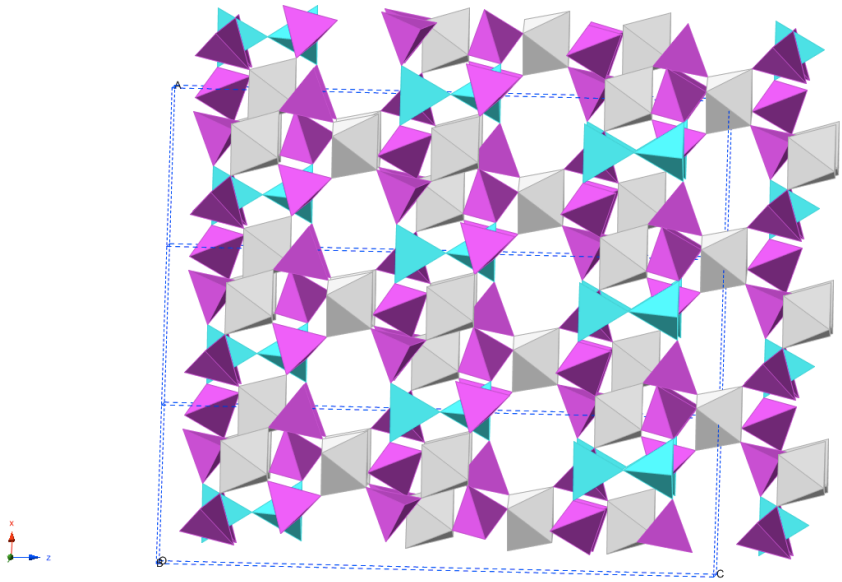

Figure 58 *View down the b-axis of just over three stacked unit cells of the parent composition. The turquoise colour represents the Si-tetrahedra, purple colour is for phosphorus tetrahedra and the grey octahedra are the silicon octahedras. Note the channel structure that becomes apparent.*

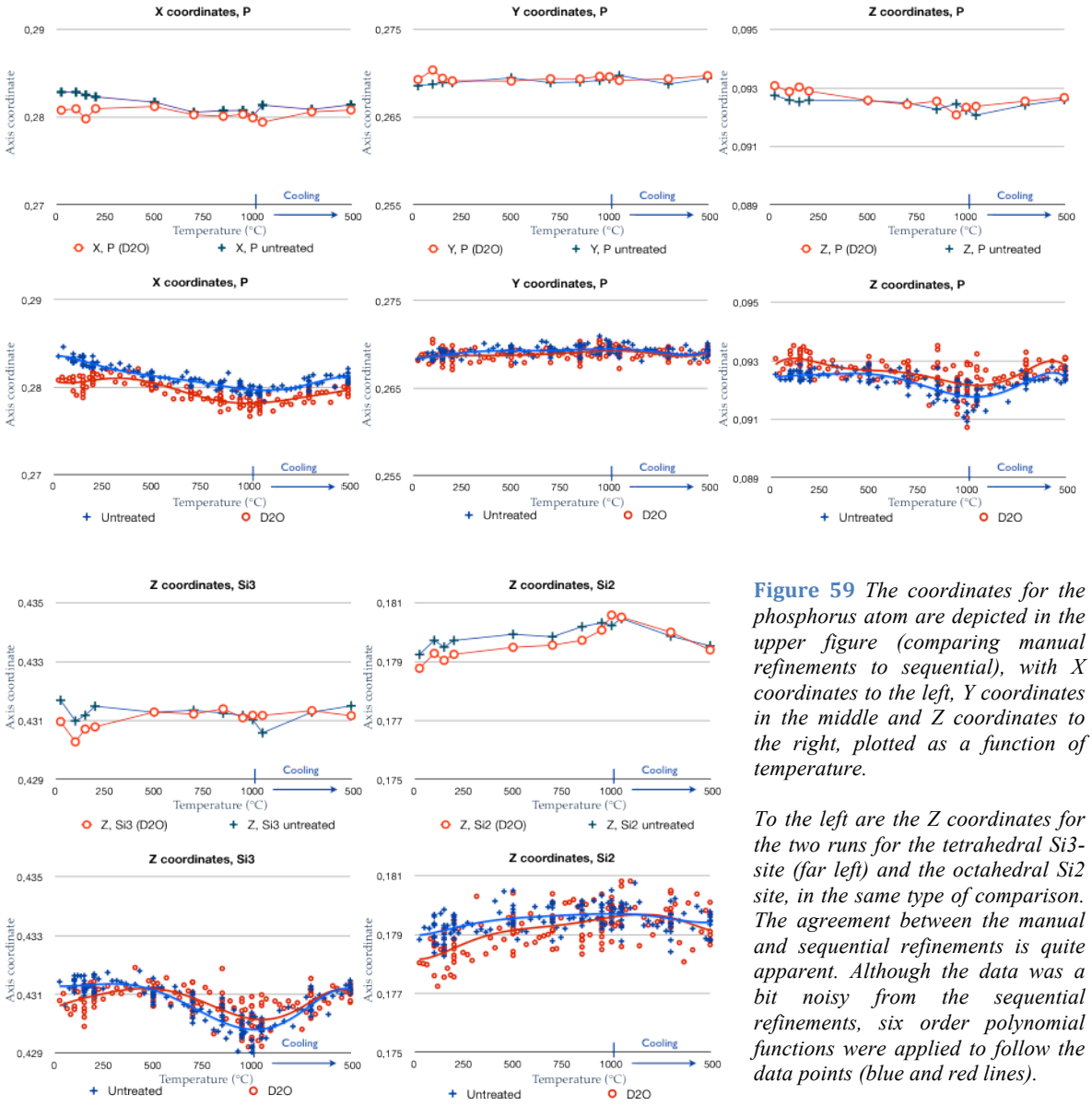

Figure 59 *The coordinates for the phosphorus atom are depicted in the upper figure (comparing manual refinements to sequential), with X coordinates to the left, Y coordinates in the middle and Z coordinates to the right, plotted as a function of temperature.*

To the left are the Z coordinates for the two runs for the tetrahedral Si3-site (far left) and the octahedral Si2 site, in the same type of comparison. The agreement between the manual and sequential refinements is quite apparent. Although the data was a bit noisy from the sequential refinements, six order polynomial functions were applied to follow the data points (blue and red lines).

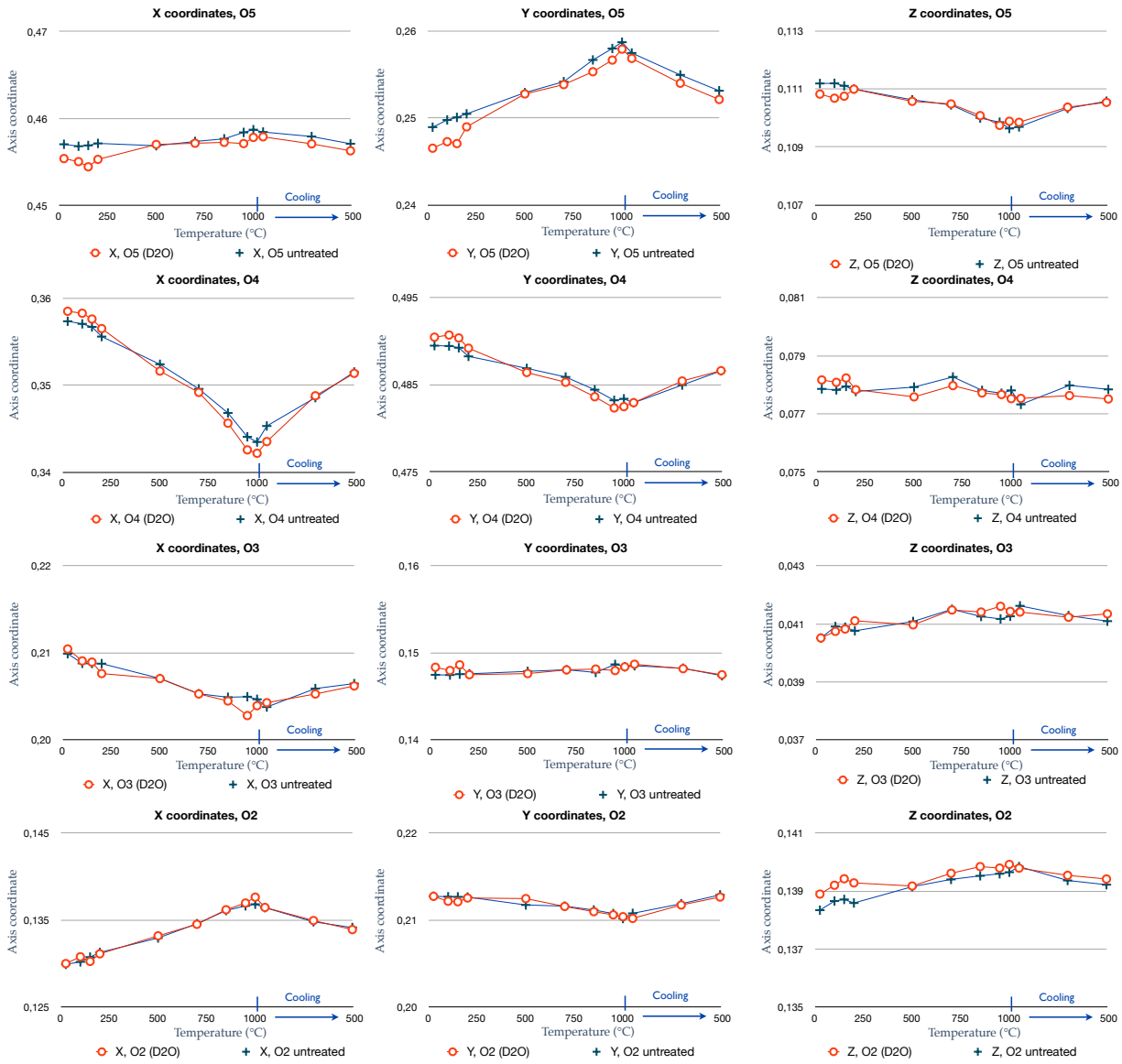

Figure 60 *The resulting coordinates for O5-O2 (from top to bottom) from the manual refinements of the neutron diffraction results, presented as a function of temperature. X coordinates to the left, Y coordinates in the middle and Z coordinates to the right; untreated sample (blue data, +) and hydrothermally treated sample (red data, o).*

The oxygen connecting the two Si3 tetrahedra is the O1, and since it is in a special position it is fixed. Coordinates for the other oxygens as a function of temperature are presented in Figure 60. The only other oxygen connected to the tetrahedral Si3 is the O4, and there are some differences as a cause of hydrothermal treatment. O2, O3, O4 and O5 are all connected to the tetrahedral phosphorus atom, and all of these show differences in the lower temperatures.

These coordinates[8] give rise to bond lengths which are plotted in Appendix E1 and

[8] The referred bond lengths are from the first refinement in which no occupancies were varied (the previously discussed positions are from the secondary refinement in which some occupancies were

given in table form in Appendix E2. Interesting to note from the graphs in Appendix E1 is that there is a correlation between the average P_O bond with that of the c-axis as temperature changes (cf. Figure 54). Why this is the case is not quite clear, however it could be because of some sort of element substitution.

4.7 Correlations between physical and chemical properties

Low temperature conductivity of the hydrothermally treated compositions is linked to the unit cell parameters of the untreated compositions, in particular the a,b axes, see Figure 61. This means that the measured conductivity occurs in the crystalline phase and is related to the expansion of the a,b axes. Most likely the protonic conduction is along these pathways (i.e. the three dimensional tunnels).

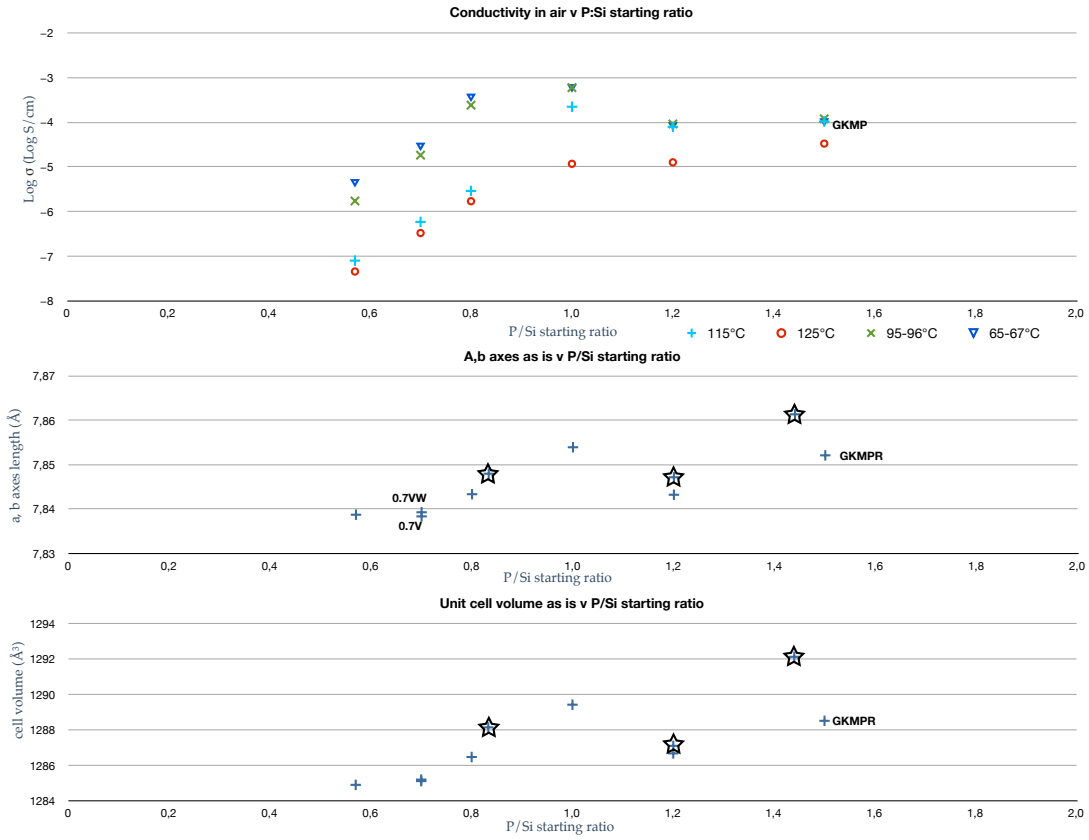

Figure 61 *Conductivities in air for hydrothermally treated compositions versus their respective P-Si starting ratio (top) compared to the a,b axes for the same samples before they are hydrothermally treated (middle), also compared to the unit cell volume for the same versus P-Si starting ratio (bottom). Note the very similar trends. Data points that are stars were from neutron diffraction data, corresponding conductivity data missing. The sample with P/Si starting ratio 1.5 was refined after an extra firing (thus giving a close approximation to the cell parameters of the actual measured sample).*

varied, however these two refinements still have very similar bond lengths due to that the position parameters (XYZ) were disabled throughout the secondary refinements).

Untreated compositions with the same P/Si starting ratios as those tested in TG/DTA were scanned for the chemical shift of the - 44 ppm in ^{31}P NMR. When plotting the exact chemical shift against P/Si starting ratio, a pattern occurs that is a reflection of the temperatures at which the DTA peaks occur for the hydrothermally treated compositions – this pattern is also much the same as for the low temperature conductivity, see Figure 62. This means the crystalline $Si_5O(PO_4)_6$ units are responsible for the protonic conductivity.

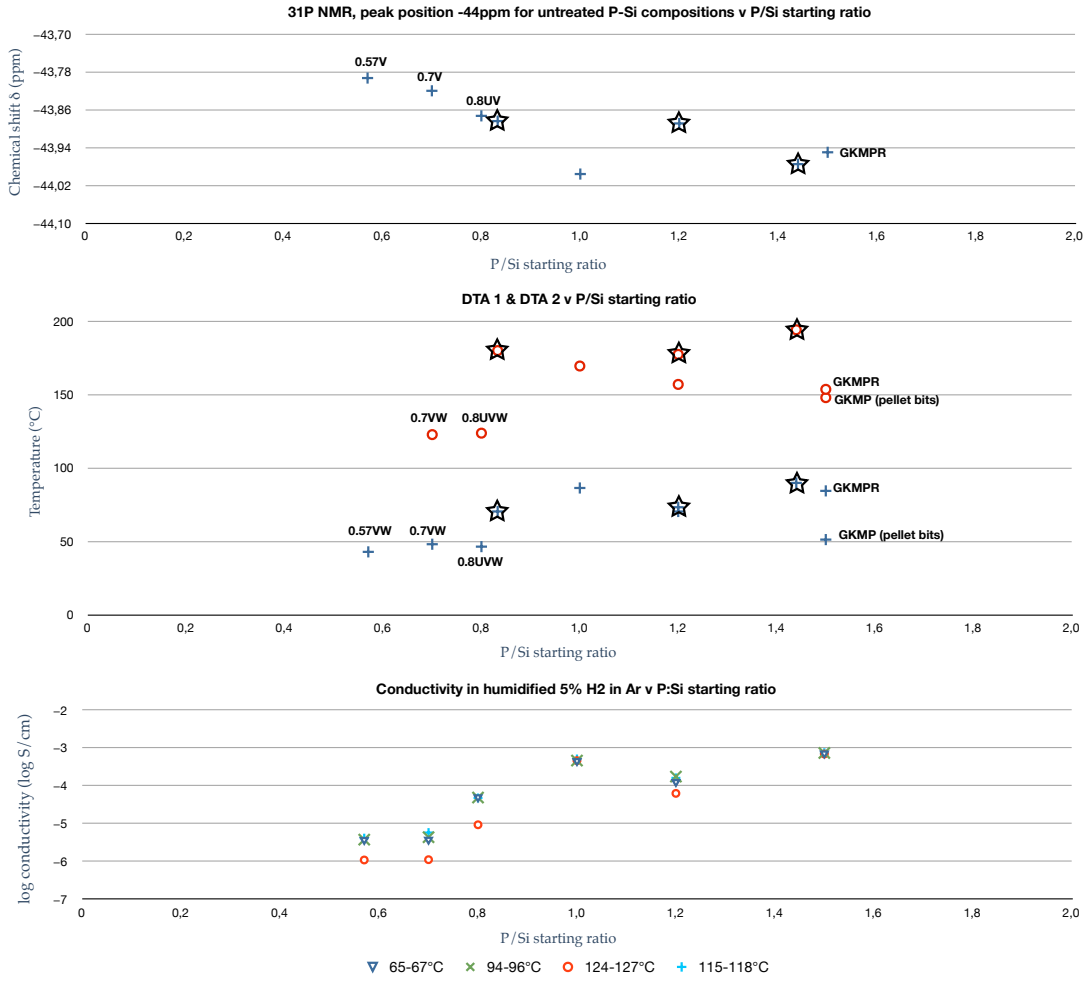

Figure 62 *Correlation between the chemical shift for the - 44 ppm peak in ^{31}P NMR (top) in untreated compositions with that of the temperature at which the DTA peaks occur for hydrothermally treated compositions (middle) and low temperature conductivity for hydrothermally treated compositions measured in humidified 5% H_2 in Argon (bottom). This all points to that the conductivity is linked to the phosphate group and its differing ability to bind water as a function of composition.*

In Figure 63 and Figure 64 the linear conductivity for two hydrothermally treated compositions is plotted against temperature, also the DTA and TG data for the same samples. What is interesting to note is that the DTA and TG peaks correlates quite well to the conductivity. One has to bear in mind though that each point in the EIS

measurements has been allowed to reach equilibrium, which is not the case for the DTA/TGA. If the latter had been run at a much slower rate it would likely become more matched with the EIS results.

The anomaly seen at the beginning for each DTA and TG measurement is likely instrumental as the measurements start with an isotherm so that the system and equipment can reach equilibrium.

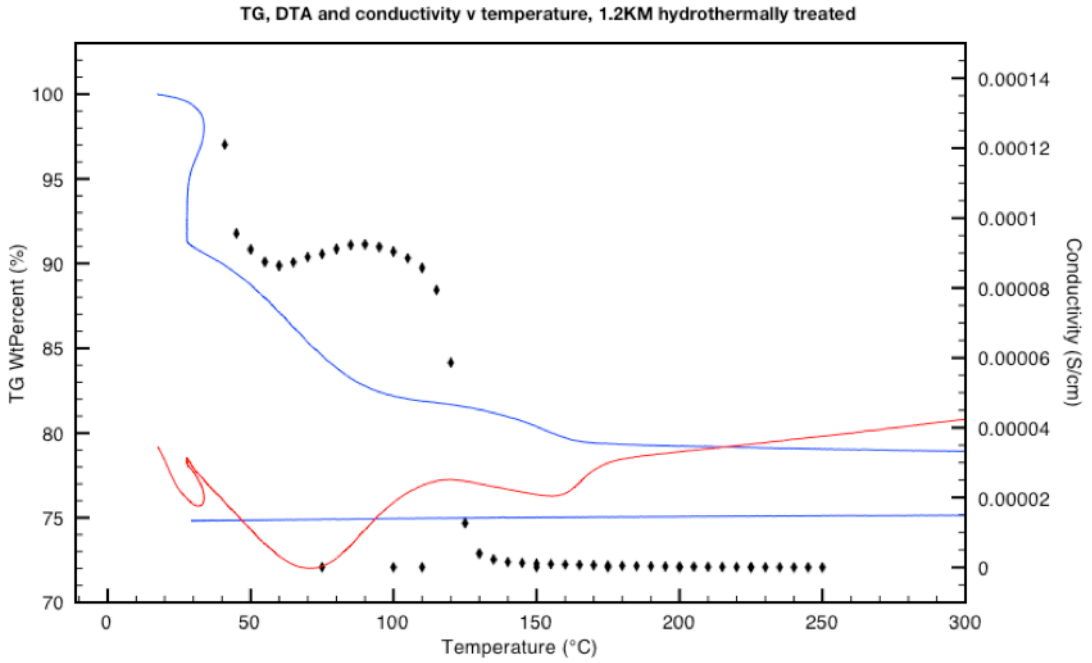

Figure 63 *TG (blue line) and DTA data (red line) and low temperature conductivity (black dots) plotted against temperature for hydrothermally treated parent composition. All measurements were done in air.*

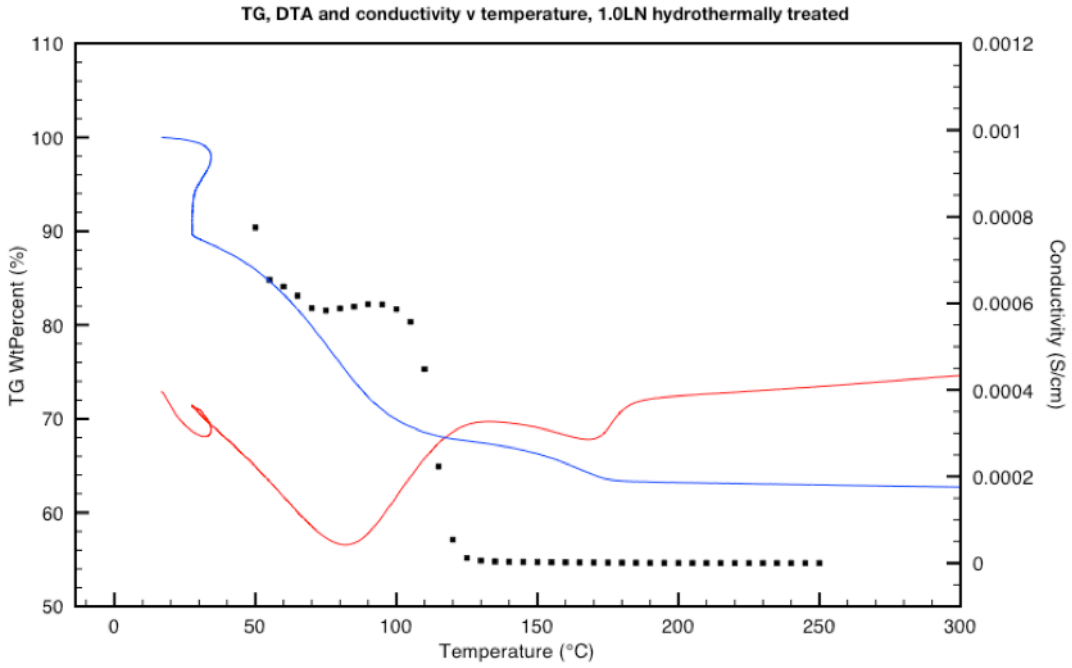

Figure 64 *TG (blue line) and DTA data (red line) and low temperature conductivity (black dots) plotted against temperature for hydrothermally treated P/Si 1.0 composition. All measurements were done in air.*

4.7.1 Electrochemical properties

Conductivities were calculated from impedance data obtained from hydrothermally treated samples in the low temperature range. These had typically been hydrothermally treated with H_2O at 120°C for two hours. At an early stage impedance was done on a few samples (primarily 1.5, 1.2 and 1.0 P/Si starting ratios).

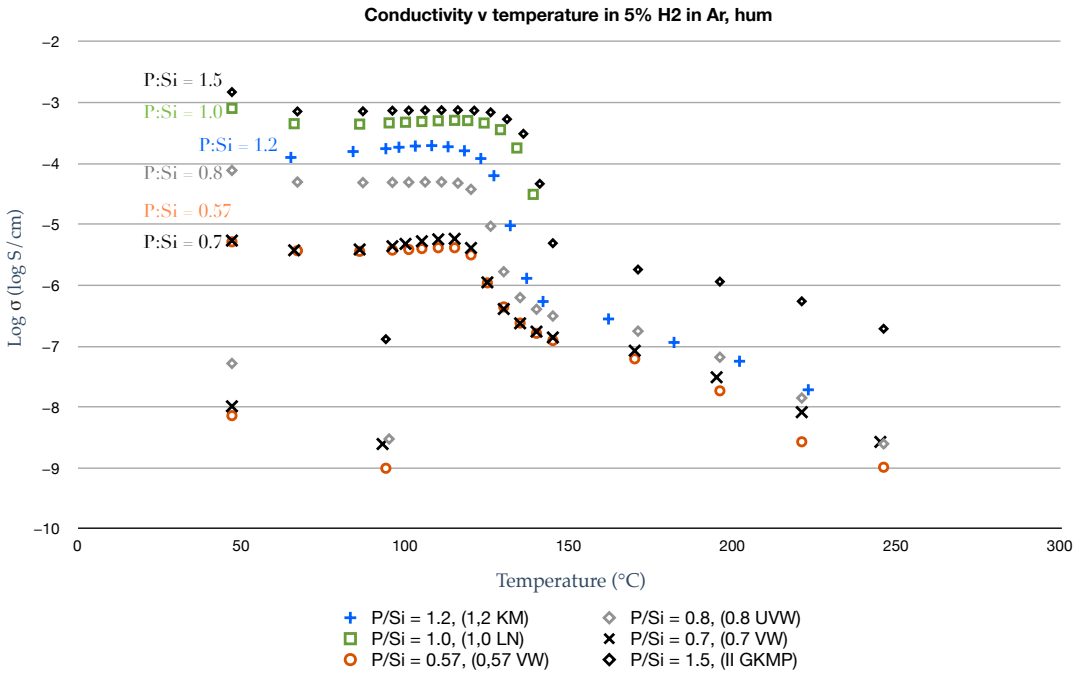

Figure 65 *Conductivities obtained from impedance measurements on hydrothermally treated P/Si pellets, undertaken in humidified 5% H_2 in argon. Note the inferior conductivity for the silicon-rich compositions, in particular P/Si = 0.57 and 0.7. The 0.8 composition shows vastly better conductivity up until 125°C, from which it decreases and is only marginally better. The 1.0 composition is better yet, especially above 130°C. The parent composition was best at about 120°C, yet for temperatures approaching 150°C P/Si = 1.5 was better.*

With the early samples it was found that an increased amount of silicon meant that the protonic conductivity increased. Therefore it was postulated that a further increase in silicon (a P/Si starting ratio below 1.0) would increase the conductivity even further. However, when investigated this was found not to be the case. Compositions of higher silicon content tend to be the worst from a conductivity point of view. One reason for this could be because the phosphoric acid content is lower, as indicated by Figure 31. This in turn is linked to the untreated compositions a,b axes – the longer these axes, the better protonic conductivity after hydrothermal treatment. Also the different P-Si starting ratios were reflected in the conductivity measurements that were done in air, especially at 125°C (cf. top part of Figure 61).

Some measurements were done in air (Figure 20) while others were done in humidified 5% H_2 in Argon (Figure 65).

4.7.2 Cell parameters and conductivity

Cell parameters for the untreated P-Si compositions were coupled with the conductivities obtained from the same hydrothermally treated samples, shown in Figure 66. These cell parameters were primarily obtained from high resolution XRD data that had been Rietveld refined. EIS was measured in air.

Electrical impedance measurements were done on hydrothermally treated pellets with platinum electrodes. The data was selected from four different temperatures that occurred on or very closely to: 65°C, 95°C, 115°C and 125°C.

There is a clear trend when it comes to conductivity versus the P/Si starting ratio at 125°C: the more phosphorus the better protonic conductivity is attained. The exception is for the lower temperatures where the peak occurs for a P/Si starting ratio of 1.0. If this ratio is lower than 1.0, the protonic conductivity seems to be lower and the trend is a decrease in conductivity as the P/Si starting ratio decreases further.

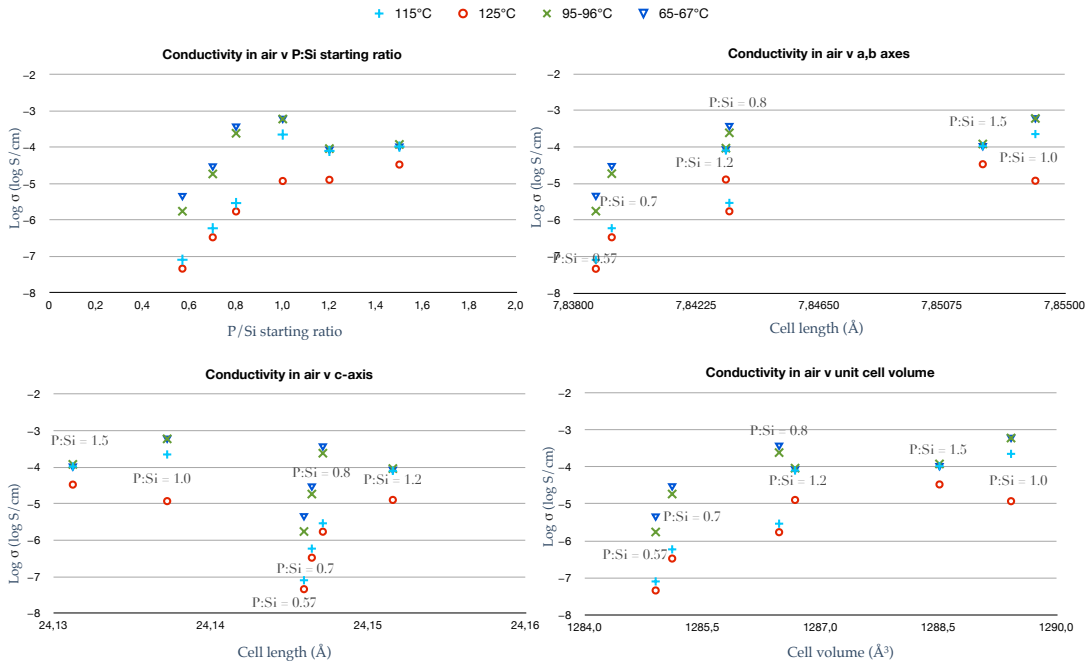

Figure 66 *Conductivities of the hydrothermally treated samples measured in air plotted against the P/Si starting ratio (above, left). Also pictured are the cell parameters for the untreated compositions: a,b axes (above, right), against the c-axis (below left) and versus the unit cell volume (below right). The trends are all similar in these plots except in the case for the c-axis. The sample with P/Si starting ratio 1.5 was refined after an extra firing (thus giving a close approximation to the cell parameters of the actual measured sample).*

In Figure 67 impedance measurements were instead done in humidified 5% H_2 in argon. This data shows a bit less variance over the temperature range and at the same time improved conductivity, yet the overall trends remain the same as the measurements done in air.

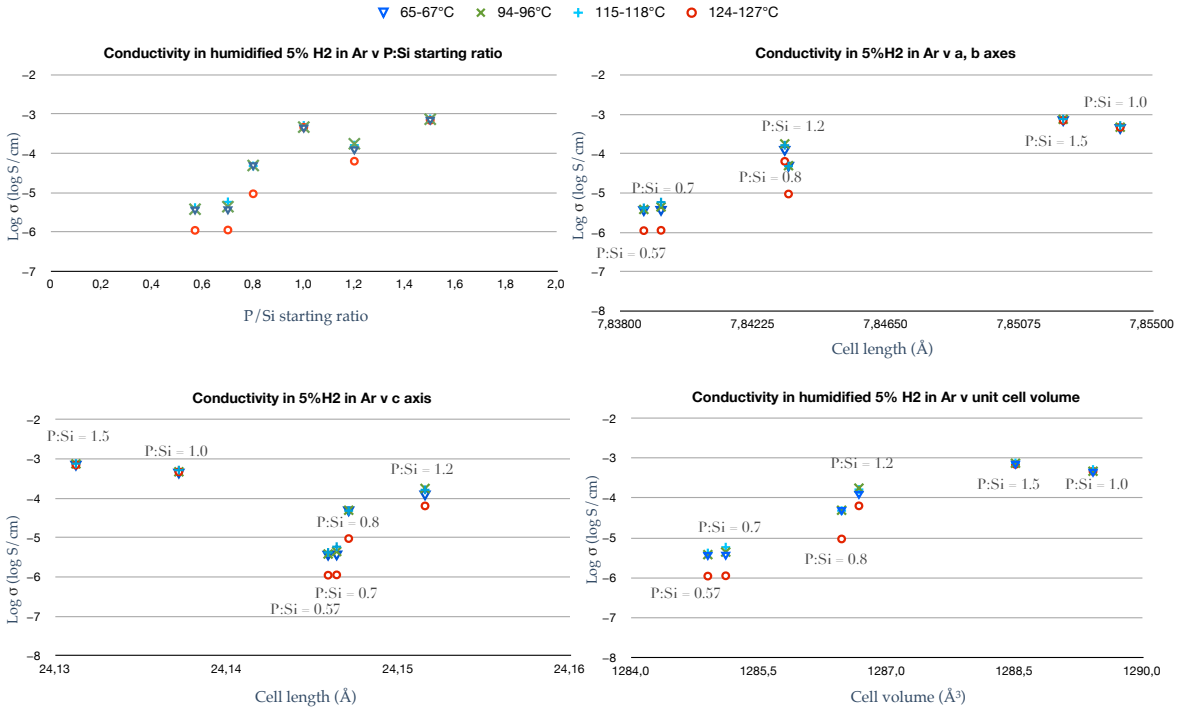

Figure 67 *Conductivities of the hydrothermally treated samples measured in humidified 5% H_2 in argon plotted against the P/Si starting ratio (above, left). Also pictured are the cell parameters for the untreated compositions: a,b axes (above, right), against the c-axis (below left) and versus the unit cell volume (below right). The trends are all similar in these plots except in the case for the c-axis. The sample with P/Si starting ratio 1.5 was refined after an extra firing (thus giving a close approximation to the cell parameters of the actual measured sample).*

Looking further to low-intermediate temperature desorption of water and how this could be related to any other properties. The desorption of water was quantified from TG data and plotted against the P/Si starting ratio as seen in the top graph of Figure 68.

The length of the c-axis for the untreated compositions (bottom graph in Figure 68) seems to be linked to the water desorption of the hydrothermally treated compositions. This holds true for compositions that range from a P/Si starting ratio of 0.57 – 1.0, especially when considering the behaviour at 100°C, see Figure 68. For compositions 1.2 – 1.5 there may still be a correlation to the c-axis, although it now appears as an inverse correlation compared to the case of the silicon-rich

compositions. The length of the a,b axes for the untreated compositions (mid graph in Figure 68) cannot be linked to the water desorption in any confident way, however, as was previously shown this cell parameter property is linked to the conductivity (compare e.g. mid-graph in Figure 68 with top-left graph of Figure 67).

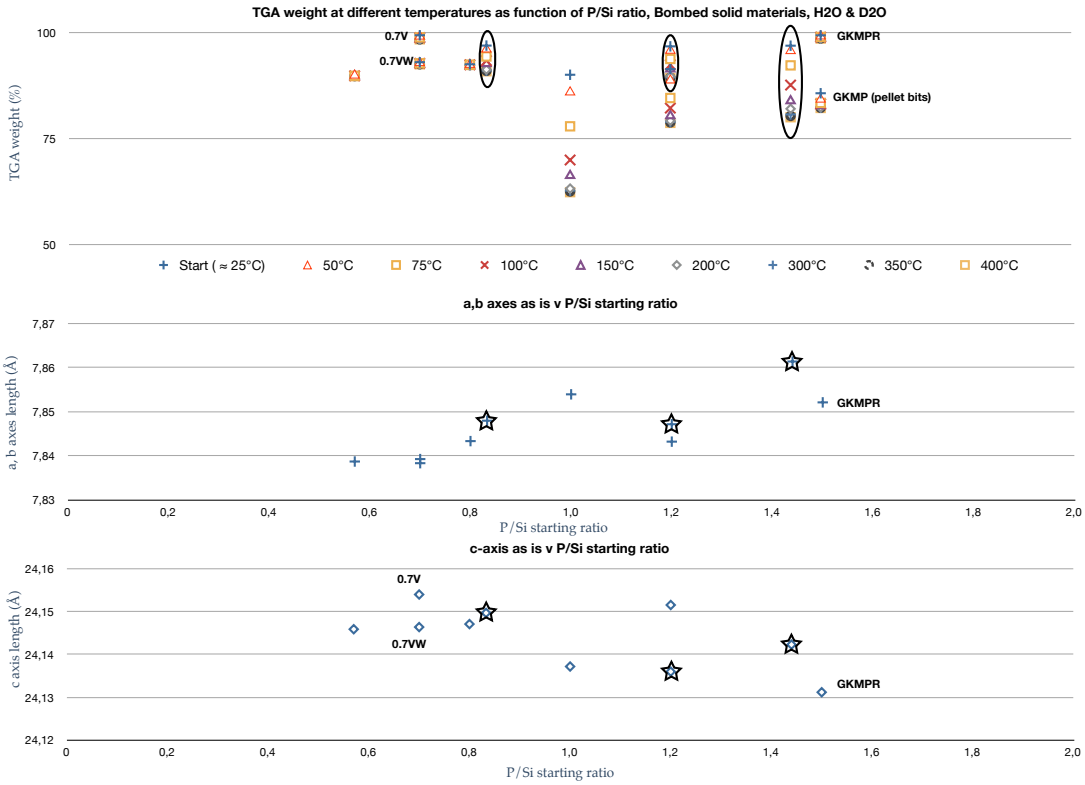

Figure 68 *TGA weight loss for hydrothermally treated compositions (top) v P/Si starting ratio, pictured against the cell parameters for the untreated P/Si compositions – the a,b-axes v P/Si starting ratio (middle) and the c-axis v P/Si starting ratio (lower). Note the correlation in regards to the c-axis and the TGA weight loss.*

The sample with P/Si starting ratio 1.5 was refined after an extra firing (thus giving a close approximation to the cell parameters of the actual measured sample).

4.7.3 Acid-doped compositions

Impedance measurements were carried out on solid-state sintered materials that had been boiled in 85% phosphoric acid, using a reflux apparatus. These materials came from the same batches as some previously mentioned compositions, they were spare pellets that had not been painted with platinum paste or hydrothermally treated. Each pellet was in the boiling concentrated phosphoric acid for about 1.5 hours, after which they were carefully rinsed off on the outside with de-ionised water and then dried with paper. Each side of the pellet was painted with silver paste, with a brief five minutes in the drying oven to dry top and bottom layer. The conductivity data for the tested samples is given in Figure 69, the atmosphere being air.

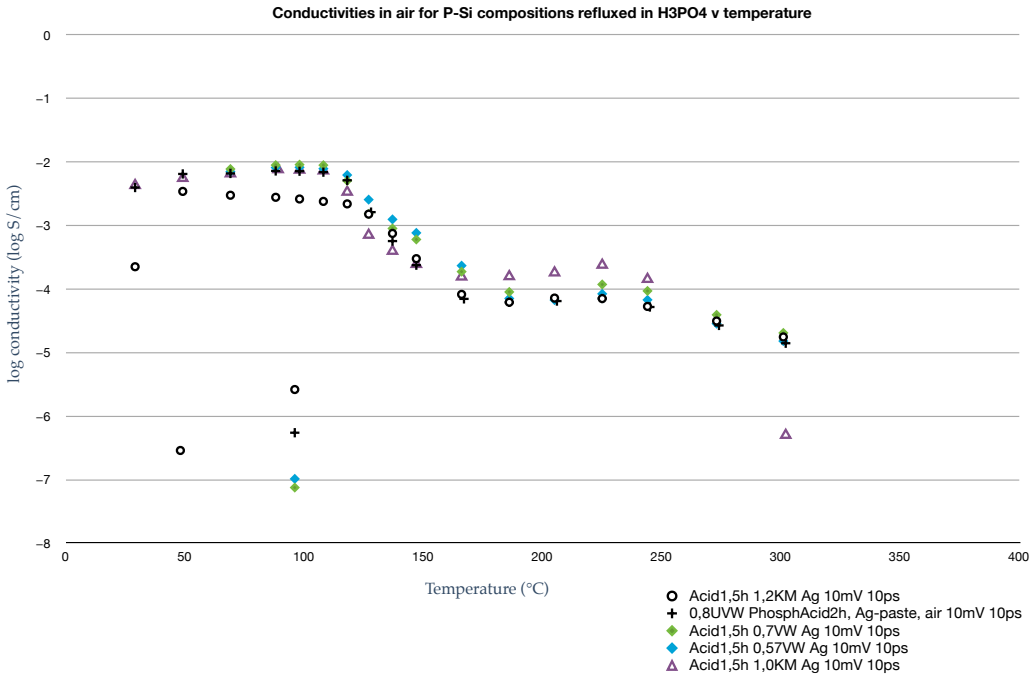

Figure 69 *Conductivities plotted against temperature for P/Si pellets that were refluxed in 85% H_3PO_4.*

The consequence of the concentrated phosphoric was that it enabled even higher protonic conductivity. The differences are quite remarkable compared to hydrothermally treated compositions (compare results in Figure 69 to Figure 20). Nyquist plots for the parent composition, $Si_5O(PO_4)_6$, and the 1.0 P/Si starting ratio at 127°C and 244°C are given in Figure 70.

No TG/DTA measurements were done on these samples because of the contamination risk in regards to phosphates could have on the instrument.

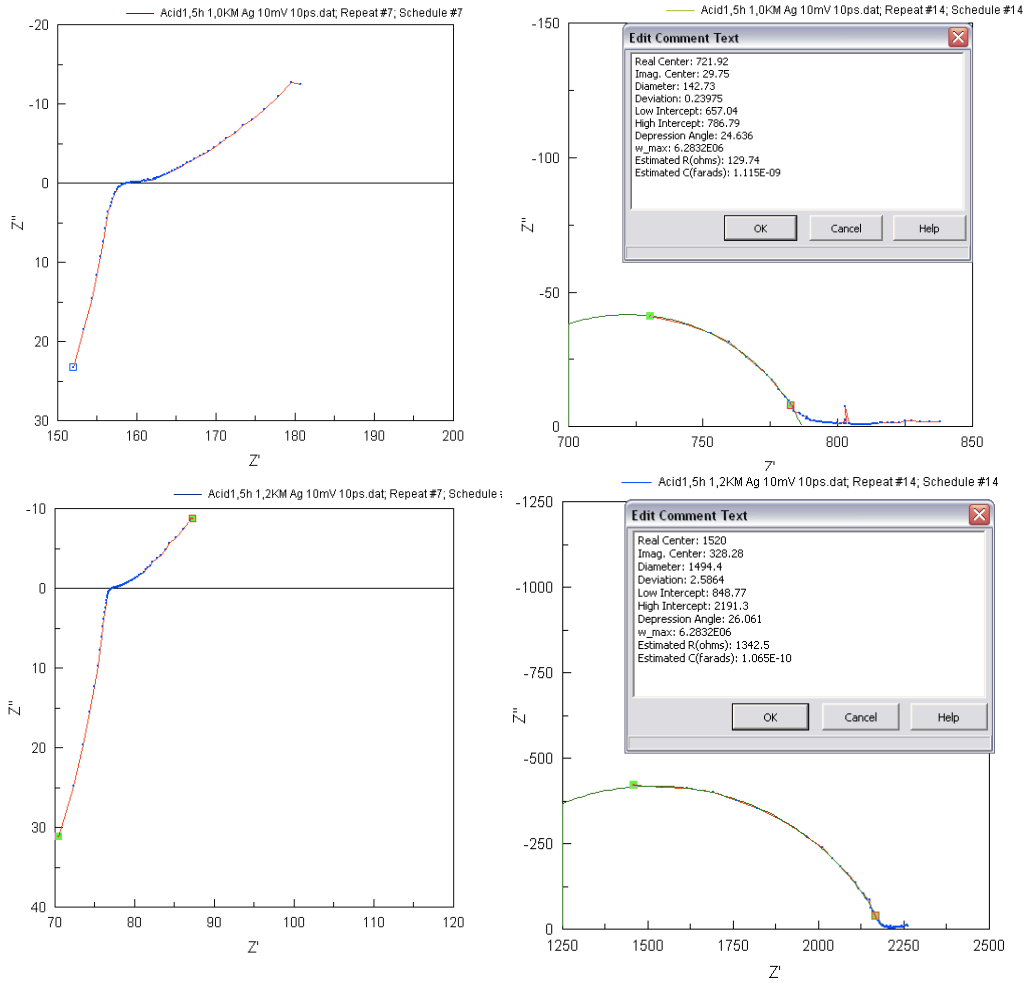

Figure 70 *Selection of Nyquist plots for P/Si starting ratio 1.0 (top) and 1.2 (bottom). The compositions were refluxed in 85% H_3PO_4. Measurement taken after letting sample stabilize at about 127°C for 20 minutes (left half of figure) and 244°C (right half of figure).*

4.7.4 P-Si gels

Conductivity work was undertaken on the precursor material for the P-Si compositions, namely the P-Si gels. The preparation consisted of mixing together a gel consisting of H_3PO_4, SiO_2 and de-ionised water which was then put in the teflon vessel. The resulting gel was then sandwiched between two pieces of mesh that were in contact with copper foil[9], or alternatively measured in a teflon setup – also that using copper electrodes, but with the gel directly onto the flat metal surface.

In the latter setup, the EIS measurements were done in a Teflon ring, which had an inner diameter of 12 mm and allowed a thickness of gel of 4 mm. The idea behind this was that the teflon ring would be sufficiently sealed all around with the prospect that no dehydration of the gel would occur, yielding perhaps better values of conductivity.

The aim was to carry out measurements from room temperature up to 300°C, as teflon melts at 326.8°C. Teflon further shows excellent chemical inertness making it ideal for testing a range of materials in the aforementioned temperature range.

The Teflon setup worked excellent in the low temperature region, however as temperatures increased the gel transformed into a pellet and eventually contact with the copper electrode was lost. It is conceivable that there was a leak somewhere that caused liquid to escape, although special care had been taken before the experiment to not only force the parts together with a spring but also insulate with Teflon tape around the interfaces to prevent short-circuiting. Worth noting further is that this occurred for all the experiments carried out with this setup, therefore it is likely either an inherent problem to the setup or a property of the gel itself. Likely the water in the gel started boiling, and even though the setup seemed intact after the experiments, water vapour might have escaped and thus dehydrated the gels.

In lieu of treatment in a furnace followed by hydrothermal treatment with water, which was the case for the other samples in this thesis, the respective gels were taken out of the hydrothermal vessel and then impedance was measured. It was imperative to avoid any higher temperatures apart from when the actual conductivity measurements were taking place.

[9] A very minute amount of the same gel was used as a thin layer of glue between the mesh and the copper foil.

Measurements were taken from low to high temperature, since the gel dehydrates with the added heat which negatively affects the conductivity. Figure 71 shows the conductivities for the gels with different P/Si ratios, there is a marked improvement compared to the solid-state sintered samples.

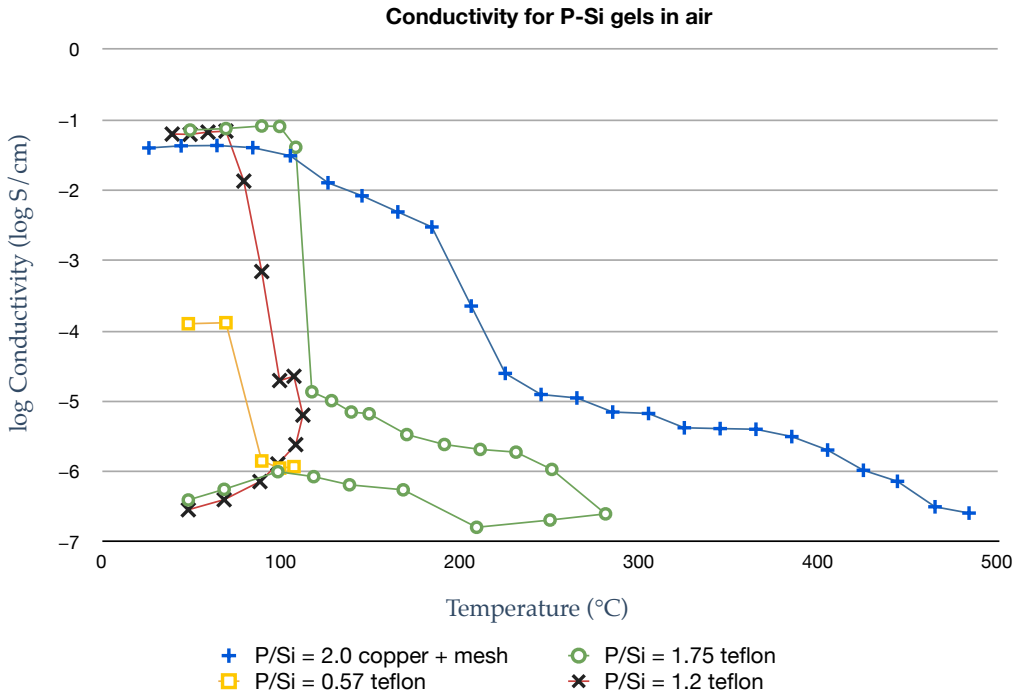

Figure 71 *Conductivities for P-Si gels with varying P/Si ratio. The 2.0 sample was measured in a different setup (copper + mesh) compared to the others which were measured in the teflon setup. This would explain the quicker drop in conductivity for the latter at around 100°C.*

TGA data reveals that the highest mass loss up to 100°C occurs for the 0.57 gel, and the smallest happens for the 2.0 gel, see Figure 72. The TG and DTA data on these gels is interesting because it looks similar to that of high temperature made P-Si compositions that had been hydrothermally treated. Indeed they are alike, except for the magnitude of the mass losses; these are much larger for the P-Si gels, albeit the shape of the TG curve is much the same. The higher mass losses for the gels can be attributed to the higher water content, as more water was added to the more silicon-rich mixtures in order to obtain similar gel-like consistency for all samples.

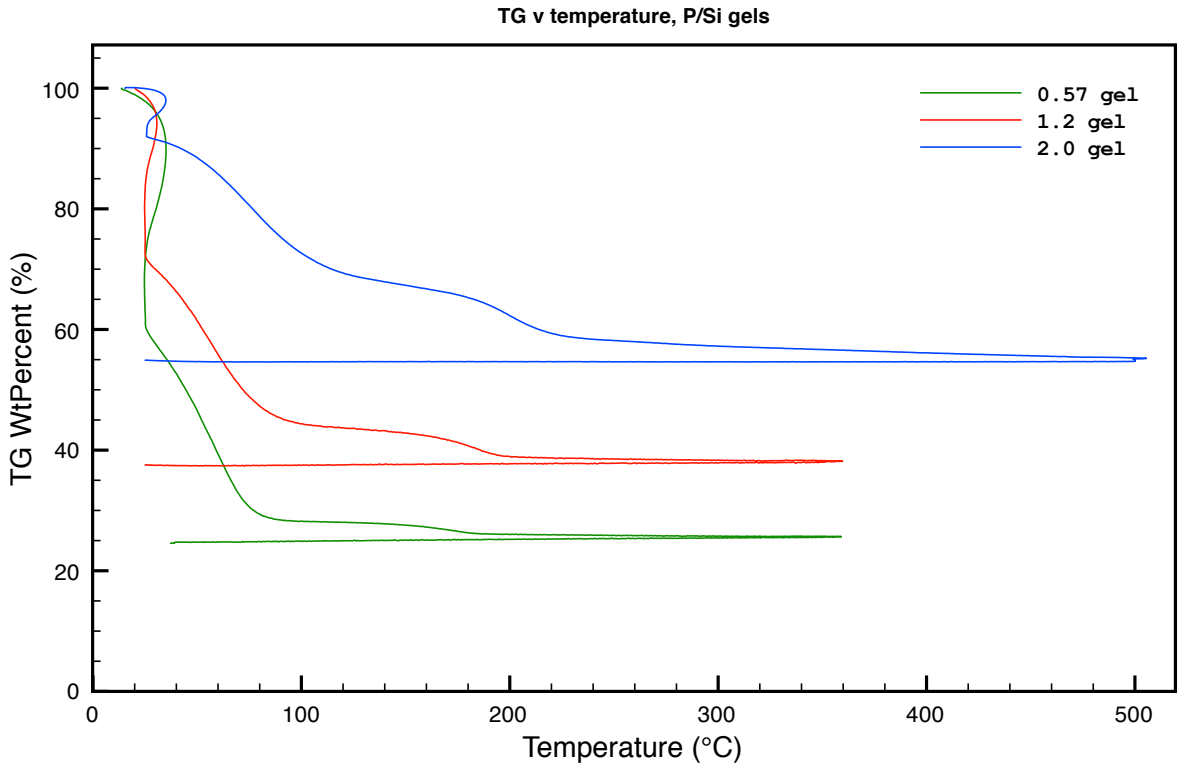

Figure 72 *TG measurements of P-Si gels compared to one another. The 2.0 gel (precursor to SiP_2O_7 was tested up to 500°C, the other two were run up to 350°C. The larger losses of water for the silicon rich sample (P/Si = 0.57) is due to that this sample contained more water which was necessary in order to form the gel. There is a shift in the curves with increasing amount of phosphoric acid where water is retained to slightly higher temperatures. Even above 200°C there is mass loss for the 2.0 gel sample, however not for the more silicon-rich samples.*

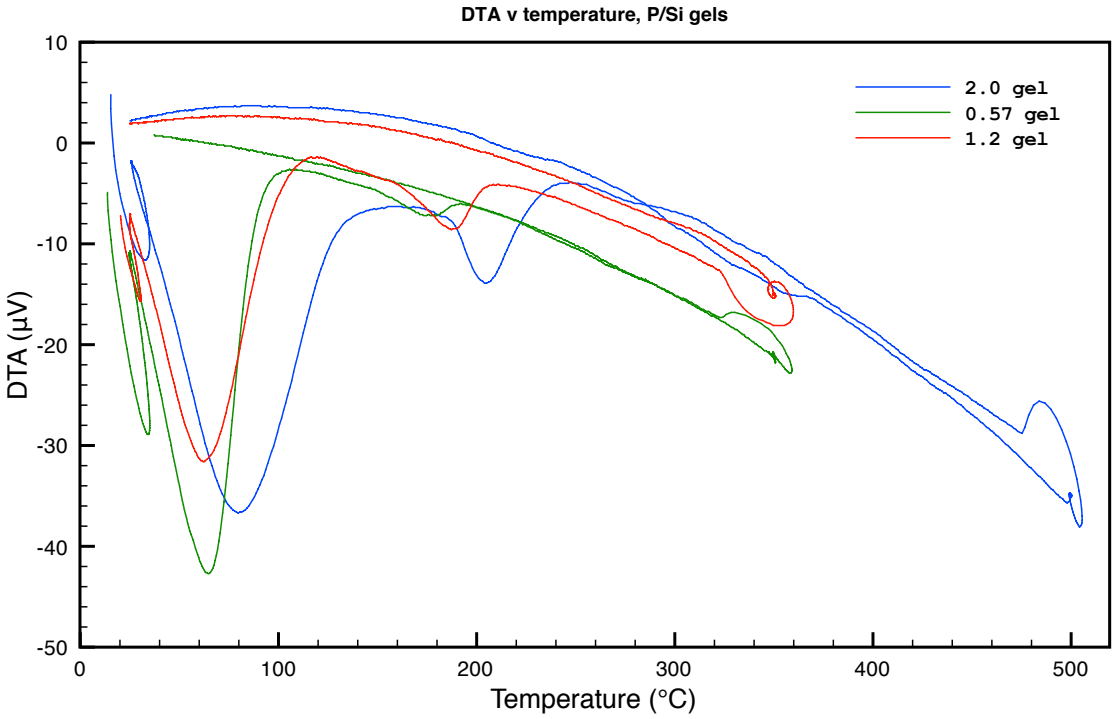

Figure 73 *DTA measurements for the gels as a function of temperature. Note the temperature dependence for the second peak on the P-Si ratio.*

The gels show some interesting trends. Not only does higher phosphate content yield better conductivity as concluded from Figure 71; also high mass losses in the low-intermediate temperature region correspond to the composition performing more inferior in terms of protonic conductivity, cf. Figure 71 with Figure 72. This can be explained by that although some water is needed for the conductivity, the phosphoric acid is needed more so. The two species likely act together, and when the P/Si ratio is sufficiently high then conductivity is fine (a situation when conductivity is less dependant on water). When however there is too much water and too little phosphoric acid (as in the case of the P/Si 0.57 gel) then the low temperature conductivity is within an order of magnitude of the results previously obtained for the hydrothermally treated compositions (P/Si ratios 0.8 – 1.5). In this case, it is conceivable that there is a very similar mechanism to those hydrothermally treated samples, a situation where there are less phosphate units and the conductivity becomes more dependant on water.

Note further from the TGA in Figure 72 that water desorption occurs later the higher the P/Si ratio is. For the P/Si 2.0 gel it appears to continue well beyond 200°C, whereas for the other two samples it has levelled off before this temperature. The same is confirmed in the DTA (Figure 73) where the second peak (at about 150°C) occurs later the higher the P/Si ratio is. For the peaks under 100°C, it could be within the margin of error for the silicon-rich gel and the 1.2 gel, as they happen almost at the same temperature.

4.7.5 Investigation into possible oxide ion conductivity

In this project the primary focus has been on protonic conductivity. However, the silicon phosphate system can also be thought of as an oxide ion conductor at higher temperatures. Initial measurements were performed at an early stage, however, due to phase impurities the data showed the tested compositions were too insulating. Toward the end of the project EIS was carried out on phase pure compositions made from H_3PO_4 at the temperatures where oxide ion conduction is thought to occur. The only modifications that had to be done were to conduct the EIS measurements at a higher voltage and make sure to use Pt-paste as the electrode on the pellet surface. Figure 74 shows a silicon-rich composition, P/Si starting ratio 0.7, that had been hydrothermally treated. A number of different measurements over the large temperature range have been combined, and the primary y-axis displays the logarithm of the conductivity (- 4

to - 9), as well as the logarithm for the characteristic frequency (5.5 to 1). The secondary y-axis shows the TGA values in weight percent, the DTA is scaled to arbitrary values. All of these measurements were done in air and are plotted against temperature.

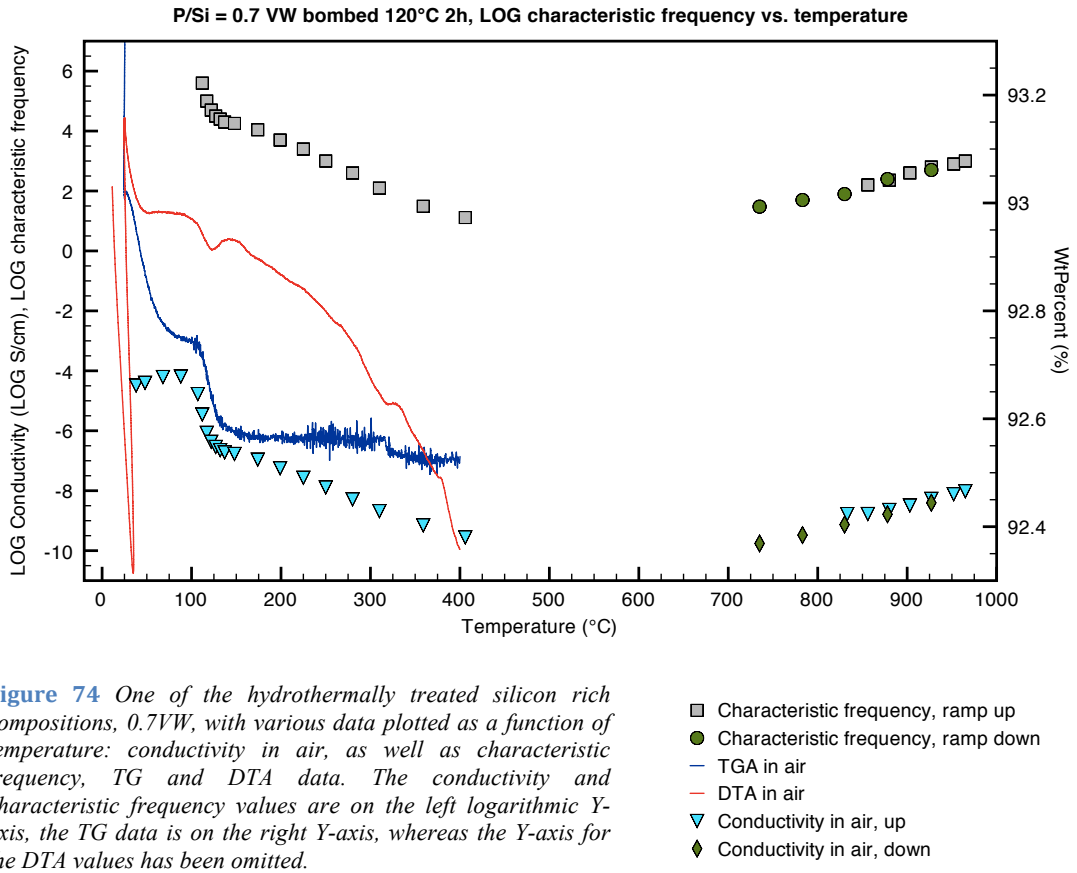

Figure 74 *One of the hydrothermally treated silicon rich compositions, 0.7VW, with various data plotted as a function of temperature: conductivity in air, as well as characteristic frequency, TG and DTA data. The conductivity and characteristic frequency values are on the left logarithmic Y-axis, the TG data is on the right Y-axis, whereas the Y-axis for the DTA values has been omitted.*

Note that the processes are temperature dependent – protonic conductivity is in the low-intermediate region, oxygen conductivity is in the high temperature region.

The parent composition showed a similar behaviour to Zhang's measurement (cf. his figure 5 in [69]), which is substantially inferior to its germanium counterpart (ibid). The range measured was from 965°C to just under 500°C for this sample which had been previously hydrothermally treated. Whereas a more silicon-rich composition was shown in the previous figure, the measurements for the hydrothermally treated parent composition are shown in Figure 75, plotted in the same way.

The primary reason for the poor oxygen conductivities may be ascribed to the presence of silicon itself. Indeed, when compared to the Germanium counterpart it is clear that the latter is orders of magnitude better even though the two materials have

the same structure.

In SOFC work the element silicon is avoided due to the negative effects of increased grain boundary resistance it brings about, even very small trace amounts of silicon contamination have shown these effects. Therefore, it is reasonable to conclude that the P-Si materials are poorly suited for the application as a fuel cell electrolyte, however the material could perhaps serve as a basis for oxygen sensors if a way to increase its oxygen conductive nature is developed.

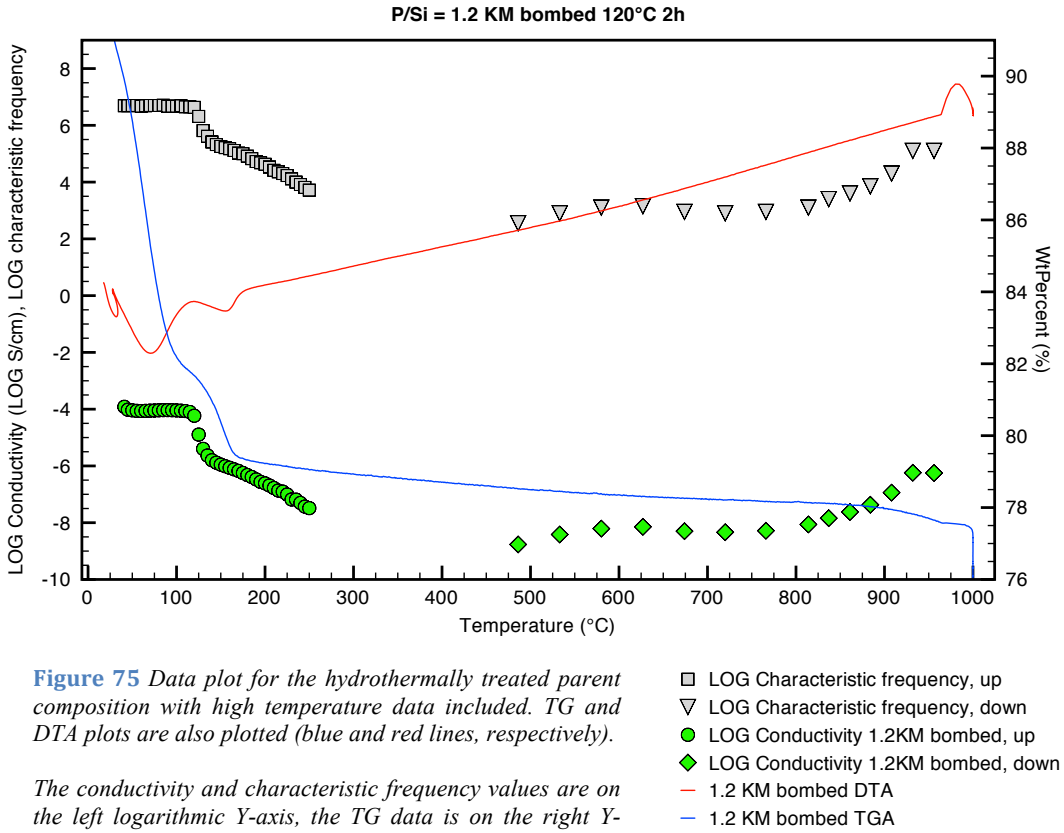

Figure 75 *Data plot for the hydrothermally treated parent composition with high temperature data included. TG and DTA plots are also plotted (blue and red lines, respectively).*

The conductivity and characteristic frequency values are on the left logarithmic Y-axis, the TG data is on the right Y-axis, whereas the Y-axis for the DTA values has been omitted.

Note the close correlation between TG data and conductivity.

4.8 Summary of findings

A good sintering method was found for producing single-phase silicon oxide phosphate, which included using H_3PO_4 as the phosphorus source, by using a gel precursor and the solid-state sintering method.

This method not only made phase purity feasible but also reduced the amount of amorphous content in the final product. Throughout the investigation it was found that

the more silicon-rich compositions tended to have more amorphous phase.

Different stoichiometries were chosen to investigate whether there was a solid solution and, if so, how this would affect the properties, especially in regards to protonic conductivity.

It was found that hydrothermally treating solid state sintered materials with water improved protonic conductivities by several orders of magnitude. Too much hydrothermal treatment though (at 180°C) made the materials amorphous. The preferred temperature and time were 120°C for two hours.

Differences were found in the microstructure between an untreated composition of $Si_5O(PO_4)_6$ and its hydrothermally treated counterpart. The latter seemed to have its surfaces covered in what looked like small crystals, whereas the former had much bigger crystals clustered in certain areas only.

The solid-state NMR data showed that there was a lot more phosphoric acid in the hydrothermally treated compositions compared to the untreated counterparts, even though only water was added in the hydrothermal treatment. The small amount of phosphoric acid that was found in the untreated compositions could be explained in that the samples absorb humidity from the air over time. Moreover, there were differences in the phosphoric acid content which could be linked to the unit cell volume.

Also the integrated area of the tetrahedral phosphorus peak could be linked to the unit cell volume. The differences here between untreated and hydrothermally treated are not as vast as in the case with the phosphoric acid amount, however, they are large and different enough to suspect that something happens to the phosphorus content upon hydrothermal treatment.

It was possible to do ^{29}Si NMR on a sample that had been enriched with 20% $^{29}SiO_2$. The sample had likely absorbed some water from the surrounding atmosphere, because there was a double peak in the ^{1}H NMR, which did not occur when the sample was refired. In both cases ^{29}Si NMR and ^{31}P NMR spectra were attained confirming the local structure of the parent composition.

The high temperature behaviour was studied for the parent composition, both the untreated and hydrothermally treated with H_2O. It was found that background of the hydrothermally treated composition was diminishing as temperature increased, especially between 125 °C and 150 °C, whereas the untreated parent composition showed no change at all. This amorphous background is likely liquid water that is being desorbed, perhaps from the channels of the structure.

4.9 Discussion

For the neutron diffraction data collection D_2O was used to hydrothermally treat three compositions with varying P/Si starting ratio (0.833, 1.2 and 1.44).

For the parent composition hydrothermally treating with D_2O made the unit cell parameters expand quite visibly, also seen in the sequential GSAS runs. Throughout the high temperature range this expansion remained, suggesting that some sort of substitution occurred during the hydrothermal treatment.

The unit cell expansion seen after hydrothermal treatment with D_2O – could this be due to a systematic error due to the placing of the samples in the furnace? Note that the parent composition experiments were done in quartz tubes, whereas the other compositions were done in sealed Vanadium cans (and for these latter samples no expansion was observed).

However, if a systematic error was solely responsible for the different results then the amount of error would be the same on all the axes. For example, an expansion in a and b of 0.25% would result in the same expansion occurring in the c-axis also. There is now a small difference in the recorded values of the a, b axes (+ 0.247%) and the c-axis (+ 0.286%) as a function of hydrothermal treatment with D_2O.

Note further that the c/a ratio is slightly different for the two samples – which can be taken as confirmation that systematic error cannot account for the entire change (if this was the case, the c/a ratio would be the same for both compositions). Moreover, there is variation of the c/a ratio with temperature for the hydrothermally treated composition which deviates from that of the untreated composition.

Thus, if the differences in observed cell parameters were solely due to systematic

error, then the c/a ratio would be the same for the two samples. It is likely therefore that there are changes in composition as a result of hydrothermal treatment.

For the other compositions, 0.833 and 1.44, there was instead contraction when hydrothermally treating with D_2O, however there are differences between the three samples; one strong trend seems to be the bigger the hydrothermally treated a,b axes are, the more phosphoric acid is picked up by the ^{31}P NMR.

Common for the neutron samples was that the hydrothermal treatment made the background (amorphous phase) more prevalent at room temperature. This greater amorphous phase largely persisted for the parent composition when going up in temperature, then gradually decreased in the region of 130 – 200°C.

Also for the high temperature XRD run with hydrothermally treatment with H_2O, the biggest decrease in amorphous phase happened between 125°C – 150°C. This is also where there is a large conductivity drop, and these two things may well be connected.

More amorphous phase does however not mean more protonic conductivity. The protonic conductivity seems to be linked to the unit cell volume as shown in Figure 66. There is moreover more direct evidence that the $Si_5O(PO_4)_6$ units are responsible for the protonic conductivity. For example, the relative shift for the – 44 ppm peak in the ^{31}P NMR, shows small variations between untreated samples. These variations correspond very well to the low temperature conductivities for the hydrothermally treated compositions, as well as to the different temperatures at which the DTA peaks occur for the same, see Figure 62.

There are many interesting differences between the compositions at room temperature. The changes that occur to cell parameters upon hydrothermal treatment appear to be linked to the occupancies of the crystal sites. Noteworthy to remember though is that even though the measurements were at room temperature, the hydrothermal treatment did not occur at room temperature – rather at around 120°C and at elevated pressure.

It is uncertain whether Poojary's model of the parent composition is the correct one, even for the untreated composition; however, it does serve well as a basic model to evaluate the neutron data.

From the neutron data there appears to be a solid solution for the P-Si system, not merely because of the trends in the total occupancies versus the P/Si starting ratio (Figure 40), but it is also indicated when looking at the individual occupancies (Figure 39) and comparing them to the cell parameters (Figure 30).

The fact that the chemical shift for the $Si_5O(PO_4)_6$ unit is slightly different for a range of untreated compositions, and that this relative difference corresponds to other observed trends, does imply a solid solution.

The P-Si materials have a lot of potential when combined with water and / or phosphoric acid. It has been established herein that the observed protonic conductivity does originate in the crystal lattice.

Although the protonic conductivities for the hydrothermally treated P-Si compositions are moderate, one could make thinner membranes in an actual fuel cell and thereby lessen a membrane's resistance to the proton flow and obtain greater protonic conductivity.

A suggestion for future research is to create thin films through e.g. pulsed laser deposition (PLD) of a solid pellet target; or by depositing a spray of finely suspended powder in ethanol by the use of an airbrush and then sintering the material. The only drawback with using an airbrush is the lack of repeatable thickness and the usage of excess material. On an industrial scale the repeatability might not be an issue, but excess material (such as say platinum) would be.

In any case, the choice of silicon oxide phosphate does have a huge advantage in that it is cheap to produce, the elements are ubiquitous, and it is environmentally friendly.

Furthermore, if hydrothermal treatment can be maintained during fuel cell operation (or when the fuel cell is at rest), then good and stable protonic conductivity would be the result. The operating temperature would exceed 100°C in either case.

If ongoing hydrothermal treatment was maintained during fuel cell operation then it is not impossible to envision an operating temperature of around 180°C. In hydrothermal conditions at 180°C all crystalline material had become amorphous, as shown in Figure 17. A simple setup for testing the protonic conductivity of P-Si

materials under hydrothermal conditions could be constructed for future work, as it is beyond the scope of this project. If this was done, a better understanding could be made of the protonic conductivity for the amorphous P-Si materials at low–intermediate temperatures when hydrothermally pressurised.

Since the best results were for P/Si compositions with concentrated phosphoric acid in them (cf. Figure 69) it would be natural to think of the phosphosilicate system as a matrix for phosphoric acid. If further investigated for this purpose, it is not impossible to envision operating temperatures of a new PAFC system at around 200°C, provided a way is found to further boost the conductivity (e.g. by operating in a humid environment).

Silicon oxide phosphates appear to be poor oxygen conductors, even at the high temperature of 960°C. This is thought to be due to the presence of silicon at the grain boundaries. It is therefore not a good material for SOFCs.

5. Substituted phosphate systems

5.1 Aluminium and titanium doping

A secondary goal in the project was to study the effects of partial substitution in the P-Si system, especially in regards to protonic conductivity. Samples were synthesised the same way according to synthesis method 1; temperatures, sintering times and starting stoichometries are given in Appendix D. The idea was to try start with the parent composition and substitute a certain amount of the silicon with either aluminium or a combination of aluminium and titanium.

There was some secondary phase of SiP_2O_7, however the major phase was various amounts of aluminium substitution of the silicon in the parent composition.

In Figure 76 the XRDs area shown for some different aluminium substitutions – blue diffractogram shows a sample that contains 2.5% aluminium, purple diffractogram a composition that has 7.5% aluminium and light green diffractogram shows a sample with 5% aluminium. The purest sample is the 2.5% composition, whereas there is a higher degree of SiP_2O_7 in the other two.

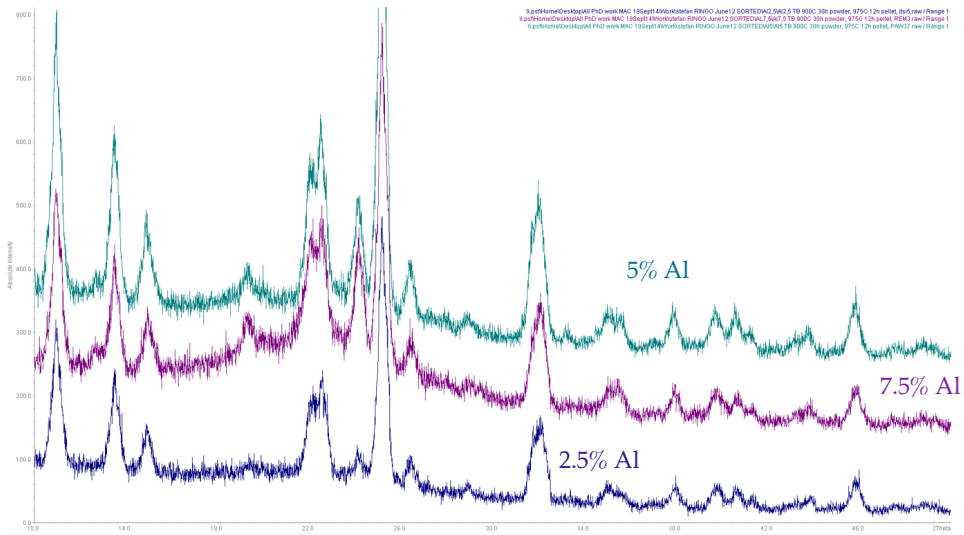

Figure 76 *Stack-plot of XRDs for the different degrees of aluminium substitution. Blue XRD is has 2.5% aluminium, light green XRD has 5% aluminium and the middle purple XRD has 7.5% aluminium. The amount of secondary phase, SiP_2O_7, increases with doping level. For the 7.5% aluminium there appears to be a bit more amorphous phase too compared to the others.*

For another set of aluminium doped compositions titanium was added as a co-dopant, the amount of aluminium was 5% and titanium was 1.66% and 5%. The XRD for these two samples is shown in Figure 77, from this figure it is clear that the amount of SiP_2O_7 is about the same as for the 7.5% aluminium doped composition seen in the previous figure.

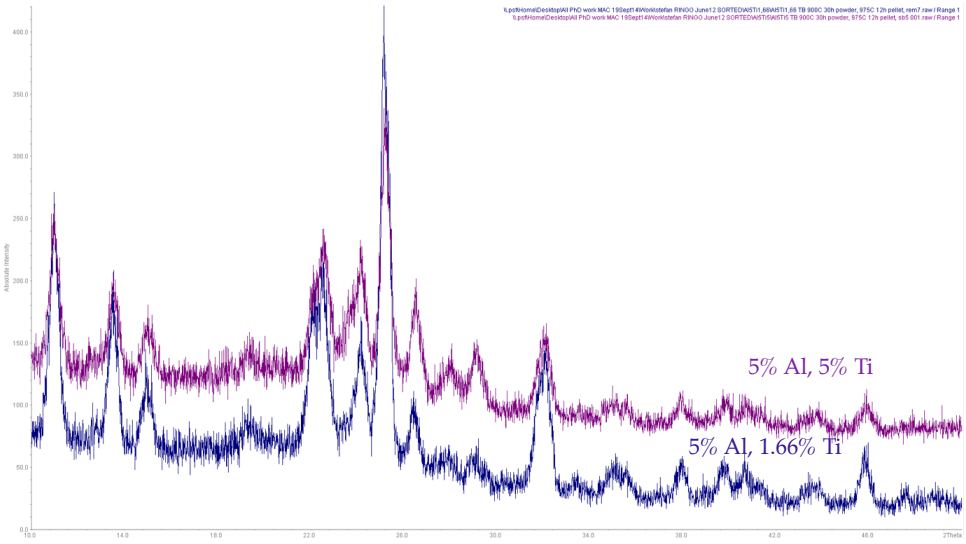

Figure 77 *XRD stack plots of untreated aluminium substituted compositions. There is some phase impurity, SiP_2O_7, most noticeable at 24° 2θ.*

The conductivity data measured in air, pictured in Figure 78, reveals that there is a difference in conductivity that is most likely due to composition. The best sample up to 135°C seems to be the 5% aluminium, narrowly followed by the 2.5% aluminium. Above 135°C, 1.66% extra titanium to 5% aluminium seems to produce better conductivity. If the aluminium content is 7.5% a decrease in conductivity is noted, and 5% aluminium with 5% titanium performs worse yet. These were all hydrothermally treated at 120°C for five hours, except the two latter compositions that were at 120°C for 2.5 hours.

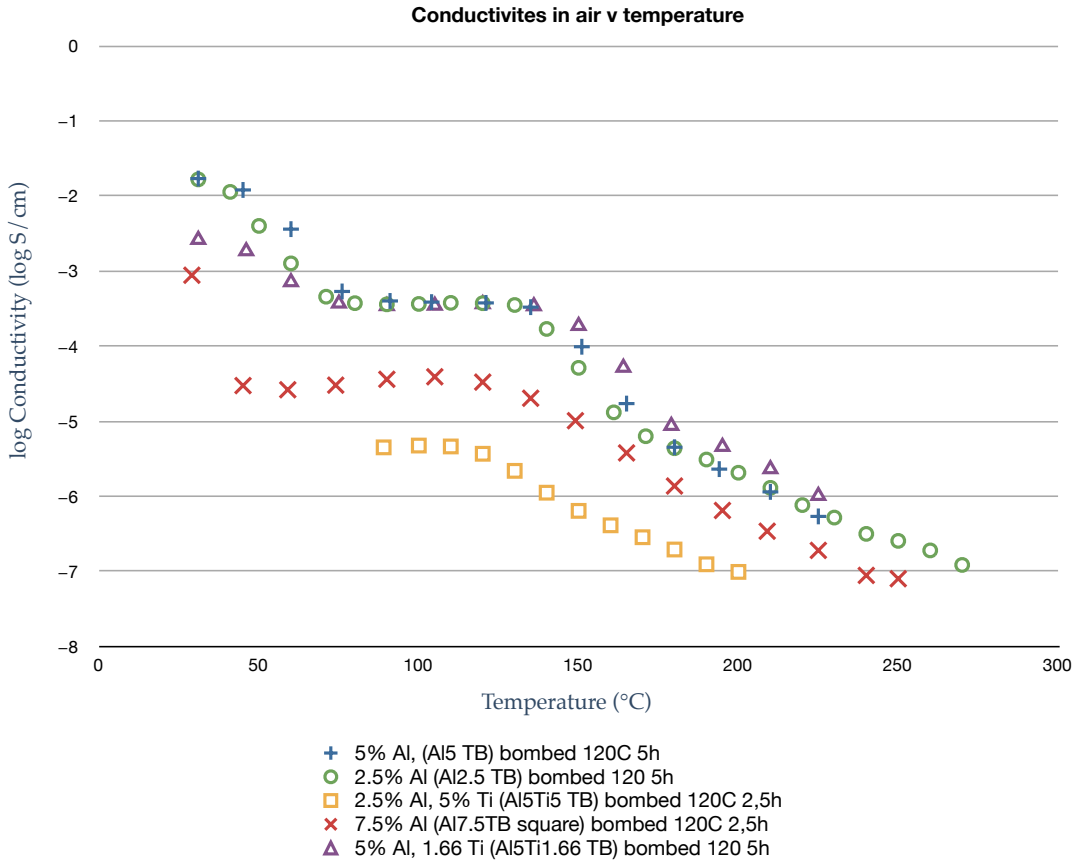

Figure 78 *Conductivities for hydrothermally treated aluminium doped P-Si compositions. A small amount of titanium (1.66%) to 5% aluminium appears to have enhanced the conductivity at about 150°C and above. Too much titanium (5%) with 5% aluminium proved to worsen conductivity.*

5.2 Germanium oxide phosphate composition

Germanium oxide phosphate, $Ge_5O(PO_4)_6$, has the same structure as silicon oxide phosphate, however a bigger unit cell due to that all the silicon atoms are substituted for larger germanium atoms.

The synthesis of these compositions was performed by Mark Tham; the EIS and ^{31}P NMR however were a collaborative effort and is here presented.

Firstly, ^{31}P NMR showed the chemical shift at - 33 ppm, which is markedly different from that of the silicon analogue (- 44 ppm), see Figure 79.

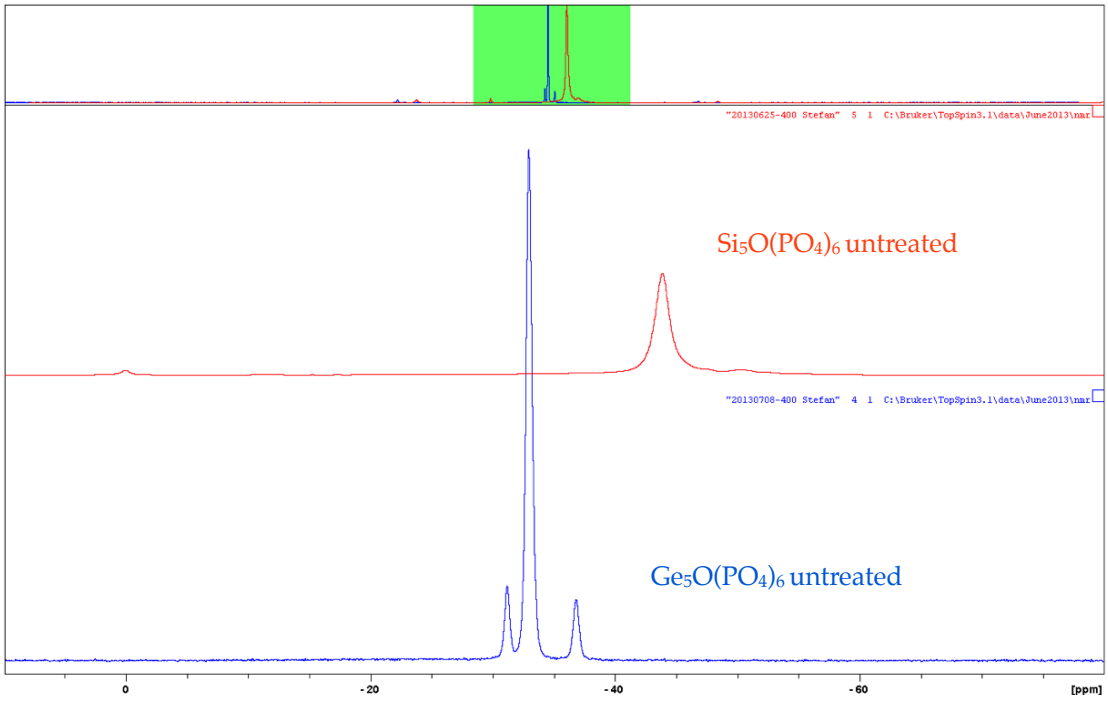

Figure 79 *^{31}P NMR of $Si_5O(PO_4)_6$ and its germanium analogue. The main chemical shift for $Ge_5O(PO_4)_6$ occurs at - 33 ppm, whereas for $Si_5O(PO_4)_6$ it is at - 44 ppm.*

Another two compositions with slightly more germanium (5% excess) were hydrothermally treated at 120°C for 2h and 72°C for three hours, respectively. Although these two latter compositions had identical stoichiometry they showed different conductivities in the low–intermediate temperature region, see Figure 80. This can be attributed to the differing hydrothermal treatments – the 120°C produced a composition that has more conductivity. It could be that the higher pressure made more water incorporate into the structure.

Another observation is that the conductivity increases with temperature, and a maximum was found at 410°C for the three hour hydrothermally treated sample, and 350°C for the two hour (120°C) sample. The Nyquist plot for both these points are shown in Figure 81. The conductivity increase with temperature is very much different behaviour to what was seen with the silicon oxide phosphate where conductivity decreased with increasing temperature.

Unfortunately no DTA or TG analysis was done on the hydrothermally treated germanium oxide phosphate compositions due to lack of material.

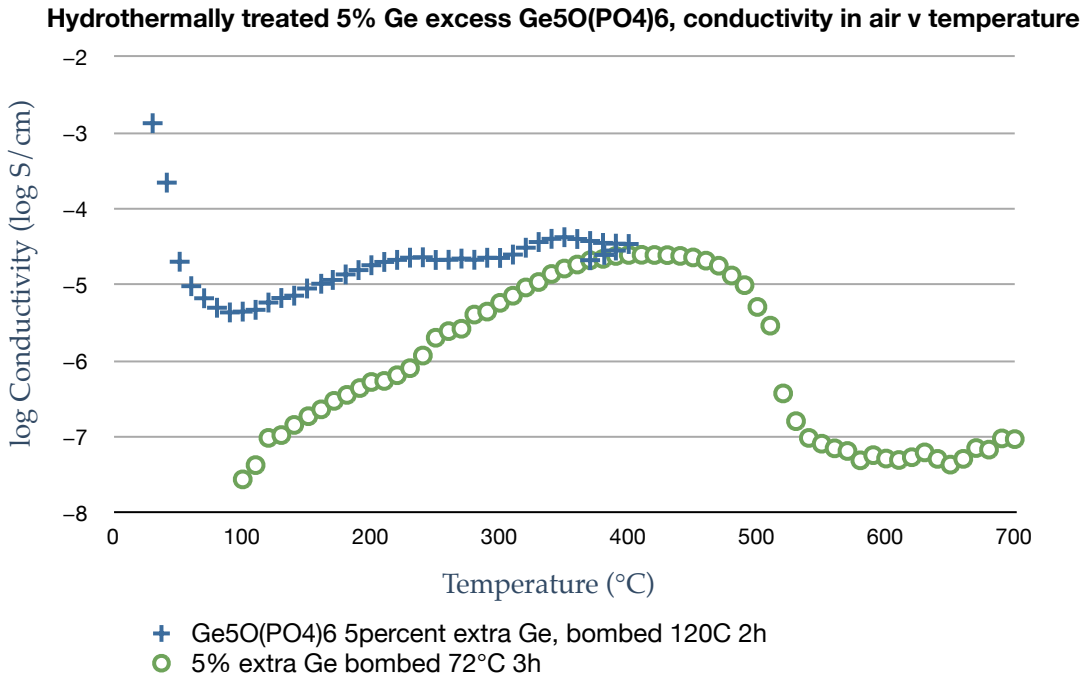

Figure 80 *Conductivities for two hydrothermally treated germanium oxide phosphate compositions, both with 5% excess germanium. The blue data came from a pellet that was hydrothermally treated at 120°C for two hours and the green data from another pellet that was treated at 72°C for three hours. Note the difference in low temperature conductivity that a higher hydrothermal pressure appears to make. Also note that the conductivity increases in both cases as a function of temperature, unlike the cases of previously shown silicon oxide phosphate compositions.*

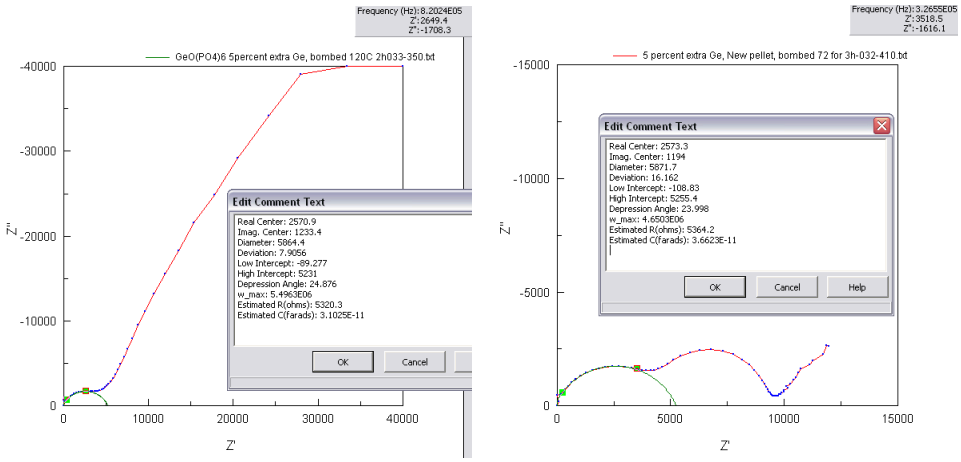

Figure 81 *Nyquist plots for the two hydrothermally treated germanium oxide phosphate compositions (5% excess Ge) at peak conductivities. Impedance data recorded in air (350°C and 410°C).*

5.3 $Ge_3Si_2O(PO_4)_6$

A composition replacing three of the five silicon atoms with germanium, i.e. a composition between $Ge_5O(PO_4)_6$ and $Si_5O(PO_4)_6$, was made. It included a final sintering step at 1100°C for 16h. It was made from the gel precursor method with phosphoric acid. The XRD clearly indicated a larger unit cell than the ordinary $Si_5O(PO_4)_6$, see Figure 82 where the sample is compared to ordinary $Si_5O(PO_4)_6$. When hydrothermally treated for two hours at 120°C, the TG and DTA shifted toward higher temperatures than what would otherwise be the case for the hydrothermally treated phosphosilicates, see Figure 83. Unfortunately there was not enough material to do conductivity measurements due to it being a small test batch, however the first DTA peak at 186°C indicates that this could be a very good proton conductor.

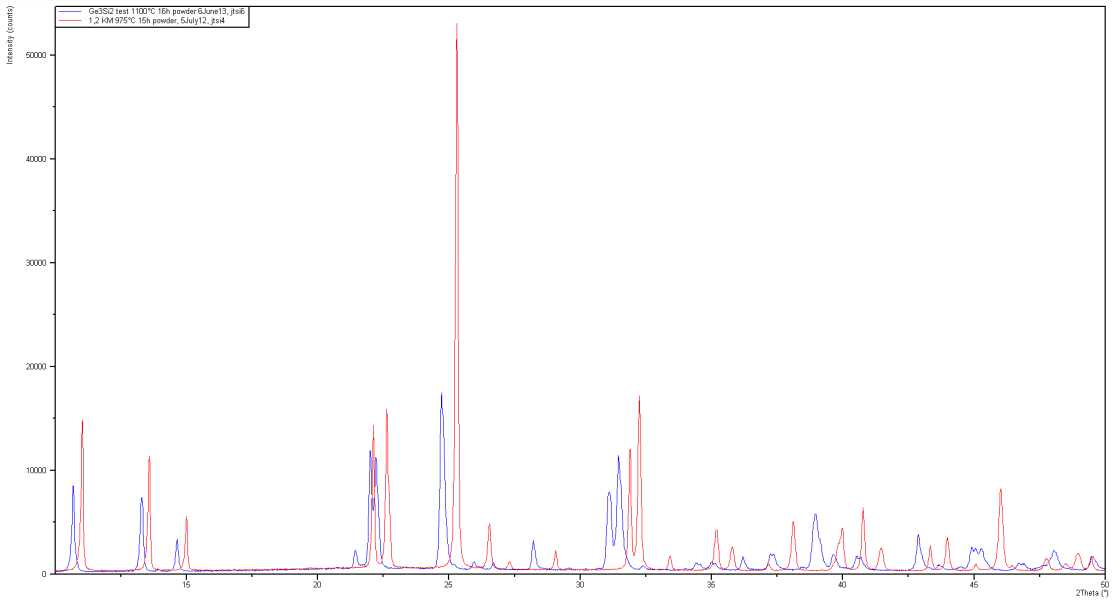

Figure 82 *XRD of $Ge_3Si_2O(PO_4)_6$ in blue, contrasted to the $Si_5O(PO_4)_6$ (red), both compositions untreated. Note the shift in peaks toward lower two theta indicating a larger unit cell for the germanium substituted composition.*

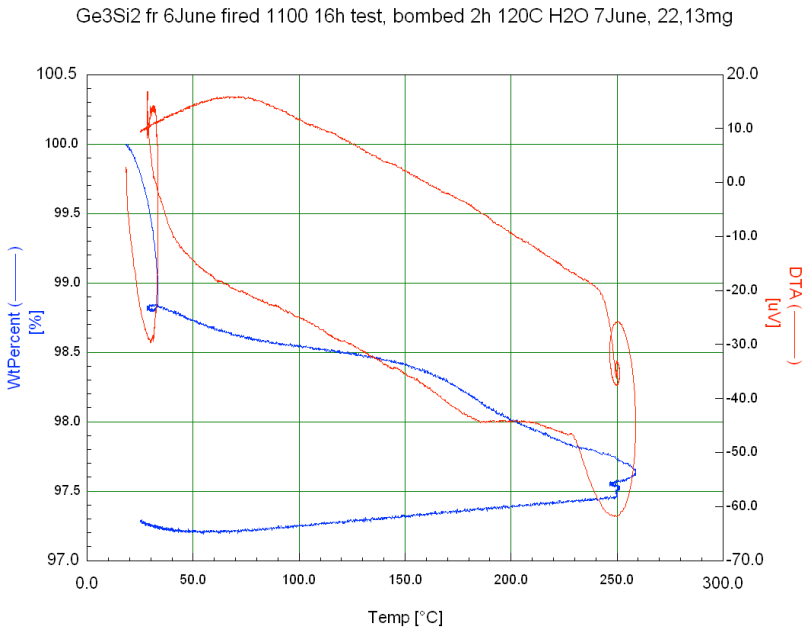

Figure 83 *The partially substituted germanium silicon oxide phosphate ($Ge_3Si_2O(PO_4)_6$ that had been hydrothermally treated. The first DTA peak occurs at 186°C, which is vastly above that of the pure silicon oxide phosphates.*

6. Conclusions

6.1 Synthesis

By employing the solid-state method it was firstly a priority to make single phase batches of primarily the parent $Si_5O(PO_4)_6$ composition (P/Si = 1.2), and then some other P/Si ratios (e.g. 1.5, 1.0 and 0.8). The first major problem encountered was phase impurity (a secondary phase of SiP_2O_7 was often the case), a second problem was high amounts of amorphous material in the synthesised materials. Although these two problems were addressed from the start of the project, it did take some time before a material that showed phase purity and only had low amounts of amorphous phase could be found and then re-produced.

The key seems to be that in order to avoid the amorphous contribution the phosphorus source should be H_3PO_4 as well as avoiding fast temperature ramps. Also, extending the sintering times has a positive effect.

The problem with obtaining phase purity was generally solved by keeping a high enough sintering temperature (1000°C) as SiP_2O_7 proved to be unstable at these temperatures. However, if the temperature was too high, the material would go into a glassy state altogether, which is not surprising since the silicon source is SiO_2.

In summary, having H_3PO_4 as the source for phosphorus greatly helped phase purity, in combination with adequate temperature settings.

6.2 This phosphosilicate system

Since the project has mainly focused on the compositions around and including $Si_5O(PO_4)_6$, conclusions with certainty can only be made on this range of compositions.

Key questions in this project have been:

• Where does the protonic conductivity occur – is it in the crystalline phase, the amorphous phase, or both? If both, which has the higher conductivity, and why?

• Can silicon oxide function as a matrix for phosphoric acid, and thereby enable greater protonic conductivity?

It has previously been suggested that the phosphorus–silicon system is a binary system, and the work for this thesis does support that.

This may be analogous to the case of alumina which forms a ternary system with phosphate and water [49].

The fact that the conductivity changes so much for the more silicon-rich samples is a strong indication for a solid solution. The more silicon in the crystalline structure the less amount of phosphate groups there will be along the channels of the structure. Phosphate groups along with interconnecting water molecules are critical for the protonic conductivity. With less amount of phosphate groups the protons will have to rely on being transported to a higher degree by water (with additional water-water proton transfers), than they otherwise would in say the 1.2 parent composition.

When phosphoric acid is incorporated in the structure the proton conducting mechanism switches to becoming almost fully dependant on the phosphoric acid, and not dependant on the host material. The fact that the protonic conductivity can be upheld well past the decomposition temperature of phosphoric acid, 213°C [70], is proof that the acid as been integrated with the host matrix, silicon oxide phosphate, and as a result is stabilized by it. Therefore the protonic conductivity is likely in this case to go also along the channels of the host, but with a different mechanism than in the case of the hydrothermal treatment, namely from one H_3PO_4 group to another.

Thus, the silicon oxide phosphate compositions appears to be able to act as matrices for H_3PO_4 which is something to take into consideration for the further development of solid state protonic conductors. The fact that a matrix supports the phosphoric acid means that one can take advantage of the solid electrolyte (without the mess of liquids), and perhaps operate the fuel cell at higher temperature than what would otherwise be permitted with liquid phosphoric acid.

There is likely a quarternary system for silica, phosphate, water and phosphoric acid. It has earlier been shown to be the case for aluminium, phosphate, water and phosphoric acid [50] and the conductivity data in Figure 69 suggests some water may

have been occupying some of the sites connected to the phosphate for the parent composition that had been refluxed in phosphoric acid.

In this work it has not always been practically feasible to make a clear distinction between the amorphous and crystalline phases, in such way that they can both be separated and tested separately for conductivity, etc. It was an assumption that the amorphous contribution was the same as the gel (or at least, very similar in composition), however, this is likely not the case. For if a gel was the cause for the protonic conductivity, then this would be reflected in a similar order of magnitude in conductivity for the gel compared to a hydrothermally treated solid sample – they are clearly different. Furthermore, from Figure 32 it is clear that although the amorphous contribution shows a broad peak in the ^{29}Si-NMR there is nothing correspondingly broad in the ^{31}P-NMR, thus the amorphous contribution is thought to be comprised of SiO_2 only.

Solid-state NMR needs to be done on the P-Si gels to fully understand differences and similarities to the hydrothermally treated silicon oxide phosphate system.

What can be said about the similarities between gel and hydrothermally treated phosphosilicates are that they both have the same elements (including water and phosphoric acid) and that their TG and DTA curves describe similar physical processes. The gels clearly showed higher mass losses than the hydrothermally treated compositions, even the extra high (P/Si 2.0 ratio) which had the lowest mass loss of the three gels, displayed a mass loss of 45 % which exceeds that of the hydrothermally treated compositions. An important point with the gels was that water was added to make the gels of similar consistency, therefore more water was added to the silica-rich gels which is why this shows the highest mass loss in the TGA.

There is a trend in the conductivity for the gels (higher P/Si ratio = better conductive behaviour), yet this is a bit different for hydrothermally treated solid materials. In any case, it can be concluded that the phosphoric acid (along with water) is what is responsible for the gels protonic conductivity.

The amorphous phase is not present to the same extent for all compositions. The greatest amorphous content was that of the silicon-rich samples, and when hydrothermally treated these showed overall lower conductivity compared to e.g.

$Si_5O(PO_4)_6$.

Regarding silicon oxide phosphate's function as a matrix for phosphoric acid, it has been shown that this is the case. In addition to this, it was discovered that the hydrothermal treatment induces phosphoric acid in the system, most likely from the phosphate units of the crystalline structure being in close proximity to water molecules. It remains to be studied the exact details of this mechanism.

Other questions that were emphasized were:

• Is there a solid-solution between SiO_2 and P_2O_5?

If yes, what are the properties and characteristics of the various compositions?

One definition of a solid solution is a *"mixture of two crystalline solids that coexist as a new crystalline solid, or crystal lattice."* [35]

Both the X-ray and neutron diffraction data show different cell parameters for different P/Si starting ratios, which strongly suggests the existence of new crystalline solids. Moreover, the conductivity data shows differing conductivities depending on the P/Si starting ratio.

Correlations can be made between the conductivity behaviour for the hydrothermally treated compositions and the unit cell parameters (a,b axes) of the untreated compositions, see Figure 61.

Furthermore, the ^{31}P NMR has the peak position (for the - 44 ppm chemical shift) in the untreated samples that correlates to the conductivity data for the hydrothermally treated compositions (Figure 62). This intrinsically ties the protonic conductivity to the $Si_5O(PO_4)_6$ crystalline lattice.

Moreover, if noting the temperatures at which the DTA peaks for the hydrothermally treated compositions occur, and these temperatures are plotted against the respective P/Si starting ratios, then the same pattern emerges as that for the conductivity when this too is plotted against the P/Si starting ratio, cf. Figure 62.

From the start it was also realized that the DTA peaks are linked to the two mass losses in the TG. These two mass losses, one occurring below 100°C and the other

occurring above 100°C occur as a result of previous hydrothermal treatment – because neither TG nor DTA peaks occur for the untreated samples in the low-temperature region, only the hydrothermally treated compositions show this behaviour.

At about 115°C conductivity starts to drop off as seen from the EIS measurements. The second DTA response occurs at a higher temperature (over 150°C), however it is likely directly linked to the drop in conductivity. Since impedance is measured on a much slower timescale compared to DTA, processes that occur with the latter technique register at higher temperatures because the ramp rate is higher compared to when things are measured at equilibrium (in the case of EIS).

Also for the first DTA curve this is the case, the DTA response occurs at about 60 – 90°C whereas the impedance shows a drop in conductivity just at the start of measurements (≈ 40°C).

The ^{2}H NMR for the hydrothermally treated compositions show a correlation in chemical shift relative to the second DTA peak for respective sample. As previously pointed out there was also a correspondence between the ^{1}H NMR for untreated compositions relative to ^{2}H NMR for hydrothermally treated compositions. This means hydrogen was present in the untreated samples (likely from air absorption), and is in the sample. When the hydrothermal treatment occurs, deuterium substitutes hydrogen – thus showing up in the ^{2}H NMR with similar relative chemical shift as for the ^{1}H NMR for the untreated. The proof for a change upon hydrothermal treatment can be derived from comparing the ^{1}H NMR for the untreated and post hydrothermally treated compositions. After hydrothermal treatment the chemical shift is much more well-defined as well as shifted – this indicates that the deuterium species is a part of the structure.

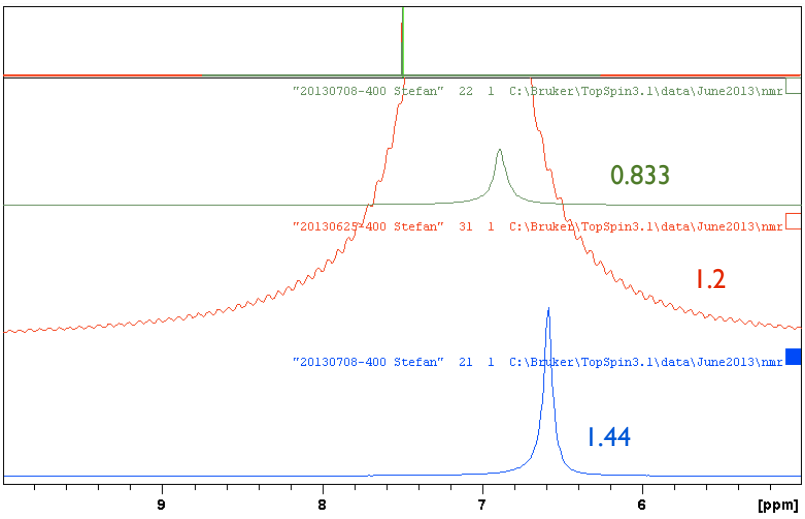

Figure 84 *^{2}H NMR spectra of the three hydrothermally treated (D_2O) P-Si compositions. The relative shift is similar to that in the previous figure. See Appendix F for scaled figure (parent composition did have a longer collection time for the ^{2}H scan, hence higher magnitude in peak).*

Figure 85 *^{1}H NMR spectra of the three untreated P-Si compositions. Note the difference in peak position for the chemical shifts.*

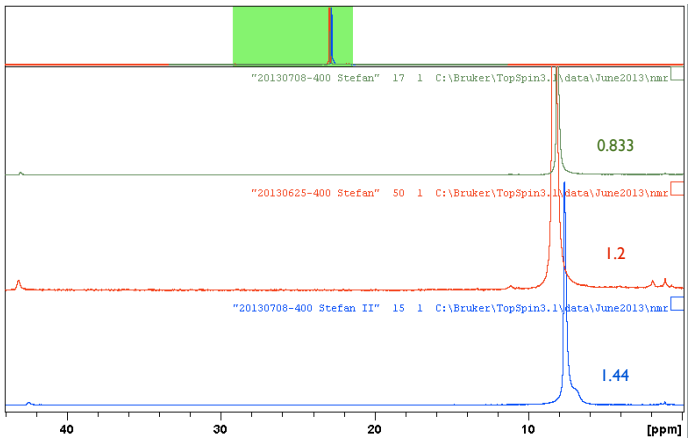

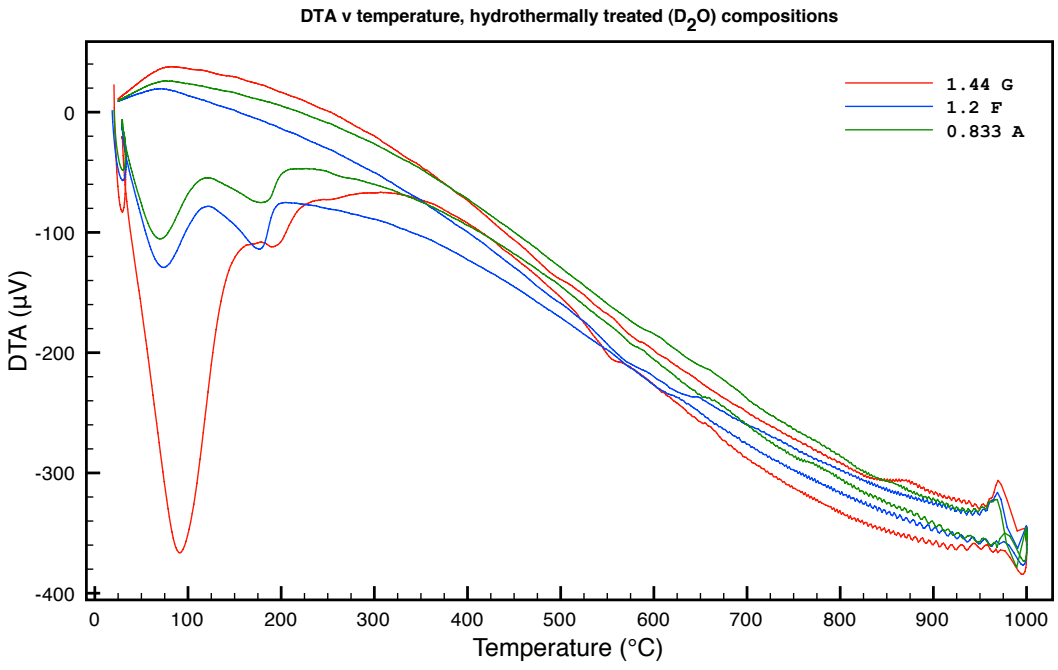

Figure 86 *DTA of the hydrothermally treated compositions as a function of temperature.*

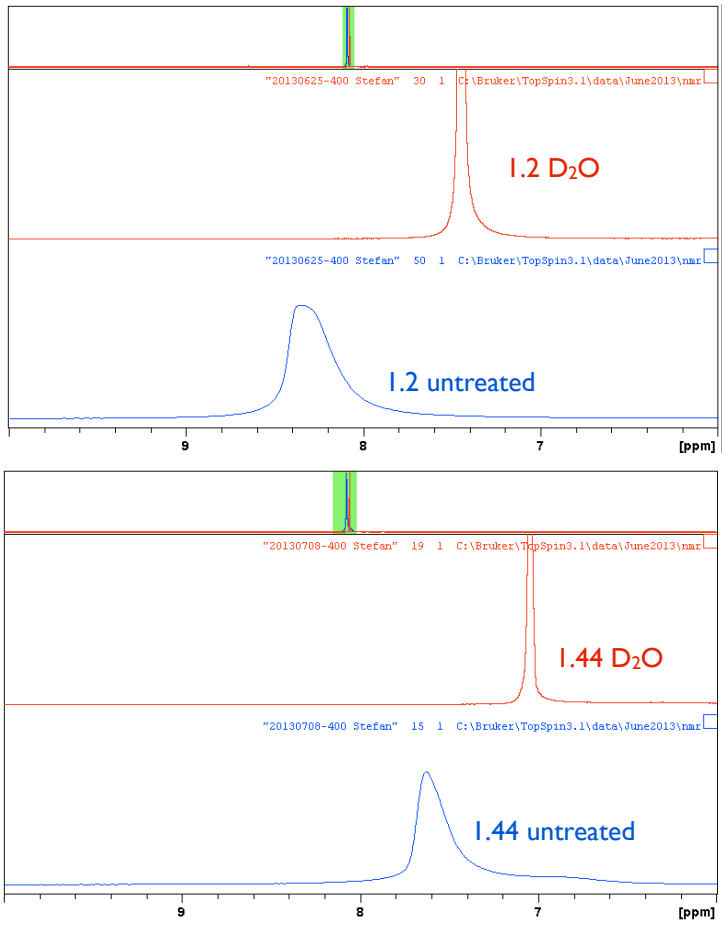

Figure 87 *Comparison of ^{1}H spectra for the parent composition (top) and the 1.44 (lower), hydrothermally treated with D_2O (red colour) v untreated (blue colour). Note the difference in peak shape as well as chemical shift.*

Furthermore, the refinement results revealed that one bond was significantly different compared to what was expected – namely, the P_O4 bond. Compared to Poojary's results this should have been much the same as the other phosphorus–oxygen bonds (1.52 Å), however in this project it was 1.57 Å, which set it apart from the other phosphorus–oxygen bonds which were as expected. This was the case for both untreated and hydrothermally treated samples, and if the previously mentioned results from the ^{2} H- and ^{1}H-NMR are taken into account, there appears to be a hydrogen in the structure. It is reasonable to suppose that this is a part of the P_O4 bond. This could be as a result of using H_3PO_4 as the phosphorus source, or it could be that the actual material does contain hydrogen, and it is just difficult to detect a small change in bond length using XRD, which is what Poojary's study used (since XRD looks at electron density, whereas neutrons pick up the actual nuclei positions).

This proton in the P_O4 bond is not sufficient to give proton conducting properties alone, however when hydrothermally treated or if phosphoric acid is in the material, then the P-Si material becomes proton conducting.

This all suggests that the protonic conductivity is a property dependent on a physical process involving an external species, specifically water (or phosphoric acid) in connection with the phosphate units. Small changes in the crystal lattice may be the cause of the different unit cell parameters and the differing chemical shifts in the ^{31}P NMR (- 44 ppm chemical shift). Most likely the different local phosphorus environment is what gives rise to the differences in conductivity when water (or phosphoric acid) becomes a part of the system. Thus, the whole system has become ternary and it is proton conductive in nature.

When adding 85% phosphoric acid to the P-Si system the drop in protonic conductivity starts at the same temperature as in the case of water. However, at this temperature there is over an order of magnitude of improved conductivity compared to the best performing hydrothermally treated composition (1.0) under the same conditions (EIS measured in air).

6.3 Summary of findings

This thesis demonstrates

• The first published solid-state synthesis of P-Si materials with varied composition (P/Si = 0.57 – 1.5), using starting ingredients of either SiO_2 and $NH_4H_2PO_4$ or SiO_2 and H_3PO_4.

• The phosphosilicate compositions that differ in stoichiometry also differ in unit cell parameters.

• The phosphate unit contains one P_O bond longer than the others (1.57 Å, compared to 1.50-1.53Å for the others), which in actuality could be a P_OH bond. This is for both untreated and hydrothermally treated samples. This means one of the bonds in the phosphate is protonated, and this can hold the key to understanding the conductivity when water or phosphoric acid is added.

• Hydrothermal treatment has an effect on the unit cell parameters of the respective P-

Si compositions, suggesting there is some substitution of elements as a result of hydrothermal treatment.

• Hydrothermal treatment increases the amount of amorphous background, as seen from the higher background in the neutron diffraction experiments, see Figure 50. This could be water in the channels.

• Hydrothermal treatment enables protonic conductivity, by addition of water to the crystalline lattice. According to ^{31}P NMR data phosphoric acid is activated in these compositions when water enters the structure, since there is a strong increase in the signal of the 0ppm chemical shift. It could be that the channels along the a, b axes hold the water and interact with the phosphate groups, and that the protonic conductivity goes along these channels. What supports this is the fact that larger a, b axes for the untreated samples yield higher conductivity when hydrothermally treated.

• The protonic conductivity differs depending on the P/Si starting ratio. The compositions that were rich in silicon tended to conduct worse than those closer to the P/Si ratio of 1.0.

• The protonic conductivity is boosted for the silicon-rich samples if they are treated with concentrated phosphoric acid, more so than when the parent $Si_5O(PO_4)_6$ undergoes the same treatment. This could be because the phosphorus-richer composition had adsorbed a bit of water already, and therefore some of the sites were already occupied by water. An experiment where fresh samples are made that are guaranteed not to have water could be done, and refluxed in concentrated phosphoric acid – this might yield different results.

• A method for measuring low temperature conductivity in phosphoric acid containing gels. The method is applicable as long as the gel is liquid. At higher temperatures it will crystallize and contract, thereby inhibiting contact. A modification could be possible to reduce the thickness of the material as it contracts, however one would have to monitor this thickness throughout the experiment. An option would be to increase the humidity.

• An interesting composition has been successfully synthesized, $Ge_3Si_2O(PO_4)_6$. This composition is between $Si_5O(PO_4)_6$ and $Ge_5O(PO_4)_6$ and has been previously reported

[71], however was now made through the method of using a phosphoric acid gel precursor.

When hydrothermally treated, the composition does display the same type of behaviour as the silicon analogue, although due to limited sample amount no conductivity data could be obtained. Apparent was that the first DTA peak occurred at a much higher temperature, 186°C, and it should therefore be of interest to measure the conductivity in its hydrothermally treated state.

There could also be a solid solution between SiO_2 and GeO_2. Attention to further research in this area deserves to be pursued, especially in connection with water being introduced and the conductivity studied.

6.4 Discussion

6.4.1 P-Si gels

In the search for an excellent protonic conductor, it would be natural to start with structure that can incorporate phosphoric acid, since liquid phosphoric acid has the highest intrinsic protonic conductivity of any known material at $\sigma \approx 0.15$ S cm^{-1} [72].

Phosphoric acid mixed with silica and water (forming the P-Si gel) proved to be a very good protonic conductor (the exception seemed to be the silica rich gel (P/Si = 0.57 which only produced very low conductivities). Gels having the P/Si ratios of 1.2 and 1.75 performed well and with reasonable conductivities in the low temperature region, at 0.069 and 0.08 S cm^{-1}, respectively, when tested in the Teflon setup. The latter was stable up to 100°C whereas the former only up to 70°C.

The main problem with the gels was the rapidly decreasing conductivities at low – intermediate temperatures. This was likely due to that the impedance measurements were only done in air for the P-Si gels and the lack of humidity severely dehydrated each gel. Future work should test conductivities in a humidified atmosphere to see if results show improvement in this temperature range.

Although only three compositions had been tested in the same setup, a relationship seems to be the case at about 100°C: the higher the P/Si ratio is the better conductivity

for the gel. This is not really surprising as it suggests that the concentration of phosphoric acid is what yields the protonic conductivity.

6.4.2 Substituted P-Si system

Generally for all the phosphosilicates tested here (both hydrothermally treated solids and P-Si gels) an increase in temperature would produce a decrease in protonic conductivity. The exception was the hydrothermally treated germanium oxide phosphate system – this increased in conductivity as temperature increased. It had a maximum of protonic conductivity at about 400°C (this is too low temperature to be oxygen conductivity). The conductivity could possibly be higher at slightly lower temperatures if silicon is incorporated into the structure, e.g. $Ge_3Si_2O(PO_4)_6$, and the material is hydrothermally treated. Incorporating phosphoric acid into a matrix like that is likely to cause even higher conductivities.

6.4.3 P-Si compositions

Looking instead to the hydrothermally treated solid compositions, it is clear that the conductivities of these samples do not follow that of the gels. Instead it seems to be linked to that of the length of the a and b axes of the untreated P-Si compositions. Therefore it is most likely not the amorphous phase that is the principal conductor, but rather the crystalline phase in combination with water.

Just sintering any P-Si composition and not hydrothermally treating it will not make a good conductor. However, when a high temperature sintered sample is hydrothermally treated (so that water can enter the structure) it will become proton conducting.

Best conductivity results were obtained when incorporating 85% phosphoric acid into a sintered pellet, and then using silver paste for electrodes. The reason conductivity was better in these cases compared to the hydrothermally treated samples could be because when the P-Si composition acts more as a matrix for the phosphoric acid the concentration of phosphoric is noticeably greater than it is in the case of hydrothermal treatment.

The reason why the Rietveld refinements were all done in accordance with the parent composition was to minimize the amount of variables. It was decided to refine the

neutron samples in the same manner – including keeping the same stoichiometry – so that any differences seen in the end result were down the uniqueness of each sample, instead of because that variations had been done in one sample's refinement which had not been done in another. In future work refinements will take into consideration differences in stoichiometry too.

One significant result that came about from keeping the refinements in the same way was the high temperature experiments for the two parent $Si_5O(PO_4)_6$. It was discovered that there indeed was a difference in coordinates for almost all atoms in the low temperature region, this is indicative of that water (D_2O in the actual case) does have an effect on the atoms' positioning in the crystalline lattice.

The total oxygen occupancy is a strong indication for a solid solution – since this goes up with increased P/Si ratio it means more negative charge to compensate for increased positive charge, indicative of more phosphorus (P^{+V}) substituting silicon (Si^{+IV}).

6.4.4 Proposed proton conducting mechanism

In this work an anomaly was found in the P_O4 bonds, as this was proved to be consistently longer compared to the other phosphorus–oxygen bonds, and also compared with what Poojary found for the P_O bond lengths [8]. It therefore becomes of interest to attempt to explain this anomaly. The suggestion is that there is a proton in the structure that makes the P_O4 bond a bit longer, and that this is important in order to understand the proton conductive nature once the material is hydrothermally treated.

Furthermore, correlation was found between the a,b axes for the untreated compositions compared to the conductivity for the hydrothermally treated – the longer the a,b axes the better the conductivity.

In Figure 88 a three unit cell deep and two unit cell high model of the parent composition is illustrated – the green atoms are O4 oxygens, red atoms are all other oxygens, purple atoms are phosphorus and turquoise atoms are Si3. The a-axis goes up, the c-axis is almost in the plane of the paper – the b-axis almost perpendicular to the plane of the paper coming out towards the reader. The figure's perspective is

slightly tilted so that that the channel structure becomes clear.

In the following figure the perspective changes to looking along the side of the channels, perpendicular to the c-axis, see Figure 89.

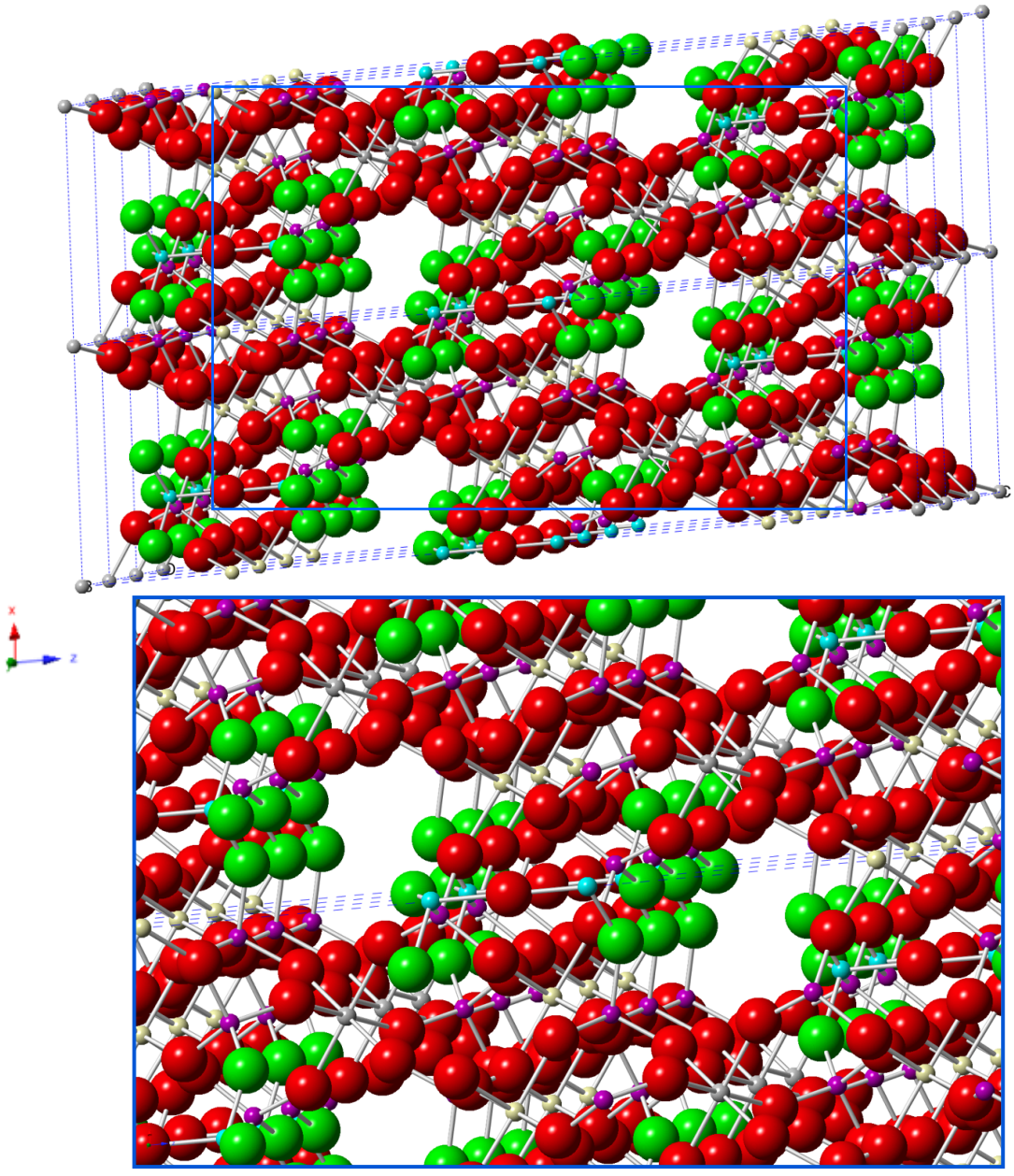

Figure 88 *View of six unit cells of the parent composition (top) looking almost perpendicular down the b-axis. Green colour is for the O4 oxygens, red is all other oxygens, purple is phosphorus and turquoise is tetrahedral silicon (Si3), grey is Si1 and light yellow is Si2. The bottom picture is the same view only a bit enlarged to see the channels in more detail.*

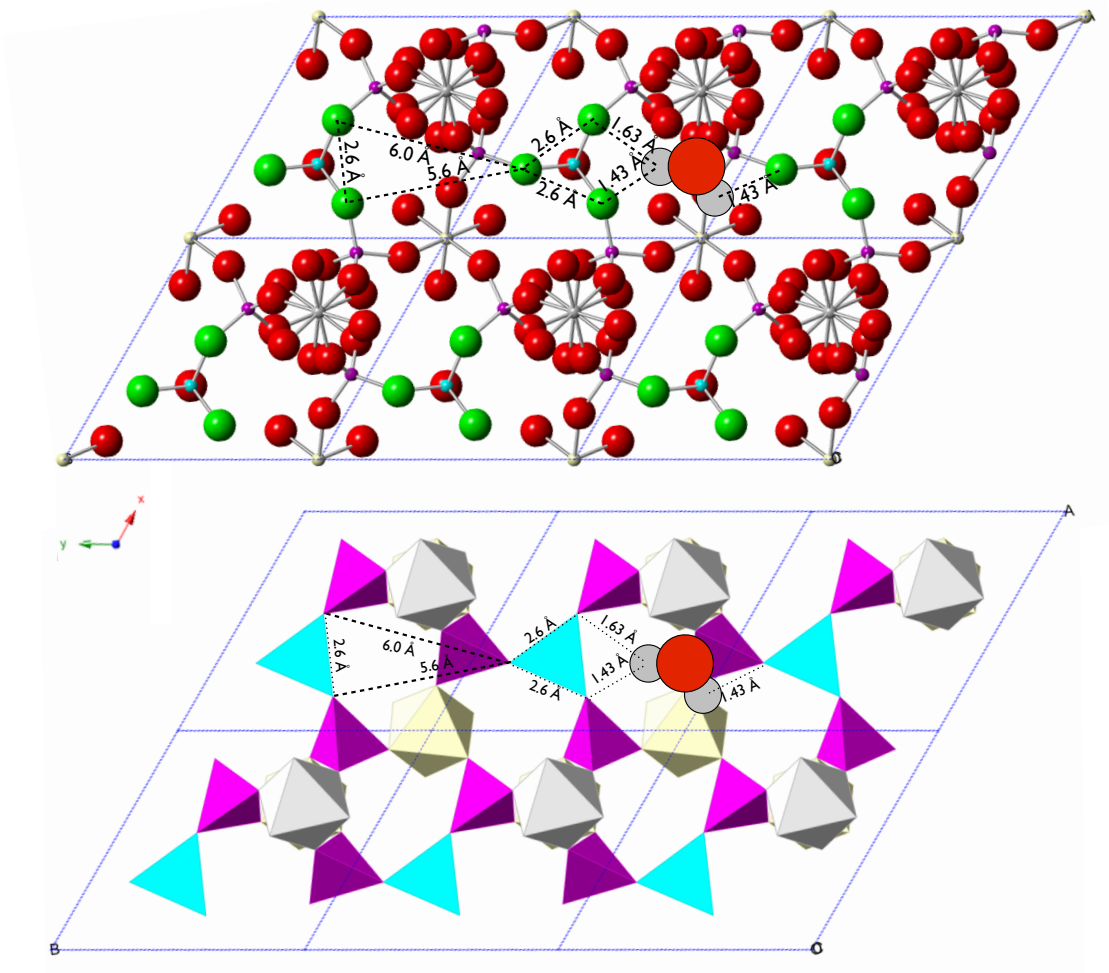

Figure 89 *A cross-section through six unit cells along where the channels run, b-axis running toward left (this is a slice of the same area as in the previous figure, only now viewed perpendicular to the c-axis). Top of figure has O4 oxygen atoms in green colour, remaining oxygens are red, phosphorus is purple and Si3 is turquoise. Bottom part of the figure show the same view but with polyhedra instead (phosphorus tetrahedra purple, Si3 tetrahedra turquoise, Si1 octahedra are grey and Si2 octahedra are light yellow).*

The shortest distance between two Si3 tetrahedra measured from an O4 to the O4 of the neighbouring Si3 tetrahedra, along the b channel, is approximately 5.6 Å. This is the longest distance to travel between two O4s and the hardest part of the way. The next part is only 2.6 Å, i.e. between two O4s linked to the same silicon, these two O4s are also individually linked to each their phosphorus).

If however there are water molecules present in these channels and a water molecule is bridging the distance between the two O4 oxygens of the different silicon tetrahedras in question, then it is likely that a proton transfer network throughout the channels can be facilitated. A water molecule has a diameter of about 2.75 Å [73], so if optimally situated the proton would only have to travel tentatively at least 1.43 Å when leaving an O4 site to go to the water molecule (and then the same distance when

leaving it to go to the next O4 linked to a phosphorus). The water molecules will act as bridges for the hydrogen and enable two separate pathways along each channel.

The second pathway will be on the opposite side of the channel wall, see Figure 91 and Figure 90. In Figure 91 the perspective is shifted 180 degrees to that of Figure 89, looking along the c-axis in the opposite direction. Although it looks a bit different opposite side of the channel wall, the same principle could apply here too. A water can bridge the longer distance between two P_OH species and thereby enable a proton conducting network.

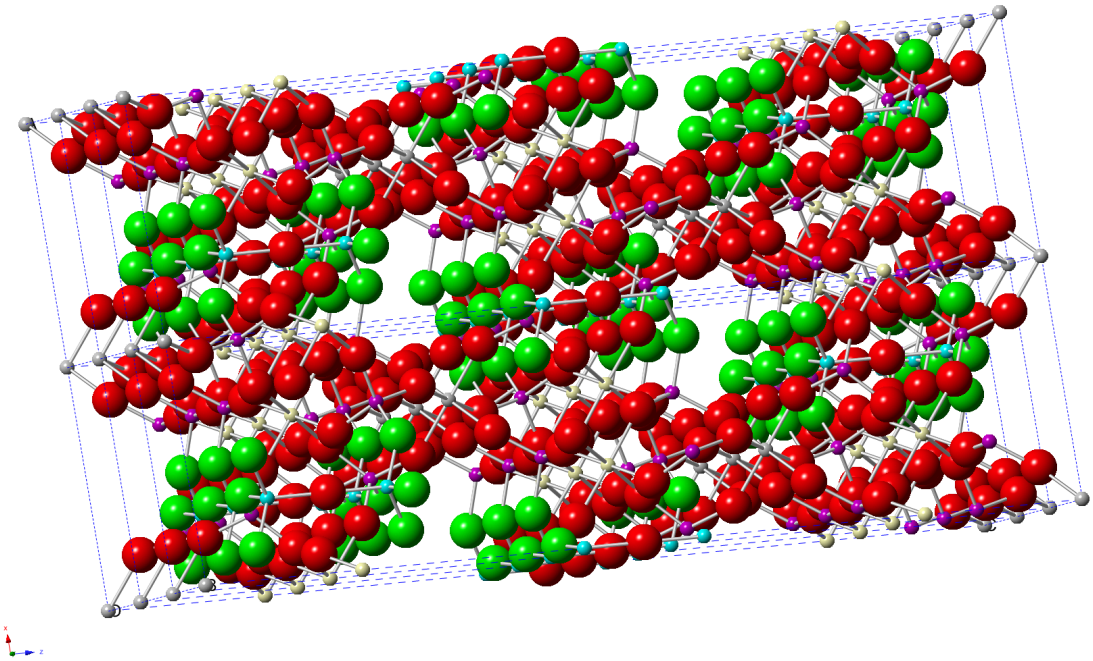

Figure 90 *The channel structure viewed almost perpendicular to the b-axis, only seen from the other side (model moved right relative to viewer compared to* **Figure 88***). Colour code as in previous figure.*

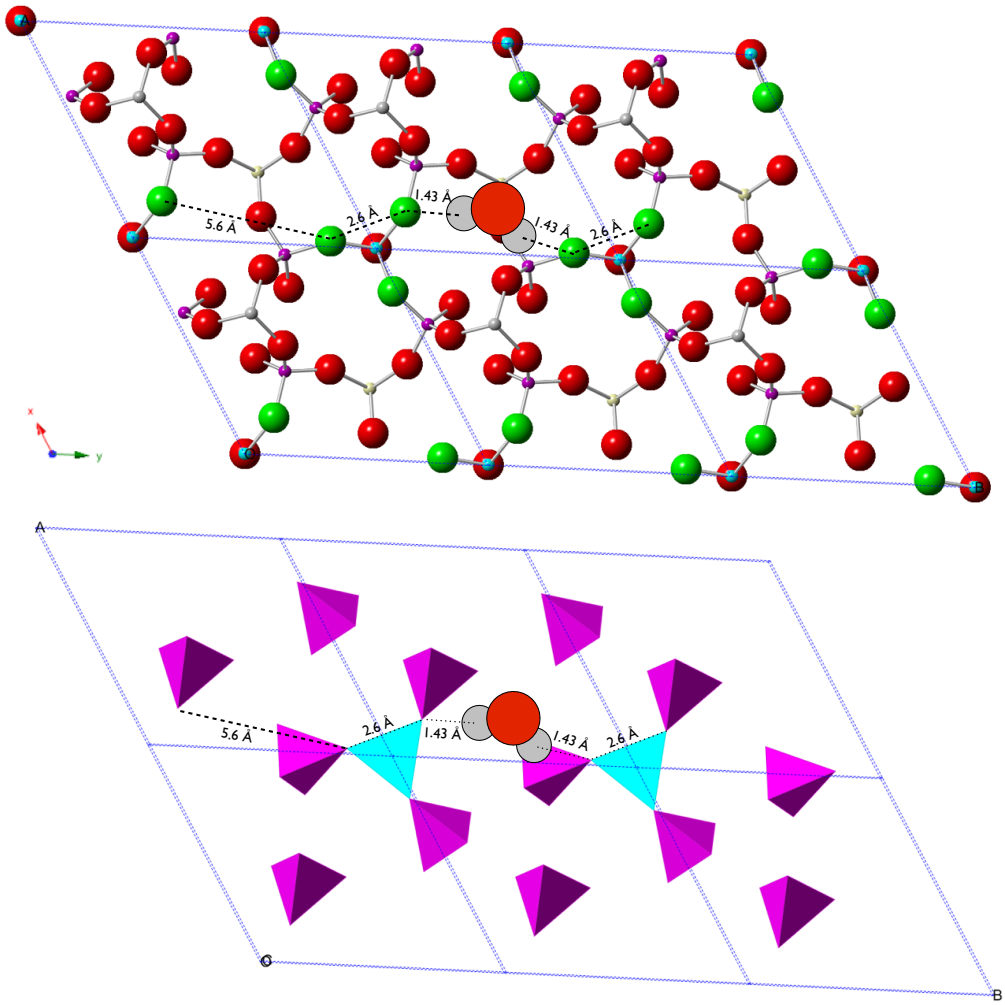

Figure 91 *A cross-section through six unit cells along where the channels run, b-axis running toward right (this is the opposite side of the channels compared to* **Figure 89***). Top of figure has O4 oxygen atoms in green colour, remaining oxygens are red, phosphorus is purple and Si3 is turquoise. Bottom part of the figure show the same view but with polyhedra instead (phosphorus tetrahedra purple and Si3 tetrahedra turquoise)*

Moreover, the available space in these channels is very close to that of the size of a water molecule, and this could explain why hydrothermal treatment is the most suited method for getting water into these channel structures.

The length of the channels depends on the length of the a,b axes – and this does matter when it comes to protonic conductivity. For a smaller a,b axes it will be more difficult to make the water molecules arrange in an optimal way, however for larger unit cells it will be easier. This is perhaps why the protonic conductivity depends on the size of the a,b, axes.

If the theory is correct that protonic conductivity is mainly along the channel structure then this can explain the observed behaviour in conductivity. At start the conductivity was very high (water present conducting protons via both sides of the channels), and then it started to drop as temperature increased. It reached a local minimum at 60°C and then began to increase somewhat. Below 60°C for the conductivity (where the DTA registers the first peak at 71°C) is where the first water inside of the channels is lost. This is the weakest bound of the two water molecules.

Then at about 90°C there is a maximum in conductivity and above that there is a small decline to about 115°C. Between 90 to 115°C could be where the second water is starting to leave the channels (picked up by the DTA at 156°C).

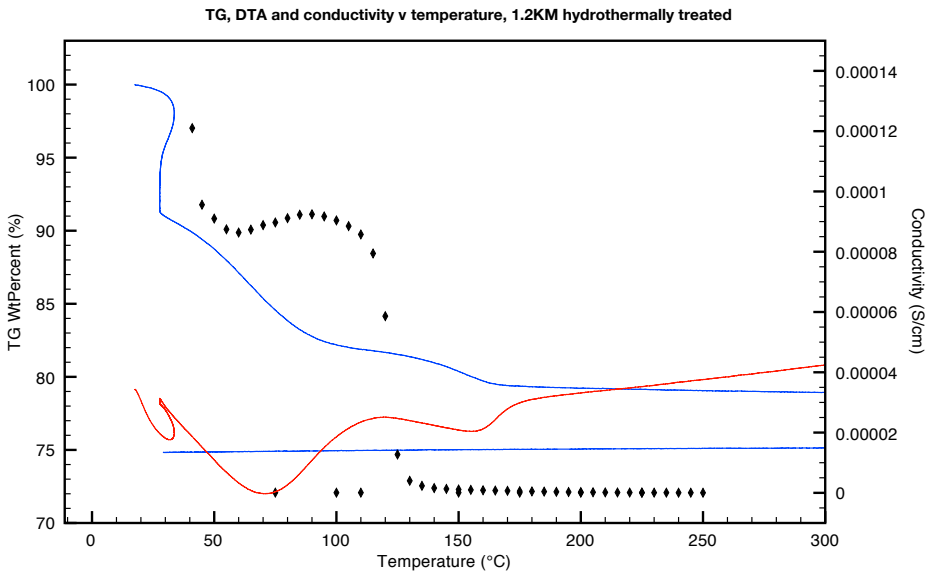

Figure 92 *TG (blue line) and DTA data (red line) and low temperature conductivity (black dots) plotted against temperature for hydrothermally treated parent composition. All measurements were done in air.*

Although the materials synthesised did not qualify for filling the low-intermediate temperature gap for protonic conductors, this thesis has shown that silicon oxide phosphate is a good starting point for designing a proton conductor that can run at higher temperatures than current low temperature options. Even if only an operating temperature of around 150-200°C was reached this would still be a good outcome. These types of materials are novel types of protonic conductors that consist of ubiquitous elements, and they would be suitable for fuel cell applications. More research should be done especially regarding incorporation of germanium to expand the lattice, and evaluate further its potential as a matrix for phosphoric acid, or perhaps other acids and how this will affect conductivity.

References

1. *Neutron Cross Section of the elements*. Available from: http://www.periodictable.com/Properties/A/NeutronCrossSection.html.
2. Robbins, C.R., E.M. Levin, and H.F. McMurdie, *Phase diagrams for ceramists, Volume 11*. Vol. 11. 1964: American Ceramic Society.
3. Maddison, A. *Statistics on World Population, GDP and Per Capita GDP, 1-2008 AD (Vertical file, copyright Angus Maddison, university of Groningen)*. Available from: http://www.ggdc.net/MADDISON/oriindex.htm.
4. Norby, T., *Solid-state protonic conductors: principles, properties, progress and prospects.* Solid State Ionics, 1999. **125**.
5. Yuan, X.-Z., et al., *Electrochemical Impedance Spectroscopy in PEM Fuel Cells Fundamentals and Applications*. 2010, Springer.
6. Benichou, L. and T. team. *The Shift Project, Data Portal*. 17 March 2015]; Available from: http://www.tsp-data-portal.org/Energy-Production-Statistics.
7. Hannon, A.C., *Results on disordered materials from the General Materials diffractometer, GEM, at ISIS.* Nuclear Instruments and Methods in Physics Research A, 2005. **551**: p. 88–107.
8. Poojary, D.M., R.B. Borade, and A. Clearfield, *Structural characterization of silicon orthophosphate.* Inorganica Chimica Acta, 1993. **208**(1): p. 23-29.
9. Grove, W.R., *On a Gaseous Voltaic Battery.* The London, Edinburgh and Dublin Philosphical Magazine and Journal of Science, 1842. **XXI**(July – December 1842): p. 417-420.
10. Perry, M.L. and T.F. Fuller, *A Historical Perspective of Fuel Cell Technology in the 20th Century.* Journal of The Electrochemical Society, 2002. **149**: p. S59-S67.
11. *When the grid fails*. 2013; Available from: www.fuelcells.org/uploads/Fuel-Cells-in-Storms.pdf.
12. Diercks, R., et al., *Raw Material Changes in the Chemical Industry.* Chem. Eng. Technol., 2008. **31**(5): p. 631-637.
13. EG&G Technical Services, I., *Fuel Cell Handbook*. 2004, U.S. Department of Energy, Office of Fossil Energy, National Energy Technology Laboratory.
14. Malnick, E., *£11m for the wind farm that was not working*, in *The Telegraph*. 2014.
15. Loisel, R., et al., *Economic evaluation of hybrid off-shore wind power and hydrogen storage system.* International Journal of Hydrogen Energy, 2015. **XXX**.
16. EveryMac.com. *http://www.everymac.com/systems/apple/macbook-air/macbook-air-faq/macbook-air-mid-2013-real-world-battery-life.html*. MacBook Air Q&A - Updated April 3, 2015 2015 April 3, 2015 April 24, 2015]; What is the battery life of the "Mid-2013," "Early 2014" and "Early 2015" MacBook Air models in "real-world" usage tests? Is it really as long as Apple claims?].
17. *http://applemuseum.bott.org/sections/computers/macport.html*. Macintosh Portable 24 April 2015].

18. Spare, B.L., et al., *Fuel cell system to power a portable computing device*, in *http://www.freepatentsonline.com/20110311895.pdf*. 2010, Apple Inc.
19. Iyer, V.M. and B.L. Spare, *Fuel cell system coupled to a portable computing device*, in *http://www.freepatentsonline.com/20110313589.pdf*. 2011, Apple Inc.
20. Jackson, P. and L. Smith, *Exploring the undulating plateau: the future of global oil supply.* Phil. Trans. R. Soc. A, 2014. **372**.
21. Alazemi, J. and J. Andrews, *Automotive hydrogen fuelling stations: An international review.* Renewable and Sustainable Energy Rewiews, 2015. **48**: p. 483-499.
22. Wise, J. *The Truth About Hydrogen*. 2006 [cited 2013 25 July]; Available from: www.popularmechanics.com/science/energy/a926/4199381/.
23. Royle, M. and D. Willoughby, *The safety of the future hydrogen economy.* Process Safety and Environmental Protection, 2011. **89**: p. 452-462.
24. Anstrom, J., *Hydrogen as a fuel in transportation*, in *Advances in Hydrogen Production, Storage and Distribution*. 2014. p. 499-524.
25. Yadav, M. and Q. Xu, *Liquid-phase chemical hydrogen storage materials.* Energy Environ. Sci., 2012. **5**: p. 9698-9725.
26. Press, T.A., *Hydrogen Fuel Cell Cars To Be Researched By Ford, Daimler And Nissan Partnership*, in *Huffington post*. 2013, http://www.huffingtonpost.com.
27. Kaiser, T., *Ballard Power Systems to Make Fuel Cells for Volkswagen*, in *DailyTech*. 2013, http://www.dailytech.com.
28. Fogelson, J., *Toyota To Share Hydrogen Fuel Cell Patents*, in *Forbes / Lifestyle*. 2015, Forbes.
29. *Fuel Cell Vehicles vs. Battery-Powered Vehicles*. 2011 October 2011; Available from: http://www.fuelcells.org/uploads/Electric-Vehicles.pdf.
30. The Guardian, M. *Toyota to begin selling hydrogen fuel cell car Mirai for first time*. 2014.
31. Edelstein, S. *Hyundai Tucson Fuel Cell Price Slashed In Korea; 200 Delivered Globally So Far*. http://www.greencarreports.com/news/1096615_hyundai-tucson-fuel-cell-price-slashed-in-korea-200-delivered-globally-so-far 2015.
32. Hyundai. *ix35 Fuel Cell*. http://worldwide.hyundai.com/WW/Showroom/Eco/ix35-Fuel-Cell/PIP/index.html 27 April 2015].
33. Ross, J. *Hyundai ix35 Fuel Cell Drives 435 Miles on a Tank of Hydrogen Fuel*. http://www.autoevolution.com/news/hyundai-ix35-fuel-cell-drives-435-miles-on-a-tank-of-hydrogen-fuel-83810.html 2014.
34. St. John, J., *Could This Be the Fuel Cell to Beat All Fuel Cells?*, in *http://www.greentechmedia.com*. 2013.
35. Perkowitz, S., *Solid solution*, in *Encyclopædia Britannica*.
36. Yang, Y., et al., *Structural and Morphological Features of Acid-Bearing Polymers for PEM Fuel Cells.* Adv Polym Sci, 2008. **215**: p. 55–126.
37. Wu, J., et al., *A review of PEM fuel cell durability: Degradation mechanisms and mitigation strategies.* Journal of Power Sources, 2008. **184**: p. 104–119.

38. Li, Q., et al., *Approaches and Recent Development of Polymer Electrolyte Membranes for Fuel Cells Operating above 100°C.* Chem. Mater., 2003. **15**: p. 4896-4915.
39. Matsui, T., et al., *Development of Novel Proton Conductors Consisting of Solid Acid/pyrophosphate Composite for Intermediate-temperature Fuel Cells.* Journal of the Japan Petroleum Institute, 2010. **53**: p. 1-11.
40. Dhathathreyan, K.S. and N. Rajalakshmi, *3: Polymer Electrolyte Membrane Fuel Cell*, in *Recent Trends in Fuel Cell Science and Technology*, S. Basu, Editor, Anamaya Publishers: New Delhi.
41. Pettersson, L.J. and R. Westerholm, *State of the art of multi-fuel reformers for fuel cell vehicles: problem identication and research needs.* International Journal of Hydrogen Energy, 2001. **26**: p. 243-264.
42. Bashyam, R. and P. Zelenay, *A class of non-precious metal composite catalysts for fuel cells.* Nature, 2006. **443**: p. 63-66.
43. *Solid Oxide Fuels Cells: Facts and Figures: Past Present and Future Perspectives for SOFC Technologies (Green Energy and Technology)*. Green Energy and Technology, ed. J.T.S. Irvine and P. Connor. 2013, London: Springer-Verlag.
44. Dupree, R., D. Holland, and M.G. Mortuza, *Six-coordinated silicon in glasses.* Nature, 1987. **328**: p. 416-417.
45. Tofield, B.C., et al., *Novel phosphosilicate.* Nature, 1974. **253**: p. 722-723.
46. Liebau, V.F., G. Bissert, and N. Köppen, *Synthese und kristallographische Eigenschaften einiger Phasen im System Si02-P205.* Zeit schrift für anorganiscbe und allgemeine Chemie, 1968. **359**: p. 113-224.
47. Krawietz, T.R., et al., *Solid Phosphoric Acid Catalyst: A Multinuclear NMR and Theoretical Study.* J. Am. Chem. Soc., 1998. **120**: p. 8502-8511.
48. Coelho, C., et al., *Efficiency of the Refocused 31P-29Si MAS-J-INEPT NMR Experiment for the Characterization of Silicophosphate Crystalline Phases and Amorphous Gels.* Inorg. Chem., 2007. **46**: p. 1379-1387.
49. Kniep, R., *Orthophosphates in the Ternary System AI2O3-P2O5-H20.* Angew. Chem Int. Ed. Engl., 1986. **25**: p. 525-534.
50. Brosheer, J.C., F.A. Lenfesty, and J.F. Anderson Jr., *Solubility in the System Aluminum Phosphate-Phosphoric Acid-Water.* J. Am. Chem. Soc., 1954. **76**: p. 5951–5956.
51. Matsuda, A., et al., *Medium temperature range characterization as a proton conductor for phosphosilicate dry gels containing large amounts of phosphorus.* Electrochimica Acta, 2001. **47**(6): p. 939-944.
52. Tadanaga, K., et al., *Structural change and proton conductivity of phosphosilicate gel–polyimide composite membrane for a fuel cell operated at 180 °C.* Journal of Membrane Science, 2008. **324**(324): p. 188-191.
53. Nakamoto, N., et al., *Medium temperature operation of fuel cells using thermally stable proton-conducting composite sheets composed of phosphosilicate gel and polyimide.* Journal of Power Sources, 2004. **138**(1-2): p. 51-55.
54. Nogami, M., K. Miyamura, and Y. Abe, *Fast Protonic Conductors of Water-Containing P205-Zr02-Si02 Glasses.* J. Electrochem. Soc., 1997. **144**(6): p. 2175-2178.

55. Poojary, D.M., et al., *Crystal Structure of Silicon Pyrophosphate (Form I) from Powder Diffraction Data.* Journal of Solid State Chemistry, 1994. **112**: p. 106-112.
56. Jin, Y., Y. Shen, and T. Hibino, *Proton conduction in metal pyrophosphates (MP2O7) at intermediate temperatures.* J. Mater. Chem., 2010. **20**: p. 6214–6217.
57. Matsui, T., et al., *Intermediate-Temperature Fuel Cell Employing CsH2PO4/SiP2O7-Based Composite Electrolytes.* Journal of The Electrochemical Society, 2006. **153**: p. A339-A342.
58. Slater, P.R., J.E.H. Sansom, and J.R. Tolchard, *Development of Apatite-Type Oxide Ion Conductors.* The Chemical Record, 2004. **4**: p. 373-384.
59. West, A.R., *Basic Solid State Chemistry*. 2nd ed. 2000: John Wiley & Sons, Ltd.
60. Lejeune, C., et al., *Studies of silicophosphate derivatives by P-31 -> Si-29 CP MAS NMR.* Solid State Nuclear Magnetic Resonance, 2005. **27**(4): p. 242-246.
61. Coelho, C., et al., *Application of the MAS-J-HMQC experiment to a new pair of nuclei {29Si,31P}: Si5O(PO4)6 and SiP2O7 polymorphs.* Journal of Magnetic Resonance, 2006. **179**: p. 114-119.
62. Irvine, J.T.S., D.C. Sinclair, and A.R. West, *Electroceramics: Characterization by Impedance Spectroscopy.* Advanced Materials, 1990. **2**: p. 132-138.
63. (1989) *Silicon Phosphate, PDF card 00-040-0457*.
64. Gottlieb, H.E., V. Kotlyar, and A. Nudelman, *NMR Chemical Shifts of Common Laboratory Solvents as Trace Impurities.* J. Org. Chem., 1997. **62**: p. 7512-7515.
65. Nowlan, C., et al., *Resolution of Chiral Phosphate, Phosphonate, and Phosphinate Esters by an Enantioselective Enzyme Library.* J. Am. Chem. Soc., 2006. **128**: p. 15892-15902.
66. Shannon, R.D., *Revised Effective Ionic Radii and Systematic Studies of Interatomie Distances in Halides and Chaleogenides.* Acta Crystallographica, 1976. **A 32**: p. 751-767.
67. Maltezou, E., et al., *Synthesis, Solution, and Structural Characterization of Tetrahydrofuranyl-2,2-Bisphosphonic Acid Disodium Salt.* Bioinorganic Chemistry and Applications, 2010. **2010**(Article ID 563875).
68. *Sequential GSAS*. 1 May 2012, at 22:08; Available from: https://wiki-ext.aps.anl.gov/ug11bm/index.php/Sequential_GSAS.
69. Zhang, Y., *Exploring Novel Functionalities in Oxide Ion Conductors with Excess Oxygen*. 2011, University of St Andrews.
70. Safety, I.I.P.o.C. *Phosphoric acid*. October 2005 5 May 2015].
71. Leclaire, A. and B. Raveau, *Ge3P6Si2O25: A Cage Structure Closely Related to the Intersecting Tunnel Structure KMo3P6Si2O25.* Journal of Solid State Chemistry, 1988. **75**: p. 397-402.
72. Vilčiauskas, L., et al., *The mechanism of proton conduction in phosphoric acid.* Nature chemistry, 2012. **4**: p. 461-466.
73. Chaplin, M. *Water Molecule Structure*. http://www1.lsbu.ac.uk/water/water_molecule.html 2014.

Appendix A1

Bond lengths from Rietveld refinement of neutron data, P/Si = 0.833

GEM63215_A_6 mm_0.833A_D2 O_3h	Structure	Bond length (Å)	Number of bonds	Angle between atoms	Angle (°)	Number of angles
0.833 D_2O	**Si octahedra**					
	Si1_O3	1.75268(14)	6 x	O3_Si1_O3	180.000(0)	3 x
				O3_Si1_O3	91.684(6)	6 x
				O3_Si1_O3	88.316(6)	6 x
	Si octahedra					
	Si2_O2	1.77518(15)	3 x	O2_Si2_O2	90.548(6)	3 x
	Si2_O5	1.74823(14)	3 x	O5_Si2_O2	89.417(6)	3 x
				O5_Si2_O2	180.000(0)	3 x
				O5_Si2_O2	89.858(6)	3 x
				O5_Si2_O5	90.178(6)	3 x
	Si tetrahedra					
	Si3_O1	1.64485(18)	1 x	O4_Si3_O1	108.529(3)	3 x
	Si3_O4	1.57594(16)	3 x	O4_Si3_O4	110.397(3)	3 x
	Phosphate group					
	P_O2	1.53485(12)		O3_P_O2	114.031(7)	
	P_O3	1.50297(12)		O4_P_O2	105.807(2)	
	P_O4	1.56684(16)		O5_P_O2	112.020(6)	
	P_O5	1.50408(15)		O4_P_O3	108.847(6)	
				O5_P_O3	106.874(3)	
				O5_P_O4	109.175(1)	

GEM63213_818_0. 833A_dry_8mm	Structure	Bond length (Å)	Number of bonds	Angle between atoms	Angle (°)	Number of angles
0.833 untreated	**Si octahedra**					
	Si1_O3	1.75441(13)	6 x	O3_Si1_O3	180.000(0)	3 x
				O3_Si1_O3	91.705(5)	6 x
				O3_Si1_O3	88.295(5)	6 x
	Si octahedra					
	Si2_O2	1.77909(13)	3 x	O2_Si2_O2	90.310(5)	3 x
	Si2_O5	1.74211(12)	3 x	O5_Si2_O2	89.475(5)	3 x
				O5_Si2_O2	89.905(5)	3 x
				O5_Si2_O2	180.000(0)	3 x
				O5_Si2_O5	90.311(5)	3 x
	Si tetrahedra					
	O1_Si3	1.63416(16)	1 x	O4_Si3_O1	108.973(2)	3 x
	O4_Si3	1.58339(14)	3 x	O4_Si3_O4	109.965(2)	3 x
	Phosphate group					
	P_O2	1.53478(10)		O3_P_O2	113.958(6)	
	P_O3	1.50290(11)		O4_P_O2	105.752(1)	
	P_O4	1.56585(14)		O5_P_O2	112.025(6)	
	P_O5	1.50638(13)		O4_P_O3	108.829(5)	
				O5_P_O3	107.000(2)	
				O5_P_O4	109.190(1)	

Bond lengths from Rietveld refinement of neutron data, P/Si = 1.2

GEM63222_HiT2_RT _start	Structure	Bond length (Å)	Number of bonds	Angle between atoms	Angle (°)	Number of angles
1.2 D_2O	**Si octahedra**					
	Si1_O3	1.77004(33)	6 x	O3_Si1_O3	180.000(0)	3 x
				O3_Si1_O3	92.261(13)	6 x
				O3_Si1_O3	87.739(13)	6 x
	Si octahedra					
	Si2_O2	1.75134(33)	3 x	O2_Si2_O2	92.541(13)	3 x
	Si2_O5	1.79262(33)	3 x	O5_Si2_O2	88.520(13)	3 x
				O5_Si2_O2	177.013(0)	3 x
				O5_Si2_O2	90.201(13)	3 x
				O5_Si2_O5	88.684(14)	3 x
	Si tetrahedra					
	Si3_O1	1.6708(4)	1 x	O4_Si3_O1	107.495(6)	3 x
	Si3_O4	1.5672(4)	3 x	O4_Si3_O4	111.373(5)	3 x
	Phosphate group					
	P_O2	1.51895(27)		O3_P_O2	116.228(15)	
	P_O3	1.51772(29)		O4_P_O2	107.846(3)	
	P_O4	1.5709(4)		O5_P_O2	112.049(14)	
	P_O5	1.53273(35)		O4_P_O3	108.645(13)	
				O5_P_O3	103.222(6)	
				O5_P_O4	108.590(2)	

GEM63046_HiT1_RT _start	Structure	Bond length (Å)	Number of bonds	Angle between atoms	Angle (°)	Number of angles
1.2 untreated	**Si octahedra**					
	Si1_O3	1.76158(23)	6 x	O3_Si1_O3	180.000(0)	3 x
				O3_Si1_O3	92.162(9)	6 x
				O3_Si1_O3	87.838(9)	6 x
	Si octahedra					
	Si2_O2	1.76052(23)	3 x	O2_Si2_O2	91.625(9)	3 x
	Si2_O5	1.76820(22)	3 x	O5_Si2_O2	89.078(9)	3 x
				O5_Si2_O2	90.088(9)	3 x
				O5_Si2_O2	178.129(0)	3 x
				O5_Si2_O5	89.187(9)	3 x
	Si tetrahedra					
	O1_Si3	1.64853(28)	1 x	O4_Si3_O1	108.332(4)	3 x
	O4_Si3	1.57313(24)	3 x	O4_Si3_O4	110.586(4)	3 x
	Phosphate group					
	P_O2	1.52241(18)		O3_P_O2	115.249(11)	
	P_O3	1.50863(20)		O4_P_O2	106.736(2)	
	P_O4	1.56934(25)		O5_P_O2	112.297(10)	
	P_O5	1.51690(24)		O4_P_O3	108.598(9)	
				O5_P_O3	104.982(4)	
				O5_P_O4	108.829(1)	

Bond lengths from Rietveld refinement of neutron data, P/Si = 1.44

GEM63416_1.44G with D2O 8mm (pos 15)	Structure	Bond length (Å)	Number of bonds	Angle between atoms	Angle (°)	Number of angles
1.44 D_2O	**Si octahedra**					
	Si1_O3	1.75587(12)	6 x	O3_Si1_O3	180.000(0)	3 x
				O3_Si1_O3	91.991(5)	6 x
				O3_Si1_O3	88.009(5)	6 x
	Si octahedra					
	Si2_O2	1.77967(12)	3 x	O2_Si2_O2	90.305(5)	3 x
	Si2_O5	1.75049(12)	3 x	O5_Si2_O2	89.882(5)	3 x
				O5_Si2_O2	180.000(0)	3 x
				O5_Si2_O2	89.889(5)	3 x
				O5_Si2_O5	89.923(5)	3 x
	Si tetrahedra					
	Si3_O1	1.60189(14)	1 x	O4_Si3_O1	110.080(2)	3 x
	Si3_O4	1.59728(13)	3 x	O4_Si3_O4	108.856(2)	3 x
	Phosphate group					
	P_O2	1.53034(10)		O3_P_O2	113.830(6)	
	P_O3	1.51110(10)		O4_P_O2	105.374(1)	
	P_O4	1.57079(13)		O5_P_O2	113.104(5)	
	P_O5	1.49647(12)		O4_P_O3	108.310(5)	
				O5_P_O3	106.850(2)	
				O5_P_O4	109.240(1)	

GEM63214_831_1, 44G_dry	Structure	Bond length (Å)	Number of bonds	Angle between atoms	Angle (°)	Number of angles
1.44 untreated	**Si octahedra**					
	Si1_O3	1.75577(12)	6 x	O3_Si1_O3	180.000(0)	3 x
				O3_Si1_O3	92.039(5)	6 x
				O3_Si1_O3	87.961(5)	6 x
	Si octahedra					
	Si2_O2	1.78066(12)	3 x	O2_Si2_O2	90.424(5)	3 x
	Si2_O5	1.75342(12)	3 x	O5_Si2_O2	89.892(5)	3 x
				O5_Si2_O2	89.939(5)	3 x
				O5_Si2_O2	180.000(0)	3 x
				O5_Si2_O5	89.742(5)	3 x
	Si tetrahedra					
	Si3_O1	1.60865(15)	1 x	O4_Si3_O1	109.974(2)	3 x
	Si3_O4	1.59854(13)	3 x	O4_Si3_O4	108.964(2)	3 x
	Phosphate group					
	P_O2	1.52306(10)		O3_P_O2	113.903(6)	
	P_O3	1.51615(11)		O4_P_O2	105.631(1)	
	P_O4	1.57083(14)		O5_P_O2	113.281(5)	
	P_O5	1.49801(13)		O4_P_O3	108.154(5)	
				O5_P_O3	106.556(2)	
				O5_P_O4	109.171(1)	

Appendix A2

Summary of Rietveld refinements from neutron data, P/Si = 0.833

Fixed occupancies

GEM63215_A_6mm_0.833A_D2O_3h_FixedF 11Feb2014	Name	X	Y	Z	Ui/Ue*100	Site sym	Mult	Type	Seq	Fractn
0.833 D_2O	O5	0.45773(22)	0.25072(20)	0.11153(6)	0.514(33)	1	18	O	1	1.0000
	O4	0.35648(21)	0.48880(19)	0.07780(7)	0.755(35)	1	18	O	2	1.0000
	O3	0.20796(24)	0.14672(22)	0.04066(8)	0.737(40)	1	18	O	3	1.0000
	O2	0.12981(24)	0.21266(23)	0.13809(7)	0.858(37)	1	18	O	4	1.0000
	O1	0.000000	0.000000	0.500000	2.418(118)	-3	3	O	5	1.0000
	P	0.28481(21)	0.26849(19)	0.09238(8)	0.350(33)	1	18	P	6	1.0000
	Si3	0.000000	0.000000	0.43187(12)	0.16(7)	3	6	SI	7	1.0000
	Si2	0.000000	0.000000	0.18013(16)	0.13(4)	3	6	SI	8	1.0000
	Si1	0.000000	0.000000	0.000000	0.13(4)	-3	3	SI	9	1.0000

GEM63213_818_0.833A_dry_8mm_FixedF 11Feb2014	Name	X	Y	Z	Ui/Ue*100	Site sym	Mult	Type	Seq	Fractn
0.833 untreated	O5	0.45836(17)	0.25118(15)	0.11163(4)	0.390(29)	1	18	O	1	1.0000
	O4	0.35609(16)	0.48827(15)	0.07768(6)	0.640(30)	1	18	O	2	1.0000
	O3	0.20822(18)	0.14642(17)	0.04068(6)	0.576(33)	1	18	O	3	1.0000
	O2	0.12994(18)	0.21256(17)	0.13798(5)	0.609(29)	1	18	O	4	1.0000
	O1	0.000000	0.000000	0.500000	1.923(86)	-3	3	O	5	1.0000
	P	0.28504(16)	0.26838(15)	0.09233(6)	0.258(28)	1	18	P	6	1.0000
	Si3	0.000000	0.000000	0.43233(10)	0.104(55)	3	6	SI	7	1.0000
	Si2	0.000000	0.000000	0.18028(13)	0.044(35)	3	6	SI	8	1.0000
	Si1	0.000000	0.000000	0.000000	0.044(35)	-3	3	SI	9	1.0000

Summary of Rietveld refinements from neutron data, P/Si = 0.833

Varied occupancies

GEM63215_A_6mm_0.833A_D2O_3h	Name	X	Y	Z	Ui/Ue*100	Site sym	Mult	Type	Seq	Fractn
0.833 D_2O	O5	0.457734	0.250716	0.111529	0.648(32)	1	18	O	1	1
	O4	0.356479	0.488804	0.077797	0.813(33)	1	18	O	2	0.9915
	O3	0.207958	0.14672	0.040661	0.763(38)	1	18	O	3	0.987
	O2	0.129808	0.212661	0.138087	0.814(36)	1	18	O	4	0.9829
	O1	0	0	0.5	2.317(105)	-3	3	O	5	0.9904
	P	0.284813	0.268489	0.092375	0.193(29)	1	18	P	6	0.9695
	Si3	0	0	0.431873	-0.14(6)	3	6	SI	7	0.9293
	Si2	0	0	0.180129	0.20(4)	3	6	SI	8	1
	Si1	0	0	0	0.20(4)	-3	3	SI	9	1

GEM63213_818_0.833A_dry_8mm	Name	X	Y	Z	Ui/Ue*100	Site sym	Mult	Type	Seq	Fractn
0.833 untreated	O5	0.458358	0.251182	0.111629	0.540(29)	1	18	O	1	1
	O4	0.356095	0.488273	0.077682	0.674(29)	1	18	O	2	0.9858
	O3	0.20822	0.146424	0.040676	0.602(31)	1	18	O	3	0.9857
	O2	0.129939	0.212558	0.13798	0.597(29)	1	18	O	4	0.9845
	O1	0	0	0.5	1.853(79)	-3	3	O	5	0.9903
	P	0.285038	0.268381	0.092332	0.107(25)	1	18	P	6	0.9679
	Si3	0	0	0.432332	-0.140(49)	3	6	SI	7	0.9413
	Si2	0	0	0.180282	0.113(34)	3	6	SI	8	1
	Si1	0	0	0	0.113(34)	-3	3	SI	9	0.9933

Summary of Rietveld refinements from neutron data, P/Si = 1.2

Fixed occupancies

GEM63222_HiT2_RT_start 12Feb2014 fixed F, 13 February 2014	Name	X	Y	Z	Ui/Ue*100	Site sym	Mult	Type	Seq	Fractn
1.2 D_2O	O5	0.4554(4)	0.2465(4)	0.11082(11)	0.43(7)	1	18	O	1	1.0000
	O4	0.3585(4)	0.4905(4)	0.07817(13)	0.41(7)	1	18	O	2	1.0000
	O3	0.2105(5)	0.1484(4)	0.04052(15)	0.77(8)	1	18	O	3	1.0000
	O2	0.1300(5)	0.2128(5)	0.13890(14)	1.72(9)	1	18	O	4	1.0000
	O1	0.000000	0.000000	0.500000	6.05(38)	-3	3	O	5	1.0000
	P	0.2808(4)	0.2693(4)	0.09308(16)	0.22(6)	1	18	P	6	1.0000
	Si3	0.000000	0.000000	0.43097(22)	-0.40(6)	3	6	SI	7	1.0000
	Si2	0.000000	0.000000	0.17878(28)	-0.40(6)	3	6	SI	8	1.0000
	Si1	0.000000	0.000000	0.000000	-0.40(6)	-3	3	SI	9	1.0000

GEM63046_HiT1_RT_start 12Feb2014 fixed F	Name	X	Y	Z	Ui/Ue*100	Site sym	Mult	Type	Seq	Fractn
1.2 untreated	O5	0.45706(29)	0.24894(25)	0.11119(7)	0.45(4)	1	18	O	1	1.0000
	O4	0.35734(26)	0.48951(24)	0.07786(9)	0.52(4)	1	18	O	2	1.0000
	O3	0.20993(30)	0.14750(28)	0.04052(10)	0.69(5)	1	18	O	3	1.0000
	O2	0.12994(32)	0.21276(31)	0.13835(9)	1.13(5)	1	18	O	4	1.0000
	O1	0.000000	0.000000	0.500000	3.30(18)	-3	3	O	5	1.0000
	P	0.28288(27)	0.26860(25)	0.09275(10)	0.24(4)	1	18	P	6	1.0000
	Si3	0.000000	0.000000	0.43170(16)	-0.12(4)	3	6	SI	7	1.0000
	Si2	0.000000	0.000000	0.17925(20)	-0.12(4)	3	6	SI	8	1.0000
	Si1	0.000000	0.000000	0.000000	-0.12(4)	-3	3	SI	9	1.0000

Summary of Rietveld refinements from neutron data, P/Si = 1.2

Varied occupancies

GEM63222_HiT2_RT_start	Name	X	Y	Z	Ui/Ue*100	Site sym	Mult	Type	Seq	Fractn
1.2 D_2O	O5	0.455416	0.246528	0.110822	0.52(6)	1	18	O	1	1
	O4	0.358489	0.490489	0.078173	0.37(6)	1	18	O	2	0.9832
	O3	0.21047	0.148371	0.04052	0.89(8)	1	18	O	3	0.9972
	O2	0.130029	0.212755	0.138903	1.72(9)	1	18	O	4	0.9883
	O1	0	0	0.5	6.01(34)	-3	3	O	5	1
	P	0.280809	0.269306	0.093082	0.09(6)	1	18	P	6	0.9714
	Si3	0	0	0.430971	-0.85(8)	3	6	SI	7	0.9378
	Si2	0	0	0.178782	-0.20(7)	3	6	SI	8	1
	Si1	0	0	0	-0.20(7)	-3	3	SI	9	1

GEM63046_HiT1_RT_start	Name	X	Y	Z	Ui/Ue*100	Site sym	Mult	Type	Seq	Fractn
1.2 untreated	O5	0.45706	0.248944	0.111189	0.62(4)	1	18	O	1	1
	O4	0.35734	0.489514	0.077863	0.58(4)	1	18	O	2	0.9888
	O3	0.20993	0.147504	0.040518	0.72(5)	1	18	O	3	0.9825
	O2	0.129937	0.212764	0.138349	1.17(5)	1	18	O	4	0.9908
	O1	0	0	0.5	3.27(16)	-3	3	O	5	1
	P	0.282877	0.2686	0.09275	0.06(4)	1	18	P	6	0.9613
	Si3	0	0	0.431697	-0.59(6)	3	6	SI	7	0.9232
	Si2	0	0	0.179251	0.06(5)	3	6	SI	8	1
	Si1	0	0	0	0.06(5)	-3	3	SI	9	1

Summary of Rietveld refinements from neutron data, P/Si = 1.44

Fixed occupancies

GEM63416_1.44G with D2O 8mm (pos 15) fixed F, 12Feb2014	Name	X	Y	Z	Ui/Ue*100	Site sym	Mult	Type	Seq	Fractn
1.44 D_2O	O5	0.45834(19)	0.25176(18)	0.11145(5)	0.490(28)	1	18	O	1	1.0000
	O4	0.35517(19)	0.48755(16)	0.07761(6)	0.539(28)	1	18	O	2	1.0000
	O3	0.20897(20)	0.14590(19)	0.04050(7)	0.530(32)	1	18	O	3	1.0000
	O2	0.12931(20)	0.21250(19)	0.13765(5)	0.507(29)	1	18	O	4	1.0000
	O1	0.000000	0.000000	0.500000	1.303(80)	-3	3	O	5	1.0000
	P	0.28535(18)	0.26769(16)	0.09260(7)	0.132(26)	1	18	P	6	1.0000
	Si3	0.000000	0.000000	0.43365(11)	0.23(6)	3	6	SI	7	1.0000
	Si2	0.000000	0.000000	0.17997(14)	0.11(4)	3	6	SI	8	1.0000
	Si1	0.000000	0.000000	0.000000	0.11(4)	-3	3	SI	9	1.0000

GEM63214_831_1.44G_dry Fixed F 12Feb2014	Name	X	Y	Z	Ui/Ue*100	Site sym	Mult	Type	Seq	Fractn
1.44 untreated	O5	0.45853(18)	0.25221(17)	0.11139(5)	0.512(28)	1	18	O	1	1.0000
	O4	0.35476(18)	0.48717(16)	0.07742(6)	0.562(28)	1	18	O	2	1.0000
	O3	0.20903(20)	0.14536(18)	0.04047(6)	0.741(34)	1	18	O	3	1.0000
	O2	0.12987(19)	0.21261(18)	0.13756(5)	0.500(28)	1	18	O	4	1.0000
	O1	0.000000	0.000000	0.500000	1.578(84)	-3	3	O	5	1.0000
	P	0.28507(17)	0.26773(16)	0.09271(7)	0.146(26)	1	18	P	6	1.0000
	Si3	0.000000	0.000000	0.43337(11)	0.29(6)	3	6	SI	7	1.0000
	Si2	0.000000	0.000000	0.17982(14)	0.21(4)	3	6	SI	8	1.0000
	Si1	0.000000	0.000000	0.000000	0.21(4)	-3	3	SI	9	1.0000

Summary of Rietveld refinements from neutron data, P/Si = 1.44

Varied occupancies

GEM63416_1.44G with D2O 8mm (pos 15)	Name	X	Y	Z	Ui/Ue*100	Site sym	Mult	Type	Seq	Fractn
1.44 D_2O	O5	0.458339	0.251758	0.111445	0.546(27)	1	18	O	1	1
	O4	0.355174	0.487549	0.077608	0.553(27)	1	18	O	2	0.995
	O3	0.208968	0.145897	0.040502	0.581(31)	1	18	O	3	0.9992
	O2	0.129311	0.212504	0.137645	0.544(28)	1	18	O	4	1
	O1	0	0	0.5	1.303(74)	-3	3	O	5	1
	P	0.285348	0.267688	0.092598	0.015(23)	1	18	P	6	0.9795
	Si3	0	0	0.433654	0.123(54)	3	6	SI	7	0.9753
	Si2	0	0	0.179974	0.120(33)	3	6	SI	8	1
	Si1	0	0	0	0.120(33)	-3	3	SI	9	1

GEM63214_831_1.44G_dry	Name	X	Y	Z	Ui/Ue*100	Site sym	Mult	Type	Seq	Fractn
1.44 untreated	O5	0.458533	0.252209	0.11139	0.559(27)	1	18	O	1	1
	O4	0.35476	0.487173	0.077417	0.596(27)	1	18	O	2	1
	O3	0.209026	0.145362	0.040467	0.773(32)	1	18	O	3	1
	O2	0.129871	0.212609	0.137556	0.525(27)	1	18	O	4	1
	O1	0	0	0.5	1.419(77)	-3	3	O	5	0.9811
	P	0.285073	0.267728	0.092714	0.059(24)	1	18	P	6	0.9864
	Si3	0	0	0.433368	0.169(55)	3	6	SI	7	0.9769
	Si2	0	0	0.179823	0.220(34)	3	6	SI	8	1
	Si1	0	0	0	0.220(34)	-3	3	SI	9	1

Appendix B

GSAS methodology, manual refinement

GEM63046_HiT1_RT_start 12Feb2014 fixed F

GEM63046 **12 February 2014**

Cell prm from original CIF-file: 1_2F_RTDRY_ALL
Fixing all F's to 1.000
Background 1, 8 terms - all histograms
Powpref

dmin - dmax, multiple banks
6 cycles

Refine cell	64.37
UISO for P	64.20
UISO for Si3	64.20
UISO for Si2, Si1:	64.19
Deactivate U's	
U for O1, O2	64.05
U for O3	64.01
U for O5	63.95
Deactivate U for all.	
X for P:	63.87
X for Si3:	63.72
X for Si2, Si1:	63.61
X for O1-O3:	62.36
X for O4, O5:	61.86
U for all, except O4	63.26
Background 1, 12 terms ALL: 31.09	
Background 1, 20 terms ALL: 14.61	
U for O4	14.50
Zero, ALL:	13.48
DIFA ALL:	13.26
beta, ALL:	10.45
switch ALL:	9.470
~~sig-0, ALL:~~	~~25.56~~
sig-1, ALL:	5.504
sig-2, ALL:	5.429
~~gam-0, ALL:~~	~~6.309~~
gam-1, ALL:	5.259
~~gam-2, ALL:~~	~~6.337~~
stec, ALL:	5.171
Couple U for Si1, Si2, Si3	
(value of Si2=…..)	5.213
PowPr + genles	**5.210**

200 variables

Decent fit.
Did this refinement pretty much exactly the same way as for the D2O one, so should be directly comparable.

I have chosen to have all UISOs free, except Si1 and Si2 which are coupled (at the end). This because Si1 was negative prior to coupling.

I will use the UISO values and XYZ values from this refinement for a new one to determine F values.

GEM63046_HiT1_RT_start 30July2014 fixed F, Si2const

GEM63046 **30 July 2014**

Copied the entire folder of
HiT1_RT_start, from the folder "RT Samples Fixed F, Feb2014"

Deactivating UISO and XYZ for all atoms, now varying the F's (which all start at 1.00). All F's can be varied except Si2 and O5.

(Starts at a chi square of 5.194)

F for P	5.182
F for Si3:	5.167
~~F for Si2:~~	
F for Si1:	5.167
F for O1:	5.168
F for O2:	5.168
F for O3:	5.171
F for O4:	5.178
~~F for O5:~~	

deactivated F for Si1-Si3
U for Si1-Si3 5.176

Deactivated F's for rest
U for all 5.166

Took away UISO constraint Si1-S3
5.111

Constrained UISO for Si1 and Si2
5.142

No U's

F for Si1, Si3	5.130
F for P, O1, O2	5.126
F for O3, O4	5.137

Powpref + genles **5.114**

Forced F to be 1 on Si1 and O1 as these were more than 1
5.114

U on all

Forced F to be 1 on Si1 and O1 5.111

No F's, U on all 5.108

Powpref + genles **5.144**

184 variables

Sequential Rietveld refinement methodology for neutron data

HiT1 – Sequential GSAS

Copied **HiT1_RT_start** from the folder:
MyWork\ISIS2013\Beam time data\RT Samples Fixed F, Feb2014\Varied_F_post_fixed_F_Si2const

Location of file: MyWork\ISIS2013\Beam time data\Sequential GSAS, post fixed F, Si2 const

renamed to shorter file name: GEM63046.EXP

tick
gam-0

untick:
gam-1
stec

genles, PowPref + genles

5.108

untick gam-0

Disabled all U's

UISOs are to be set to the values they have at 500°C on the way up (in between RT and 1000°C)

change UISO for P to: 0.00375
5.150
changed UISO for Si's: 0.00180 (coupled all)
5.260
X on all: 5.245

F on Si1, O2-O4 5.230

F on P and Si3: 5.215

Change UISO for O1 (0.05023) and O2 (0.01842) 5.331

Changed UISO for O3 (0.01828), O4 (0.01497) and O5 (0.01296 5.996

untick sig-1

PowPr + genles6.006

Make sure print option 1024 is enabled.

V4A:
5.974
All oxygens' F set to 1 and can't be varied, no profile options ticked at all. 5.980

V4B:
5.974
F for P and all Si's set to 1 and can't be varied, otherwise same as V3.
6.119

Start runs

Appendix C

Combined TG and DTA results for P-Si gels

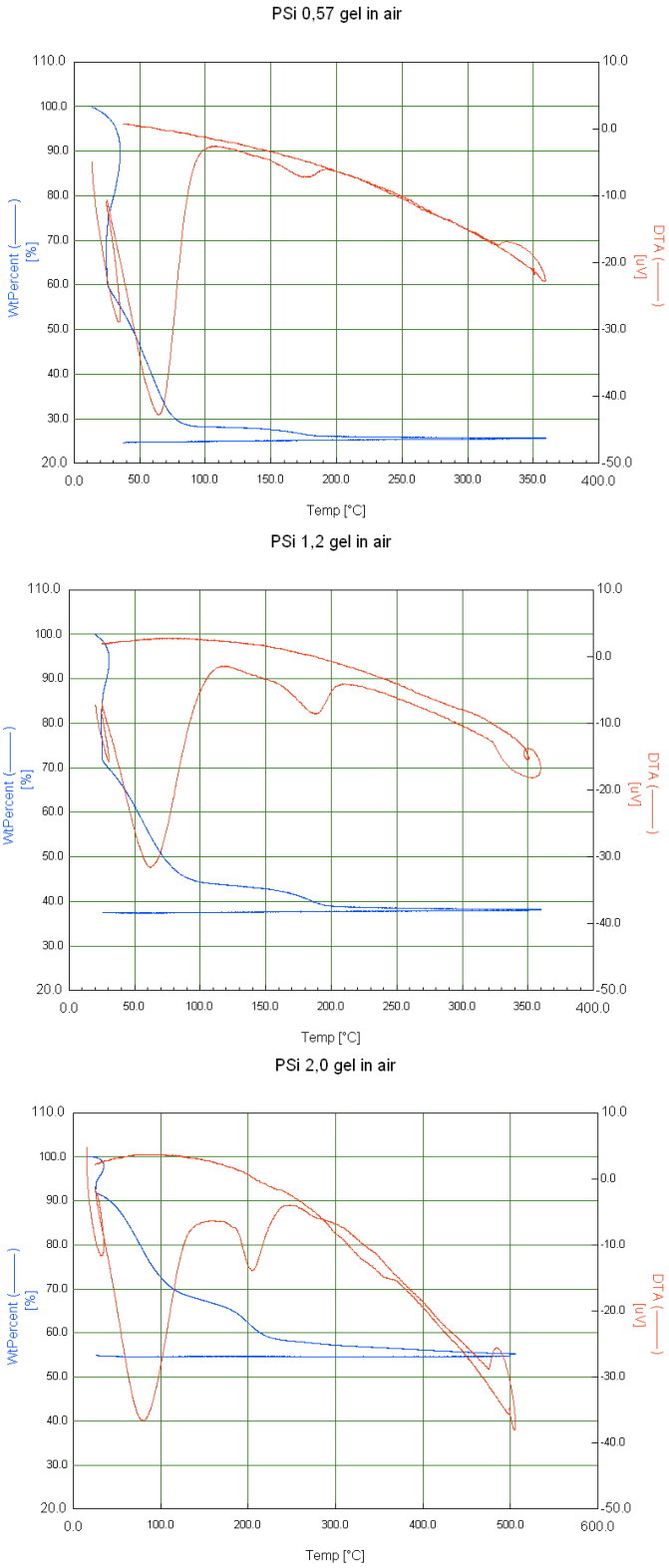

Figure 93 *TGA and DTA measurements of P-Si gels. The 2.0 gel (precursor to SiP_2O_7 was tested up to 500°C, the other two were run up to 350°C. Note the very large loss of water for the silicon rich sample (P/Si = 0.57) and that there appears to be a trend of retaining more water for higher amounts of phosphoric acid. The DTA peaks do also occur at higher temperatures for the 2.0 sample compared to the others.*

Appendix D

Sintering temperatures and times

Sample name	P/Si starting ratio	Sintering temperature (°C) and time (h)	Ramp rate (°C / hour)	Note		
0.57 V	0.57	300°C 2h, 950°C 12h	+8°C/h, -10°C/h			
0.57 VW	0.57	975°C 15h	+5°C/h, -5°C/h			
0.7 V	0.7	300°C 2h, 950°C 12h	+8°C/h, -10°C/h			
0.7 VW	0.7	975°C 15h	+5°C/h, -5°C/h			
0.8 UV	0.8	300°C 2h, 950°C 12h, 300°C 2h, 950°C 12h	+8°C/h, -10°C/h, +8°C/h, -10°C/h			
0.8 UVW	0.8	Same as 0.8 UV + 975°C 15h	+5°C/h, -5°C/h			
0.833 A	0.833	300°C 3h , 1000°C 50h	+8°C/h, -10°C/h	RT neutron		
1.0 KM	1.0	300 3h, 950°C 15h; 975°C 15h,	+8°C/h, -10°C/h ; +5°C/h, -5°C/h			
1.0 LN	1.0	300 3h, 950°C 15h; 975°C 15h	+8°C/h, -10°C/h ; +8°C/h, -10°C/h			
1.2 KM	1.2	300 3h, 950°C 15h; 975°C 15h,	+8°C/h, -10°C/h ; +5°C/h, -5°C/h			
1.2 F	1.2	300°C 3h , 1000°C 50h	+8°C/h, -10°C/h	RT and High temp neutron		
1.2 D	1.2	300°C 3h , 1000°C 50h	+8°C/h, -10°C/h			
1.2 cryst	1.2	300°C 3h , 1000°C 33.3h	+8°C/h, -10°C/h	High temp XRD		
1.2 29Si	1.2	300°C 3h, 950°C 15h	+8°C/h, -10°C/h			
	1.2	975°C 15h	+8°C/h, -10°C/h			
	1.2	975°C 24h	+8°C/h, -10°C/h			
	1.2	300°C 3h , 1000°C 30h	+8°C/h, -10°C/h			
	1.2	300°C 3h , 1000°C 33.3h	+8°C/h, -8°C/h	29Si NMR 5 weeks later		
	1.2	1000°C 1h	+8°C/h, -8°C/h	29Si NMR shortly after		
1.44 G	1.44	300°C 3h , 1000°C 50h	+8°C/h, -10°C/h			
1.44 G	1.44	Above + 1100°C for 20h		extra firing compared to 1.2F and 0.833		RT neutron
II	1.5	300 3h, 950°C 15h; 300 3h, 950°C 15h;	+8°C/h, -10°C/h ; +8°C/h, -10°C/h			
II GKMP	1.5	Above + 975°C 15h; 1100°C for 15h	+5°C/h, -5°C/h; +8°C/h, -8°C/h			
II GKMPR	1.5	Same as II GKMP + 300°C 1h , 1000°C 15h	+8°C/h, -8°C/h			
Al5 TB		240°C over night, 900°C 30h; 975°C 12h				
Al2.5 TB		240°C over night, 900°C 30h; 975°C 12h				
Al5Ti5 TB		240°C over night, 900°C 30h; 975°C 12h				
Al7.5 TB		240°C over night, 900°C 30h; 975°C 12h				
Al5Ti1.66 TB		240°C over night, 900°C 30h; 975°C 12h				
Ge3Si2O(PO4)6		300°C 3h , 1000°C 50h	+8°C/h, -10°C/h			
Ge3Si2O(PO4)6		1100°C for 16h	+8°C/h, -10°C/h			

Stoichiometries of substituted samples – chapter 5

	Al	Ti	Si	P	O	P/Si	P/(Si+dopant)
	0,0000		5,0000	6,0000	25,0000	1,200	1,200
Al 2.5	0,1250		4,8750	6,0000	25,0000	1,231	1,200
Al 5	0,2500		4,7500	6,0000	25,0000	1,263	1,200
Al 7.5	0,3750		4,6250	6,0000	25,0000	1,297	1,200
Al5 Ti1,66	0,2500	0,0833	4,6667	6,0000	25,0000	1,286	1,200
Al5 Ti5	0,2500	0,2500	4,5000	6,0000	25,0000	1,333	1,200

Appendix E1

Graphs of Si_O bond lengths from Rietveld refinement results

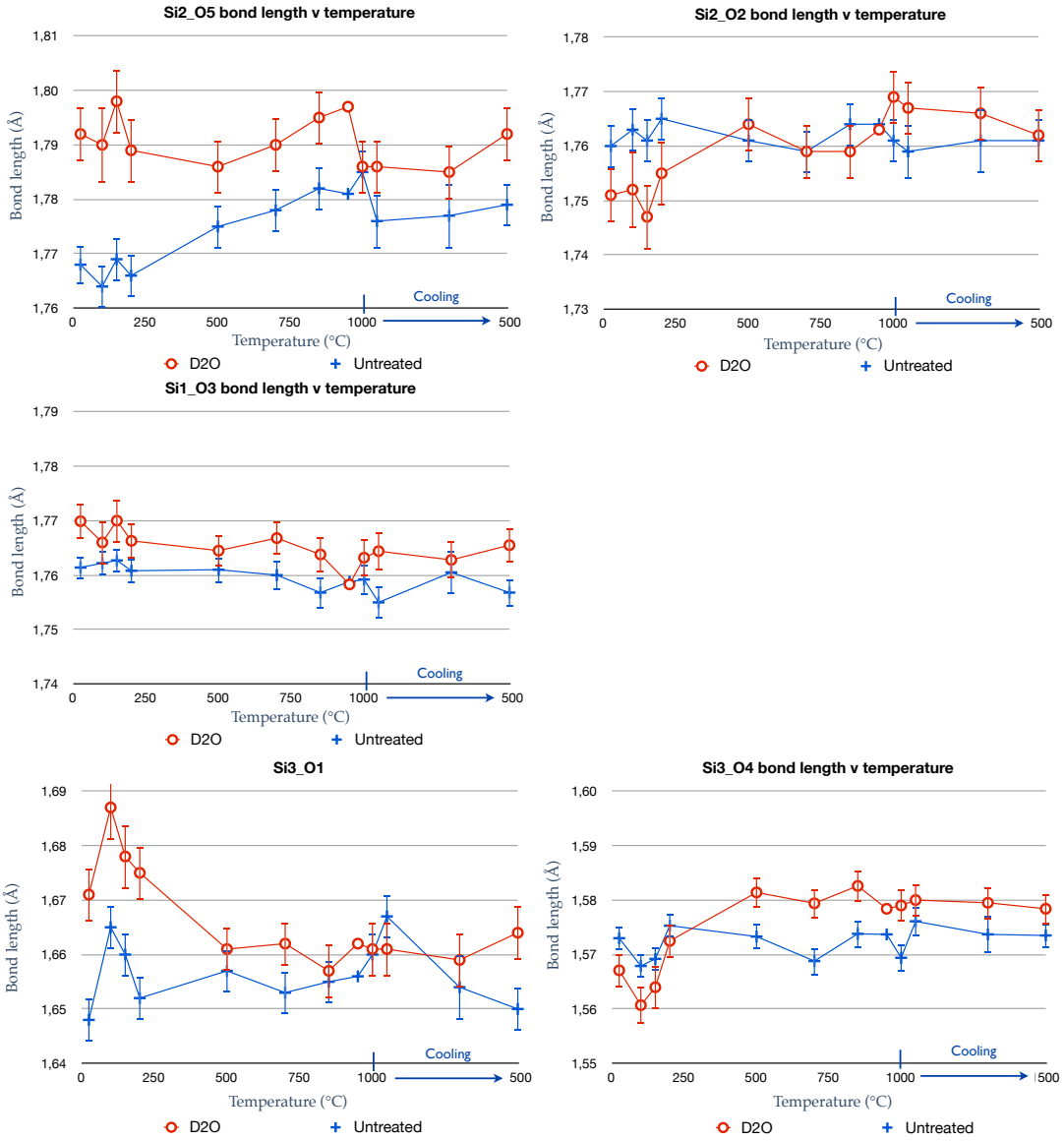

Graphs of P_O bond lengths from Rietveld refinement results

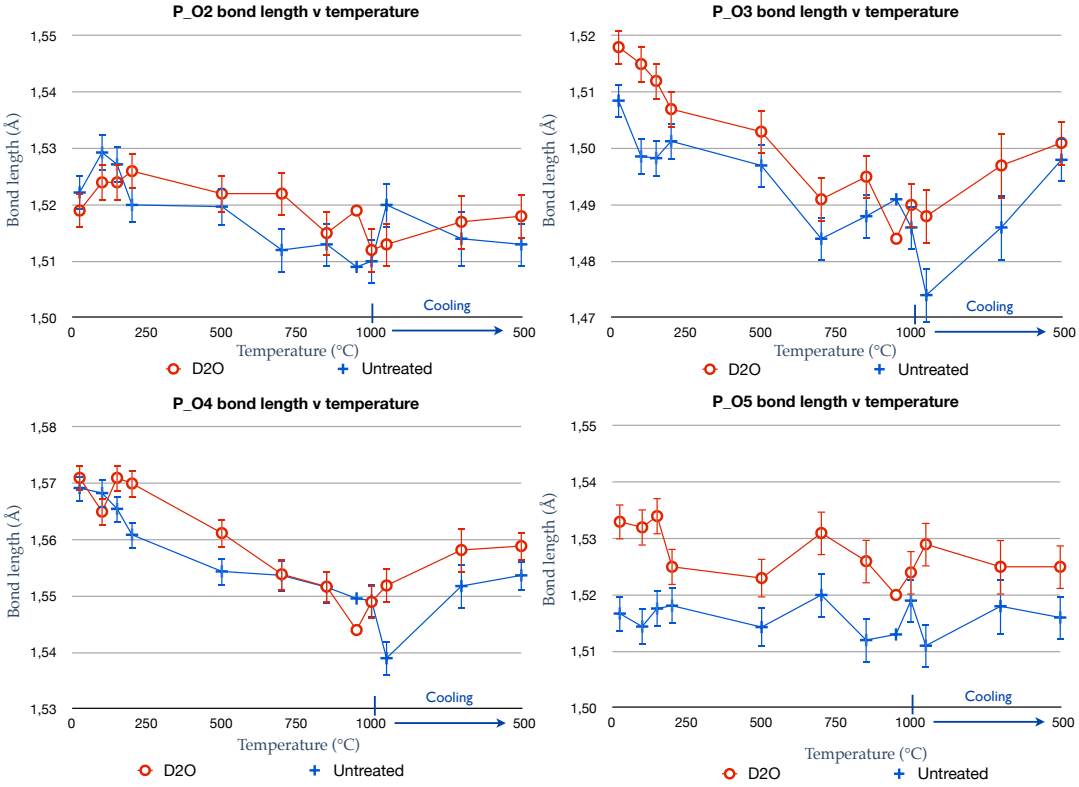

Graphs of average bond lengths from Rietveld refinement results

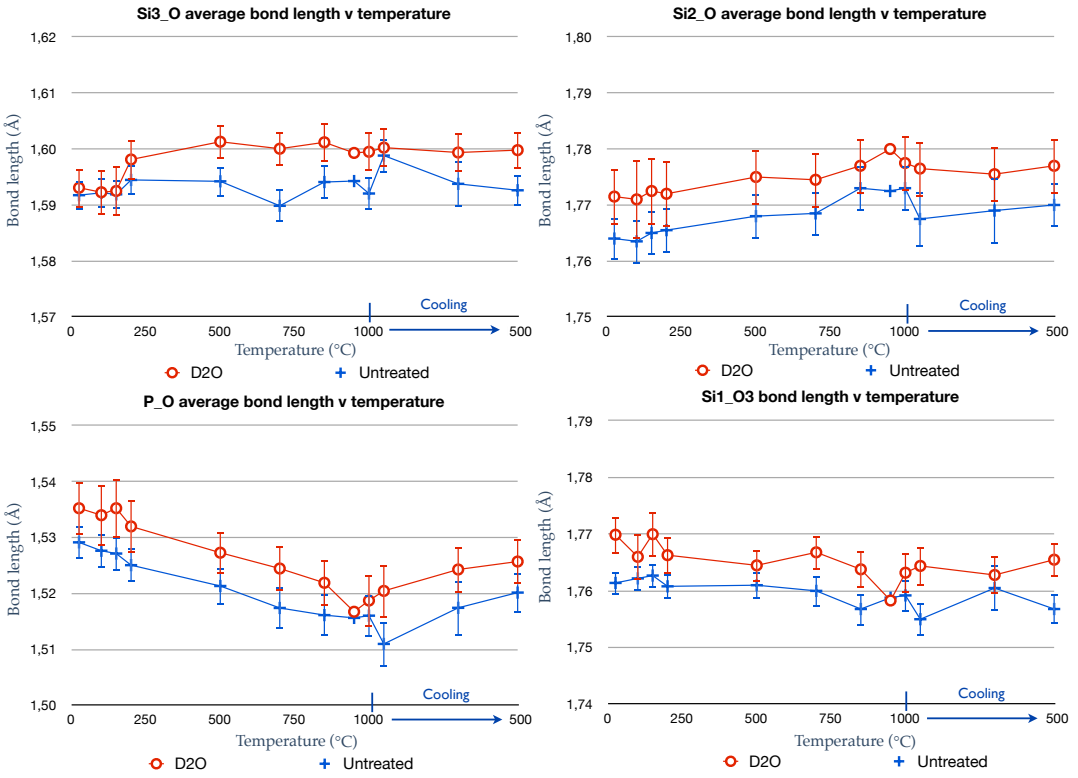

Appendix E2

Bond lengths and bond angles from Rietveld refinement results, untreated

		Bond lengths (Å)								
Number	Bond	HiT1 RT start	HiT1 100 up	HiT1 150 up	HiT1 200 up	HiT1 500 up	HiT1 700 up	HiT1 850 up	HiT1 950 up	HiT1 1000
6 x	Si1_O3	1.7614(21)	1.7622(22)	1.7627(22)	1.7608(23)	1.7610(24)	1.7600(28)	1.7568(29)	1.7588(29)	1.7592(30)
3 x	Si2_O2	1.760(4)	1.763(4)	1.761(4)	1.765(4)	1.761(4)	1.759(4)	1.764(4)	1.764(4)	1.761(5)
3 x	Si2_O5	1.7680(35)	1.764(4)	1.769(4)	1.766(4)	1.775(4)	1.778(4)	1.782(4)	1.781(4)	1.785(5)
1 x	Si3_O1	1.648(4)	1.665(4)	1.660(4)	1.652(4)	1.657(4)	1.653(4)	1.655(4)	1.656(4)	1.660(4)
3 x	Si3_O4	1.5730(22)	1.5679(22)	1.5692(22)	1.5753(22)	1.5733(23)	1.5688(26)	1.5738(26)	1.5737(26)	1.5694(27)
	P_O2	1.5222(31)	1.5293(33)	1.5272(33)	1.5200(32)	1.5197(34)	1.512(4)	1.513(4)	1.509(4)	1.510(4)
	P_O3	1.5085(31)	1.4986(33)	1.4983(33)	1.5013(33)	1.497(4)	1.484(4)	1.488(4)	1.491(4)	1.486(5)
	P_O4	1.5692(24)	1.5683(26)	1.5655(25)	1.5609(25)	1.5544(26)	1.5537(29)	1.5516(29)	1.5496(30)	1.5492(31)
	P_O5	1.5167(32)	1.5144(33)	1.5176(33)	1.5181(33)	1.5143(35)	1.520(4)	1.512(4)	1.513(4)	1.519(4)
	Angle	Bond angles (°)								
3 x	O3_Si1_O3	180.000(0)	180.000(0)	180.000(0)	180.000(0)	180.000(0)	180.000(0)	180.000(0)	180.000(0)	180.000(0)
6 x	O3_Si1_O3	92.16(10)	91.67(11)	91.72(11)	91.85(11)	91.45(12)	90.93(14)	91.16(14)	91.36(14)	91.26(15)
6 x	O3_Si1_O3	87.84(10)	88.33(11)	88.28(11)	88.15(11)	88.55(12)	89.07(14)	88.84(14)	88.64(14)	88.74(15)
3 x	O2_Si2_O2	91.62(21)	91.51(24)	91.79(24)	91.51(22)	91.86(23)	92.29(26)	92.16(26)	92.12(27)	92.20(28)
3 x	O5_Si2_O2	89.08(10)	88.98(10)	88.92(10)	88.98(10)	88.81(11)	88.57(12)	88.74(12)	88.83(12)	88.94(13)
3 x	O5_Si2_O2	178.13(26)	178.62(30)	178.22(31)	178.44(27)	178.31(30)	177.84(34)	177.99(34)	178.0(4)	177.8(4)
3 x	O5_Si2_O2	90.09(9)	89.78(9)	89.82(9)	89.96(9)	89.67(10)	89.66(11)	89.61(11)	89.60(11)	89.68(12)
3 x	O5_Si2_O5	89.19(22)	89.73(25)	89.45(25)	89.54(23)	89.64(24)	89.45(27)	89.46(27)	89.42(28)	89.14(29)
3 x	O4_Si3_O1	108.33(15)	107.77(15)	107.82(16)	108.19(16)	107.87(16)	107.65(19)	107.92(19)	107.94(19)	107.76(21)
3 x	O4_Si3_O4	110.59(14)	111.12(14)	111.07(15)	110.72(15)	111.02(15)	111.23(17)	110.98(18)	110.96(18)	111.13(19)
	O3_P_O2	115.25(15)	115.00(15)	115.16(15)	115.24(15)	115.07(16)	115.18(18)	115.20(19)	115.19(19)	115.20(20)
	O4_P_O2	106.74(16)	106.72(16)	106.80(16)	106.95(16)	107.19(17)	106.81(19)	106.82(19)	106.80(19)	106.93(21)
	O5_P_O2	112.30(19)	111.82(21)	111.62(20)	111.76(20)	111.20(22)	110.85(24)	110.64(25)	110.93(26)	110.61(28)
	O4_P_O3	108.60(21)	108.97(23)	109.18(23)	108.84(23)	109.08(26)	109.46(29)	109.18(29)	108.50(30)	109.09(32)
	O5_P_O3	104.98(16)	105.45(16)	105.31(17)	105.20(17)	105.45(18)	105.88(20)	106.21(20)	106.27(21)	106.10(22)
	O5_P_O4	108.83(15)	108.74(15	108.63(15)	108.71(15)	108.71(17)	108.54(19)	108.66(20)	109.03(20)	108.80(21)

		Bond lengths (Å)		
Number	Bond	HiT1 950 down	HiT1 700 down	500 down
6 x	Si1_O3	1.755(4)	1.7605(26)	1.7568(25)
3 x	Si2_O2	1.759(6)	1.761(4)	1.761(4)
3 x	Si2_O5	1.776(6)	1.777(4)	1.779(4)
1 x	Si3_O1	1.667(6)	1.654(4)	1.650(4)
3 x	Si3_O4	1.5761(34)	1.5737(24)	1.5735(23)
	P_O2	1.520(5)	1.514(4)	1.5130(34)
	P_O3	1.474(6)	1.486(4)	1.498(4)
	P_O4	1.539(4)	1.5518(27)	1.5537(26)
	P_O5	1.511(5)	1.518(4)	1.5160(34)
	Angle	Bond angles (°)		
3 x	O3_Si1_O3	180.000(0)	180.000(0)	180.000(0)
6 x	O3_Si1_O3	90.78(20)	91.24(13)	91.35(12)
6 x	O3_Si1_O3	89.22(20)	88.76(13)	88.65(12)
3 x	O2_Si2_O2	92.2(4)	92.30(25)	92.51(23)
3 x	O5_Si2_O2	88.74(16)	88.73(11)	88.62(10)
3 x	O5_Si2_O2	177.9(5)	177.77(32)	177.56(30)
3 x	O5_Si2_O2	89.62(15)	89.63(10)	89.60(9)
3 x	O5_Si2_O5	89.4(4)	89.29(25)	89.23(23)
3 x	O4_Si3_O1	107.67(26)	107.80(17)	108.13(16)
3 x	O4_Si3_O4	111.21(25)	111.09(16)	110.78(15)
	O3_P_O2	114.57(25)	115.35(17)	115.32(16)
	O4_P_O2	107.09(28)	106.61(18)	106.98(17)
	O5_P_O2	110.4(4)	111.03(23)	111.18(22)
	O4_P_O3	109.0(4)	109.07(27)	109.05(25)
	O5_P_O3	106.61(29)	105.99(19)	105.40(17)
	O5_P_O4	109.10(27)	108.65(18)	108.78(16)

Bond lengths and bond angles from Rietveld refinement results, hydrothermally treated

		Bond lengths (Å)								
Number	Bond	HiT2 RT start	HiT2 100C	HiT2 150 up	HiT2 200 up	HiT2 500 up	HiT2 700 up	HiT2 850 up	HiT2 950 up	HiT2 1000C
6 x	Si1_O3	1.7699(33)	1.766(4)	1.770(4)	1.7663(33)	1.7645(29)	1.7668(31)	1.7638(33)	1.7583(35)	1.7632(35)
3 x	Si2_O2	1.751(5)	1.752(7)	1.747(6)	1.755(6)	1.764(5)	1.759(5)	1.759(5)	1.763(5)	1.769(5)
3 x	Si2_O5	1.792(5)	1.790(7)	1.798(6)	1.789(6)	1.786(5)	1.790(5)	1.795(5)	1.797(5)	1.786(5)
1 x	Si3_O1	1.671(5)	1.687(6)	1.678(6)	1.675(5)	1.661(4)	1.662(4)	1.657(5)	1.662(5)	1.661(5)
3 x	Si3_O4	1.5671(31)	1.5607(35)	1.564(4)	1.5725(31)	1.5814(28)	1.5794(28)	1.5826(29)	1.5784(30)	1.5790(30)
	P_O2	1.519(5)	1.524(6)	1.524(6)	1.526(5)	1.522(4)	1.522(4)	1.515(4)	1.519(5)	1.512(5)
	P_O3	1.518(5)	1.515(6)	1.512(6)	1.507(5)	1.503(4)	1.491(5)	1.495(5)	1.484(5)	1.490(5)
	P_O4	1.571(4)	1.565(4)	1.571(4)	1.570(4)	1.5612(32)	1.5539(33)	1.5517(34)	1.544(4)	1.549(4)
	P_O5	1.533(5)	1.532(6)	1.534(5)	1.525(5)	1.523(4)	1.531(4)	1.526(4)	1.520(5)	1.524(5)
	Angle	Bond angles (°)								
3 x	O3_Si1_O3	180.000(0)	180.000(0)	180.000(0)	180.000(0)	180.000(0)	180.000(0)	180.000(0)	180.000(0)	180.000(0)
6 x	O3_Si1_O3	92.26(17)	91.87(20)	91.83(19)	91.38(17)	91.57(15)	90.96(16)	90.99(17)	90.63(18)	91.01(17)
6 x	O3_Si1_O3	87.74(17)	88.13(20)	88.17(19)	88.62(17)	88.43(15)	89.04(16)	89.01(17)	89.37(18)	88.99(17)
3 x	O2_Si2_O2	92.54(31)	92.3(4)	92.7(4)	92.55(35)	92.43(27)	92.75(29)	92.85(31)	92.52(32)	92.20(31)
3 x	O5_Si2_O2	88.52(15)	88.38(17)	88.26(17)	88.37(14)	88.74(13)	88.38(13)	88.27(13)	88.44(14)	88.39(14)
3 x	O5_Si2_O2	177.0(4)	177.4(5)	177.2(5)	177.6(5)	177.6(4)	177.4(4)	177.2(4)	177.6(4)	178.1(4)
3 x	O5_Si2_O2	90.20(14)	90.14(16)	89.85(16)	89.60(13)	89.60(11)	89.55(12)	89.65(12)	89.68(13)	89.55(13)
3 x	O5_Si2_O5	88.68(31)	89.1(4)	89.1(4)	89.4(4)	89.19(28)	89.27(30)	89.17(31)	89.32(33)	89.84(32)
3 x	O4_Si3_O1	107.50(22)	107.00(24)	107.24(24)	107.58(21)	108.15(19)	107.75(20)	108.10(21)	107.89(23)	108.10(23)
3 x	O4_Si3_O4	111.37(20)	111.82(22)	111.61(22)	111.30(20)	110.76(18)	111.14(19)	110.81(20)	111.00(21)	110.81(22)
	O3_P_O2	116.23(23)	115.76(26)	116.26(26)	115.54(22)	115.43(19)	115.28(20)	115.31(21)	114.71(22)	115.22(22)
	O4_P_O2	107.85(24)	108.34(29)	108.17(28)	107.72(24)	107.11(20)	107.22(21)	107.31(22)	106.80(23)	107.21(24)
	O5_P_O2	112.05(30)	111.3(4)	111.41(35)	111.40(30)	111.36(26)	110.49(28)	110.49(29)	110.00(31)	110.06(31)
	O4_P_O3	108.64(32)	109.2(4)	108.9(4)	108.86(34)	108.73(30)	109.37(33)	108.76(34)	109.2(4)	108.7(4)
	O5_P_O3	103.22(23)	103.32(28)	103.40(27)	104.56(24)	105.29(21)	105.61(22)	105.69(23)	106.40(24)	106.15(25)
	O5_P_O4	108.59(22)	108.71(25)	108.43(25)	108.57(22)	108.76(20)	108.74(21)	109.17(23)	109.66(24)	109.38(24)

		Bond lengths (Å)		
Number	Bond	HiT2 950 down	HiT2 700 down	HiT2 500 down
6 x	Si1_O3	1.7644(34)	1.7628(31)	1.7655(30)
3 x	Si2_O2	1.767(5)	1.766(5)	1.762(4)
3 x	Si2_O5	1.786(5)	1.785(5)	1.792(5)
1 x	Si3_O1	1.661(5)	1.659(5)	1.664(4)
3 x	Si3_O4	1.5800(30)	1.5795(28)	1.5784(28)
	P_O2	1.513(4)	1.517(4)	1.518(4)
	P_O3	1.488(5)	1.497(5)	1.501(4)
	P_O4	1.5519(35)	1.5582(33)	1.5589(32)
	P_O5	1.529(4)	1.525(4)	1.525(4)
	Angle	Bond angles (°)		
3 x	O3_Si1_O3	180.000(0)	180.000(0)	180.000(0)
6 x	O3_Si1_O3	91.06(17)	91.20(16)	91.10(15)
6 x	O3_Si1_O3	88.94(17)	88.80(16)	88.90(15)
3 x	O2_Si2_O2	92.05(32)	92.33(29)	92.77(27)
3 x	O5_Si2_O2	88.54(14)	88.41(13)	88.38(12)
3 x	O5_Si2_O2	178.1(4)	177.9(4)	177.3(4)
3 x	O5_Si2_O2	89.72(13)	89.63(12)	89.59(11)
3 x	O5_Si2_O5	89.66(32)	89.60(29)	89.21(28)
3 x	O4_Si3_O1	108.08(22)	108.16(20)	108.13(19)
3 x	O4_Si3_O4	110.83(21)	110.75(19)	110.77(18)
	O3_P_O2	115.37(22)	115.29(20)	115.34(19)
	O4_P_O2	107.36(23)	107.30(21)	107.56(21)
	O5_P_O2	110.39(30)	110.76(28)	110.98(26)
	O4_P_O3	108.66(35)	108.73(32)	108.88(30)
	O5_P_O3	105.87(24)	105.65(22)	104.94(21)
	O5_P_O4	109.07(23)	108.98(21)	109.02(20)

Appendix F

^{2}H NMR spectra of hydrothermally treated compositions

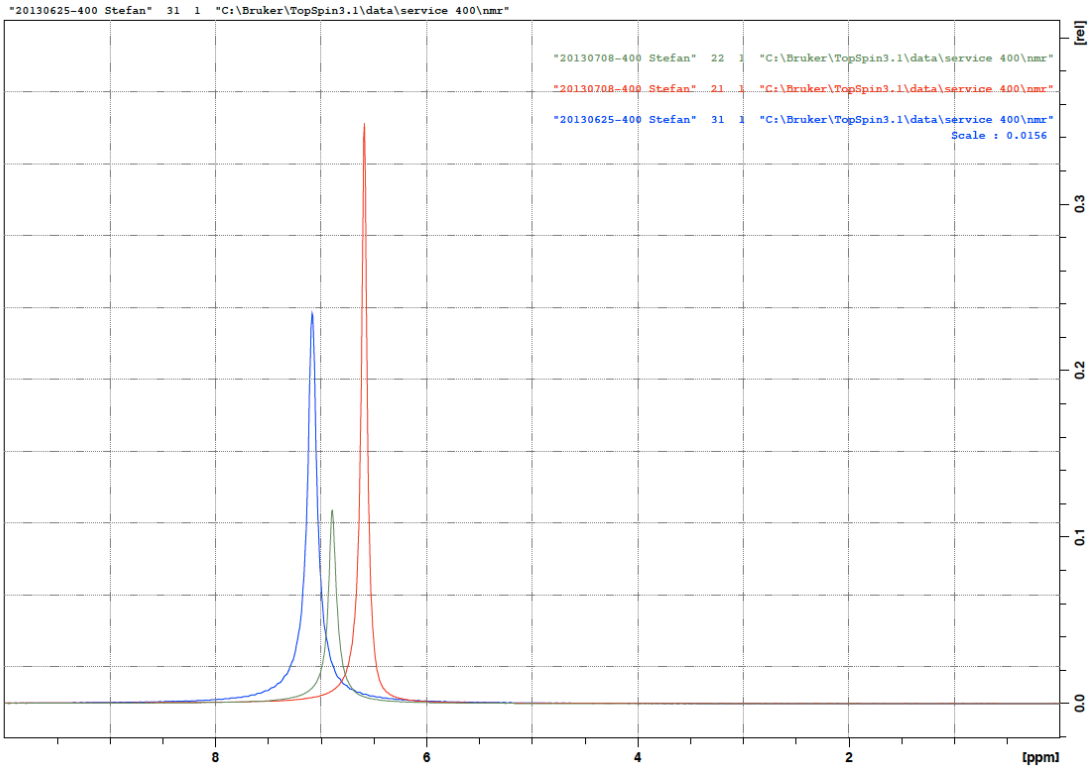

Figure 94 *^{2}H NMR spectra of the three hydrothermally treated (D_2O) P-Si compositions. The 1.2 composition (blue) has been scaled down to compensate for the longer collection time and sensitivity.*

Credit: Dr Daniel Dawson

Appendix G

Neutron data and Rietveld refinement room temperature, P/Si = 1.2, banks 1-3

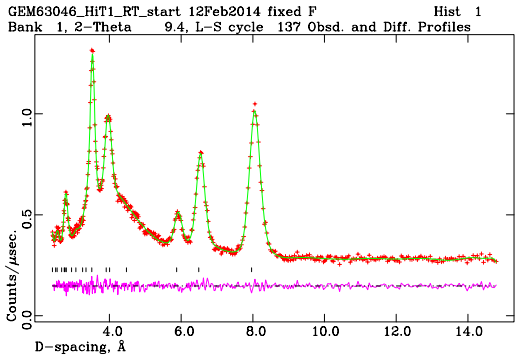

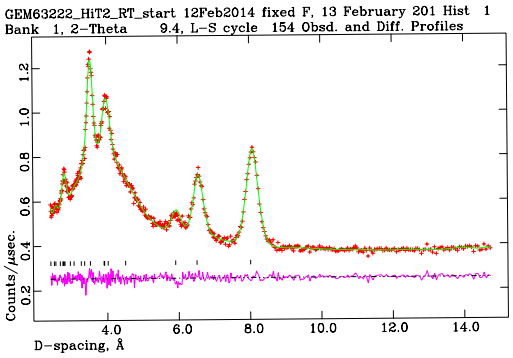

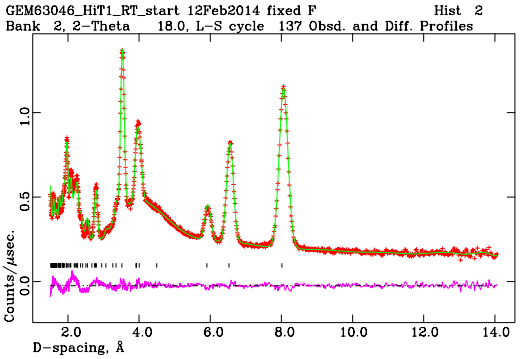

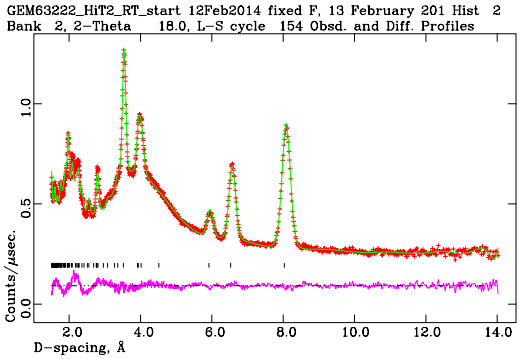

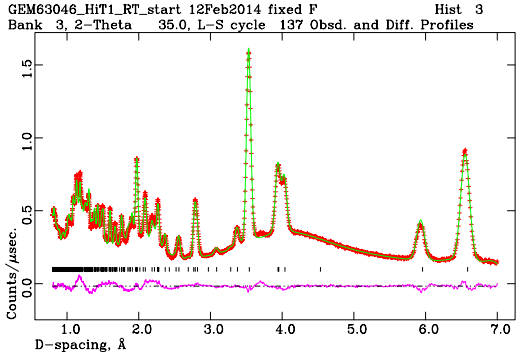

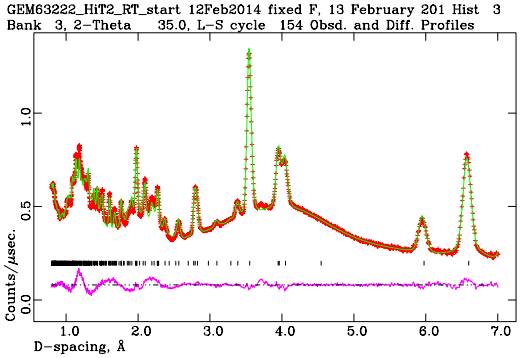

Neutron data and Rietveld refinement room temperature, P/Si = 1.2, banks 4-6